Low-Mass Companions Orbiting δ Scuti Stars

Simon J. Ebo

A thesis submitted in partial fulfilment
of the requirements for the degree of
Doctor of Philosophy

Jeremiah Horrocks Institute for Mathematics, Physics and Astronomy
University of Central Lancashire

May 2024

Declaration

Type of Award: Doctor of Philosophy

School: Physical Sciences and Computing

I declare that while registered as a candidate for the research degree, I have not been a registered candidate or enrolled student for another award of the University or other academic or professional institution.

I declare that no material contained in the thesis has been used in any other submission for an academic award and is solely my own work.

No proof-reading service was used in the compilation of this thesis.

Simon J. Ebo

May 2024

Abstract

A substantial fraction of exoplanets exist around M-type stars, but few systems have host stars hotter than the Sun and even fewer orbit hot stars that pulsate.

The discovery of planets around pulsating stars provides a laboratory that offers the opportunity for the most precise studies of exoplanet systems. To search for new systems, an exclusively UK-based exoplanet and variable star survey using UCLan's Moses Holden Telescope (MHT) was established — MOSES: MHT Optical Star and Exoplanet Survey. The MOSES field was formed of a 4×4 tiled array covering a 7-square degree region of the sky observing over 65,000 stars, 60-s per exposure strategy in the Johnson V-band. Of all stars observed during the initial 10-month MOSES campaign, just 13 were flagged to be of a variable nature with a confidence of $>5\sigma$. 10 of these 13 stars were sufficiently observed to be designated as MOSES Objects of Interest (MOIs), but the data were not of the quality required for the stellar and planetary modelling desired for the work in this thesis. As such, we ruled out a ground-based observing approach using this data set.

The Transiting Exoplanet Survey Satellite (TESS) data were scoured for δ *Scuti* host stars, suitable targets as their signature pulsation frequencies allow them to be well-modelled. Main-sequence δ Scuti host stars are extremely rare: only seven are known in the literature. Two TOIs were chosen to be studied in detail, TIC 409934330 and TIC 156987351. A grid of stellar models was built with software MESA, based on a calculated range of stellar parameters; each model was then set pulsating by the software GYRE. In parallel, the TESS data for each target were analysed in PERIOD04 to extract, separately, the orbital frequency (and its harmonics) and the pulsation frequencies of the two targets. Finally, a chi-squared analysis was employed to determine the best-fit model star for each target, by comparing the

respective GYRE frequencies with the TESS-extracted frequencies. The final models produced a mass and radius for each target of $2.10 \pm 0.19\,\mathrm{M}_{\odot}$ and $4.72 \pm 0.44\,\mathrm{R}_{\odot}$, and $1.63 \pm 0.15\,\mathrm{M}_{\odot}$ and $3.05 \pm 0.28\,\mathrm{R}_{\odot}$, respectively, amongst other parameters.

Spectroscopic ground-based observations of these targets using the Southern African Large Telescope (SALT) provided spectra that were analysed in the software iSpec, determining a T_{eff} of $8062 \pm 29\,\mathrm{K}$ for TIC 409934330 and $7231 \pm 63\,\mathrm{K}$ for TIC 156987351. The software EXOFASTv2 used these parameters to deduce the nature of the transiting companions: TIC 409934330 hosts a $2.5^{+31.0}_{-2.1}\,\mathrm{M_J}$, $1.03^{+0.85}_{-0.49}\,\mathrm{R_J}$ "hot-Jupiter", and TIC 156987351 hosts a $0.39^{+7.90}_{-0.33}\,\mathrm{M_J}$, $0.97^{+0.56}_{-0.67}\,\mathrm{R_J}$ "hot-Saturn". Hence, we have added two more examples to the δ Scuti host star population.

Populating the HR diagram with all nine now-known examples, it became clear they all existed within a very narrow region of parameter space that we labelled "The δ Scuti Cone" — furthermore, all nine stars lay at the very base of the δ Scuti region in the classical instability strip. We explained this using the hypothesis that the more luminous δ Scuti stars disrupt their proto-planetary discs with their stellar winds before their planets can form. In addition, we included β Pictoris in our final investigation since it is a well-studied pre-main sequence δ Scuti host star, and its position on the HR diagram is consistent with our sample. We explored the theoretical δ Scuti instability strip according to Dupret et al. (2004), but show that it is too narrow and does not agree with our population, which agrees better with the empirical δ Scuti instability strip of Murphy et al. (2019).

It is recommended to investigate, in detail, the remaining planet candidates that lie in and around the The δ Scuti Cone, to ascertain their physical properties and environments that support, or otherwise, the Cone's presence: such results could lead to defining a new sub-region on the classical instability strip.

Contents

List of Tables

List of Figures

Acknowledgements

First and foremost, I wish to sincerely thank Dr. Daniel Holdsworth and Professor Derek Ward-Thompson for being gracious supervisors during my time as a PhD student: their wealth of knowledge and guidance was invaluable. I would also like to thank Professor Don Kurtz, who during my very first Astronomy lecture at UCLan fired my enthusiasm for an academic career in this field. In addition, my utmost thanks goes to Amy for her support throughout the last few years, especially helping me adapt my PhD-life during the COVID-19 pandemic. Further thanks goes to my parents, who bought me my first telescope when I was six years old; and to my Grandma, who bought me an interactive astronomy CD-ROM (!) that I loved playing on when I was a child. Finally, I wish to thank everyone that I shared the postgrad office with, especially those who made every single day enjoyable — you know who you are (CVP).

Dedication

This thesis is dedicated to Mr. Clive Jones of Upton-by-Chester High School, who told me whilst I was writing my undergraduate application to UCLan:

"*Applying to University in general is too ambitious for you, let alone to study Astrophysics*"

Chapter 1

An Introduction to Asteroseismology and Exoplanets

1.1 An Introduction to Asteroseismology

"At first sight it would seem that the deep interior of the Sun and stars is less accessible to scientific investigation than any other region of the universe. Our telescopes may probe farther and farther into the depths of space; but how can we ever obtain certain knowledge of that which is hidden behind substantial barriers? What appliance can pierce through the outer layers of a star and test the conditions within?"

— Sir Arthur Stanley Eddington

The Internal Constitution of the Stars
(Eddington, 1926)

1.1.1 Praefatio

Stars are the fundamental repository for all astrophysical understanding of the Universe. Once we understand stars, we can begin to understand other phenomena. But to understand stars themselves, we need to study their light.

Starlight provides a great wealth of information that astronomers can exploit to help interpret stellar astrophysics, but a comprehensive command of the latter is vital for preventing the measured photons that have journeyed billions of miles across the universe from being wasted. Some stars also vibrate — they have sounds in them, which can be utilised as a tool for calculating stellar structure. The following Sections introduce the field of Asteroseismology: the music of the Spheres.

1.1.2 Why is Asteroseismology Important?

The mass of a single, lone star is a property that cannot be measured directly via observation. The mass-luminosity relationship (Kuiper, 1938) can provide adequate estimates, but only if a ball-park mass value is already known; the relationship changes for different mass ranges which could provide multiple mass values for a single luminosity measurement. Knowledge of the effective temperature ($T_{\rm eff}$) of a star from its $B-V$ magnitude would reveal its position on the HR Diagram, when plotted against its luminosity, reducing the ambiguity of the mass-luminosity relationship. For "normal" stars, without employing Kepler's 3$^{\rm rd}$ Law on observations of any companions[1] (Kepler, 1619), this is the best approximation for mass.

But some stars pulsate! They grow and shrink periodically, physically changing in size, temperature and colour. This concept was first theorised over 100 years ago

[1]Throughout this thesis the term "companion" is used a lot in place of "exoplanet", as in many instances the signature of an exoplanet can also be produced by other objects such as brown dwarfs, and the exact identity of an object may not be immediately known. Hence, "companion" encompasses all possibilities until further information about the object is known.

by Sir Arthur Stanley Eddington, who proffered that stars could oscillate in their natural frequencies if subjected to instability by an internal driving force; and the frequencies themselves would be governed by the physics of stellar structure (Eddington, 1917, 1926). The field of studying pulsating stars is known as "Asteroseismology", from literal Ancient Greek: "the study of oscillations in stars". The reader is directed to the fundamental text for a comprehensive asteroseismic guide: Aerts, Christensen-Dalsgaard & Kurtz (2010).

Measuring the brightness of pulsating stars over time can build light curves, revealing their brightness fluctuations induced from the pulsations: many types of pulsators display unique patterns in their light curves, and the areas where different pulsators exist on the HR diagram is well defined, so just by observing these stars good constraints on their parameters can be deduced. Furthermore, these stars and their pulsations can be accurately modelled, producing precise masses and radii amongst other parameters (see § 3.1 and § 3.2). Once we know the mass of a star, we can determine the mass of any companions it may host too.

But not only this; asteroseismology is the only branch of astrophysics that allows us to "see" inside stars. The frequencies at which pulsating stars oscillate can be exploited to map stellar interiors: they give clues about the temperature and density gradients at different depths within stars, which directly affect the local sound speed and hence the frequencies of pulsation. Furthermore, different frequency modes probe to different stellar depths, allowing the potential for full surface-to-core profiles of stars to be determined. In short: asteroseismology is the "appliance" Sir Arthur Stanley Eddington was searching for.

1.1.3 Pulsation Mode Quantum Numbers

Stars can pulsate with a variety of different pulsation modes (patterns). These modes divide up a star via latitudinal, longitudinal and radial nodes — lines of stationary points that separate the oscillating regions. The lines are represented by the letters ℓ, m and n, which are respectively called the *degree*, *azimuthal order* and *overtone*, respectively, and collectively they are called quantum numbers.

The value of the degree gives the total number *surface* of nodes on a star, so ℓ can take any integer value from zero onwards ($\ell = 0, 1, 2, 3...$). The azimuthal order is how many of those nodes lie as lines of longitude — specifically $|m|$ gives this, as m can take any value from $-\ell$ to ℓ depending on whether the pulsational wave(s) propagate in a retrograde or prograde direction, respectively (if $m = 0$, the modes are classed as axisymmetric). Hence, the number of nodes that lie as lines of latitude is given as $\ell - |m|$, and for every degree of ℓ there exists $2\ell + 1$ modes. Finally, n represents the number of concentric nodes at various fractional radii within the star, splitting the star into layers that oscillate above and below the radial nodes.

Imagine a star that expands and contracts uniformly, like an inflating and deflating balloon. This is the fundamental radial pulsation mode ($n = 0$), described by the quantum numbers: $\ell = 0$, $m = 0$, $n = 0$. If the star were to pulsate with a first overtone radial mode, $n = 1$, one concentric radial node would exist as a stationary point and oscillations would occur in the region above and below it, separately. Two concentric radial nodes would exist for the second overtone, and so on.

For a pulsation in a star described as: $\ell = 1$, $m = 0$, $n = 0$, a single node would exist across the star's equator (0° latitude) such that an oscillation would travel between the north and south hemispheres of the star, expanding and contracting each in turn at half a phase: hence, an $\ell = 1$ mode is called a dipole mode. For $\ell = 2$, an extra line of latitude exists and both lines would lie at at $\pm 35^\circ$, splitting the star into three equal regions; here, both polar regions would expand whilst the equatorial

region contracts, and vice versa — these are quadrupole modes. $\ell = 3$ modes are octupole modes, further dividing up the $\ell = 2$ regions, and hence it follows that for every degree ℓ there exists 2^l-upole *radial* modes. However, only for $\ell = 0$ do radial modes exist: for $\ell \geq 1$, all modes become non-radial.

For an $\ell = 1$, $|m| = 1$, $n = 0$ star, the single node now exists longitudinally and passes through the poles of the star, so now the oscillations travel across the east and west hemispheres. For $\ell = 2$, $|m| = 1$, $n = 0$, the star is split into four quadrants such that each quadrant is either half of a northern or southern hemisphere and half an eastern of western hemisphere (the lines cross on the east and west poles of the star); here, two diagonally-opposite quadrants expand whilst the other two contract, and vice versa. For $\ell = 2$, $|m| = 2$, $n = 0$, two lines of longitude now split the star in quadrants such that the aforementioned quadrants have been rotated by 90°; again, the diagonally-opposite quadrants expand and contract in sync.

The number of modes, nodes and oscillating regions mentioned above would increase by a factor of n for every pulsational overtone that additionally exists within a star: every oscillating region within a hemisphere, quadrant or further-divided region can itself be split up radially (Aerts, Christensen-Dalsgaard & Kurtz, 2010; Kurtz et al., 2014; García & Ballot, 2019).

Figure 1.1, taken from Aerts, Christensen-Dalsgaard & Kurtz (2010, their Fig. [1.3]), shows how different combinations of ℓ, m and n exist in 2D space, such as on the skin of a drum, representing a cross-section of a pulsating star. Figures 1.2 and 1.3, taken from García & Ballot (2019, part of their Fig. [7]), and Aerts, Christensen-Dalsgaard & Kurtz (2010, their Fig. [1.4]), respectively, show the different combinations of ℓ and m described above in 3D-space, representing various strains of real pulsating stars. Finally, Figure 1.4, taken from García & Ballot (2019, also part of their Fig. [7]), shows how complicated some pulsating stars can be, with an example of an $\ell = 20$, $|m| = 16$, $n = 14$ star.

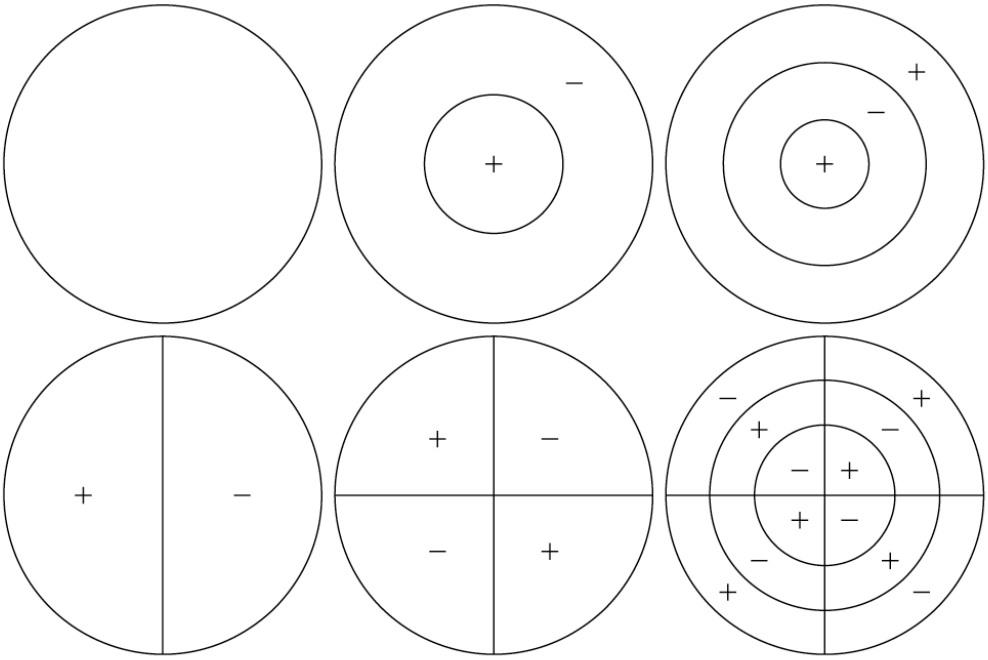

Figure 1.1: *The six 2D circles here represent the cross-sections of six 3D pulsating stars, each with a different arrangement of the quantum numbers ℓ, m and n. The vertical, horizontal and circular lines within the circles are the stationary nodes, splitting up the pulsating regions that themselves are labelled + or -, denoting which regions expand or contract in sync. If the six circles were labelled from left to right as 1.1a) to 1.1f), such that 1.1a) was the top left circle and 1.1f) was the bottom right, their quantum number configurations would be as follows:*

1.1a) $\ell = 0$, $m = 0$, $n = 0$
1.1b) $\ell = 0$, $m = 0$, $n = 1$
1.1c) $\ell = 0$, $m = 0$, $n = 2$
1.1d) $\ell = 1$, $|m| = 1$, $n = 0$
1.1e) $\ell = 2$, $|m| = 1$, $n = 0$
1.1f) $\ell = 2$, $|m| = 1$, $n = 2$

This Figure is taken from Aerts, Christensen-Dalsgaard & Kurtz (2010, their Fig. [1.3]).

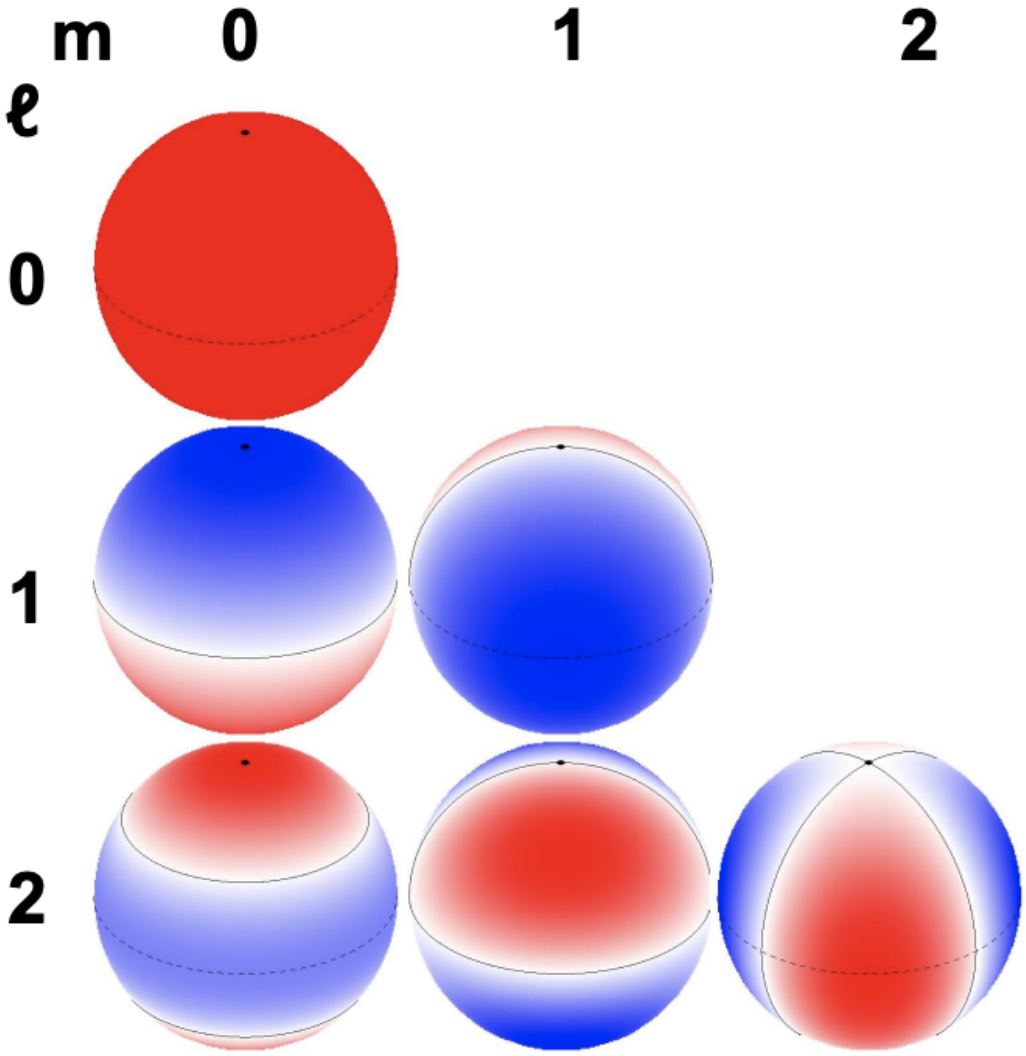

Figure 1.2: *Here are five different variations of pulsating stars, showing how different nodes and oscillating regions exist in 3D-space. The + and - notation of Figure 1.1 has been replaced by the colours red and blue. On the top row the* $\ell = 0$, $m = 0$ *star pulsates radially so is entirely one colour. But it is divided up into two hemispheres by the* $\ell = 1$ *mode on the second row, with the node being latitudinal on the equator when* $m = 0$ *or longitudinal through the poles when* $m = 1$. *The additional node for the* $\ell = 2$ *stars on the third row exists as a second latitudinal line when* $m = 0$, *a polar longitudinal line for* $m = 1$ *with one equatorial latitudinal line, or both lines as polar when* $m = 2$. *There are three equally-sized oscillating regions for the* $\ell = 2$, $m = 0$ *star, with the latitudinal node each lying at* $\pm 35^{\circ}$. *For the* $\ell = 2$, $m = 1$ *star, four oscillations regions exist as quadrants that are divided such that there is an east and west pole. This arrangement is rotated by* 90° *for the* $\ell = 2$, $m = 2$ *star, with two polar longitudinal lines. For the stars split into quadrants, diagonally-opposite quadrants expand and contract in sync. This Figure is taken from García & Ballot (2019, part of their Fig. [7]).*

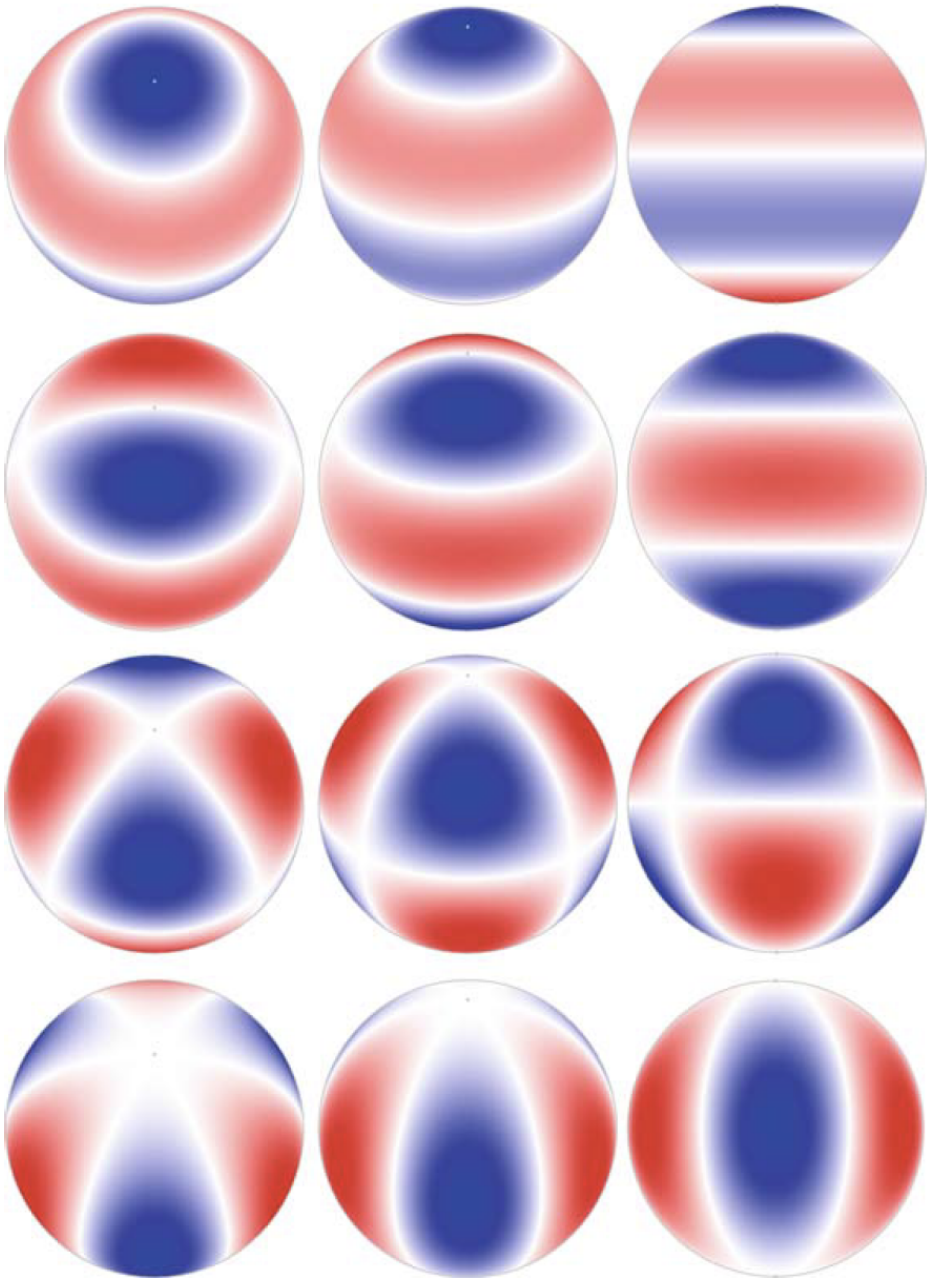

Figure 1.3: *Here shows the form of octupole modes ($\ell = 3$) in four different stars, each with a different value of $|m|$. There is one star per row, with each column providing a different viewpoint to represent different inclinations: from left to right, 60°, 30° and 0°, respectively. If the four stars were labelled from top to bottom as 1.3a) to 1.3d), their quantum number configurations would be as follows:*

1.3a) $\ell = 3$, $m = 0$, $n = 0$
1.3b) $\ell = 3$, $|m| = 1$, $n = 0$
1.3c) $\ell = 3$, $|m| = 2$, $n = 0$
1.3d) $\ell = 3$, $|m| = 3$, $n = 0$

This Figure is taken from Aerts, Christensen-Dalsgaard & Kurtz (2010, their Fig. [1.4]).

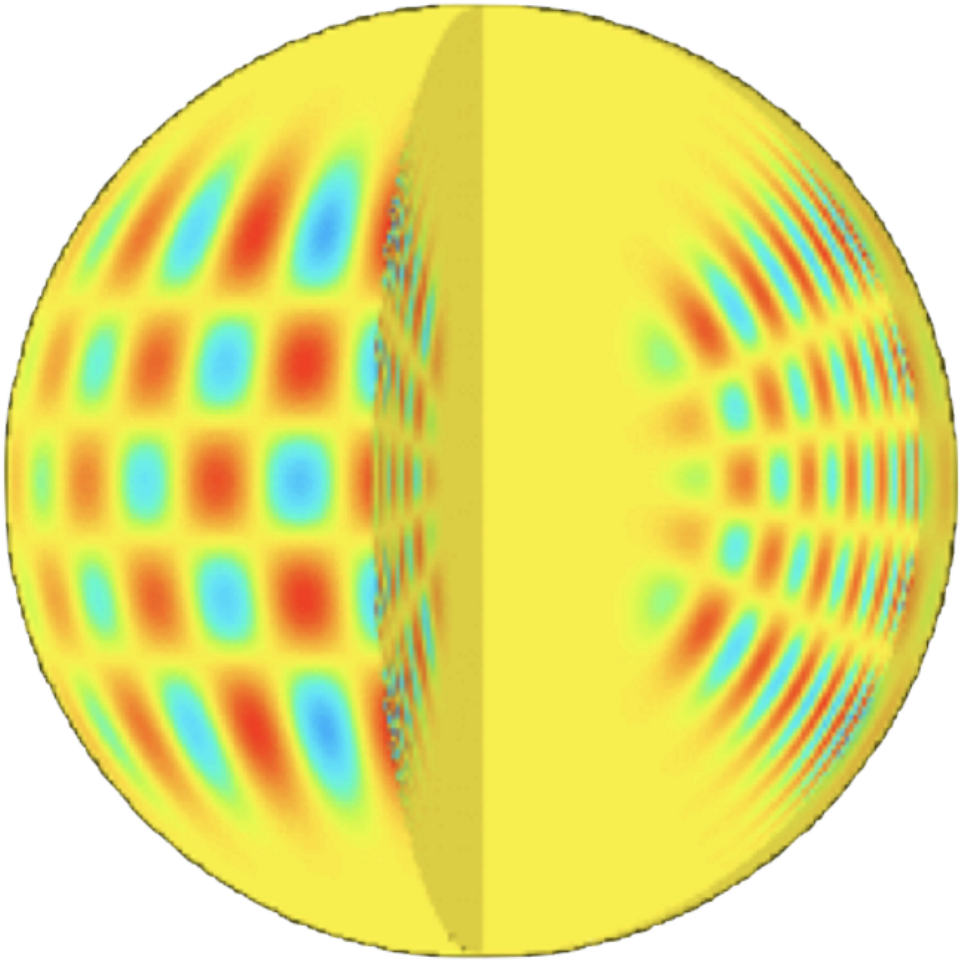

Figure 1.4: *Pulsating stars can have very complicated configurations of quantum numbers, such as this star which oscillates with the following modes:*

$\ell = 20$, $|m| = 16$, $n = 14$

This Figure is taken from García & Ballot (2019, part of their Fig. [7]).

1.1.4 Describing 3D Oscillations with Spherical Coordinates

Naturally, modes of ℓ, m and n propagate in three dimensions throughout a star, so the nodes between oscillating regions occur perpendicularly to each other in three directions. These three directions can be described by a spherical coordinate system, with coordinates of r, θ and ϕ.

r is the radial distance from the core of the star, for describing the concentric shells of nodes for the overtone order n; θ is *co*-latitude (like normal latitude but measured from the poles instead of the equator), for describing the azimuthal order m; and ϕ is longitude, for describing the degree ℓ.

For an ideal pulsator — a star that is spherically symmetric — the displacements undergone in each dimensional direction, ξ_r, ξ_θ and ξ_ϕ, over the timescale of an oscillation, t, are given as Equations 1.1, 1.2 and 1.3. These are the wave equation solutions for the respective spherical dimensions r, θ and ϕ, taken from Aerts, Christensen-Dalsgaard & Kurtz (2010, their Eqns. [1.1], [1.2] and [1.3]):

$$\xi_r(r,\theta,\phi,t) = a(r)Y_l^m(\theta,\phi)^{-\mathrm{i}2\pi\nu t}, \tag{1.1}$$

$$\xi_\theta(r,\theta,\phi,t) = b(r)\frac{\partial Y_l^m(\theta,\phi)}{\partial\theta}^{-\mathrm{i}2\pi\nu t}, \tag{1.2}$$

$$\xi_\phi(r,\theta,\phi,t) = \frac{b(r)}{\sin\theta}\frac{\partial Y_l^m(\theta,\phi)}{\partial\phi}^{-\mathrm{i}2\pi\nu t} \tag{1.3}$$

– Where $a(r)$ and $b(r)$ are respective amplitudes, ν is the frequency of pulsation, and $Y_l^m(\theta,\phi)$ is the spherical harmonic(s) (partially derived for ξ_θ and ξ_ϕ), given as Equation 1.4 (Aerts, Christensen-Dalsgaard & Kurtz, 2010, their Eqn. [1.4]):

$$Y_l^m(\theta,\phi) = (-1)^m\sqrt{\frac{2(\ell+1)}{4\pi}\frac{(\ell-m)!}{(\ell+m)!}}P_\ell^m(\cos\theta)^{\mathrm{i}m\phi} \tag{1.4}$$

– Where $P_\ell^m(\cos\theta)$ itself is a Legendre polynomial, given as Equation 1.5 (Aerts, Christensen-Dalsgaard & Kurtz, 2010, their Eqn. [1.5]):

$$P_\ell^m(\cos\theta) = \frac{1}{2^\ell \ell!}(1-\cos^2\theta)^{\frac{m}{2}} \frac{\mathrm{d}^{\ell+m}}{\mathrm{d}\cos^{\ell+m}\theta}(\cos^2\theta - 1)^\ell \tag{1.5}$$

1.1.5 *p*-modes, *g*-modes and more

The modes described above osciallte in different forms, probing to different depths within a star and pulsating with different frequencies. The two main types are p-modes & g-modes, but additionally there exist f-modes and r-modes, as described below.

1.1.5.1 Acoustic "Pressure" *p*-modes

The acoustic waves that propagate throughout the surface and interior regions of a star (the lower the frequency the deeper the wave) form p-modes. The waves travel *vertically*, and as they penetrate deeper into the star the local density, pressure and temperature all increase. This also means the local sound-speed increases too, and since p-modes are acoustic waves their speed increases. But the path of a wave curves with increasing density, until it is totally internally refracted back towards the surface of a star. The wave then reflects off the internal stellar surface due to the sharp density gradient with the vacuum of space, and it travels back towards the stellar interior — the total internal refraction and surface reflection are the two pivotal points which a wave travels between, trapping its energy within a star. This process repeats, and the waves travel around the star forming huge arcs, with the number of surface reflection points increasing with higher values of ℓ (i.e., higher frequency; Tassoul, 1980). Hence, higher degree modes have waves which penetrate to shallower depths than the lower degree modes, that have waves with only a few reflection points: see Figure 1.5, taken from Cunha et al. (2007, their Fig. [5a]).

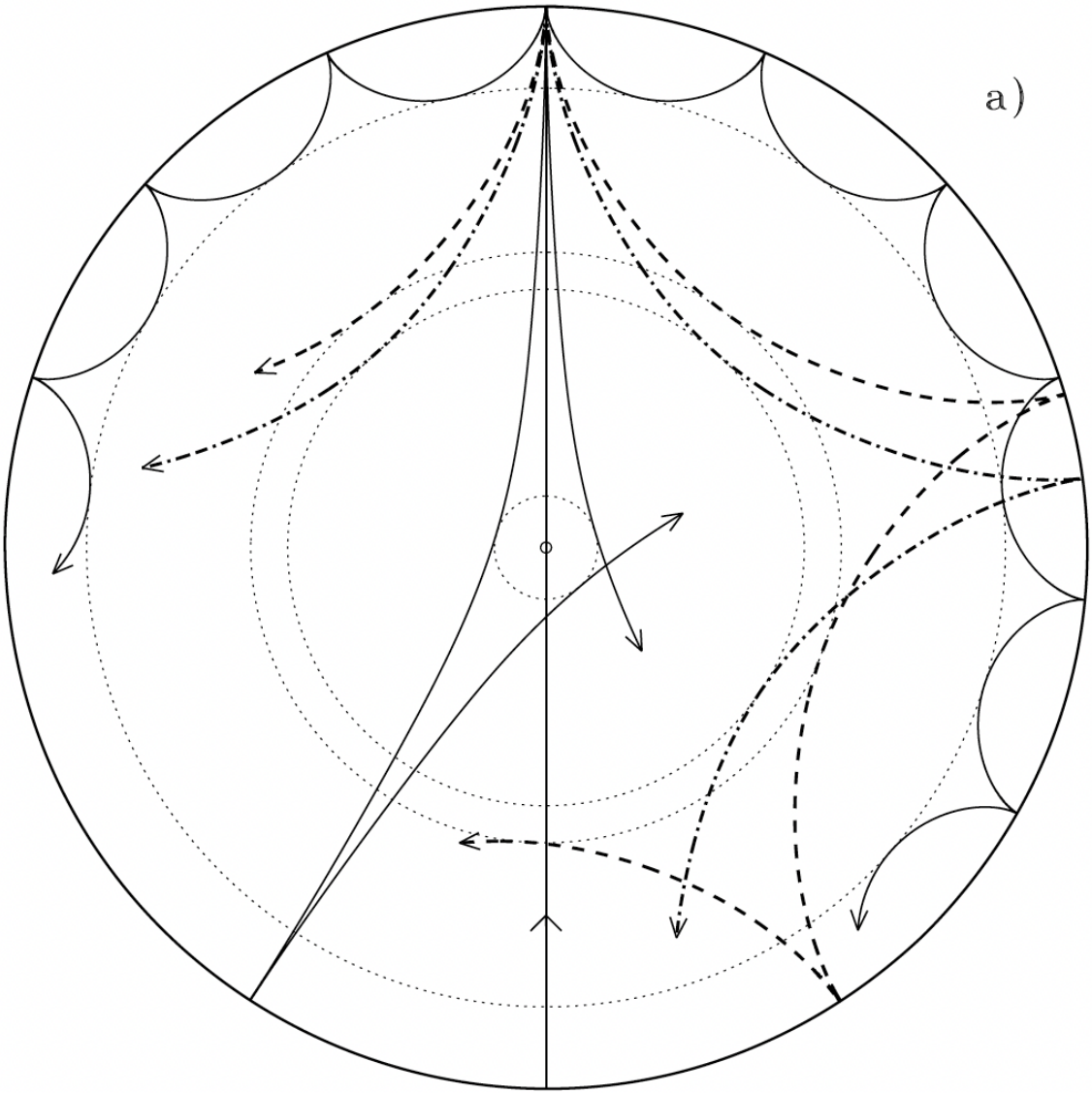

Figure 1.5: *p-mode waves act like balls bouncing around the inside of this 2D star: each wave reflects off the surface and travels towards the core, but its path is curved due to increasing local density and temperature until total internal refraction causes the waves to travel towards the surface again. Higher degree p-modes (larger values of ℓ) have higher frequencies, so only penetrate shallower than lower frequency p-modes. Hence, the frequencies of p-modes are powerful tools for measuring the conditions within a star. This Figure is taken from Cunha et al. (2007, their Fig. [5a]).*

The measured frequency of a p-mode is its surface frequency: that is, how often a surface reflection occurs, which is determined by the travel time of a wave across one arc, and so is defined by the conditions of the stellar interior. Hence, it is possible to calculate the properties of stellar interiors by determining what pressure, temperature and densities are required for such a p-mode to exist — and with multiple p-modes all oscillating with different frequencies, multi-depth surface profiles of stellar interiors can be mapped. As Aerts, Christensen-Dalsgaard & Kurtz (2010) say:

"[This] is an ultimate goal of asteroseismology."

The "p" in p-mode stands for "pressure", and it is this parameter that changes within a star during p-mode pulsations. A perturbation within a star, caused by some turbulent convection, increases the density of material at some fractional stellar radius r. The gravitational strength of the star increases, and the star shrinks in size causing it to become hotter and brighter (this excitation could also be tidally induced by a companion star, such as in so-called "heartbeat" binaries; Thompson et al., 2012; Handler et al., 2020). Over time, the temperature gradient reaches a maximum before radiative diffusion takes over and dissipates the thermal energy back to the lower-density regions, dampening the density build-up. During this diffusion the star expands, becoming cooler and dimmer. This continues until the expanding material is gravitationally accelerated back towards the star, where its momentum increases the local density and the entire oscillatory behaviour repeats. With the gas pressure from density (temperature) gradients existing as the driving force behind these pulsations (as opposed to other forces such as magnetic) the dominant equilibrium-restoring force for p-mode pulsations is the *pressure* gradient (Aerts, Christensen-Dalsgaard & Kurtz, 2010).

With increasing overtones — radial nodes, n — the frequencies of p-modes *also* increase, forming the shallower arcs seen with higher values of ℓ (see Figure 1.5).

For a star with $n \gg \ell$, the *frequencies* of its p-modes tend towards equal spacing in an asymptotic relation dependent on the size of n.

Equation 1.6, taken from Kjeldsen & Bedding (1995), gives this asymptotic approximation of p-mode frequencies based on the overtone and degree (n and ℓ) of the modes:

$$\nu_{n\ell} \simeq \Delta\nu \left(n + \frac{\ell}{2} + \epsilon_{n\ell} \right) \tag{1.6}$$

– Where $\Delta\nu$ is the frequency of large separation and $\epsilon_{n\ell}$ is a unit-less constant ($\epsilon_{n\ell} \simeq$1.6 for the Sun; Kjeldsen & Bedding, 1995).

The frequency of large separation, $\Delta\nu$, is defined as the inverse of the sound travel time of a p-mode's surface-to-core journey and back again. Asteroseismic measurements of $\Delta\nu$ and frequency of maximum oscillation power provide a direct measurement of the stellar mass and radius (Epstein et al., 2014), by scaling to the mass, radius and $\Delta\nu$ of the Sun; Equation 1.7, taken from Kjeldsen & Bedding (1995, their Eqn. [9]), shows this relation:

$$\Delta\nu = \left(\frac{M}{\mathrm{M}_\odot} \right)^{\frac{1}{2}} \left(\frac{R}{\mathrm{R}_\odot} \right)^{\frac{-3}{2}} \Delta\nu_\odot \tag{1.7}$$

The frequency of large separation of the Sun, $\Delta\nu_\odot$, is 134.92 μHz (11.657 c/d; Toutain & Froehlich, 1992), and as mentioned above is the inverse of twice the surface-to-core sound speed time. This is calculated by integrating the sound speed over the radius of a star, given as Equation 1.8 (Aerts, Christensen-Dalsgaard & Kurtz, 2010, their Eqn. [1.11]), and can be substituted into Equations 1.6 and 1.7.

$$\Delta\nu = \left(2 \int_0^R \frac{\mathrm{d}r}{c(r)} \right)^{-1} \tag{1.8}$$

1.1.5.2 "Gravity" *g*-modes

g-modes are rather different to *p*-modes: they propagate throughout a star *horizontally*, confined towards the core and inner regions of a star's interior (but in higher mass stars they can be observed on the surface too), and typically exist with much lower frequencies. However, the paths that they draw out within the stellar interior are constrained by the same mechanisms as *p*-modes: if starting from their highest radial position they propagate through a star horizontally, but they exist in cooler, less dense material and so as the material sinks towards the core the *g*-modes spiral towards the stellar centre. Instead of a total internal refraction, the *g*-modes reach a region of higher density far quicker deep in the deep stellar interiors, and overshoot their equilibrium point. Now with a far greater external density near the convective core, the *g*-modes sharply change direction and spiral radially outwards. This continues until gravity becomes the dominant force — hence "gravity" being the "*g*" in *g*-mode — and again whilst they are in cooler material the oscillatory motion starts over: see Figure 1.6, taken from Cunha et al. (2007, their Fig. [5b]). The dominant equilibrium-restoring force for *g*-mode pulsations is *buoyancy* (Aerts, Christensen-Dalsgaard & Kurtz, 2010).

With increasing overtones — radial nodes, n — the frequencies of *g*-modes *decrease*, forming longer paths and reaching higher fractional radii from the stellar core (see Figure 1.6). For a star with $n \gg \ell$, the *periods* of its *g*-modes tend towards equal spacing in an asymptotic relation dependent on the size of n, thereby being the inverse of the *p*-mode $n \gg \ell$ asymptotic relation.

This *g*-mode period spacing also allows for the determination of stellar mass and radius, but now stellar ages can be constrained too. This is in addition to the conditions deep in a star's interior, such as its density, temperature, and chemical composition. Hence, measuring the frequencies of *g*-modes, and combining measurements of *g*-modes, full surface-to-core profiles of stellar interiors can be mapped

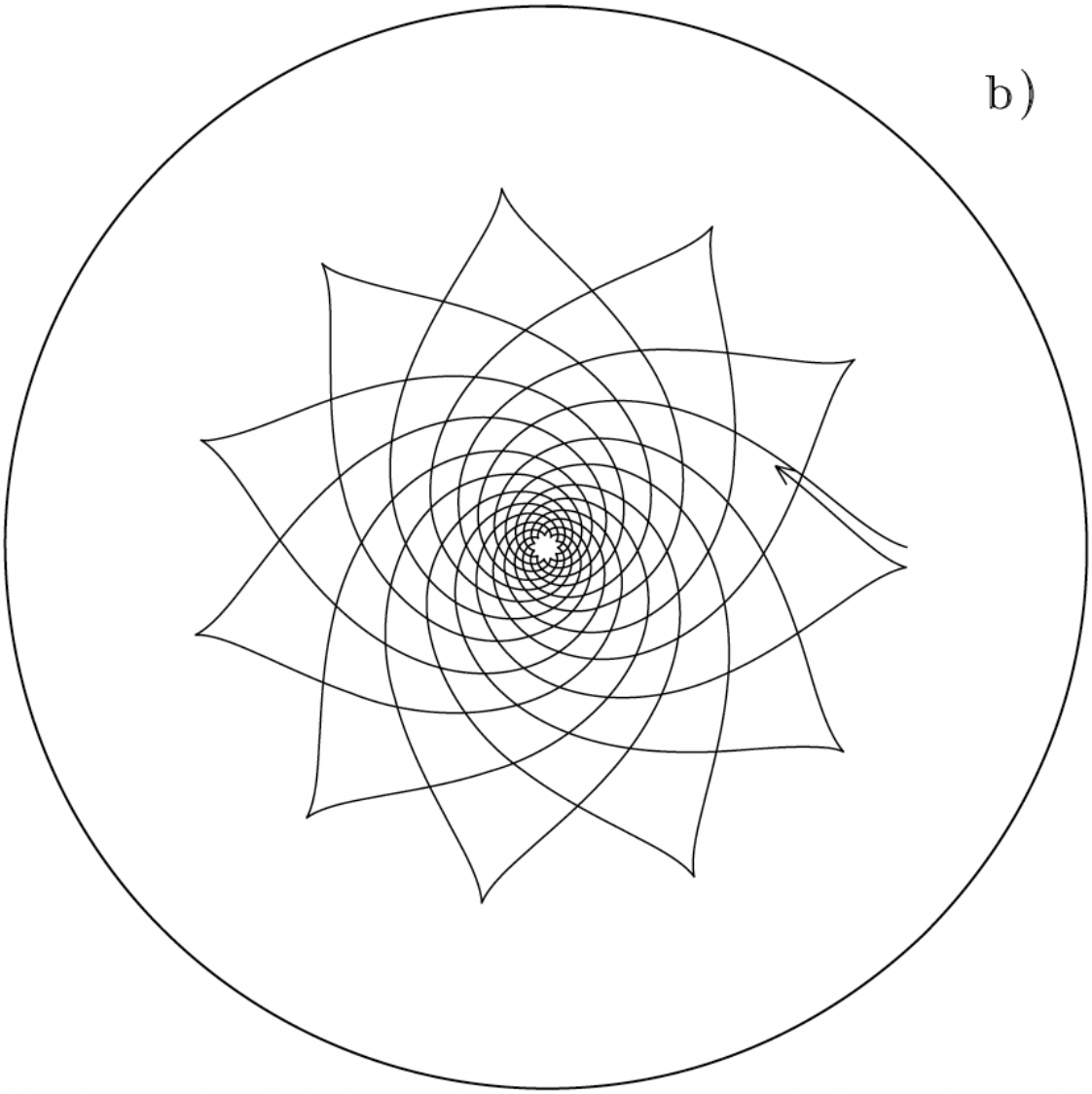

Figure 1.6: *g-mode waves act like an inflatable ball being brought underwater and then being released: buoyancy quickly changes their direction due to the high external pressure. The wave then continues radially outwards until gravity becomes dominant and the waves again sharply change direction. g-modes travel through a star horizontally, but as they overshoot their equilibrium positions to and from the core, the paths they trace form a radially shrinking and increasing spiral. Hence, the frequencies of g-modes are also powerful tools for measuring the conditions within a star. This Figure is taken from Cunha et al. (2007, their Fig. [5b]).*

(Aerts, Christensen-Dalsgaard & Kurtz, 2010), and hence internal structures and compositions.

Equation 1.9, taken from Aerts, Christensen-Dalsgaard & Kurtz (2010, their Eqn. [1.12]), shows the asymptotic relation of the g-mode periods:

$$\Pi_{n\ell} = \frac{\Pi_0}{\sqrt{\ell(\ell+1)}}(n+\epsilon) \tag{1.9}$$

– Where $\Pi_{n\ell}$ is the g-mode period, dependent on the degree, ℓ, and overtone, n, of the mode, and ϵ is a constant.

Π_0, a g-mode period benchmark, is itself based on N, the Brunt-Väisälä frequency. This frequency is a measure of the oscillations in a fluid when it becomes displaced from its equilibrium state, dependent on the fluid's temperature and density — in this context, the fluid is the convective material in a star, and N is given as Equation 1.10:

$$N = \sqrt{\frac{g}{\theta}\frac{\mathrm{d}\theta}{\mathrm{d}r}} \tag{1.10}$$

– Where g is the gravitational strength, θ is the local gas temperature and r is the radial height.

Hence, Π_0 is given as Equation 1.11, taken from Aerts, Christensen-Dalsgaard & Kurtz (2010, nomenclature-modified from their Eqn. [1.13]):

$$\Pi_0 = 2\pi^2 \left(\int \frac{N}{r} \mathrm{d}r \right)^{-1} \tag{1.11}$$

Here, N is integrated over the fractional radius of the star where the g-modes exist, and hence Π_0 is a tool used to examine the stratification of stellar interiors (i.e., the internal radial density profile of a star can be thought of as many vertical

layers each with different densities).

1.1.5.3 *f*-modes and *r*-modes

f-modes and r-modes are beyond the scope of the work in this thesis, but have been included for completion:

"fundamental" *f*-modes

Cowling (1941) discovered that some stars exhibit for each degree ℓ (for $\ell \geq 2$) an intermediate mode(s) sitting between p- and g-modes, with properties of both: the intermediate modes are surface gravity waves. He found that these modes oscillate only for the radial order $n = 0$, so labelled them as "fundamental" modes — hence "f" (Christensen-Dalsgaard & Gough, 2001). f-modes are closer in frequency to p-modes, and exist more commonly for higher degrees of ℓ. Equation 1.12, taken from Aerts, Christensen-Dalsgaard & Kurtz (2010, nomenclature-modified from their Eqn. [7.12]), gives the frequency of an f-mode as:

$$\nu^2 \simeq g_s \frac{R}{L} \tag{1.12}$$

– Where g_s is the surface gravity, R is the photospheric radius of the star and $L = \sqrt{\ell(\ell+1)}$ (Aerts, Christensen-Dalsgaard & Kurtz, 2010).

f-modes allow measurements of conditions deep towards of the core of a star, and are sensitive to a the mass (gravity) and radius of a star.

"Rossby" *r*-modes

Papaloizou & Pringle (1978) were the first to notice that within rotating stars their existed non-trivial toroidal modes that were akin to the Rossby waves found in the Earth's oceans and atmosphere: large-scale waves driven by the Coriolis effect (Rossby, 1939; Platzman, 1968). Papaloizou & Pringle (1978) were the first to label

such modes as r-modes ("r" for "Rossby"): they are the rarest of the four mode-types, only being discovered in γ Doradus stars, for example, as recently as 2015 (Van Reeth et al., 2015).

It is the Coriolis forces within stars that cause r-modes to be seen: the combination of the toroidal motion of the r-modes with global rotation of a star causes temperature changes that are measured as brightness fluctuations (Saio et al., 2018). Since r-modes are dependent on the rotation of a star, the equation of their frequencies has different forms for stars with different rotation rates — and the rotation rate, Ω, is itself proportional to stellar mass and radius: $\Omega \propto \sqrt{\frac{GM}{R^3}}$.

For slowly rotating stars, defined by Saio et al. (2018) as when $\Omega \ll \sqrt{\frac{GM}{R^3}}$, the frequency of an r-mode is given as Equation 1.13, taken from Saio et al. (2018, their Eqn. [3]):

$$\nu_{\mathrm{rm}}^{\mathrm{co}} \approx \nu_{\mathrm{rot}} \left[\frac{2m}{\ell(\ell+1)} + q(n) \frac{\Omega^2}{\frac{GM}{R^3}} \right] \tag{1.13}$$

– Where $\nu_{\mathrm{rm}}^{\mathrm{co}}$ is the r-mode frequency in a corotating frame, $\nu_{\mathrm{rot}} = \frac{\Omega}{2\pi}$, and $q(n)$ is a constant.

For faster rotating stars, the frequency of an r-mode is given as Equation 1.14, taken from Saio et al. (2018, their Eqn. [6]):

$$\nu^{\mathrm{co}} \approx \frac{\sqrt{\lambda}}{2\pi^2 n} \int \frac{N}{r} \mathrm{d}r \equiv \frac{\sqrt{\lambda}}{n} \nu_0 \tag{1.14}$$

– Where the eigenvalue λ replaces $\ell(\ell+1)$, and, as above, N is the Brunt-Väisälä frequency.

r-modes are sensitive to the mass and radius of stars, and are characterised by their degree, ℓ, and azimuthal order, m. They give insight into angular momentum transport and mixing processes in rotating stars.

1.1.6 Pulsation Mechanisms

1.1.6.1 The κ-Mechanism

The κ-mechanism (historically the *Eddington valve* mechanism; Tao, Spiegel & Umurhan, 1998) is the driving force behind the oscillations in many types of pulsating stars, particularly the classical pulsators that lie on the instability strip (the region on the HR diagram spanning the spectral types A – K that perpendicularly intersects the main sequence; Gautschy & Saio, 1996). The driving force is based on opacity, hence the use of κ in the name.

For a star in equilibrium, there is a perfect balance maintained between the temperature and pressure of the stellar material. Should a region within a star become perturbed (via convection, for example), a region of local high pressure and temperature will form; likewise elsewhere in the star, a region of relatively low pressure and temperature now exists too. This perturbation has now formed a gradient across the star, and for most stars (i.e. non-pulsating stars) the opacity of the star *decreases* with increasing temperature such that thermal energy and material can dissipate around the star and equilibrium can be restored (this inversely-proportional relationship has effects on the limb darkening of stars too).

However, for stars where opacity *increases* with increasing temperature, they become unstable and begin oscillating. Here, a perturbation moves stellar material inwards creating a region of local high pressure and temperature, but high opacity. High opacity stops thermal energy from diffusing, so the temperature continues to increase as well as the pressure. This acts as a buoyancy force, which eventually pushes (restores) the perturbed stellar region back outwards, until gravity becomes the dominant force and the region moves inwards again (de Boer & Seggewiss, 2008).

Specific to the stars in the instability strip, the perturbations arise from partly-ionised helium. In stellar photospheres, helium remains stable (neutral). Deeper in the radiative zone, below the surface, helium undergoes ionisation and becomes

He II. This region increases in temperature and pressure during the contraction phase of a pulsation, and the helium ionises again to become doubly-ionised helium: He III; this occurs deep inside stars where the temperatures reach in excess of 50,000 K. After the buoyancy force-restoration starts the expanding phase of a pulsation, the temperature decreases causing the opacity to also decrease, and the He III recombines to He II (Gautschy & Saio, 1996).

The cyclic phenomena of pulsations cause stars to expand and contract over time, physically changing in size and becoming cooler and hotter respectively. But this also correlates directly to the brightness of the stars, which get brighter during contraction and dimmer during expansion (hence, over time, light curves of stars can reveal their pulsations). Furthermore, the greater the distance the He II zone lies from the photosphere the more phase-shifted the pulsations and brightness changes become, because a deeper He II zone induces pulsations to become nonlinear from their interactions with upper levels of the stellar interior (i.e., the hydrogen ionisation zone). This chiefly occurs with overtone pulsations, which cause the luminosity amplitude and pulsation phase-shift variations (Baker & Kippenhahn, 1965). So instead of a uniform sinusoidal light curves, some stars exhibit a sharp increase in brightness followed by gradual decrease — per pulsation — as, for example, demonstrated by the RR Lyrae stars (known as a "saw-tooth" shape; see § 1.1.7.2). The pulsation modes described here are the p-modes.

1.1.6.2 The Convective Blocking Mechanism

The term "Convective Blocking" was first coined by Pesnell (1987), and was devised as a pulsation mechanism independent of the κ and other classical mechanisms (Li, 1992; Guzik et al., 2000). Here, pulsation modes are stochastically-excited from turbulent pressure at the base of the convective zone, where temperatures reach 200,000 – 480,000 K (Breton, Brun & García, 2022). But the pulsations only remain

if the local convective time scale — the ratio of the local pressure scale height and the local convective velocity — is longer than the pulsation period, otherwise energy dissipates over time and the star returns to equilibrium. With increasing depth of the convection zone base, the range of pulsation frequencies narrows, but localised convection zones are still produced. Having these localised convection zones deep within a star provides the conditions required for pulsation modes to exist, which in turn induces flux modulations which are observed as brightness changes on the surface of the star (Turcotte, 2000; Guzik et al., 2000). Since this mechanism drives pulsations deep within a star, it is describing the g-modes and hence is applicable to the γ Doradus stars (see § 1.1.7.4).

1.1.7 A Taxonomy of Pulsators: A Brief Asteroseismic Journey Along the Classical Instability Strip

It is well-known that pulsators exist across the entire HR diagram, and the reader should see Chapter 2 of Aerts, Christensen-Dalsgaard & Kurtz (2010) for an extensive discussion of every type of pulsator, but for the scope of the work in this thesis we stick locally to the instability strip.

The instability strip is a region on the HR diagram perpendicular to the main sequence, stretching from the aforementioned up to the supergiant branches. It plays home to a variety of different flavours of pulsating star, which all have one attribute in common: they all have the same pulsation driving force; the ionised helium-based κ-mechanism (see § 1.1.6.1; Gautschy & Saio, 1996). The instability strip spans across the spectral types of M/K – A, encapsulating stars with $T_{\rm eff}$ between $3700 - 9700\,\mathrm{K}$ and masses from $0.5 - 20 + \mathrm{M}_{\odot}$ (Turner, 1996; Pecaut & Mamajek, 2013; Jurkovic, 2021). The following Sub-Sections describe the different classes of pulsators that lie on the instability strip, ordered by increasing luminosity to mirror

from bottom to top their stars' positions up the instability strip, with each class highlighted by a different colour on the pulsational HR diagram in Figure 1.7.

1.1.7.1 The δ Scuti Stars

The δ Scuti stars — the red region in Figure 1.7 — range in mass between 1.5 – 2.5 $M_\odot$, and most exhibit pulsations with periods between 0.02 – 0.25 d (30 min – 6 hr; 48 – 4 c/d; Balona, 2016) but some have been observed with periods as low as ≈0.125 d (≈18 min; ≈80 Amado et al., 2004; Bedding et al., 2020). The pulsations intrinsically change the brightness of the classical δ Scuti stars by ≤ 0.3 mag, but up to 1.0 mag for the high-amplitude δ Scuti stars (HADS; Sun et al., 2021). The δ Scuti stars lie on the HR diagram where the classical instability strip intercepts the main sequence track, across a spectral type range of F5 – A0 with $T_{\rm eff} = 6300\,{\rm K} - 9700\,{\rm K}$ (Pecaut & Mamajek, 2013; Balona, 2016; Zhou et al., 2016). δ Scuti pulsations can be both radial and non-radial modes, which exist as p-modes with low orders of ℓ (Uytterhoeven et al., 2011), and pulsations have been found to exist in the chemically peculiar stars, too (specifically the Am stars, e.g., HD 1097; Kurtz, 1989). However, pulsations in the Am stars are constrained to stars within a $T_{\rm eff}$ range of 6900 – 7600 K and the occurrence of pulsations correlates inversely to the degree of peculiarity (higher metallicity leads to fewer Am pulsators; Smalley et al., 2017).

δ Scuti pulsations are driven by the κ-mechanism (see § 1.1.6.1), which excites pulsation modes in the He II ionisation region of the stars, facilitated by their outer convective envelopes — as such, the δ Scuti stars oscillate with p-modes. More evolved δ Scuti stars have larger convective cores, so can additionally pulsate with internally-trapped g-modes: if the frequencies of the two sets of modes become similar then so-called "mixed-modes" can exist as well. δ Scuti stars that exhibit both p-mode and g-mode oscillations are known as "hybrid" pulsators (Handler, 2009).

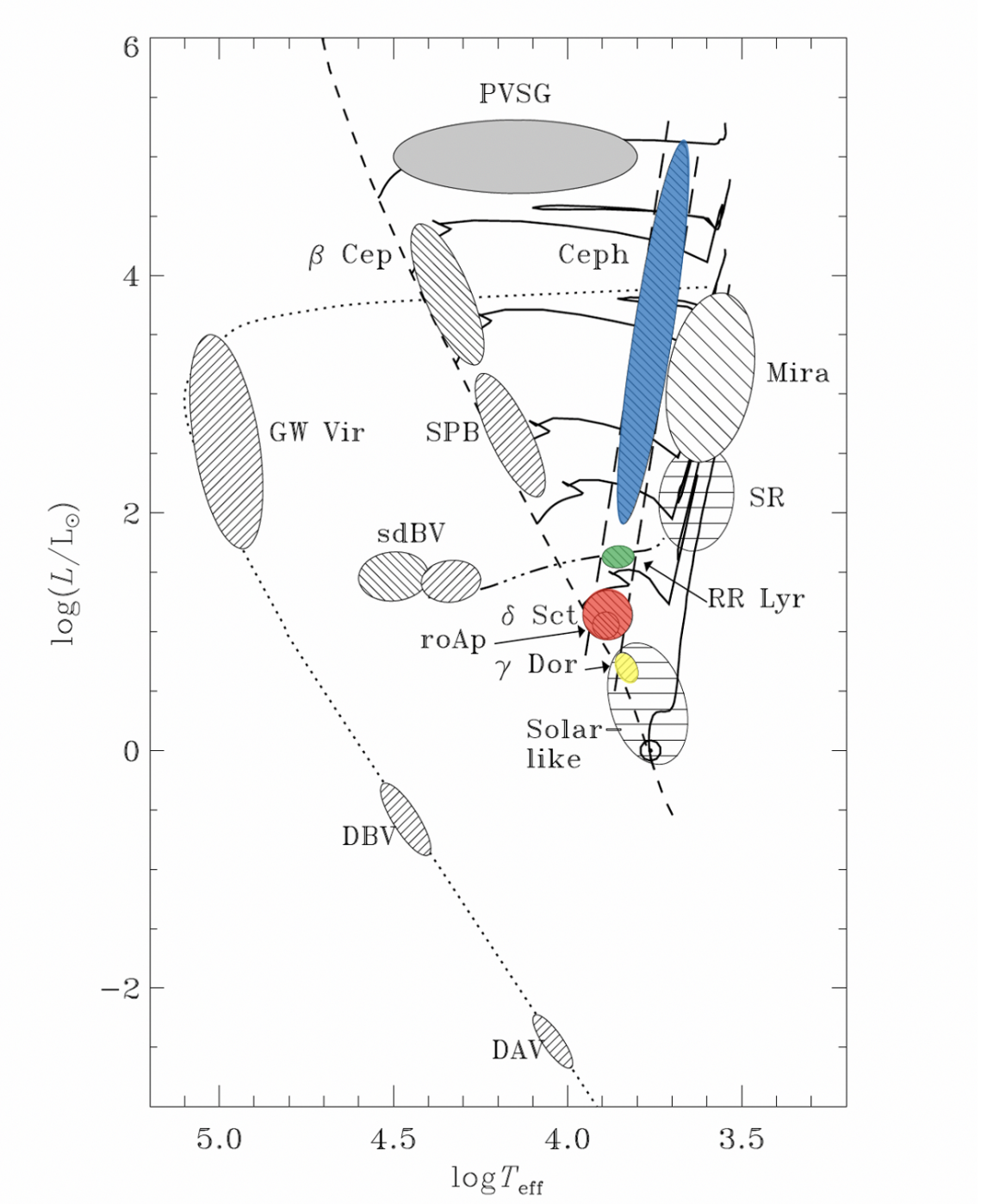

Figure 1.7: *The pulsational HR diagram. The δ Scuti stars lie where the classical instability strip crosses the main sequence, shown by the region highlighted in red. The RR Lyrae stars lie on the instability strip above the δ Scuti stars, their location coloured in green. The blue region shows the position of the Cepheid variables, which occupy most of the instability strip above the δ Scuti stars and the RR Lyrae stars. The γ Doradus stars lie on the main sequence, touching the the cooler boundary of the instability strip, in the yellow-highlighted area. This Figure is taken from Aerts, Christensen-Dalsgaard & Kurtz (2010, their Fig. [1.12]).*

The prototype δ Scuti pulsator is HD 172748 — the namesake δ Scuti — first classified in the late 1930s (Fath, 1937; Sterne, 1938).

1.1.7.2 The RR Lyrae Stars

The RR Lyrae stars, contained within the green region in Figure 1.7, are pulsators that are more evolved and as such lie in the instability strip above the main sequence. This makes them old stars, over 10 Gyr in age, with masses between $0.5 - 0.8\,M_{\odot}$ (spectral type M1 – K2; $T_{\rm eff} = 3600 - 5100$ K; Pecaut & Mamajek, 2013; Bhardwaj et al., 2022). The prototype RR Lyrae star was its namesake — also designated HD 182989 (Pickering & Bailey, 1895; Burnham, 1978) — but with more RR Lyrae star discoveries Bailey (1902) noticed that some exhibited slightly different light curves, and hence sub-classified RR Lyrae stars as RRa, RRb and RRc. RRab stars make up over 90% of the RR Lyrae star population, and pulsate in the fundamental mode which induces a sharp rise to maximum brightness and a slower decline to minimum brightness over a pulsation cycle, giving their light curves the signature "saw-tooth" luminosity fluctuations of up to 1 mag, with periods between 0.3 – 1.0 d (8 – 24 hr; 3 – 1 c/d Jurcsik & Kovacs, 1996). The newest subclass are the RRd stars: double-mode pulsators, exhibiting both fundamental and overtone modes simultaneously (Jurcsik et al., 2015). The RRd stars are rare, forming <1% of all known RR Lyrae stars, but there are rarer RR Lyrae stars still; a sub-subclass within the RRd star known as the triple-mode RR Lyrae stars — only several dozen examples of triple-mode RR Lyrae stars are known (e.g., Kurtz et al., 2016).

The fame of RR Lyrae stars originates from their period-luminosity relationship, the property that their absolute brightness change during the course of one pulsation cycle is proportional to the period of the pulsation. This relation is not well observed at visual wavelengths, but is strongest in the infrared wavelengths such as the K-band. As the brightness profile per pulsation period is well known, for any RR Lyrae

star a very accurate distance to it can be measured using the distance modulus. This makes RR Lyrae stars very useful tools for measuring distances, hence their pseudonyms of "distance indicators" and "standard candles"; they have been used to calculate distances to globular clusters, for example (Brown et al., 2004; Székely et al., 2007; Bhardwaj et al., 2022). Like the δ Scuti stars, the κ-mechanism is responsible for the pulsations in RR Lyrae stars (see § 1.1.6.1).

1.1.7.3 Cepheid Variables

Like the RR Lyrae stars, Cepheid variables are powerful tools for accurately determining distances due to their period-luminosity relationship — but here their period-luminosity relationship exists across all visual wavelengths. Cepheids are the most massive stars to live on the instability strip, and the most diverse in mass and luminosity too: they take up ≈80% of all instability strip-space and cross into the giant branches, as shown by the blue region in Figure 1.7. The Cepheid class is named after the star δ Cephei (HD 213306; Goodricke, 1786), but it is argued that the true prototype is the star η Aquilae (HD 187929) as it exhibits Cepheid variable-type characteristics and was discovered a few months earlier (Pigott, 1785) — however, it took over 125 years before their period-luminosity relationship was discovered (Leavitt, 1908; Leavitt & Pickering, 1912).

Cepheid variables exist as one of two main types: Classical Cepheids and Type II Cepheids (Packer, 1890). Classical Cepheids have masses in the range of $4-20\,M_\odot$ across spectral types of G5 – F5 ($T_{\rm eff} = 5650-6550\,K$), and can have luminosities of up to $100{,}000\,L_\odot$ (Turner, 1996, 2010; Aerts, Christensen-Dalsgaard & Kurtz, 2010; Pecaut & Mamajek, 2013). All Cepheids pulsate radially, and during a typical pulsation cycle of $1-50$ d ($1-0.02$ c/d) the stars can grow and shrink by up to 25% in size corresponding to a ≤ 2 mag brightness change (Rodgers, 1957; Aerts, Christensen-Dalsgaard & Kurtz, 2010). The furthest Classical Cepheids that have

ever been observed are in the galaxy NGC 4603, determined by the Cepheids to be $33.3^{+1.7}_{-1.5}$ Mpc (Newman et al., 1999). A later red-shift analysis gave a distance to NGC 4603 as ≈ 33 Mpc, so the two distances are in good agreement (Crook et al., 2007). Hence, Classical Cepheids have even been employed to constrain the Hubble Constant (H_0; Ngeow & Kanbur, 2006).

Type II Cepheids are not as famous as their Classical counterparts due to Type II's having a fainter period-luminosity relationship per respective period, and their typical properties are not as well constrained (Harris & Welch, 1989). They are much smaller in mass, only $0.5 - 0.6\,M_\odot$, with $T_{\rm eff}$ between $5000 - 6000$ K (K2 – F9; Pecaut & Mamajek, 2013; Jurkovic, 2021). They can be split up further into three sub-groups, dependent on their pulsations periods: BL Herculis stars with cycles of $1 - 3$ d ($1 - 0.$d c/d), W Virginis stars with periods of $4 - 20$ d ($0.25 - 0.05$ c/d), and RV Tauri stars with periods of $20 - 150+$ d ($0.05 - <0.007$ c/d). Even though Type II Cepheids are fainter than Classical Cepheids, they still have a role as cosmic yard-sticks and other work such as mapping extinction (Majaess, Turner & Lane, 2009). Both Classical and Type II Cepheids have pulsations powered by the κ-mechanism (see § 1.1.6.1).

1.1.7.4 The γ Doradus Stars

The γ Doradus stars, isolated by the yellow region in Figure 1.7, are amongst the lowest-mass main sequence pulsators on the HR diagram, overlapping with the Solar-like pulsators. They lie across a spectral type range of F5 – A7, with masses of $1.3 - 1.8\,M_\odot$ and $T_{\rm eff}$ of $6500 - 7700$ K (Pecaut & Mamajek, 2013; Ma et al., 2022). They pulsate predominately in g-mode pulsations, with frequencies of $0.4 - 3$ c/d that translate to periods of $2.5 - 0.3$ d ($72 - 12$ hr), inducing brightness changes of up to 0.05 mag (Uytterhoeven et al., 2008; Ouazzani et al., 2019). The pulsational mechanism behind the γ Doradus pulsations is a convection-driven flux modulation

induced deep within the convective zone ("Convective Blocking", see § 1.1.6.2; Guzik et al., 2000). The "hybrid" pulsators mentioned in the discussion about δ Scuti stars above are sometimes specifically called δ Scuti – γ Doradus hybrids.

The γ Doradus stars lie on the main sequence where the cooler boundary of the instability strip exists (Dupret et al., 2005). The prototype γ Doradus pulsator is HD 224638 — γ Doradus itself — which became the first of its namesake class in the early 1990s (Mantegazza & Poretti, 1991; Krisciunas, 1993; Balona, Krisciunas & Cousins, 1994). Whilst γ Doradus stars themselves do not strictly lie in the instability strip, they have been included here for completeness as examples of g-mode pulsators.

1.1.8 A-Type Main Sequence Stars

A-type main sequence stars receive their own Sub-Section in this thesis as almost all classically pulsating host stars are such spectral type.

Some A-type stars are known as chemically peculiar (CP), showing over-abundances of certain chemical species. The CP stars are split into four sub-groups, based on their temperatures and by which chemicals are over-abundant, defined by Preston (1974). § 1.1.8.2 discusses Am (CP1) stars as TIC 409934330 — the target star in Chapter 5 — is a member of the sub-class; and since TIC 409934330 also hosts a companion, Am stars as exoplanet hosts are discussed in § 1.2.6. Together, all CP stars make up ∼10% of the population of A-type stars (Landstreet et al., 2007).

1.1.8.1 Chemically-Normal A-type Stars

The A-type stars populate the third group on the HR diagram, in decreasing temperature. They have masses ranging between 1.7 – 2.2 $M_\odot$, and a $T_{\rm eff}$ range of 7000 $\leq T_{\rm eff} \leq$ 10,000 K. They can be up to 25 times as luminous as the Sun, but only live for one tenth as long (1 Gyr; Pecaut & Mamajek, 2013).

The A-type stars have strong hydrogen Balmer absorption lines in their spectra, at 410 nm, 434 nm, 486 nm, and 656 nm (Balmer, 1885; Nave, 2006). They are fast rotators, with a maximum rotational velocity ($\Omega_{\rm rot}$) ∼80% that of their critical rotational velocity (the velocity at which the star would break apart; $\frac{\Omega_{\rm rot}}{\Omega_{\rm crit}} < 0.8$; Zorec & Royer, 2012).

1.1.8.2 The Am Stars

The Am stars exist as one of the chemically peculiar sub-classes of standard A-type stars (CP1), differentiating from standard A-type by an appreciably weaker Ca II K line, but they lie across similar mass and $T_{\rm eff}$ ranges — it is after the metallic line strength deficiencies that the sub-class is so named; the "m" denoting the phenomenon. Most Am stars are not intrinsically variable, but some evolved Am stars do display δ Scuti-like pulsations (these evolved stars still lie on the main sequence, however; North & Debernardi, 2004) — TIC 409934330, the target-system within Chapter 5, is such a pulsating Am star.

The Am class can be sub-divided further into "classical", "marginal" and "hot" Am stars. "Classical" Am stars have spectral types obtained from the Ca II K line and Fe-group elements that vary by five or more spectral sub-types, whilst for "marginal" Am stars this is fewer. "Hot" Am stars are defined as having spectral types between A0–A3 (Smalley et al., 2017).

The Am stars were first classified by Titus & Morgan (1940), who noted that such stars would have otherwise been classified as F-type from their weak K lines, but remained considered as A-type stars from their categorisation in the Henry Draper Catalogue. Later, Roman, Morgan & Eggen (1948) distinguished that Am stars flaunt a "strikingly strong" over-abundance of several elements, confirmed by Conti (1970) to be Cr, Fe, Mn, Ni; and in contrast, that Am stars inversely exhibit a deficiency of Ca and Sc. Table 1.1 is a recreation of Table [3] of Conti (1970),

listing their full set of elemental species with respective abundance anomalies.

Table 1.1: *A recreation of Table [3] of Conti (1970), listing their full set of elemental species with abundance anomalies.*

	Well Determined	Not as Well Determined
Deficient	Ca, Sc	C, O
Normal	Mg, Ti	N, Na, K
Possibly overabundant	Si, V	Al, S, Co, Zr
Overabundant	Cr, Mn, Fe, Ni	Cu, Zn, Sr, Y, Ba, Re

Such abundance-abnormalities exist on account of Am stars having slower rotation rates than their normal A-type counterparts: the more-stable stellar atmospheres encapsulate radiative "settling" and "levitation" of the aforementioned elements giving rise to their abundance irregularities (overabundant by factors of up to 10 when compared with Solar abundances; Abt, 2009).

As mentioned above, Am stars as a population are slow rotators for their spectral type (Wolff, 1983). This imposes narrow (sharp) lines in their spectra, after which — as mentioned earlier — the sub-class is named (this makes them especially good targets for radial velocity observations, for example [see § 1.2.3.1]). Abt & Moyd (1973) measured the rotational velocity of 66 known Am stars and found the mean value to be $v \sin i = 33\,\mathrm{km/s}$, with the highest rotational velocity not exceeding $v \sin i = 95\,\mathrm{km/s}$. The latter was considered a soft upper limit for Am stars, but a higher rotational velocity of $v \sin i = 120\,\mathrm{km/s}$ was known (Smith, 1972). This scenario is most likely solitary, as the upper limit for Am rotation velocity is generally accepted to be $v \sin i = \approx 100\,\mathrm{km/s}$ (Burkhart, 1979; Abt & Levy, 1985; Kunzli & North, 1998; Debernardi et al., 2000; North & Debernardi, 2004; Iliev et al., 2006), differentiating the Am stars from the chemically-normal A-type stars as two succinct groups (Abt, 2000; Balona et al., 2015).

The cause of the slow rotation in Am stars is believed to be effectuated by tidal

interaction through their high binary fraction, where the gravitational interaction decreases the angular momentum in the stars' rotational velocities (Roman, Morgan & Eggen, 1948; Abt, 1961; Abt & Levy, 1985; Smalley et al., 2014), or by magnetic breaking for the solitary Am stars (Mathys, 1988; Hill & Landstreet, 1993; Lanz & Mathys, 1993; Gray, 2014; Smalley et al., 2014). Discoveries of new Am stars will continue with the TESS mission (see § 2.3) in parallel with ground-based follow-up spectroscopy; a highlight of which is the first known Am star – brown dwarf binary pair (Šubjak et al., 2020). It is also of note, and perhaps not well known, that the brightest star in the night sky, Sirius A, is also an Am star (Kohl, 1964; Abt, 1979; Kervella et al., 2003).

1.2 An Introduction to Exoplanets

"...most stars are much too far away for us to discover their planets at all — if there are any"

— Hans augusto Rey

A New Way to See the Stars

(Rey, 1966)

1.2.1 Praefatio

On the day I was born, Saturday, 5$^{\text{th}}$ November 1994, only *five* exoplanets had been discovered — five planets that existed outside of our Solar System; five planets that orbited stars other than the Sun. Incorporating the nine[2] planets in our own Solar System, only 14 planets were known to exist in the whole Universe — but of course, millions more were theorised. Of those five exoplanets, four were discovered around

[2]Pluto had yet to be demoted

pulsars from the planets causing irregularities in the timings of the received pulses, and one exoplanet was discovered via the radial velocity (RV) movements of its host star. Not even the famous 51 Peg b, the first exoplanet orbiting a main sequence star, had been discovered yet!

Six years prior, *no* exoplanets were known. This field of astrophysics is very young, but it has grown exponentially over the past 30 years: at the time of writing (May, 2023), there are now 5,347 known exoplanets populating 4,010 exoplanetary systems, with 9,618 exoplanet candidates awaiting confirmation[3]. The exoplanets discovered have a wider diversity of size, semi-major axes and hosts stars than could ever have been predicted, completely re-defining planetary system formation models (and proving that our Solar System is far from normal).

1.2.2 A Brief History of Exoplanets

The first widely-accepted exoplanets to be discovered were PSR B1257+12 c and PSR B1257+12 d[4], orbiting the 6.2 ms pulsar PSR B1257+12. They were discovered from observations using the 305-m Arecibo radio telescope, where variations of ± 0.7 ms were found in the period curve from the 430 MHz observations; the authors deduced that variations could only exist due to the influence of planetary bodies orbiting the pulsar (Wolszczan & Frail, 1992).

The actual first exoplanet discovered was γ Cephei Ab, orbiting one of the γ Cephei binary pair (HD 222404), but announcing this exoplanet as the true first is controversial as while it was suspected to exist from as early as 1988 (Peterson, 1988; Campbell, Walker & Yang, 1988; Lawton & Wright, 1989; Vidal-Madjar, 1989), it was not fully confirmed until 15 years later (Hatzes et al., 2002, 2003). γ Cephei Ab was

[3]https://exoplanets.nasa.gov

[4]PSR B1257+12 b was discovered 2 years later than the first two planets (Wolszczan, 1994), but back then the "a, b, c..." naming convention had not been implemented and the three exoplanets were initially named "PSR B1257+12 B, PSR B1257+12 C and PSR B1257+12 D". When their names were changed to the lower case nomenclature they were labelled by radial distance from their host star, rather than by discovery date as is the norm today

discovered via the RV method (see § 1.2.3.1), using four RV data sets spanning observations between 1989 – 2002. The discoveries of PSR B1257+12 c, PSR B1257+12 d and γ Cephei Ab alone argued against contemporary theories of planet formation, which were based on our Solar System (Lissauer, 1993).

The above discoveries were identified from ground-based observational data, which yielded a few exoplanet discoveries per year. By the middle of the 2000s, exoplanet discoveries were the subject of space missions with the launch of the first space-based mission in 2006: ***Co****nvection,* ***Ro****tation et* ***T****ransits planétaires* (**CoRoT**; Baglin et al., 2006), followed by the Kepler Space Telescope in 2009 (*Kepler*; Borucki et al., 2010), and the Transiting Exoplanet Survey Satellite (TESS; Ricker et al., 2015) launched in 2018 (see § 1.2.4 for *Kepler* and § 2.3 for TESS). CoRoT increased the number of known exoplanets quickly, but *Kepler* completely revolutionised the field and almost solely brought the exoplanet count up to 4000; with TESS, this number is predicted to increase five-fold over its lifetime (Ricker et al., 2015), and now the James Webb Space Telescope (JWST) is contributing to the effort (Ment et al., 2023).

We now know that exoplanets exist around our closest stellar neighbour: two confirmed planets and one candidate are known to orbit Proxima Centauri (Anglada-Escudé et al., 2016; Faria et al., 2022; Artigau et al., 2022) — and conversely, we know of two exoplanets over 8.5 kpc away: SWEEPS-04 orbiting SWEEPS J175853.92-291120.6 and SWEEPS-11 orbiting SWEEPS J175902.67-291153.5, the current furthest known exoplanets (**S**agittarius **W**indow **E**clipsing **E**xtrasolar **P**lanet **S**earch: **SWEEPS**; Sahu et al., 2006, 2008). We know of exoplanets larger than Jupiter and smaller than Mercury, with the current largest being TYC 8998-760-1 b at $3.0^{+0.2}_{-0.7}\,R_J$ ($34.0^{+2.2}_{-7.9}\,R_\oplus$; Bohn et al., 2020), and the current smallest being Kepler-37 b at $0.774\pm0.097\,R_{Mer}$ ($0.296\pm0.037\,R_\oplus$; Barclay et al., 2013). The exoplanet with the longest orbital period that we know of is COCONUTS-2b (**CO**ol **C**ompanions

ON Ultrawide orbi**TS**: **COCONUTS**; Zhang et al., 2020), with an angular separation on the sky between the exoplanet and star of 594″ that equates to a semi-major axis of 6471 au, and an orbital period of over 1.1 Myr (Zhang et al., 2021); on the other end of the scale there is SWIFT J1756.9-2508, with an orbital period of just 0.03799 d (54 min 42.3 s; Krimm et al., 2007). Finally, we know systems that are multi-star in nature, with planets orbiting one star in a binary, both binaries, triple star systems, and even quadruple star systems, such as PH1 b (**P**lanet **H**unters 1: **PH**1; Fischer et al., 2012; Schwamb et al., 2012, 2013).

One of the most important discoveries to-date was by *Kepler*: that the most common exoplanets discovered have radii between $1 - 10\,R_\oplus$ — between the radii of Earth and Neptune[5] — and such planets do not exist in our solar system; these planets are dubbed "Super-Earths" if they are rocky, or "Mini-Neptunes" if they are gaseous. Also, only one other system has been found with as many planets as ours, the Kepler-90 system (Shallue & Vanderburg, 2018), and no system is known to have more — the TRAPPIST-1 system comes close (**TRA**nsiting **P**lanets and **P**lanetes**I**mals **S**mall **T**elescope: **TRAPPIST**; Gillon et al., 2011), hosting seven exoplanets, but it is far more compact than our Solar System: the entire TRAPPIST-1 system is similar in size, both in size of the host star and the semi-major axes of the orbiting planets, to Jupiter and the four Galilean moons (Gillon et al., 2017; Luger et al., 2017; Grimm et al., 2018). Both the Kepler-90 and TRAPPIST-1 discoveries emphasise that our Solar System is not at all "standard".

Statistics from microlensing observations have deduced that on average every single star hosts at least one planet (1.6 per star; Cassan et al., 2012), and with $\approx 10^{11}$ stars in the Milky Way (Freedman, Geller & Kaufmann, 2014), upwards of 1.6×10^{11} planets could exist in our Galaxy alone.

[5] https://exoplanets.nasa.gov/keplerscience

1.2.3 Exoplanet Detection Methods

Of the 5,347 exoplanets known to-date, each were discovered by one or more of 25 methods[6]. The following Sub-Sections explore the five highest-yielding detection methods, itemised in chronological order from the date of their first confirmed detection, and the respective pros and cons of each method are discussed. However, the Transit Method has been placed last as it plays a substantial role in many areas of work in this thesis, so it has the most in-depth discussion. More detection methods than the following do exist, but are either yet to be successful or still remain hypothetical, and for such reasons are omitted here but are instead listed in Table 1.2 (the reader is directed to Perryman (2018) for an extensive review of each exoplanet detection method, and for exoplanet science as a whole).

1.2.3.1 The Radial Velocity Method

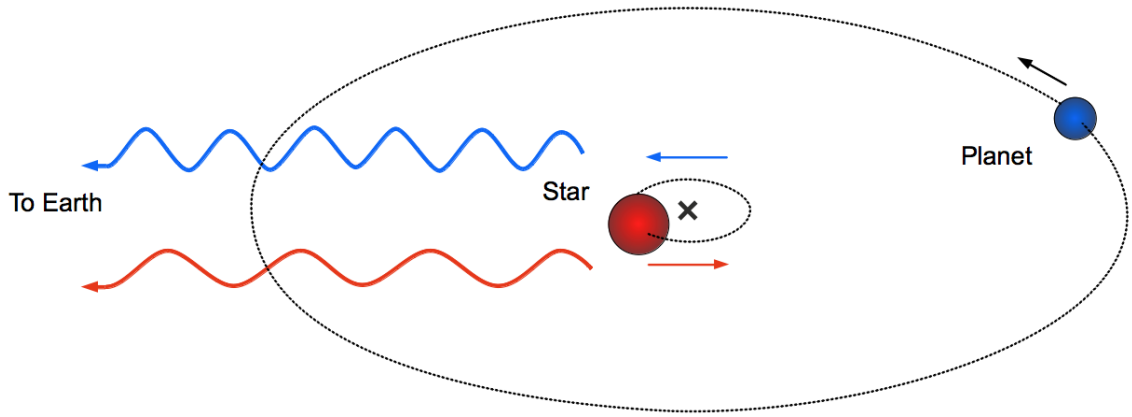

Figure 1.8: *A diagram displaying The Radial Velocity Method. Both the star and the planet orbit the barycentre of their system, so during one orbital period of the planet the star moves relatively towards and away from the Earth, periodically inducing blue and red doppler shifts in its spectra. Multiple measurements can build an RV curve, the semi-amplitude of which can be used to determine a physical velocity of the star (and furthermore the mass of the planet). This diagram is original work by Tenefifi, CC0, via Wikimedia Commons.*

All stars in the Milky Way move along their orbits around the Galactic centre,

[6]Some of these methods are only theoretical

and relative to the Earth we observe this as a doppler shift. But the motion of some stars can be perturbed from our point of view, due to the gravitational influence of orbiting companions.

We can measure the line-of-sight motion of a star via spectroscopic observations, determining its relative velocity to the Earth via the relative doppler-shift between the absorption lines in its spectra and those of synthetic spectra on Earth. For a star without a companion, all observations will produce the same magnitude of velocity as there is nothing to perturb its relative motion. But for stars with one or more companions, all bodies will be orbiting the barycentre of the system and as such the star will move at a certain velocity relative to the Earth, the magnitude of which will increase and decrease periodically as the companion's gravitational influence pulls on its host star. This the star's radial velocity (RV) — but it is inclination dependant, with the maximum measured RV occurring for a companion that orbits its host star at 90° to the plane of the sky (edge-on). Hence, relative to the Earth, the star will move towards and away from the observer during the orbit of the companion, as shown in the diagram in Figure 1.8, producing a small-but-measurable doppler-shift in the host star's spectra. Multiple observations over time will produce different measurements of the host star's RV, which when corrected to remove the motion of the Earth's orbit around the Sun (the Barycentric correction) will be both positive and negative in relation to the mean motion of the star from the Earth. Plotting the RV measurements against time will construct an RV curve, and the more-circular the orbit of the companion (less eccentric; $e \rightarrow 0$), the more sinusoidal in shape the RV curve will be. Hence this method is known as the Radial Velocity Method (and sometimes is referred to as the Doppler Spectroscopy Method; Lindegren & Dravins, 2003).

With sufficient observations, an RV curve can be phase-folded to determine the orbital period of the companion. Furthermore, the semi-amplitude of the curve

can be exploited to give a *minimum* mass of the companion, $M_P \sin i$, using Equation 1.15 (the mass of the host star must be known; equation taken from Perryman (2018, their Eqn. [2.28])):

$$K = 28.4\,\mathrm{ms}^{-1} \left(\frac{P}{1\,\mathrm{yr}}\right)^{\frac{-1}{3}} \left(\frac{M_P \sin i}{\mathrm{M_J}}\right) \left(\frac{M_*}{\mathrm{M}_\odot}\right)^{\frac{-2}{3}} \tag{1.15}$$

- Where K is the semi-amplitude of the RV curve, P is the orbital period of the companion, $M_P \sin i$ is the minimum mass of the companion (i is the inclination of its orbit), and M_* is the mass of the host star.

Only $M_P \sin i$ can be obtained without knowledge of the inclination of the orbit. The magnitude of K is proportional to i, so only for a system where the companion's orbit is exactly in the line of sight ($i = 90°$) will the magnitude of K directly give the mass of the companion ($\sin(90°) = 1$). But for an inclined orbit, the magnitude of K is measured smaller than its absolute value, and hence the companion is determined to have a smaller mass than is true. Therefore, information about the inclination of the companion's orbit corrects for any mass underestimates (Perryman, 2018).

The RV method is an excellent tool for detecting exoplanets, and excels where other detection methods may struggle: it can detect the presence of companions around bright stars where transit signals may be too faint to see, or where companions orbit close-in to their host star and the glare from the star washes out any chance of directly imaging them. But the RV method is also limited, however, to companions with low inclinations relative to the line of sight of an observer: for systems where the companions orbit face-on, the host star will have no movement relative to the Earth and as such its relative RV will be impossible to detect. Also, this method is well-suited to companions that have short orbits as RV curves can be built and phase-folded over a short period of time from relatively few observations — a short orbit also favours the relation between an RV amplitude and the

inverse square root of the semi-major axis (see by substituting Kepler's 3rd Law in Equation 1.15), which would help make detections more likely: for companions with long orbital periods, the work could be decades- to centuries-long before sufficient observations have been taken to phase-fold the light curves.

The idea of using RVs to detect exoplanets was first proposed as early as the 1950s (Struve, 1952), but the first exoplanet detected with this method was not found until over 40 years later, with the discovery of 51 Peg b around the star 51 Pegasi (HD 217014) — not only was this the first RV-discovered exoplanet, but also the first exoplanet discovered around a main sequence star (Mayor & Queloz, 1995)[7]. To-date, the RV Method has confirmed 1,036 exoplanets[8], and until 2012 it was the highest-yielding exoplanet detection method.

1.2.3.2 The Gravitational Microlensing Method

This method works for detecting planets around foreground stars that act as gravitational lenses, magnifying the light of distant stars. Stars that are close to the Earth move across the sky relatively faster than the more-distant stars do, and occasionally two stars line up from the Earth's line-of-sight. The gravitational well of the foreground star "bends" the light of the distant star as it passes in front, briefly magnifying its intensity and causing the distant star to appear brighter (Refsdal, 1964), as shown in the diagram in Figure 1.9. When measuring the brightness of the distant star over time a single spike will appear in its light curve, representing an increase in flux from the brief alignment. However, if the foreground star also hosts a companion, a second, smaller peak will also appear in the light curve of the distant star, due to the companion's gravitational well also magnifying the starlight (this small peak would either appear in front of or behind the main peak, dependent on the location of the companion in its orbit; Perryman, 2018).

[7]The authors went on to win the Nobel Prize in Physics for this work in 2019
[8]https://exoplanetarchive.ipac.caltech.edu/docs/counts_detail.html

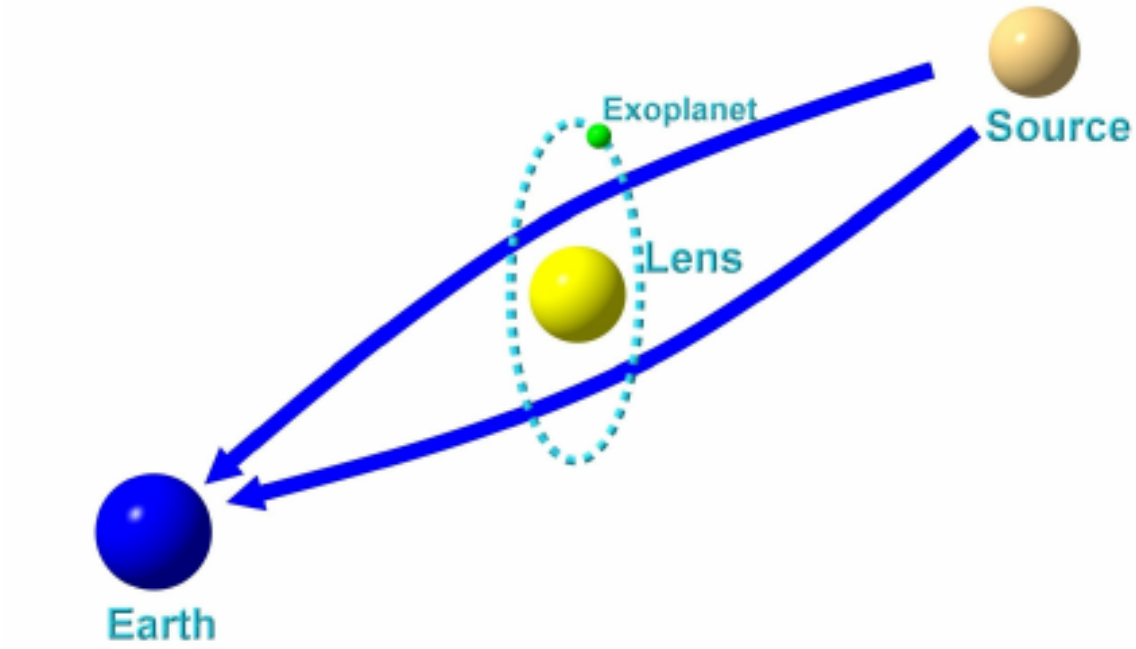

Figure 1.9: *A diagram displaying the The Gravitational Microlensing Method. The gravity of the foreground star magnifies the light of a distant star during a chance alignment, measured as a spike of flux increase in the distant star's light curve. If the foreground star also hosts a planet, a secondary (smaller) spike will also be observed due to the planet's gravity magnifying the light of the distant star as well. This diagram is taken from Christie (2006, their Fig. [1]).*

The Gravitational Microlensing Method allows for exoplanets thousands of parsecs away to be detected, around stars far too faint and/or distant to be observed using any other exoplanet detection method, and with large orbits that would otherwise be undetectable with the RV and transit methods. But the main limiting factor is that companions detected via this method are only seen once — and microlensing events are unpredictable. Hence, vast areas of the sky must be constantly monitored for chance alignments, and with only one observation per system it is difficult to constrain the companions' physical parameters.

The first exoplanet detected via a microlensing event was in 2004 (exactly 300

years since light was first theorised to be affected by gravity): OGLE-2003-BLG-235L b was discovered from phase three of the **O**ptical **G**ravitational **L**ensing **E**xperiment survey (**OGLE-**III; Udalski, 2003; Bond et al., 2004). More recently, this method has found "free-floating" planets that are not gravitationally-bound to any stars (Mróz et al., 2020). To-date, the Microlensing Method has confirmed 193 exoplanets[9].

1.2.3.3 The Direct Imaging Method

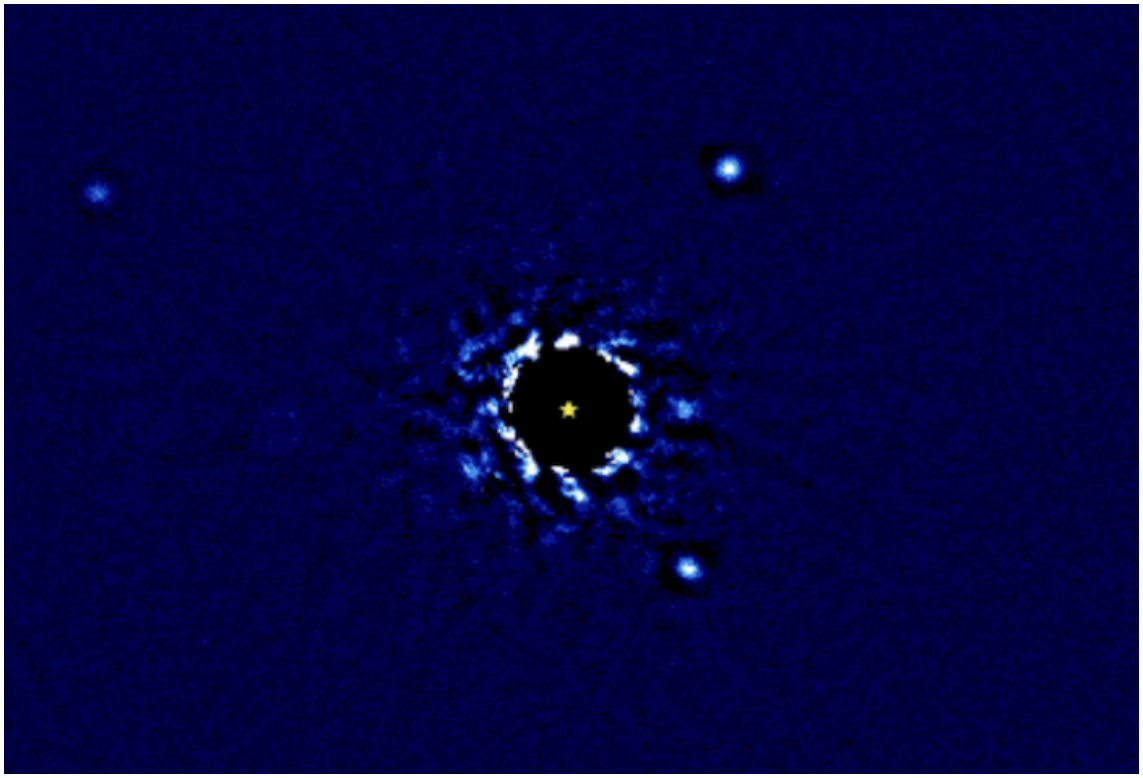

Figure 1.10: *A direct image of the HR 8799 system taken from observations by Wang et al. (2018). The star symbol in the centre represents the location of HR 8799 behind the coronagraph, which is blocking out its starlight. The four bright white dots are the exoplanets in orbit, labelled "b", "c", "d", and "e" in reverse radial distance from their host star (due to the order in which they were discovered).*

The concept behind the Direct Imaging Method is self-explanatory, but in practice it is difficult to achieve. Exoplanet systems are so distant that the angular separation between stars and their companions are extremely small, and the companions

[9]https://exoplanetarchive.ipac.caltech.edu/docs/counts_detail.html

are often lost within starlight glare. So to directly image them, a coronagraph is placed at the centre of the field-of-view of a telescope to block out the light from the host stars, thus removing their glare and revealing the orbiting companions as bright points of light from the starlight they reflect (Perryman, 2018). Taking images of these systems over time allows observers to physically *see* exoplanets orbiting their host stars; most famously this was done with the HR 8799 (HD 218396) system, where a video of its exoplanets moving along their orbits has been created using data from 12 years of observations from the W. M. Keck Observatory[10] — a still of which can be seen in Figure 1.10 (Marois et al., 2008, 2010; Wang et al., 2018).

Direct Imaging dominates where the RV and transit methods fall down: it can detect companions around stars that have face-on orbits, and it does not rely on measurements of the host star at all. However, it is one of the more time-consuming methods as only wide-orbit companions can be directly imaged: either they are caught in the glare from the host star, or they are blocked by the coronagraph. Hence, systems that are directly imaged must be monitored for many years before orbital characteristics become well-constrained, and whilst the mass of the companion remains poorly understood, atmospheric properties such as chemical compositions and the existence of clouds can be deciphered by imaging the exoplanets in specific wavelength bands (such as $5-28\,\mu$m for ammonia; Danielski et al., 2018; Currie et al., 2023). For companions on very wide orbits, far away from their hosts stars, very little starlight gets reflected; whilst they might not be detectable through direct imaging, it is possible that they can be detected via their thermal emission instead (Brooks, Stahl & Arnold, 2015).

The first exoplanet discovered via direct imaging was 2M1207 b, which was also the first exoplanet discovered orbiting a brown dwarf (Chauvin et al., 2004). To-date, the Direct Imaging Method has confirmed 67 exoplanets[11].

[10] https://jasonwang.space/orbits.html
[11] https://exoplanetarchive.ipac.caltech.edu/docs/counts_detail.html

1.2.3.4 The Transit Timing Variation Method

The Transit Timing Variation (TTV) Method applies to systems with two or more planets. For mono-planet systems, with no external forces causing perturbations, the orbital period of their exoplanets remain strictly constant. But with the addition of an extra planet(s), external gravitational forces can cause the orbital period of the first planet to change: the orbital resonance of two or more planets in a system can affect the orbit of one of the planets during an alignment, either speeding up or slowing down its orbital velocity. This effect alternates during every planetary alignment, such that variations in the orbital period are regular and of the same magnitude; naturally, the magnitude of the timing variation is proportional to the mass and separation of the planets. Hence, otherwise "unseen" exoplanets can be discovered, based on the observations of another exoplanet (Perryman, 2018).

The TTV Method is one of the most sensitive exoplanet detection methods, capable of detecting very low mass planets which would otherwise not have produced RV semi-amplitudes large enough, or transit dips deep enough, for detection with other methods (Miralda-Escudé, 2002; Holman & Murray, 2005; Agol et al., 2005) — indeed, TTVs was even the method by which Uranus and Neptune were discovered (Herschel & Watson, 1781; Le Verrier, 1846; Galle, 1846; Adams, 1846). Yet, as mentioned above, this method can only work for systems with two or more planets, and not much information can be obtained about planets discovered through TTVs; only the maximum mass of the "unseen" planet, plus its orbital period.

The first exoplanet discovered by TTVs was V391 Pegasi b (Silvotti et al., 2007). To-date, the TTV Method has confirmed 25 exoplanets[12].

[12]https://exoplanetarchive.ipac.caltech.edu/docs/counts_detail.html

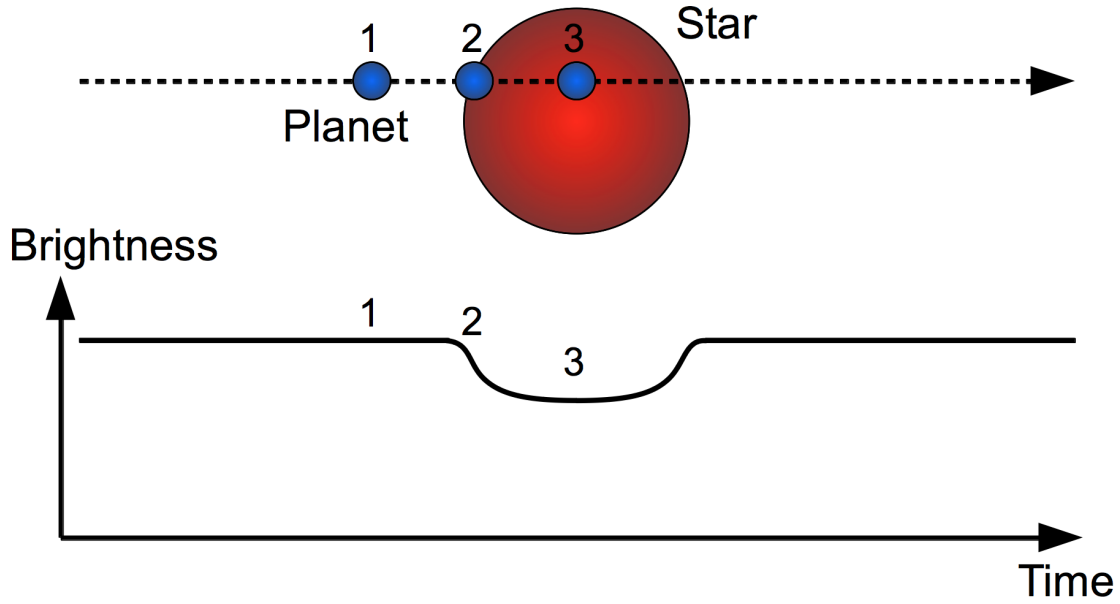

Figure 1.11: *A diagram of The Transit Method. If an object passes in front of a star it blocks out a fraction of starlight that is measured as a brightness dip in the star's light curve. If the same-sized dip periodically appears in the light curve, the object causing it must be gravitationally bound to the star. The depth of the dip represents a size ratio between the object and the star, suggesting whether the nature of the object is stellar, a large gas giant or a small rocky planet. This diagram is original work by Hans Deeg, CC BY-SA 4.0 <https://creativecommons.org/licenses/by-sa/4.0>, via Wikimedia Commons.*

1.2.3.5 The Transit Method

Conceptually the most simple exoplanet detection method, the Transit Method can be described by drawing an analogy to a solar eclipse: when the Moon passes in front of — or transits across — the Sun in the line of sign of an observer, part (or all) of the Sun becomes blocked and as such, less sunlight reaches the Earth.

We can observe smaller versions of this phenomenon from the Earth too, such as transits of the planets Mercury and Venus. When these transits occur, the ratio of the projected area of cross section of the transiting planet's disc on the Sun, to that of the Sun's disc, is directly proportional to the amount of sunlight obscured. So by measuring the amount of sunlight received over time, a transit could be detected without directly seeing the planet. Hence, this concept can be applied to planets in

other star systems that cannot be directly observed.

If monitoring the light of a star over time, a light curve of the star's intensity could be constructed which would display a horizontal line of maximum intensity, but at the time of the transit there would be a small brightness dip. If just one dip is measured, then it cannot be certain an exoplanet caused it (an exoplanet, an interstellar dust cloud, or a calibration fault in the detector could all theoretically produce a dip). But if the dip is repeating — specifically periodically — and it is the same magnitude in depth each time, then its origin can be confidently thought of as an object gravitationally bound to the system, orbiting the monitored star.

The light curve of a star with a transiting planet can reveal a lot of information about the system's characteristics. Firstly, as mentioned above, the depth of a dip in the light curve — denoted as δ in units of ppm, when multiplied by 10^6 — is directly proportional to the ratio of the radius squared of the companion to its host star. This relation can be seen in Equation 1.16:

$$\delta \equiv \frac{\Delta F}{F_0} = \left(\frac{R_\mathrm{p}}{R_*}\right)^2 \tag{1.16}$$

- Where ΔF is the decrease in flux received during the mid-point of a transit (when δ is at maximum), F_0 is the amount of out-of-transit flux received (100% intensity), R_p is the radius of the companion, and R_* is the radius of the host star.

And in Equation 1.17 in terms of a $2\,\mathrm{R}_\oplus$ exoplanet orbiting a Sun-like star, taken from Ricker et al. (2015, their Eqn. [1]):

$$\delta = (337\,ppm)\left(\frac{R_\mathrm{p}}{2R_\oplus}\right)^2\left(\frac{R_*}{R_\odot}\right)^{-2} \tag{1.17}$$

However it must be stressed that as this is a ratio, the nature of the companion is not initially known: an exoplanet orbiting a small star could produce an

identically-sized dip to a brown dwarf orbiting a large star. In addition, a certain-sized companion would produce different transit depths dependent on the luminosity of the host star (but the fractional depth would remain the same).

Secondly, the separation between each maximum δ provides a direct measurement of the orbital period, P, of the companion, giving insight to its proximity to its host star. In addition, the width of a dip gives T, the transit duration, used to further prove the transit is caused by a singular object, as opposed to dust rings or a comet trails which would otherwise produce uneven dips with very extended transit durations (as famously seen with Tabby's Star: KIC 8462852; Meng et al., 2017)[13].

Furthermore, T allows for an impact parameter, b, to be calculated, which represents a distance from the stellar centre ($b = 0$) to the limb ($b = 1$): for a high impact parameter, the transit is considered to be *grazing* (T is dependent on the mean stellar density, ρ_*, of the host star as well; Ricker et al., 2015; Perryman, 2018). In combination with the T, the shape of a dip also reveals whether a companion transits completely interior to the disc of the star, or whether or not the transit is grazing — a more-grazing transit produces a more-"V-shaped" dip.

Hence, grazing transits occur when the companion never fully transits within the stellar perimeter (Emilio et al., 2012). And with the more-"V-shaped" dip, the light curve from a grazing transit is not a true representation of the companion: δ will also be too shallow, leading to the companion being mischaracterised[14]. Equation 1.18 shows a relation between T, ρ_* and b in terms of an exoplanet on a 10-d orbit around a Sun-like star, taken from Ricker et al. (2015, their Eqn. [2]):

$$T = (3.91\,h)\left(\frac{\rho_*}{\rho_\odot}\right)^{\frac{-1}{3}}\left(\frac{P}{10\,\mathrm{d}}\right)^{\frac{1}{3}}\sqrt{1-b^2} \tag{1.18}$$

The Transit Method is a very powerful exoplanet detection method, providing

[13]Not alien megastructures

[14]WASP-67 b was the first exoplanet discovered which also had a grazing transit (Hellier et al., 2012), and its true parameters were corrected for by taking into account its impact parameter (Mancini et al., 2014)

direct evidence of the existence of transiting objects from dips in light curves. It is very sensitive, revealing very small exoplanets around stars that otherwise would produce weak RV measurements, and it can detect exoplanets very close to their host stars that would not be seen in direct images.

However, the Transit Method alone cannot be used to solely confirm the existence of exoplanets: all transiting companions require an RV measurement for validation (Panahi et al., 2022). Without RV follow-up observations, many exoplanets detected via light curve dips would remain as candidates — other planet-validation methods do exist, such as observing transits in multicolour (Parviainen et al., 2019). Also, as the Transit Method is most sensitive to large companions orbiting small stars (larger size ratios), many transiting signals of small exoplanets orbiting large, bright stars are lost in the noise as the fraction of light blocked out is very small (Perryman, 2018). Furthermore, many companions will remain as candidates if they only have a single transit in their light curves: three or more identical transits are required before a companion can be confidently declared as gravitationally bound to the host star (otherwise the orbital period of the companion remains unknown and hence the origin of the dip is not well understood; Perryman, 2018).

Finally, there is an observational bias of companions with short orbital periods as the Transit Method is a time consuming process: for some mono-transit objects it could be millennia before a second transit it seen. This also means that multi-planet systems can have a combination of confirmed and candidate exoplanets: the faster-orbiting ones can be detected, undergo RV follow-up observations and be validated before enough transits are detected for the slower-orbiting ones — and exoplanets with strong orbital resonances can occasionally line up during a transit, producing deeper and wider dips than expected which injects a mischaracterised-larger planet into the system that does not actually exist. And all of the above is only if the plane of the system is inclined with respective the observer: only the most edge-on

companions will transit across their host star from the point of view of the Earth ($i = 80 - 90^{\circ}$; Borkovits et al., 2011), all other companions will be missed.

The Transit Method has been the most prolific exoplanet detection method to-date, at almost 4000 exoplanets (≈80% of the known total)[15]. The first exoplanet discovered using the Transit Method was OGLE-TR-56 b, detected in 2002 and confirmed via RV follow-up in 2003 (Udalski et al., 2002; Konacki et al., 2003).

It is hoped that the reader will note how the different methods described above all compliment each other, and how a combination of all of them allows for almost any type of system to be characterised.

1.2.3.6 Other Exoplanet Detection Methods

As mentioned above, there are a total of 25 methods through which exoplanets can be detected. The five highest-yielding are discussed above, but for completeness the remaining 20 methods are listed in Table 1.2 in descending order of their yield, along with the respective number of exoplanets discovered for each, the year of the first discovery, and a reference to that publication. It should be noted that some of these methods are still theoretical: these appear below the horizontal-dashed line.

1.2.4 Previous Exoplanet Surveys

This Section explores examples of previous exoplanet-dedicated surveys that specifically used the transit method for detection, and whose data can also be used for asteroseismic analysis — they were inspiration for the exoplanet survey discussed in Chapter 4. The highest-yielding ground-based and space-based surveys are discussed: The Wide-Angle Search for Planets and The Kepler Mission. Many more surveys do exist, using the same or other methods, and their importance is not undermined by their omission in this Section.

[15] https://exoplanetarchive.ipac.caltech.edu/docs/counts_detail.html

Table 1.2: *The remaining 20 exoplanet detection methods that have not been discussed in-depth, listed in descending order of their yield (where known). Methods below the horizontal dashed line are still theoretical and have yet to detect any exoplanets. Data of the number of exoplanets discovered has been extracted from the NASA Exoplanet Archive.*
† *The NASA Exoplanet Archive has grouped these separate methods together, so the exact number for each is not confidently known and Kepler-76 b is claimed to be the first discovery of both methods.*
†† *Currently this is the only method capable of detecting exoplanets in other galaxies (Di Stefano et al., 2020).*
††† *This method has been confirmed to work using the known exoplanet HD 189733 b (Berdyugina et al., 2008).*

Method	Number of Exoplanets Found	Name of First Found	Year of First Discovery	Reference
Eclipse Timing Variations	17	DP Leo b	2009	(Qian et al., 2010)
Orbital Brightness Modulations	$\leq 9^{\dagger}$	Kepler-76 b	2013	(Faigler et al., 2013)
Relativistic Beaming	$\leq 9^{\dagger}$	Kepler-76 b	2013	(Faigler et al., 2013)
Pulsar Timing Variations	7	PSR B1257+12 b	1992	(Wolszczan & Frail, 1992)
Reflection and Emission Modulations	2	Kepler-70 b & c	2011	(Charpinet et al., 2011)
Pulsation Timing Variations	2	V0391 Peg b	2007	(Silvotti et al., 2007)
Astrometry	2	DENIS-P J082303.1-491201 b	2013	(Sahlmann et al., 2013)
Disc Kinematics	1	HD 97048 b	2019	(Pinte et al., 2019)
X-ray Eclipse††	1	M51-ULS-1 b	2020	(Di Stefano et al., 2020)
Transit Duration Variations	—	Kepler-16 b	2011	(Doyle et al., 2011)
Auroral Radio Emissions	0	—	—	
Dust Trapping around Lagrangian Points	0	—	—	
Eclipsing Binary Minima Timing	0	—	—	
Ellipsoidal Variations	0	—	—	
Flare and Variability Echo Detection	0	—	—	
Magnetospheric Radio Emissions	0	—	—	
Modified Interferometry	0	—	—	
Optical Interferometry	0	—	—	
Polarimetry	$0^{\dagger\dagger\dagger}$	—	—	
Transit Imaging	0	—	—	

CHAPTER 1

The Wide-Angle Search for Planets

The **W**ide **A**ngle **S**earch for **P**lanets (**WASP**; Pollacco et al., 2006) consortium first met in 2000 and created one of the first large-scale ground-based sky surveys, with the primary objective of detecting exoplanets using the transit method. The WASP Project consisted of two observatories, one in each hemisphere of the Earth, each housing SuperWASP cameras. SuperWASP-North is located at the Observatorio del Roque de los Muchachos on La Palma, the Canary Islands. SuperWASP-South is located at the Sutherland Station of the South African Astronomical Observatory (SAAO). The main aim of the WASP is to detect transiting exoplanets around bright host stars suitable for spectroscopic follow-up observations. In its first six months of operation, SuperWASP-North achieved ∼6.7 million unique light curves with a total of 12.9 billion data points (Pollacco et al., 2006).

Each instrument in the SuperWASP cameras had a field-of-view of 482 $\deg^2$ and a pixel scale of 13.7″ pix^{-1}. Combing these two observatories allowed WASP to survey the entire visible sky with a 40-minute cadence (Collier Cameron et al., 2007).

To-date, WASP has discovered 192 exoplanets[16].

The Kepler Mission

Kepler was the first deep-space mission with the sole objectives of searching for exoplanets and observing pulsating stars, independent of Earth-restricted viewing (Borucki et al., 2008, 2009, 2010). It was launched in 2009 into an Earth-trailing orbit around the Sun, with a period of 372.5 d (Basri, Borucki & Koch, 2005) — *Kepler* currently drifts away from Earth at the rate of 0.1 au per year.

Kepler completely revolutionised the transit method search for exoplanets (Borucki et al., 2003). It observed the same part of the sky continuously during its original

[16]https://wasp-planets.net/wasp-planets

3.5-year mission, observing over 150,000 stars simultaneously with the ability to discover exoplanets with orbits identical to Earth's with unprecedented precision.

The photometer onboard *Kepler* was composed of an array of 42 CCDs, which coupled with *Kepler's* 0.95-m telescope provided a field-of-view 12° across. The spacecraft took data in two different cadences, "long" and "short", giving integrated data points every 29.4 min and 58.9 s, respectively (Koch et al., 2010).

The original mission ended abruptly after the failure of a second reaction wheel compromised the telescope's pointing stability. *Kepler* instead began observing for an updated mission: K2 ("*Kepler* Second Light;" Howell et al., 2014). The new target areas were based only in the ecliptic as the torque from Solar radiation pressure was uniform across the spacecraft. The new observing sessions, called Campaigns, were only ∼80 d long due to Solar pressure not remaining uniform as *Kepler* moved along its orbit: the spacecraft was rotated periodically to counter this effect (and to stop it eventually pointing at the Sun; Sage, 2012; Haas et al., 2014).

K2 ended on 15th November 2018 — 388 years to the day after the death of Johannes Kepler — as *Kepler* had run out of fuel: the space-craft was then deactivated[17]. To-date, *Kepler* has confirmed the discovery of 2,709 exoplanets — almost half of all transit method-based exoplanet discoveries — and has detected an extra 2,053 exoplanet candidates[18].

1.2.5 Stars Hosting Exoplanets

The principal objective of observing exoplanet transits is to determine system properties. As mentioned above, only a planet-to-star radius ratio and an orbit inclination angle can be established from a light curve alone: absolute measurements of an exoplanet demands knowledge of the host star's fundamental properties. Stars can

[17]https://www.jpl.nasa.gov/news/kepler-telescope-bids-goodnight-with-final-commands
[18]https://exoplanetarchive.ipac.caltech.edu/docs/counts_detail.html

be modelled to have their masses, radii and rotation rates determined, and spectroscopic follow-up data an be utilised to infer host-star $T_{\rm eff}$ and $v \sin i$.

The metallicity of a star can be an indicator that helps determine whether a star has planets, and, if so, what type of planets as there exists a direct metallicity – exoplanet correlation. It has been demonstrated that there is a connection between a star's metallicity and it hosting gas giant planets: the more metal-rich a star is during its early evolution, the more metal rich its proto-planetary disc is and thus the greater the likeliness that exoplanets will form (Fischer & Valenti, 2005). Metallicity also has an affect on the chromaticity of a star, such that two stars can be equal in terms of mass and age, but with one bluer or redder than the other depending on whether it has a lower or higher metallicity, respectively (less metal-rich stars also emit less UV light; Arimoto, 2005; Wang & Fischer, 2015).

Observing exoplanet transits via multicolour observations has the potential to show transits with different relative depths per waveband, due to colour-dependency of both host-star luminosity and planet atmospheric absorption. This can further constrain an exoplanet's radius, will give insight into its atmospheric properties, will resolve the inclination of the orbit by determining the impact parameter of the transit, and will allow derivations of the limb-darkening values of the host star (Jha et al., 2000; Deeg, Garrido & Claret, 2001). Mandel & Agol (2002) produced an extensive list of equations relating to a plethora of scenarios that describe every point of any transit with any size-combination of star and planet.

The majority of known-exoplanets orbit M-type stars, but this may be an observational bias as planets orbiting M-dwarfs are easier to detect — nevertheless, there is a sparsity of systems with host stars hotter than the Sun. Fewer than 300 exoplanets are confirmed around main sequence A-type stars, only ∼6% of the currently-known total — to-date, the main sequence $T_{\rm eff}$ upper limit is $18,310 \pm 320\,{\rm K}$, from the main-sequence host star b Centauri (HD 129116; Janson et al., 2021).

Zhou et al. (2016) published the discovery of the fourth-known exoplanet orbiting an A-type star, KELT-17 b[19], and noted that only 26 exoplanets (all hot-Jupiters) exist around host stars hotter than 6250 K. Furthermore, Zhou et al. (2016) stated that 18 of the 26 hot-Jupiters in their sample (69%) were spin-orbit misaligned ($|\lambda| > 10°$), and that all four of the exoplanets around A-type stars had severely misaligned orientations too, suggesting that this spin-orbit misalignment will be common amongst the ∼300 exoplanets with A-type hosts. Of these, a small sub-set of the hot host stars also pulsate, and these systems are even rarer.

1.2.6 Pulsating Stars Hosting Exoplanets

Asteroseismic analysis of exoplanet systems enables the most-precise determination of its properties. Pulsating stars can be modelled by utilising their pulsation frequencies to determine the highest precision stellar parameters, giving clues about the stars' internal structures as well: hence, the more meticulous the host stars are characterised, the better understood its companions are too. Therefore, the discovery of planets around pulsating stars provides a laboratory which offers the opportunity for the most precise studies of exoplanet systems (Schuh, 2010).

Chapters 5 and 6 contain in-depth scientific analyses of two stars observed by TESS: TIC 409934330 and TIC 156987351. The data for these stars were obtained from the TESS Object of Interest (TOI) database, after implementing a $T_{\rm eff}$ threshold of ≥6300 K established from Zhou et al. (2016). TIC 409934330 and TIC 156987351 were flagged as TOIs as their light curves showed signatures of exoplanet transits. However, these stars were not chosen only for their companions: Fourier transforms of the stars' light curves revealed that both exhibit δ Scuti pulsations.

The frequencies of δ Scuti pulsations allow such stars to be well-modelled, increasing the precision of their exoplanet characterisation. WASP-33 was the first

[19]KELT-17 is of interest as, like TIC 409934330 in Chapter 5, it is an Am host star (but non-pulsating; Saffe et al., 2020)

δ Scuti variable host star discovered (Collier Cameron et al., 2010; Herrero et al., 2011), yet at the time of writing there are only *seven* known examples of exoplanets orbiting main-sequence δ Scuti stars in the literature, emphasising their rarity.

Asteroseismology presents another unique opportunity for the synergy between it and exoplanet science, too. It is known that the orbital period of an exoplanet changes if it tidally-interacts with its host star (Privitera et al., 2016), but exoplanets that orbit very close to their hosts stars can induce tidal pulsations in them, in resonance with the exoplanets' orbit (de Wit et al., 2017): this is seen in binary star systems as well (e.g., "heartbeat stars"; Hambleton et al., 2018). Thus, the detection of multiple pulsation modes in host stars allows for the use of asteroseismic tools to conduct complete stellar and exoplanet modelling (see § 3.1, 3.2 and 3.3).

1.2.7 Conclusions

As mentioned above, there are only seven known examples of exoplanet – δ Scuti systems in the literature (one of the stars hosts two planets, so eight planets around main-sequence δ Scuti stars in total). These δ Scuti host stars are listed in Table 1.3, and their respective exoplanets are listed in Table 1.4. The population of such systems is too small to be able to confidently derive statistical conclusions; it is not known whether there is a most-common characteristic of a δ Scuti host star or a most-common type of exoplanet orbiting a δ Scuti host star, for example. Therefore, the work in this thesis will aim to advance the understanding of this duo of asteroseismic and exoplanet science by modelling and describing two *new* exoplanet – δ Scuti systems, adding to the small population of exoplanets orbiting main sequence δ Scuti stars.

Table 1.3: *The seven known δ Scuti host stars, along with their parameters and respective references, listed in order of discovery.*
† *Whilst there is no formal mention in the literature of these stars being δ Scuti stars, they exhibit δ Scuti pulsations in their TESS light curves.*

C.C.10, H.11, G.18 = (Collier Cameron et al., 2010; Herrero et al., 2011; Goyal et al., 2018),
R.13, G.14, C.18 = (Rameau et al., 2013; Galicher et al., 2014; Chauvin et al., 2018),
R.14, M.19, H.21 = (Rowe et al., 2014; Murphy et al., 2019; Hey et al., 2021),
M.16 = (Morton et al., 2016),
C.17 = (Chauvin et al., 2017),
T.17 = (Temple et al., 2017),
H.19 = (Hellier et al., 2019).

Star Designation	Spectral Type	$T_{\rm eff}$ (K)	$\log g$ ($\log \mathrm{cm\,s^{-2}}$)	$v \sin i$ ($\mathrm{km\,s^{-1}}$)	M_* ($\mathrm{M_\odot}$)	R_* ($\mathrm{R_\odot}$)	Reference
HD 15082	kA5hA8mF4	7471 ± 63	4.35 ± 0.07	90 ± 10	1.495 ± 0.031	1.444 ± 0.034	C.C.10, H.11, G.18
HD 95086†	A8	7750 ± 250	4.0 ± 0.5	20 ± 10	1.6 ± 0.1	—	R.13, G.14, C.18
Kepler-340	F6	8150 ± 376	$4.3772400^{+0.0914693}_{-0.1062500}$	—	$1.870000^{+0.383933}_{-0.226349}$	$1.4666800^{+0.0871834}_{-0.0841834}$	R.14, M.19, H.21
Kepler-1171†	—	$7044.000^{+277.693}_{-199.093}$	$4.38^{+0.17}_{-0.09}$	—	$1.580^{+0.179}_{-0.168}$	$1.950^{+0.513}_{-0.384}$	M.16
HD 116434†	A2	8840 ± 200	—	299 ± 9	1.96 ± 0.04	1.77 ± 0.05	C.17
CD-34 8618	F1	6900 ± 150	—	52 ± 8	1.59 ± 0.08	1.79 ± 0.05	T.17
HD 134004†	A1	9360 ± 50	4.31 ± 0.04	8.2 ± 0.6	2.07 ± 0.11	1.67 ± 0.07	H.19

Table 1.4: *The eight known exoplanets orbiting δ Scuti host stars, along with their parameters and respective references, listed in order of discovery.*

C.C.10, H.11, G.18 = (Collier Cameron et al., 2010; Herrero et al., 2011; Goyal et al., 2018),
R.13, G.14, C.18 = (Rameau et al., 2013; Galicher et al., 2014; Chauvin et al., 2018),
R.14, M.19, H.21 = (Rowe et al., 2014; Murphy et al., 2019; Hey et al., 2021),
M.16 = (Morton et al., 2016),
C.17 = (Chauvin et al., 2017),
T.17 = (Temple et al., 2017),
H.19 = (Hellier et al., 2019).

Exoplanet	P (d)	M_p (M_J)	R_p (R_J)	a au	Reference
WASP-33 b	1.2198669 ± 0.0000012	<4.1	1.497 ± 0.045	0.02555 ± 0.00017	C.C.10, H.11, G.18
HD 95086 b	$288.6^{+11.5}_{-176.5}$ yr	4.5 ± 0.5	—	$52.0^{+12.8}_{-24.3}$	R.13, G.14, C.18
Kepler-340 b	14.844387 ± 0.000473	—	0.226 ± 0.054	0.1340	R.14, M.19, H.21
Kepler-340 c	22.824669 ± 0.000481	—	0.301 ± 0.069	0.1780	R.14, H.21
Kepler-1171 b	$1.44259224 \pm 0.00000219$	—	$0.228^{+0.061}_{-0.045}$	—	M.16
HIP 65426 b	$\sim$600 yr	9.0 ± 3.0	1.5 ± 0.1	$\sim$92	C.17
WASP-167 b	2.0219596 ± 0.0000006	<8	1.58 ± 0.05	0.0365 ± 0.0006	T.17
WASP-178 b	3.3448285 ± 0.0000012	1.66 ± 0.12	1.81 ± 0.09	0.0558 ± 0.0010	H.19

Chapter 2

Instrumentation Used in this Thesis

"If you wish to make an apple pie from scratch, you must first invent the universe"

— Carl Sagan

Cosmos: A Personal Voyage
(Sagan, 1980)

2.1 Praefatio

The wide range of telescopes and instruments used for the work in this thesis were employed either directly (Moses Holden Telescope; MHT), remotely (South African Astronomical Observatory; SAAO 40″), through service observations (Southern African Large Telescope; SALT) or via a public database (Transiting Exoplanet Survey Satellite; TESS). It is worthy of note that: the MHT is the largest-working-teaching telescope used in a university in England (see § 4.1); the University of Central Lancashire is a constituent of the UK SALT Consortium (UKSC), and as

such receives yearly guaranteed time; and the University of Central Lancashire is affiliated with the TESS Follow-Up Programme as part of the Sub Group 1 team (TFOP SG1; the affiliation was achieved by the author of this thesis).

2.2 The Moses Holden Telescope (MHT) at Alston Observatory, Preston, UK

The Moses Holden Telescope (MHT) is a 0.7-m PlaneWave™ Instruments CDK700[1] Alt-Az reflector telescope, situated at Alston Observatory eight miles north-east of Preston, close to a designated "dark-sky" region of the North West of England. Its geographical coordinates are $53^\circ\,48'\,02''$ N, $02^\circ\,35'\,37''$ W, situated at an elevation of 62 m above sea level.

The MHT is named after one of the founding fathers of the University of Central Lancashire (then called The Institution for the Diffusion of Knowledge, in 1828): Moses Holden. Alston Observatory has been a functioning observatory since 1957 (then called The Wilfred Hall Observatory), and the MHT is the latest addition to Alston's array of telescopes. The MHT was opened by Holden's biographer, Stephen Halliwell, in April 2016 — Holden's three-times great-grandson was present — and first light was achieved the same year.

The MHT's sole capability is photometry, employing three fused-silica (quartz) mirrors. The primary mirror is the namesake 0.7-m (700 mm; 27.56 in), the secondary mirror is spherical (as opposed to parabolic) and has a diameter of 312.4 mm (12.30 in), and the tertiary mirror is 152.4 mm (6.00 in) across, which can be rotated between an eye piece and a CCD at any time (the two being on opposite sides of the telescope; see Figure 2.1). This triple-mirror configuration yields a focal ratio of $f/6.5$ and a 4540 mm focal length, producing an unvignetted field-of-view of $28' \times 28'$

[1] CDK = Corrected Dall-Kirkham

that has since been increased by a focal-reducer to $40.2' \times 40.2'$. Additionally, there are no gears within the MHT's housing: instead, its Direct Drive motors are powered by electromagnets, ensuring smooth slewing and tracking at up to 50 deg/sec over a complete Right Ascension coverage and a $>10°$ elevation above the horizon, equating to Declinations of $-26°$ to $+90°$ (depending on RA). The best seeing at Alston is $\sim 2.5''$.

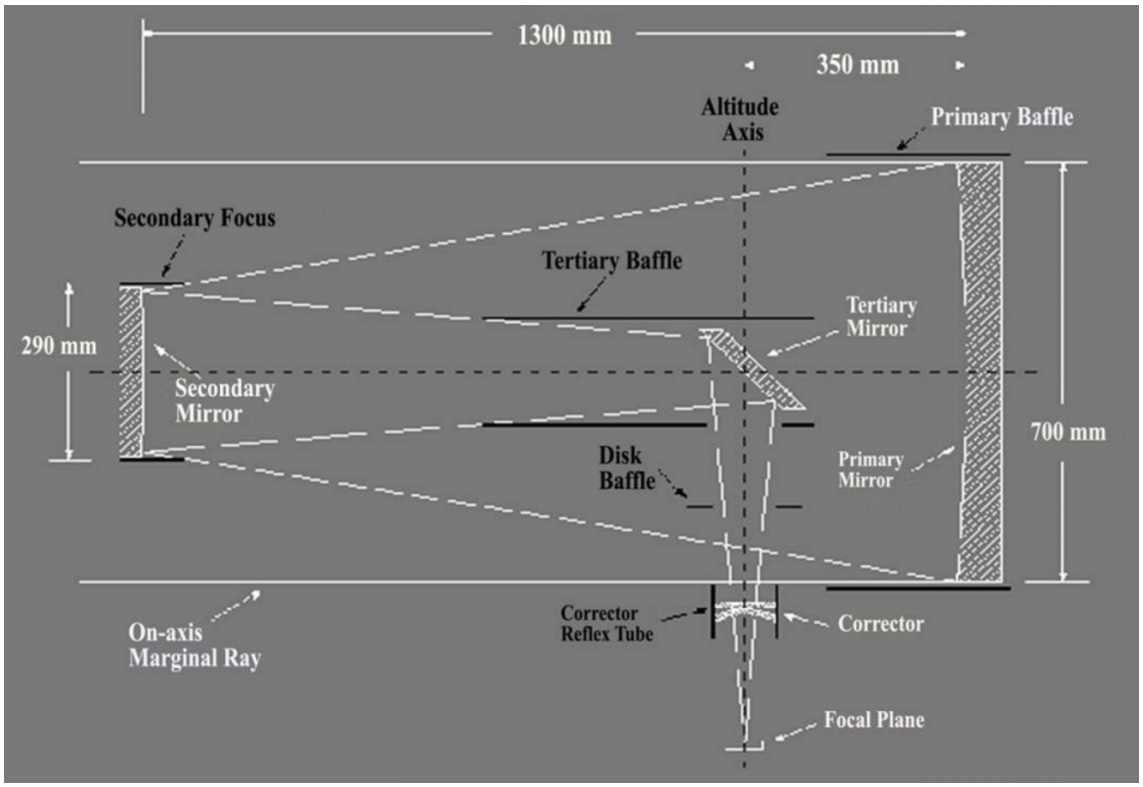

Figure 2.1: *A schematic of the MHT.*

An Apogee Aspen CG16M 4096×4096 CCD is fitted to the MHT, resulting in an un-binned pixel scale of $0.41''$/pix without the focal reducer; $0.59''$/pix with. Fitted in-front of the CCD is a filter wheel containing the Johnson *UBVRI* filters, Hα (656 nm), [O III] (501 nm), [S II] (672 nm), & *L* filters[2], available for all observations. The CCD can be cooled to -35°C, allowing observations of stars down to the MHT's

[2]"L" stands for Luminance; this filter is clear but blocks UV light below 400 nm and IR light above 680 nm to allow more visible light to be gathered during work such as astrophotography.

limiting magnitude of 18$^{\text{th}}$ magnitude in a single 60-s exposure. The shortest exposure time possible is 0.1 s — limited by the shutter speed of the CCD — and there exists no hard upper limit, but a soft upper limit of five minutes is imposed to reduce the risk of wasted time from corrupted frames (also, the dome does not track, so the soft upper limit also avoids the risk of the telescope slewing out of the dome's observing window whilst still imaging). Figure 2.2 shows an image of the MHT housed within its dome at Alston Observatory.

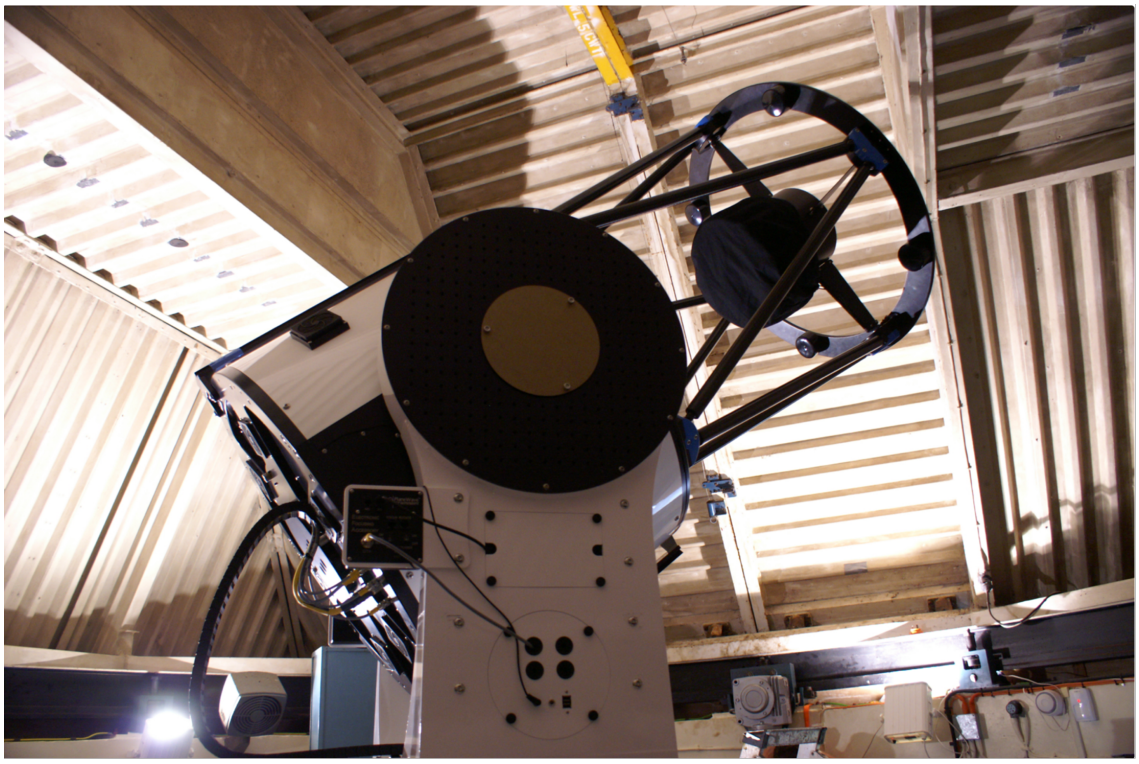

Figure 2.2: *A photograph of the MHT at Alston Observatory, extracted from https://www.star.uclan.ac.uk/albums/moses-holden-telescope.*

2.3 The Transiting Exoplanet Survey Satellite (TESS)

2.3.1 Mission Overview

The Transiting Exoplanet Survey Satellite (TESS; Ricker et al., 2015), shown in Figure 2.3, is the latest generation exoplanet space mission. Launched in 2018, it became the first mission of its kind: performing an almost full-sky survey of the nearest and brightest stars during its two-year primary mission, hunting for transiting exoplanets. TESS observes with a bandpass of 600 – 1000 nm, chosen to favour the detection of transiting exoplanets around the smaller, cooler M-type stars (see Figure 2.4), but TESS is able to provide data on stars across the whole HR diagram, and young hot stars (A-type and hotter) that still possess discs may appear brighter in TESS observations. TESS is predicted to discover over 20,000 new exoplanets during its lifetime (Huang et al., 2017), with an objective of finding tens of Earth-analogues. In addition, TESS is predicted to detect p-mode oscillations in over 6000 stars (Ricker et al., 2014) — some of which may be planet hosts — marrying the two branches of asteroseismology and exoplanet astrophysics.

After reaching its 13.7-d geocentric 2:1 lunar resonance orbit (apogee and perigee of 3.76×10^5 km and 1.08×10^5 km, respectively), TESS observed over 85% of the sky throughout its two-year primary mission, collecting data from across both hemispheres, only missing out observing the ecliptic and a segment of the northern hemisphere due to the location of the Moon (see Figure 2.6).

In mid-2020 TESS began its first extended mission, "filling in the gaps" in the ecliptic whilst also re-visiting previously observed areas of the sky. This ended in September of 2022, instantaneously marking the start of the second extended mission. As of October 2022 TESS has discovered 256 confirmed exoplanets, with

another 5908 candidates[3], catalogued as TESS Objects of Interest (TOIs) in a continually-being-added-to publicly-available database (Guerrero et al., 2021).

2.3.2 Establishing TESS Target Stars

TESS observes the brightest stars nearest to the Earth. It can be assumed that the full range of stars across the main sequence are distributed across the sky, with population densities increasing towards the Galactic Plane. However, it held reason to omit certain spectral types from the planet-hunting TESS target list.

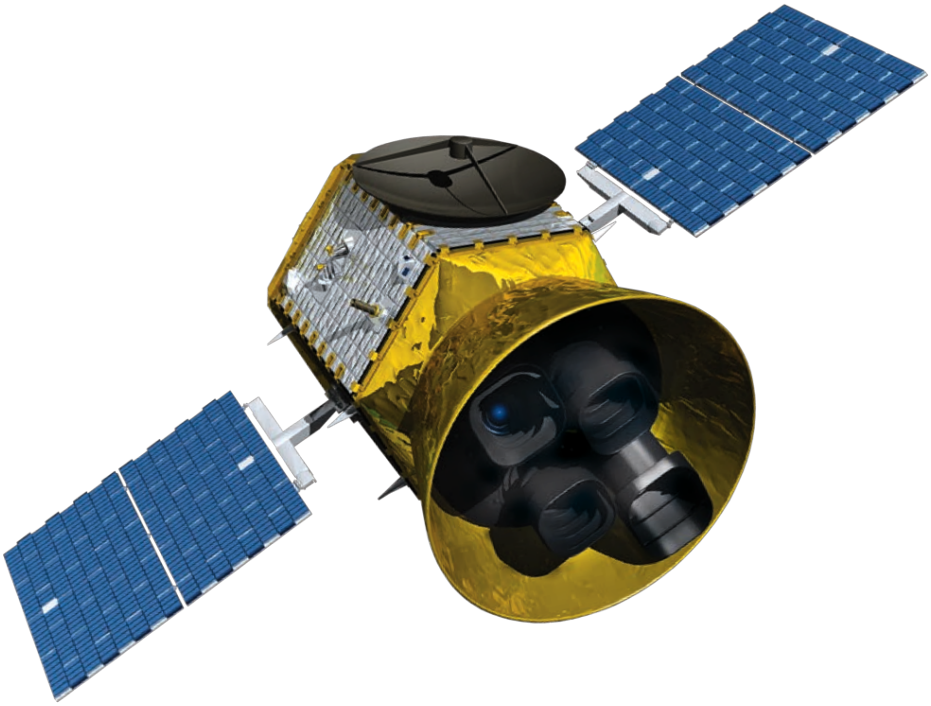

Figure 2.3: *An artist's impression of TESS, extracted from https://en.wikipedia.org/wiki/Transiting_Exoplanet_Survey_Satellite*

Stars of spectral type O are both too rare and too young to host exoplanets, and do not live long enough for planets to form (Weidner & Vink, 2010; Podolak, 2018). B-type stars exhibit similar properties, so were dropped as well (a handful of

[3]https://exoplanets.nasa.gov/tess

multi-Jupiter-mass-sub-stellar companions have been confirmed around stars bordering between late B-type/early A-type stars (Carson et al., 2013; Lafrenière et al., 2011; Gaudi et al., 2017), but it was determined to be too inefficient to search for more when it was considered their very high luminosities make it difficult to detect dips from transiting planets. A-type planet hosts are also rare, but these stars were included in the final TESS target list for their asteroseismic possibilities. But in general, the TESS target stars for exoplanet discoveries lay in the spectral range of FGKM – and further justification for this is three-fold: stars in this spectral range (specifically F5 and later, but also including the Am stars) rotate slowly, providing sharp lines in their spectra that can be used to build high-precision RV curves; exoplanets orbiting FGKM stars have higher planet-to-star radius ratios, making detections clearer; and low-mass main sequence stars are the most abundant, with 75% of the solar neighbourhood being stars between M0 - M5 (Winters et al., 2019).

Later-type M dwarfs (M6 onwards), were not optimal for this set up. They are very faint, and as such their spatial occurrence is not well understood (Ahmed & Warren, 2019). Further, planet-detection around these stars is possible from ground-based observations (MEarth; Charbonneau et al., 2009). Hence, Ricker et al. (2015) agreed that the majority of TESS target stars were to be in the spectral range of F5-M5, but hotter target stars are included.

Now that the target stars were decided, predictions were made for the abundance of exoplanet detections. TESS is primarily focused on detecting "super-Earth/sub-Neptune"-sized exoplanets, the most common-sized planet discovered by the Kepler Space Mission (*Kepler*) (Kite et al., 2019, and, very interestingly, a size of planet that does not exist in our Solar System). Further, due to the short timebase of the TESS observations, close-in orbiting super-Earths with orbital periods shorter than 10 days were favoured (Ricker et al., 2015).

From the initial *Kepler* results of 1235 planetary candidates, Borucki et al.

(2011) elucidated that 288 of them fell into the super-Earth/sub-Neptune category of $1.25\,R_\oplus \leq R_p < 2\,R_\oplus$ ($3\,M_\oplus \leq M_p < 10\,M_\oplus$; 23% of the total[4]). However, when the sub-10 d orbital period threshold was implemented, this proportion reduced to just 5%. Ricker et al. (2015) extrapolated from this that one super-Earth would be detected for every 500 stars monitored, and to achieve the goal of discovering many hundreds of these-sized planets with just a 0.2% occurrence rate, observations of over 100,000 stars were required.

Next, the limiting magnitude of the target stars was considered. The Girardi et al. (2005) Galactic star count models yielded that there are 100,000 stars brighter than $\approx 10^{\text{th}}$ magnitude in the I_C band (800 nm, on which the TESS bandpass is centred; see Figure 2.4). As TESS is observing the nearest and brightest stars, and is required to observe 100,000 to reach its science goal, the Galactic star count models very conveniently addressed the limiting magnitude topic. Ricker et al. (2015) decided to implement a target catalogue of twice this number – accounting for stars where detectability is more important than brightness (such as for M dwarfs) – concluding with a limiting magnitude for TESS of $T_{\text{Mag}} < 15$ across all target stars.

2.3.3 Cameras on TESS

TESS performs photometry with four cameras mounted in a 1×4 array. Each camera is an assembly of five spherical and two aspherical lenses, all contained within a lens barrel that produces a focal ratio of $f/1.4$, with a small 10.5 cm-aperture (to avoid spherical aberration occurring). An optical element within each camera is coated with a long-pass filter, forming the 600 nm boundary of TESS's bandpass; the other boundary of 1000 mn is set by the quantum-efficiency of the CCD chips.

Each of the four cameras are backed by a CCID-80 device, each exhibiting a 2048×2048 imaging array of $15 \times 15\,\mu$m pixels. Each of the four 2048×2048

[4]We now know that super-Earth sized planets are the most abundant planets in the Galaxy.

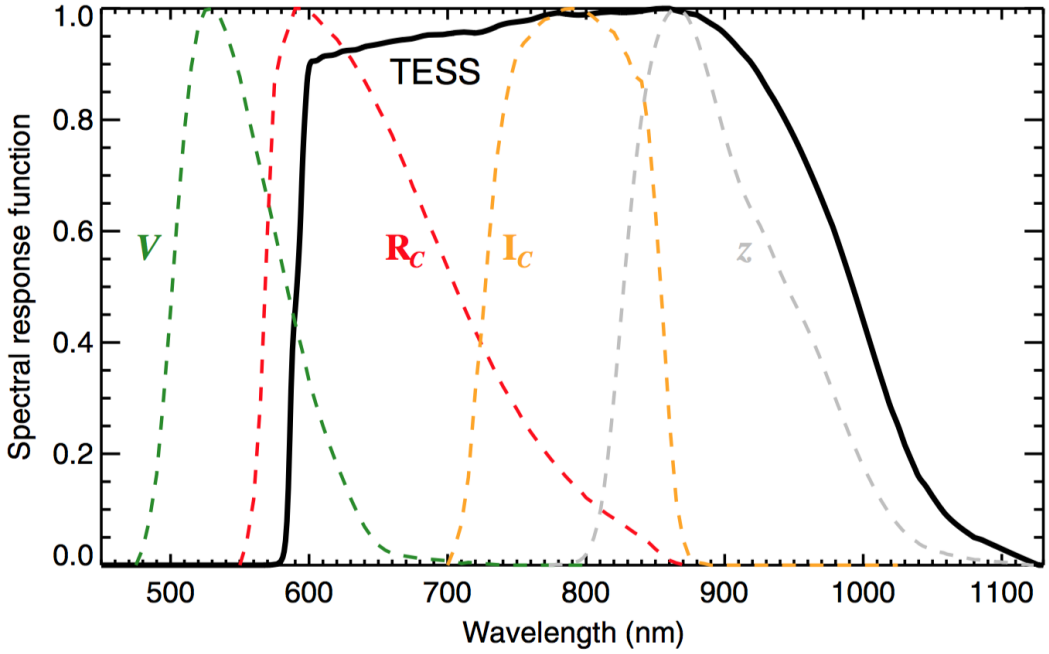

Figure 2.4: *A plot of the TESS bandpass (black line) as wavelength vs intensity, normalised to unity. For reference, the Johnson filters V (green), R_C (red) and I_C (orange), and the SDSS filter z (grey), are included for comparison. Image extracted from https://heasarc.gsfc.nasa.gov/docs/tess/the-tess-space-telescope.html*

CCDs are themselves comprised of four 512 × 512 chips, hence the total imaging area contains 16 tiles. The field-of-view for each camera is 24° × 24°, resulting in a simultaneous field-of-view for TESS of 24° × 96° ($2304^{\circ 2}$).

TESS takes continuous images every two seconds. Onboard computers combine these images into groups of 60, and sum them to produce an effective 2-min exposure time. This 2-min cadence exists for 20,000 of the TESS targets per Sector, but 30-min cadence data also exists for the Full Frame Images (FFIs, stacked from the 2-min data; Ricker et al., 2015). New for the TESS extended missions, a 20 s cadence exists for up to 1000 targets per Sector, and 10-min cadence for all FFIs[5].

TESS operates in a thermally constant ∼-75° C (198 K) environment throughout its orbit, making dark-current noise insignificant. The CCD chips are read-out at

[5]https://heasarc.gsfc.nasa.gov/docs/tess/the-tess-extended-mission.html

625 KHz, producing a $<10 e^-$ per pixel readout noise. Once per orbit, TESS pauses observations to downlink the data to Earth (Ricker et al., 2015).

2.3.4 Primary Mission Observing Strategy

The orbit is inclined from the ecliptic to avoid Earth-Moon eclipses, ensuring continuous observation time (excluding data downlink events). The perigee is such that TESS remains above the Earth's radiation belts, yet close enough to the Earth for an efficient data download once per TESS orbit, each lasting up to 16 h. The orbit is stable on the timescale of decades (Ricker et al., 2015).

The TESS observations are divided into "Sectors". During the primary mission (Sectors 1 – 26) there were 13 per hemisphere, each lasting for two TESS orbits (27.4 days) before the pointing moved longitudinally east in the ecliptic by 27°. TESS observes with four cameras in a columned field-of-view comprising an area of $24° \times 96°$ on the sky. This 1×4-shaped window stretches from the ecliptic pole down to an ecliptic latitude of $\pm 6°$. With each Sector, the pointing rotates around the ecliptic pole, with observations of stars ranging from 27 d at the ecliptic equator to 351 d at the ecliptic poles. After one year, TESS changed hemispheres and continued this configuration for the next 13 Sectors. Hence, over the two-year primary mission, TESS completed an almost-full sky survey covering 85% of the total sky ($30,000°^2$, see Figure 2.5; Ricker et al., 2015).

2.3.5 Alterations to the Observing Strategy, and Extended Missions

It was soon learned that the original 85%-sky coverage goal could not be met during the primary mission. The position of the Moon compromised Sectors 14, 15, and 21 - 26, all of which had to be manipulated north. Figure 2.6 shows the updated region of the sky that TESS observed during its primary mission.

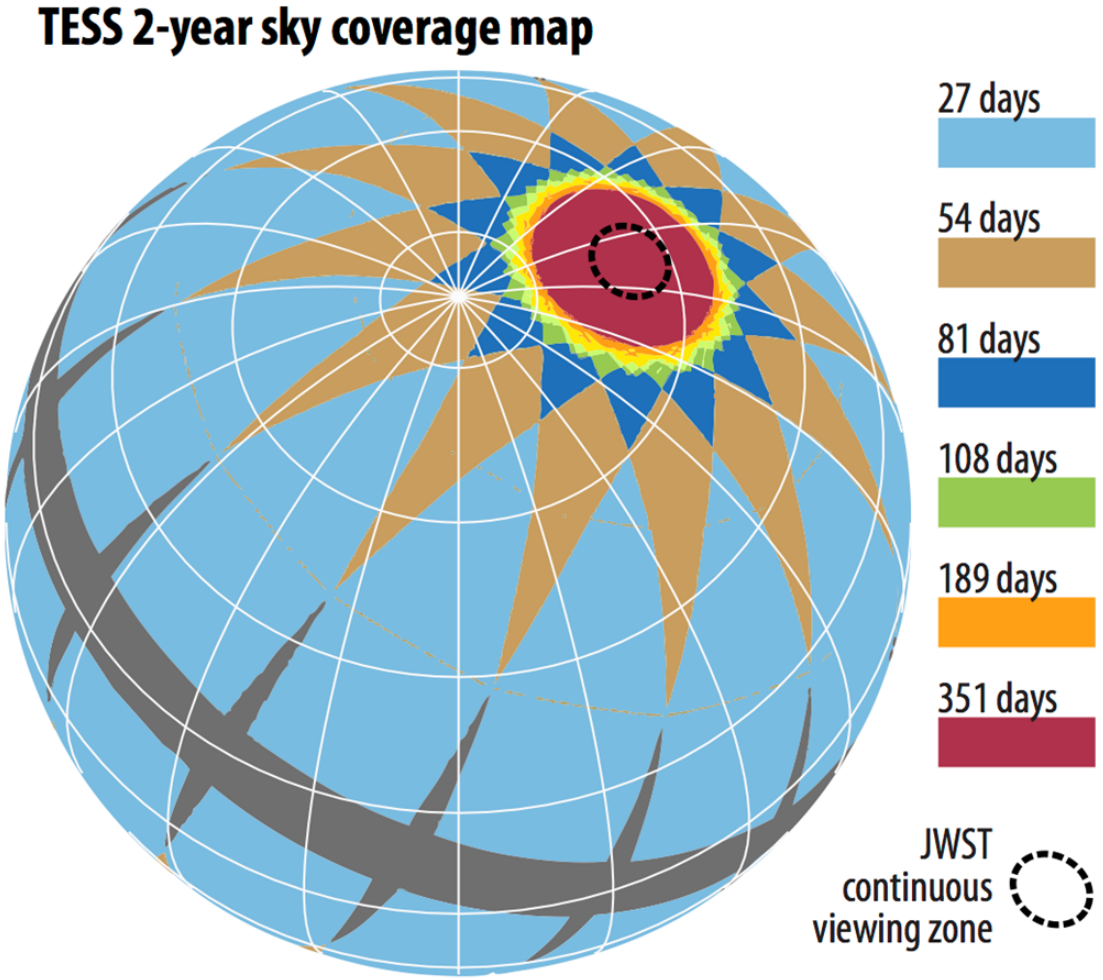

Figure 2.5: *A graphic showing the original observing strategy for the TESS primary mission, extracted from https://tess.mit.edu The 27 - 351-d timebase for varying latitudes can be seen, formed by the* 1×4 *camera array.*

Year's 3 and 4 comprised the first extended mission (EM1; Sectors 27 – 55). Year 3 consisted of entirely southern observing, and Year 4 was a mixture of northern and ecliptic observing to start "filling in the gaps" that were otherwise not observed during the primary mission. Now in the second extended mission (EM2; Sectors 56 – 96), TESS is revisiting the northern and southern hemispheres with Sectors that overlap earlier observations, lengthening the data sets of 1000s of stars. Figure 2.6 shows the updated Sector formation on the sky that TESS observed during the primary mission, and Figure 2.7 shows the most up-to-date Sector diagram, showing

all Sectors from the primary mission, EM1 and EM2.

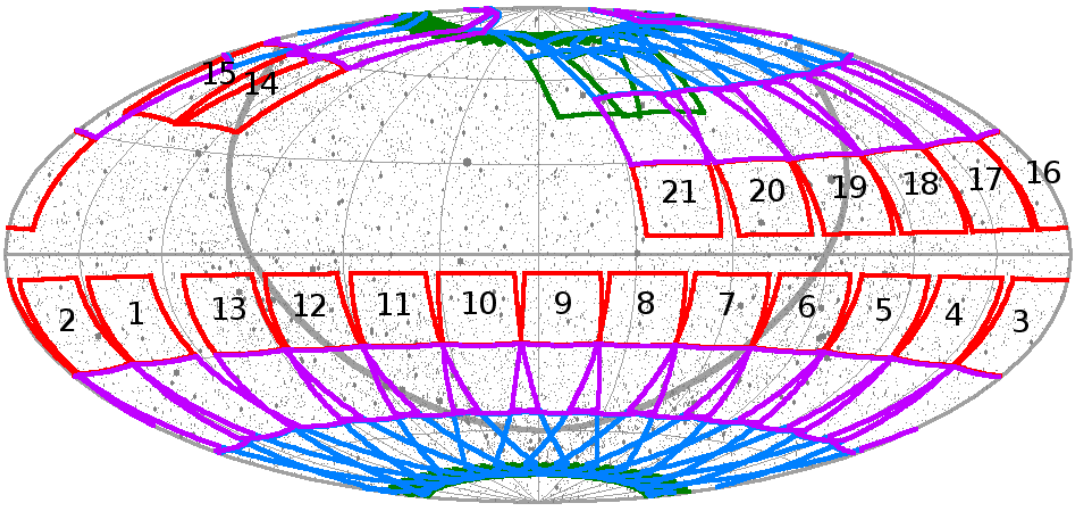

Figure 2.6: *The updated Sectors that were moved north, due to the location of the Moon. Image extracted from https://heasarc.gsfc.nasa.gov/docs/tess/update-on-tess-pointing-in-year-2.html*

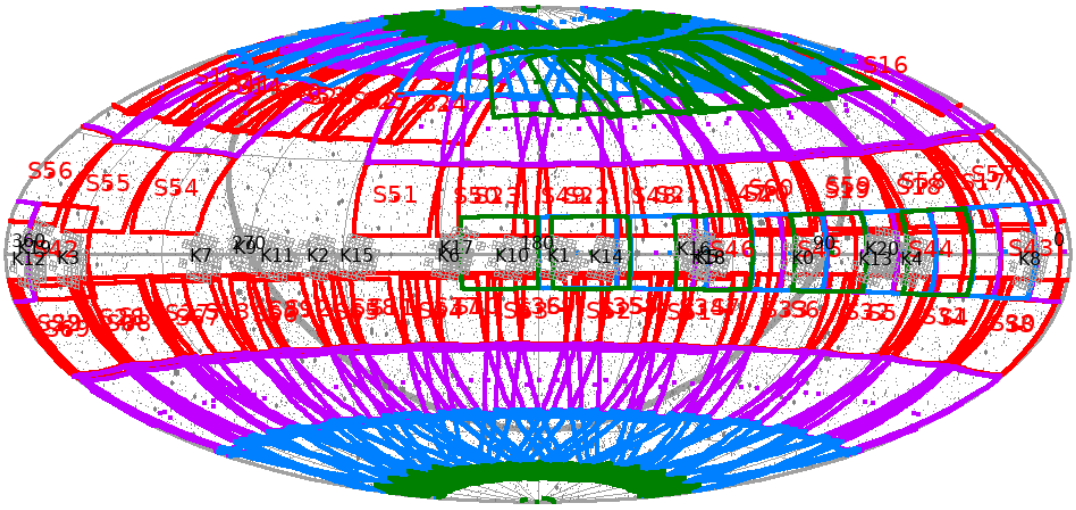

Figure 2.7: *The complete Sector diagram, showing the 26 primay mission Sectors alongside the EM1 and EM2 Sectors. It can be seen that TESS has a higher sky coverage now compared with the primary mission, and the ecliptic Sectors overlaps with some K2 Campaigns from Kepler's extended mission (shown in grey). The gap at 270° is due to scattered light from the Earth and Moon. Image extracted from https://tess.mit.edu/observations*

2.4 The 40″/1.0-m Telescope at the South African Astronomical Observatory (SAAO)

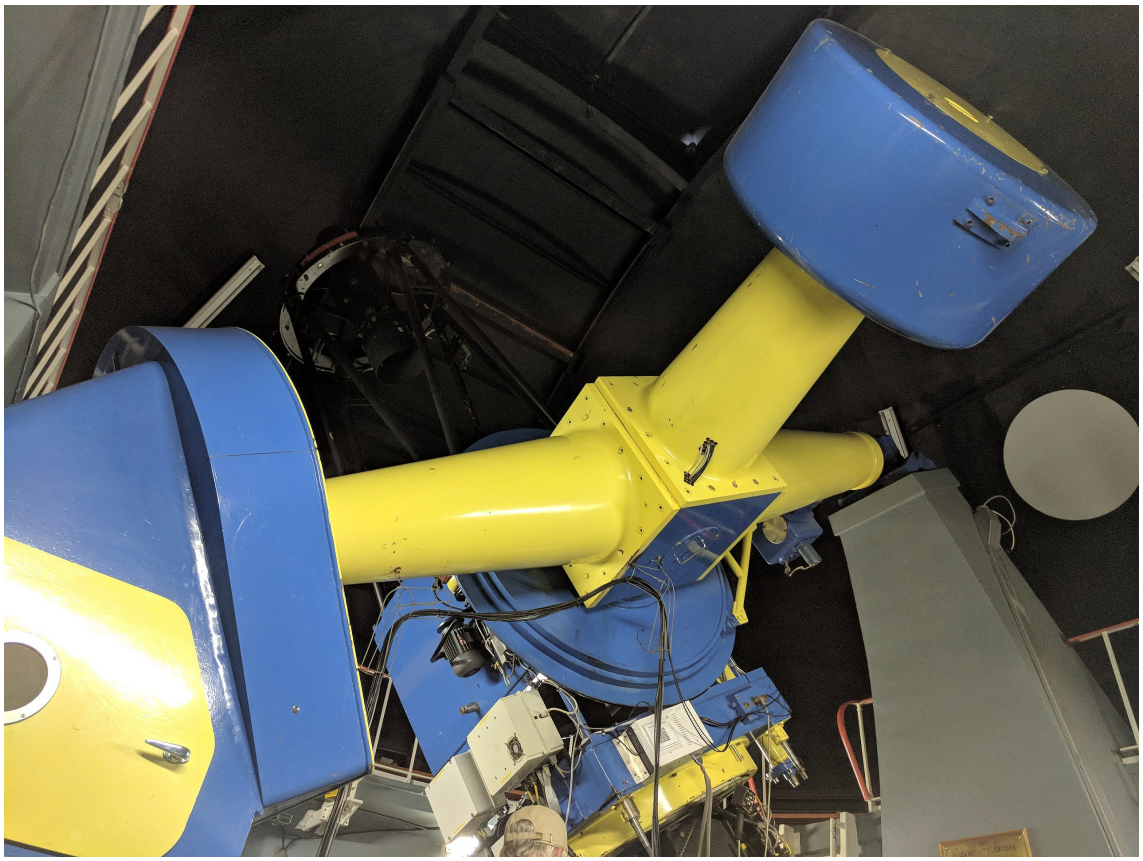

Figure 2.8: *A photograph of the 40″ telescope at the SAAO, extracted from https://en.wikipedia.org/wiki/South_African_Astronomical_Observatory*

The 40″/1.0-m reflector telescope (Sefako, 2015) is one of 25 telescopes situated at the South African Astronomical Observatory (SAAO) in Sutherland, 230 miles (370 km) North-East of Cape Town, South Africa. Its geographical coordinates are 32° 22′ 47″ S, 20° 48′ 38″ E, situated at an elevation of 1765 m above sea level. Built in 1964 by Grubb Parsons, it was originally established in Cape Town before it moved to its current location. Its primary function is photometry.

The primary mirror is 1.0 m (39.37 in) across and the secondary mirror has a diameter of 300 mm (11.81 in). With the Cassegrain focus, a focal ratio of $f/16$ is

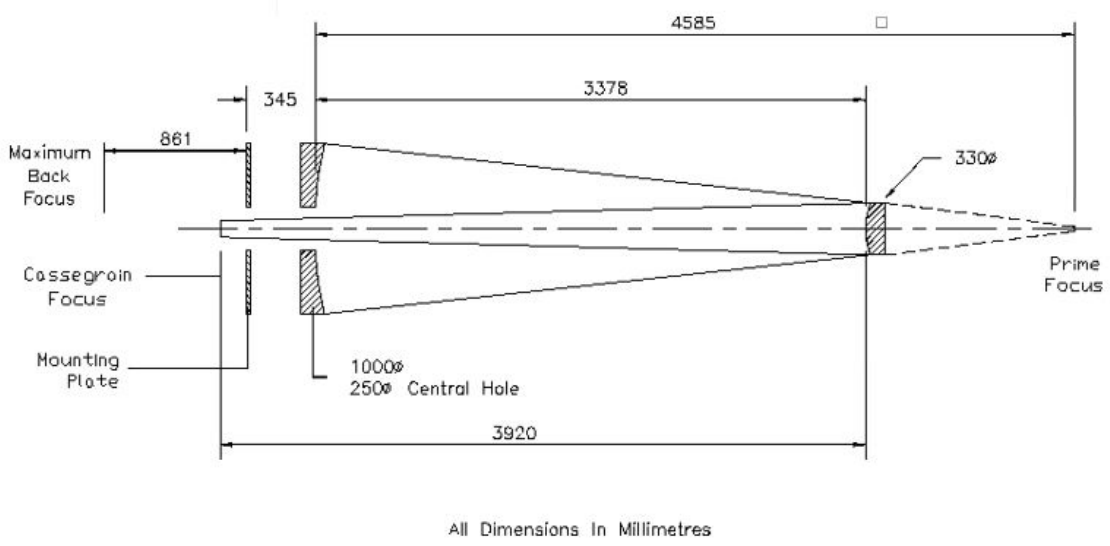

Figure 2.9: *An optical diagram for the 40″ telescope at the SAAO, extracted from https://www.saao.ac.za/astronomers-old/telescopes-1-0m*

achieved, producing a plate scale of ∼12.94″/mm.

However, the telescope is hindered by pointing limits between Hour Angles of ∼-3 and +5 — due to the possibility of an observer either crashing the telescope tube into the railings on the walkway around the top of the dome, or crashing an attached instrument into one of the dome pillars — and Declinations of -90° to +30°. The best seeing at the observatory is on the order of <1.0″.

The 40″ has two filter wheels that between them contain the Johnson *UBVRI* filters, SDSS *u'g'r'i'z'* filters, BG38 (470 nm), [O III] (501 nm), Hα wide (20 nm) and Hα narrow (3 nm), both at 656 nm, red-shifted Hα at 667, 681 & 686 nm, UKIDSS *Z* (882 nm), and clear slots for white light. Figure 2.8 shows an image of the 40″, and a detailed optical schematic is shown in Figure 2.9.

2.4.1 The Sutherland High Speed Optical Camera (SHOC)

The Sutherland High Speed Optical Camera "SHOC'n'awe" (SHOC; Coppejans et al., 2013) is one of several instruments that can be mounted on the 40″ telescope. SHOC is comprised of two Andor iXon 888 EM 2048×1024 CCD cameras

that can achieve frame rates of up to 20 frames/s, and it provides an un-binned plate scale of 0.167″/pixel (but 2×2 binning is recommended).

There are three readout modes available: 1 MHz, 3 MHz and 10 Mhz, and three gain settings: 1, 2.5 and 5; all of which are altered depending on the cadence of the data being taken. The SAAO provides a S/N and exposure time calculator for users to prepare observation strategies.

The filters available for use with SHOC are listed in § 2.4. Figure 2.10 shows a detailed schematic of SHOC.

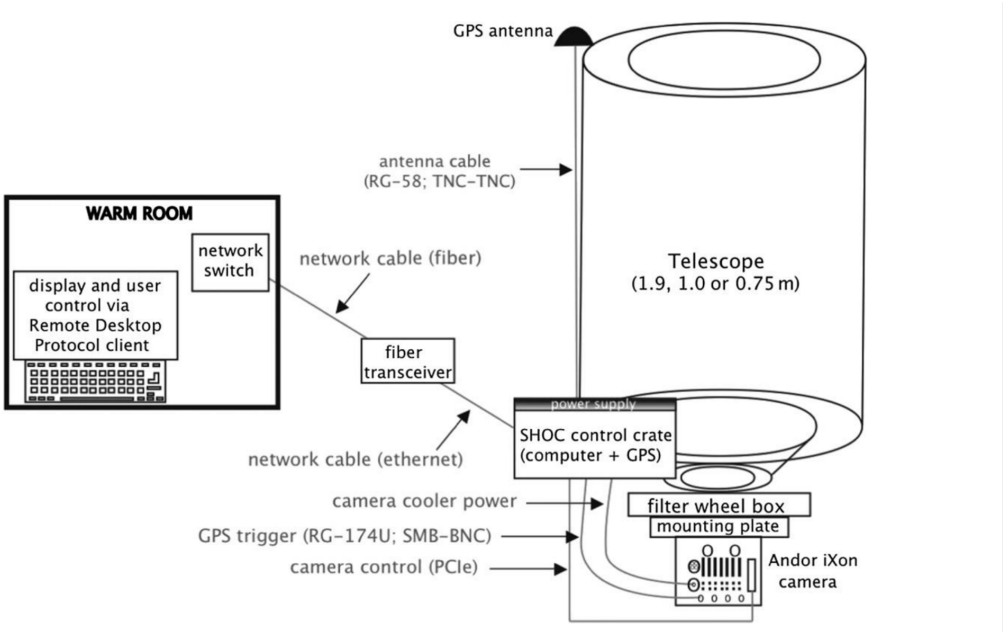

Figure 2.10: *A schematic diagram for SHOC, taken from Coppejans et al. (2013). Their caption reads: "Schematic illustrating SHOC's mounting and setup, with cables shown in gray. The 1.9 m telescope can have a focal reducer mounted between the filter wheel box and the mounting plate. The drawing is not to scale." SHOC was fitted to the 1.0-m telescope during this work.*

2.5 The Southern African Large Telescope (SALT)

The Southern African Large Telescope (SALT; Stobie, Meiring & Buckley, 2000) is a 10-m class telescope and, like the 40″ telescope, is one of 25 telescopes situated at the South African Astronomical Observatory (SAAO). The primary mirror is not one single piece of glass: instead, it is comprised of 91 separate hexagonal aluminium-coated Astrositall mirrors – each with an inscribed diameter of 1 m – creating one large hexagonal mirror 11.1×9.8 m in size, with a 26.165 m radius of curvature (Stobie, Meiring & Buckley, 2000). SALT has the largest mirror in the Southern hemisphere, and its primary function is spectroscopy.

Each of the 91 separate mirror segments can be individually tipped or tilted as required to ensure the full mirror remains in perfect alignment; the position of each segment is measured via lasers sited on a tower situated next to the dome. A Shack–Hartmann wavefront sensor in the tower searches for alignment deviations, calculating which mirrors need to be moved and by how much. The tower is called the Center of Curvature Alignment System (CCAS; O'Donoghue et al., 2008).

For cost-effective reasons, SALT is not a fully steerable telescope. Instead, it lies at a fixed angle of 37° to the zenith, but it has full azimuthal rotation. However, the structure remains stationary during an observation, so a target can only be observed when it resides in the ∼12°-wide annular field-of-view. This setup propagates to 70% of the southern sky being fully observable (Buckley & Stobie, 2001).

A payload resides at the prime focus of the primary mirror. In the payload resides the calibration system: the Spherical Aberration Corrector, which counteracts spherical aberration caused by the non-parabolic primary mirror to ensure the best-possible image quality; the Atmospheric Dispersion Compensator, which uses two prisms to correct for the difference in dispersion the atmosphere exerts on blue and red light based on an object's altitude in the sky; a baffle, which blocks light that is not reflected off the primary mirror; the Berkeley Visible Image

Tube (BVIT) detector, which counts photon events down to a temporal resolution of 25 ns, providing high-resolution photometric observations; the Fibre Instrument Feed (FIF), which contains the fibres that feed the light from observations to the High-Resolution Échelle Spectrograph (HRS; see below); SALTICAM, which acts as a target-finder and allows astronomers to place identified targets on the required instrument (SALTICAM can also perform deep-sky imaging); the Robert Stobie Spectrograph (RSS), which captured SALT's first-light image and is utilised for normal long-slit and multi-object spectroscopy at resolutions up to R $\simeq$12,000; fold mirrors, which deflect light to different instruments within the payload; and slit view mirrors, which reflect a fraction of the light that is sent to the RSS back to SALITCAM, allowing the latter to be used to monitor the positions of targets whilst observing with the RSS.

2.5.1 The High Resolution Échelle Spectrograph (HRS)

Beneath the main structure of SALT lies the spectrometer room, which houses the High Resolution Échelle Spectrograph (HRS; Bramall et al., 2010, 2012; Tyas, 2012). This spectrometer was used in this work.

The HRS is a R4 fibre-fed spectrograph, achieving three different resolutions of R$\approx$16000, 37000, 67000, respectively across four different modes of low-, medium- and high-resolution, and high-stability (HS; the latter two both at R$\approx$67000), over a spectral wavelength range of 370-890 nm (Crause et al., 2014). In the HS mode, an iodine cell can be inserted into the light path. A Thorium-Argon "ThAr" lamp can be injected into a second fibre, for precise wavelength calibration.

Light reflected from the primary mirror of SALT is split by a dichroic beam-splitter in to two fibres, blue (370-550 nm and red (550-890 nm).

As a performance example, HRS can achieve a S/N of 100:1 at the central wavelength of a V=13.6 mag star in $\approx$5 minutes at R$\approx$16,000. This S/N is for each

extracted half-resolution element within the diffraction grating (Barnes et al., 2008).

Data that SALT has taken using the HRS is downloadable to the observer already in reduced form: observational data is automatically processed via the SALT Munich Image Data Analysis System (MIDAS) pipeline (Kniazev et al., 2004; Kniazev, Gvaramadze & Berdnikov, 2016, 2017). The pipeline performs basic data reduction, wavelength calibrations, sky subtraction, blaze correction and order merging. See Appendix A for details on the workings of MIDAS.

Chapter 3

Software Used in This Work

"All models are wrong, but some are useful"

— George E. P. Box

Robustness in the Strategy of Scientific Model Building

(Box, 1979)

3.1 The Stellar Evolution-Modelling Software: MESA (r12115)

3.1.1 An Introduction to MESA

The Modules for Experiments in Stellar Astrophysics (MESA ; Paxton et al., 2011, 2013, 2015, 2018, 2019) is a FORTRAN 95-based stellar modelling software that enlists the one-dimensional stellar evolution module `MESA star` to simulate any stellar evolution scenario, starting from pre-main sequence stars right through to cooling white dwarfs, for any initial stellar parameters. The interior sound-speed profile, mass-loss over time, dominant burning mechanism, temperature-density profiles and fundamental stellar parameters are example of the data that `MESA star` can produce.

The initial version of MESA (Paxton et al., 2011) was born as a result of the author attempting to improve the "Evolve ZAMS" (EZ) stellar evolution code (Eggleton, 1971; Paxton, 2004), and MESA itself has evolved via several updates: it can now model Planets, Oscillations, Rotation, and Massive Stars (Paxton et al., 2013); Binaries, Pulsations and Explosions (Paxton et al., 2015); Convective Boundaries, Element Diffusion, and Massive Star Explosions (Paxton et al., 2018); and Pulsating Variable Stars, Rotation, Convective Boundaries, and Energy Conservation (Paxton et al., 2019) — and whilst all these updates advance the capabilities of what MESA can produce, the under-lying stellar physics from the first paper (2011) remains the same. Importantly for the work in this thesis, the 2015 update allowed MESA models to be fed into the stellar pulsation modelling software GYRE (see § 3.2; Townsend & Teitler, 2013), forming robust and complete models of pulsating stars.

MESA is comprised of 23 different modules, each superintending different aspects of the software that altogether build the stellar evolution models. The modules are split into four main sub-groups: Macrophysics, Microphysics, Stellar Structure and Evolution (to borrow the nomenclature of Paxton et al. (2011)). The following Sections describe each.

3.1.1.1 Macrophysics

The dominant macrophysics module encoded in MESA is `MESA star`. It governs the Mixing Length Theory (MLT) of convection (`mlt` module), convective overshoot, atmospheric boundary conditions (`atm` module), and diffusion and gravitational settling (`MESA diffusion` module; Paxton et al., 2011). Each are discussed below:

CHAPTER 3

The Mixing Length Theory of Convection

The MLT of convection is an energy transport model used to describe the physics of stellar convective zones. An identity of material within the convective zone may rise or sink depending on the temperature gradient between itself and its surrounding environment (hence a density gradient, driven by a buoyancy force), but the material itself will be able to move adiabatically over a certain distance before it reaches thermal equilibrium and diffuses into the neighbouring material: the distance it moves before it dissipates is the namesake *mixing length*, $\mathbf{\Lambda}$. As the entity of material reaches its mixing length and begins to thermalise, it releases an amount of heat per unit mass that is transferred to adjacent convective cells which increases their average velocity (all whilst remaining at a constant pressure). In MESA models, the user can model different values of $\mathbf{\Lambda}$ by changing a parameter, $\boldsymbol{\alpha_{\mathrm{MLT}}}$, which when multiplied by the local pressure scale height, $\boldsymbol{\lambda_P}$, is the total *mixing length* within the model, given as Equation 3.1:

$$\Lambda = \alpha_{\mathrm{MLT}} \lambda_P \tag{3.1}$$

MESA employs the Cox & Giuli (1968) MLT of convection by default, but the user can change to the Henyey, Vardya & Bodenheimer (1965) MLT of convection when modelling lower-mass stars with convective zones near their outer layers (but this was not applicable to the stars studied in this work). For intermediate mass stars with convective zones below their radiative zones — as are the stars studied in this thesis — the pressure scale height is defined as $\boldsymbol{\lambda_P = \frac{P}{g\rho}}$, which diverges to zero with decreasing radius from the stellar centre (as $\boldsymbol{g \rightarrow 0}$; Paxton et al., 2011). The reader should see Table [6] in Paxton et al. (2011) for a list of all possible output-able parameters from `mlt`.

CHAPTER 3

Convective Overshoot

Convective overshoot is the physical diffusive process of the above-mentioned hot or cool material penetrating or sinking between the core, convective zone or radiative zone. For intermediate mass stars with convective cores (such as those studied in this thesis), an identity of material can overshoot from the core into the convective zone if it possesses sufficient momentum generated from the buoyancy force arising from a temperature gradient. The mass is able to travel a small fraction of the local pressure scale height into the convective zone before it dissipates (not very far relative to the star's radius due to the mass's slow velocity: $\approx$Mach 5×10^{-4}; Rempel, 2004). The cavity formed in the core is replenished by neighbouring material to the overshooting globule sinking from the convective zone, inducing a potentially larger core mass (this has a strong effect on main sequence and post-main sequence stellar evolution of a star, as more hydrogen can be transported into its core which allows it to continue burning for longer than it otherwise would — this is beyond the scope of this work but is important to include here for completeness; Johnston, 2021).

The magnitude of overshooting is dependant on the stellar radius, $\boldsymbol{r}$, pressure scale height, $\boldsymbol{\lambda_P}$, and $\boldsymbol{f_{ov}}$ which is a scale height parameter that the user physically changes within the MESA software. $\boldsymbol{D_{ov}}$ is the final overshooting distance, in terms of $\boldsymbol{r}$ and $\boldsymbol{D_0}$: a diffusion coefficient calculated by the `mlt` module which is then implemented by the `MESA star` module via Equation 3.2 (based on Eqn. [2] of Herwig (2000) but using the above nomenclature for consistency):

$$D_{\rm ov} = D_0^{\left(\frac{-2r}{f_{\rm ov}\lambda_{\rm P}}\right)} \tag{3.2}$$

Atmospheric Boundary Conditions

`MESA star` requires an atmospheric model to describe the outermost layers of stars. The `atm` module is engaged here, which determines the pressure and temperature of a model atmosphere based upon the model's mass, radius and luminosity (the latter three can either be user inputted, MESA-calculated, or a combination of both). `atm` assumes the standard surface gravity equation ($\boldsymbol{g = \frac{GM}{R^2}}$) and standard luminosity equation ($\boldsymbol{L = 4\pi r^2 \sigma T^4}$), with an option to include optical depth, $\boldsymbol{\tau_s}$. The module then does one of two things (user-dependent): it either integrates the hydrostatic balance equation with a $\boldsymbol{T - \tau}$ relation (Eddington, 1926; Krishna Swamy, 1966), or interpolates the model atmosphere from tables.

Equation 3.3, in-text in § [5.3] of Paxton et al. (2011), shows the hydrostatic balance pressure differential dependent on $\boldsymbol{g}$ and $\boldsymbol{\kappa}$ (opacity) in terms of $\boldsymbol{T}$:

$$\frac{dP_{\rm gas}}{d\tau} = \frac{g}{\kappa} - \left(\frac{a}{3}\right)\frac{dT^4}{d\tau} \tag{3.3}$$

This is then integrated with $\boldsymbol{d\tau = -\kappa \rho \, dr}$ using the above-mentioned $\boldsymbol{T - \tau}$ relation to form: $\boldsymbol{T^4(\tau) = 3T_{\rm eff}^4 \frac{(\tau + \frac{2}{3})}{4}}$.

If tables are used, then the initial conditions decide which atmospheric model table is employed. Spanning across all tables, the following stellar parameters and respective ranges are covered: $\log(\frac{Z}{Z_\odot})$ =-4 − 0.5 (using the Grevesse & Noels (1993) Solar value as a reference point), and $\log g$ = -0.5 − 5.5 $\log \mathrm{cm\,s^{-2}}$. The 'PHEONIX' table spans $T_{\rm eff} = 2000 - 10,000$ K (Hauschildt, Allard & Baron, 1999; Hauschildt et al., 1999), and the Castelli & Kurucz (2003) table conducts hotter stars up to $T_{\rm eff}$ = 50,000 K. Either method is how `atm` calculates pressure and temperature (should $\boldsymbol{\tau_s}$ be utilised, then Eqn. [3] of Paxton et al. (2011), combined with the Eddington $\boldsymbol{T - \tau}$ relation, is used; Eddington, 1926).

Diffusion and Gravitational Settling

It is discussed above that convection within stars is a diffusive process.
`MESA diffusion` is built upon the Burgers equations of fluid dynamics (Bateman, 1915; Burgers, 1948, combined with the diffusion coefficients of Thoul, Bahcall & Loeb (1994)), which calculate the average diffusive velocities of particles within convective material. The particles are separated into elemental mass fractions, such that hydrogen, helium, and other metals have their velocities calculated separately (Paxton et al., 2011). Processes such as gravitational settling and radiative levitation are also available from `MESA diffusion` (but are superfluous for the stars studied in this thesis as those processes were built for modelling hot, evolved stars such as sub-dwarf B-type stars (sdBs) and White Dwarfs; Paxton et al., 2015).

3.1.1.2 Microphysics

Microphysics modules within MESA administer the smaller-scale physics, including mathematical constants, equations of state (EOS), opacities, and thermonuclear reactions. Each of the aforementioned modules are discussed below:

Mathematical Constants

When creating stellar models it is of paramount importance that mathematical constants and reference values remain consistent, otherwise results quickly become unreliable. For MESA, Paxton et al. (2011) loaded the module `const` with mathematical and astrophysical constants from the 'CODATA Recommended Values of the Fundamental Physical Constants' database (all in cgs units; Mohr, Taylor & Newell, 2008). Some Solar parameters were built in as reference values too, including $Age_{\odot}$, $M_{\odot}$, $R_{\odot}$ and $L_{\odot}$ (all defined as unity; Bahcall et al., 2005).

CHAPTER 3

Equations of State

EOS are mathematical tools used to describe the dynamics of matter and how it behaves over time within physical conditions defined by — for example — pressure, temperature, or spacial volume (density), all within a theoretical closed potential formulated as the Helmholtz free energy.

Within MESA, the `eos` module utilises gas pressure, temperature and density as the independent variables. It consists of tables of externally pre-determined values for each parameter to save computation time (but these tables are finite and Paxton et al. (2011) warns of long runtimes if the EOS table boundaries are exceeded). The tables are a combination of the updated 'OPAL' EOS tables of Rogers & Nayfonov (2002) of the original by Iglesias, Rogers & Wilson (1987); the 'SCVH' EOS tables from Saumon, Chabrier & van Horn (1995); and the 'HELM' and 'PC' EOS tables from Timmes & Swesty (2000) and Potekhin & Chabrier (2010), respectively.

For the work in this thesis, the OPAL EOS tables were used as they were built from parameters of intermediate mass stars (the SCVH[1] EOS tables are for cooler and less-dense stars, and the HELM and PC[2] EOS tables are for stars with enormous temperatures and pressures; see Fig. [1] of Paxton et al. (2011) to see how the different EOS tables represent different stars across $\boldsymbol{T-\rho}$ parameter space). `eos` calculates values for a range of parameters such as gas pressure, internal energy, entropy per gram, specific heat temperature gradients, and partial derivatives for each as well (see Table [3] of Paxton et al. (2011) for the full list). The calculations are performed using the free energy equation from Rogers, Swenson & Iglesias (1996); their Eqn. [7], given here as Equation 3.4:

$$\frac{P}{kT} = \frac{n_e I_{\frac{3}{2}}(\alpha_e)}{I_{\frac{1}{2}}(\alpha_e)} + n_p + \frac{P_{\text{ex}}}{kT} + \frac{P_{\text{DH}}}{kT} f_p(\gamma_{ee}, \gamma_{ei}) \tag{3.4}$$

[1] "SCVH" stands for the initials of the authors.
[2] "PC" stands for the initials of the authors.

combined with the update of Eqn. [3] of Rogers & Nayfonov (2002), given here as Equation 3.5, which includes the relativistic effects of electron pressure which would alter the evolution of higher-temperature model stars if neglected:

$$P_e^{\rm id} = \frac{2kT}{\lambda_e^3}\left(F_{\frac{3}{2}} + \frac{5}{4}T_r F_{\frac{5}{2}}\right) \tag{3.5}$$

Tables 3.1 and 3.2 provide a definition for every parameter used in Equations 3.4 and 3.5, respectively. The final values of each parameter are determined via interpolating the calculated values using bicubic splines:[3] a routine that is written into the MESA mathematical methods module `interp_2d`, based on the grid-fitting algorithm of Akima (1996) and bivariate interpolation algorithm of Renka (1999, see § [3] of Paxton et al. (2011) for a full discussion on this).

Table 3.1: *Definitions for the parameters used in Equation 3.4, taken from Rogers, Swenson & Iglesias (1996).*

Parameter	Definition
P	Pressure
k	Boltzmann constant
T	Temperature
n_e	Electron free-energy
I	Fermi function
α_e	Degeneracy parameter: $\alpha_e = \frac{\mu_e}{kT}$
n_p	Proton free-energy
$P_{\rm ex}$	First order electron exchange: $\frac{P_{\rm ex}}{kT} = \frac{2\pi}{3V}\int r^2\left(\frac{e^2}{r}\right)[g_{ee}r - 1]dr$
$P_{\rm DH}$	Debye-Hückel (D-H) pressure-correction
f_p	Quantum-diffraction correction to classical D-H pressure
γ_{ee}	Diffraction parameter
γ_{ei}	Diffraction parameter

[3]The third-order polynomials which form the cubic splines are interpolated in parallel over 2D grids

Table 3.2: *Definitions for the parameters used in Equation 3.5, taken from Rogers & Nayfonov (2002).*

Parameter	Definition
P_e^{id}	Ideal relativistic electron pressure
k	Boltzmann constant
T	Temperature
λ_e	Electron thermal de Broglie wavelength: $\lambda_e = \left(\frac{2\pi\hbar^2}{m_e kT}\right)^{1.2}$
F	Relativistic Fermi integral: $F_k(\alpha, T_k) = \frac{1}{\Gamma(k+1)} \int_0^\infty \frac{x\sqrt{1+\left(\frac{T_r x}{2}\right)}}{e^{x-\alpha}+1} dx$
T_r	Relativistic temperature: $T_r = \frac{kT}{m_e c^2}$

Opacities

$\boldsymbol{\kappa}$ represents the opacity of stars; a measure of their photon-absorbing power. That is: how the internal temperatures of stars govern how efficient their radiative energy transport is. Photons carry energy away from stellar cores, but they can be absorbed and re-emitted ad infinitum by hydrogen atoms during their "walk" out towards photospheres. The efficiency of this energy transport system is directly correlated with the magnitude of photon absorption that occurs: the hotter the internal temperature, the more hydrogen that remains ionised. This leads to less photon absorption occurring, meaning more energy will be transported over a set amount of time than for low-mass stars, where the vice-versa will occur (this is why hotter stars are brighter than cooler stars; Rybicki & Lightman, 1986).

MESA calculates $\boldsymbol{\kappa}$ using Eqn. [1] of Paxton et al. (2011), here Equation 3.6; a log-relation between opacity, $\boldsymbol{\kappa}$, entropy, $\boldsymbol{S}$, radius $\boldsymbol{R}$, and temperature, $\boldsymbol{T}$:

$$\log\kappa = S\log\kappa_U(R,T) + (1-S)\log\kappa_L(R,T) \tag{3.6}$$

Over the evolution of a model star, the module `kap` builds every MESA-calculated value of $\boldsymbol{\kappa}$ into a table, to which it then appends radiative opacity values from two

different external opacity tables (or just one, depending on the model's $T_{\rm eff}$). The MESA models used for the work in this thesis will take from both: the opacity table from Ferguson et al. (2005), which spans a temperature range of $2.7 \leq \log T_{\rm eff} \leq 4.5$ ($\approx$500 K $\leq T_{\rm eff} \leq \approx$31,600 K), and the OPAL opacity table from Iglesias & Rogers (1993, 1996), which spans $3.75 \leq \log T_{\rm eff} \leq 4.5$ ($\approx$5600 K $\leq T_{\rm eff} \leq \approx 5\times10^8$ K). As with the EOS, `kap` produces the final opacity values from bicubic spline interpolation over all of the above using `interp_2d`.

Thermonuclear Reactions

Thermonuclear reactions within stars, also called stellar nucleosynthesis, are the processes of chemical element creation via nuclear fusion reactions (Hoyle, 1946, 1954). For stars on the main sequence that convert hydrogen to helium, one of two process occurs depending on the mass of the star. For stars with $M \lessapprox 1.3\,{\rm M}_\odot$, the p-p chain is dominant mechanism.

Initially, two protons (two ionised hydrogen atoms) fuse to form a deuteron (ionised deuterium). This then fuses with a single hydrogen atom, forming an atom of helium-3 (and also some energy which is released) (5.493 MeV; Iliadis, 2007). Finally, the helium-3 atom fuses with another helium-3 from a parallel reaction, and helium-4 is formed (with two hydrogens and energy as excess products) — the net energy released from the p-p chain is 26.7 MeV (Iliadis, 2007).

For stars with $M \gtrapprox 1.3\,{\rm M}_\odot$, the CNO cycle is dominant: again, four hydrogen atoms fuse to two helium atoms (plus energy released: 26.7 MeV; Iliadis, 2007) but this time via a catalytic set of carbon, nitrogen and oxygen atoms all gaining and losing protons from the hydrogen atoms throughout the reaction. The $\approx 1.3\,{\rm M}_\odot$ cutoff (Salaris & Cassisi, 2005) is due to how efficient each process is with respect to stars' internal temperatures: the p-p chain occurs for $4 \times 10^6 < T \leq 1.7 \times 10^7$ K (Reid & Hawley, 2005), above which the CNO cycle becomes dominant (Schuler, King & The, 2009) — but the net energy production from the two processes are

identical.

These temperature-based nuclear reaction rates are implemented in MESA with the `rates` module, which is built upon the some-300 nuclear reaction rates of Caughlan & Fowler (1988) and Angulo (1999) that include all elements up to nickel. With the stars studied in this thesis existing in their main-sequence phase, a lot of the reaction rates implemented within MESA are beyond the scope of this work.

3.1.1.3 Stellar Structure and Evolution

Within MESA the user defines an initial mass for the model star, then `mlt` and `eos` use the differential equation solver in the module `num` (described in § 3.2.2.1) to determine ρ_c, the central density of the model. From here, a spherically-symmetric one-dimensional polytrope is built and split into k number of *cells*, each numbered by decreasing radii and separated by similarly-numbered *faces* (Fig. [9] of Paxton et al. (2011) details a schematic of this cell-face-cell-face setup). All implemented physics modules then each calculate the physical parameters for each cell separately.

The density evolution per cell is calculated using a linearised version of the mass conservation equation; Eqn. [5] of Paxton et al. (2011), given here as Equation 3.7:

$$\ln r_k = \frac{1}{3} \ln \left[r_{k+1}^3 + \frac{3}{4\pi} \frac{dm_k}{\rho_k} \right] \tag{3.7}$$

The temperature of each cell, T_k, is dependent on the internal energy transport across the face boundaries between cells, defined by `mlt` as $\nabla_{T,\,k}$ where $\nabla_{T,k} = \frac{d\ln T}{d\ln P}$. The average temperature at face k is interpolated based on the user-inputted mass via Equation 3.8, and likewise for the average face pressure using Equation 3.9 (both from Paxton et al. (2011), in-text):

$$\overline{T}_k = \frac{T_{k-1}\, dm_k + T_k\, dm_{k-1}}{dm_k + dm_{k-1}}, \tag{3.8}$$

$$\overline{P}_k = \frac{P_{k-1}\, dm_k + P_k\, dm_{k-1}}{dm_k + dm_{k-1}} \tag{3.9}$$

Therefore, the temperature gradient *across* cells can be calculated using Eqn. [8] of Paxton et al. (2011), given here as Equation 3.10:

$$T_{k-1} - T_k = \overline{dm_k} \left[\nabla_{T,\,k} \left(\frac{dP}{dm} \right)_{\text{hydrostatic}} \frac{\overline{T}_k}{\overline{P}_k} \right] \tag{3.10}$$

The temperature, T, and pressure, P, internally to the cells has been accounted for, but the boundary T and P between cell 1 and the model star's surface (effectively the vacuum of space) are defined by `atm`. Here, surface pressure, P_s, is calculated using hydrostatic equilibrium, given as Equation 3.11, and surface temperature, T_s, is found via the multiplying the surface pressure with the `mlt` $\nabla_{T,\,1}$, given as Equation 3.12 (both are from Eqn. [9] of Paxton et al. (2011)):

$$dP_s = \frac{G m_1 dm_1 / 2}{4\pi r_1^4}, \tag{3.11}$$

$$dT_s = dP_s \nabla_{T,\,1} \frac{T_1}{P_1} \tag{3.12}$$

The above sets of equations calculate a stellar model for a snapshot in time, but for stellar evolution there needs to be time-steps over which the above equations can iterate. Built into MESA is a low-pass filter that measures the difference between successive values of parameters such as T_{eff}, L_*, M_*, T_c and ρ_c. If the values are changing quickly, then the increment of the time-steps is increased to ensure a high resolution evolution. Vice versa; if the parameter values are not changing by much then the increments are decreased to "speed-up" the current stage of evolution. The result is stellar evolutions that can converge in a small number of iterations, but still with high resolution evolutions (Paxton et al., 2011).

MESA converges to a solution using the Newton–Raphson scheme in Eqn. [15]

of Paxton et al. (2011). At every time step a convergence is attempted on a trial solution, and each of the MESA modules involved output analytic partial derivatives for each numerical quantity. All of the aforementioned is then used as a basis for the next convergence, with Jacobian matrices calculating the residuals between each iteration. A final solution is accepted when a trial solution reaches any implemented convergence criteria; e.g., a parameter limit, such as stopping below a certain $T_{\rm eff}$, or an evolution limit, to stop the model evolving beyond the TAMS.

Above describes the stellar evolution modules built into MESA that are relevant to the work in this thesis. But MESA is capable of doing far more than what was employed here, so the reader is directed to all five MESA papers for more extensive in-depth discussions on the further capabilities of the MESA software: Paxton et al. (2011, 2013, 2015, 2018, 2019).

3.1.2 Inlists

MESA requires three separate input files to run. The first input file, called an "inlist" file, is unique to a specific stellar model and contains the variable parameters and physics modules required. The second input file, called `pgstar`, is dedicated to plotting the evolution in real-time: it exhibits an HR diagram with evolving stellar tracks, and a temperature-density line profile plot showing current chemical burning, internal mechanisms, mass-loss, and the age of the model star. The final input file is the master inlist file, which calls the other two files and executes the evolution run (see § 3.1.2 for an in-depth description of each inlist).

Several output files are the result of every evolution run. "`.mod`" files record the history of the model evolution in user-defined step sizes, such that the files can be the starting points for continuations of the runs if they were paused at the zero-age main sequence (ZAMS), for example. Likewise, "`.profile`" files record the history of the temperature-density plots visible during the run, and "`.mesa`" files are the

stellar models themselves, which can then be fed into softwares such as GYRE to set the model pulsating (see § 3.2). The values of stellar parameters at the point where the model stopped are stored in a file called "`history.data`", from which HR diagrams and other plots can be created (see § 3.1.3).

3.1.2.1 Model Inlist

Model 'inlist' files contain all the physics modules and variable parameters required for a specific model star, user-inputted as "flags"[4]. An example MESA model inlist file, used to model the star TIC 409934330 in Chapter 5, can be found in Appendix B.

The MESA model inlist file is split into two sections, with the headings of `&star_job` and `&controls`.

`&star_job`

Here reside the more administrative flags, such as those that dictate whether models are saved (and what they are saved as), and those that decide whether `pgstar` is implemented to show live plotting. In addition, physics flags to control pre-main sequence evolution, stellar rotation and angular momentum variables exist here too.

`&controls`

The majority of the physics flags are implemented here, propagating through the stellar parameter values to the modules that build and evolve the models. These include parameters such as mass, age, temperature, metallicity, mixing length and convective overshoot (in § 3.1.3 the role of each within MESA will be discussed).

3.1.2.2 Master Inlist

The Master 'inlist' file is used to physically run MESA. It is split into three sections, with the headings of `&star_job`, `&controls` and `pgstar` respectively. The former

[4] A full list can be found at *https://docs.mesastar.org*

two sections read in respective sections of the model inlist file (or multiple inlist files, one model at a time), and the latter section controls the live plotting (see § 3.1.2.3). An example master inlist file, used to model the star TIC 409934330 in Chapter 5, can be found in Appendix C.

3.1.2.3 `pgstar`

`pgstar` is plotting software built upon `PGPLOT` that displays live plots of a currently-running MESA model, showing real-time stellar evolution. `pgstar` is initiated via a separate inlist file, and read-in by the master inlist file. Within the `pgstar` inlist file the user can employ flags to set the size and aspect ratio of the windows of the live plots, as well as setting their axes limits. The `PGPLOT` function itself is initialised when MESA is running, refreshing after every 'interval': that is; the user can define after how many steps the next step in the model's evolution is plotted by `PGPLOT`, over-plotting the previous and therefore "live-plotting" the stellar evolution. The interval rate can be set under the `&controls` section of the Model Inlist file, as well as at separate intervals for terminal outputs and saved files (the higher the interval of the latter, the smoother the user can re-plot the evolution tracks).

3.1.3 Output 1: HR and Temperature-Density Diagrams

Two main plots are displayed during a MESA run: an HR diagram and a temperature-density line profile plot. Figures 3.1 and 3.2 show an example of each, respectively, generated by `pgstar`, in their raw form, from a simple evolution of a $2.0\,M_{\odot}$ star. Figures after this Sub-Section will be produced in Python for reasons of clarity.

3.1.4 Output 2: The Effect of Variable Parameters

The following Sub-Sections are purely for illustrative purposes, to demonstrate the effect certain parameters have on stellar evolution. All of the following runs evolved

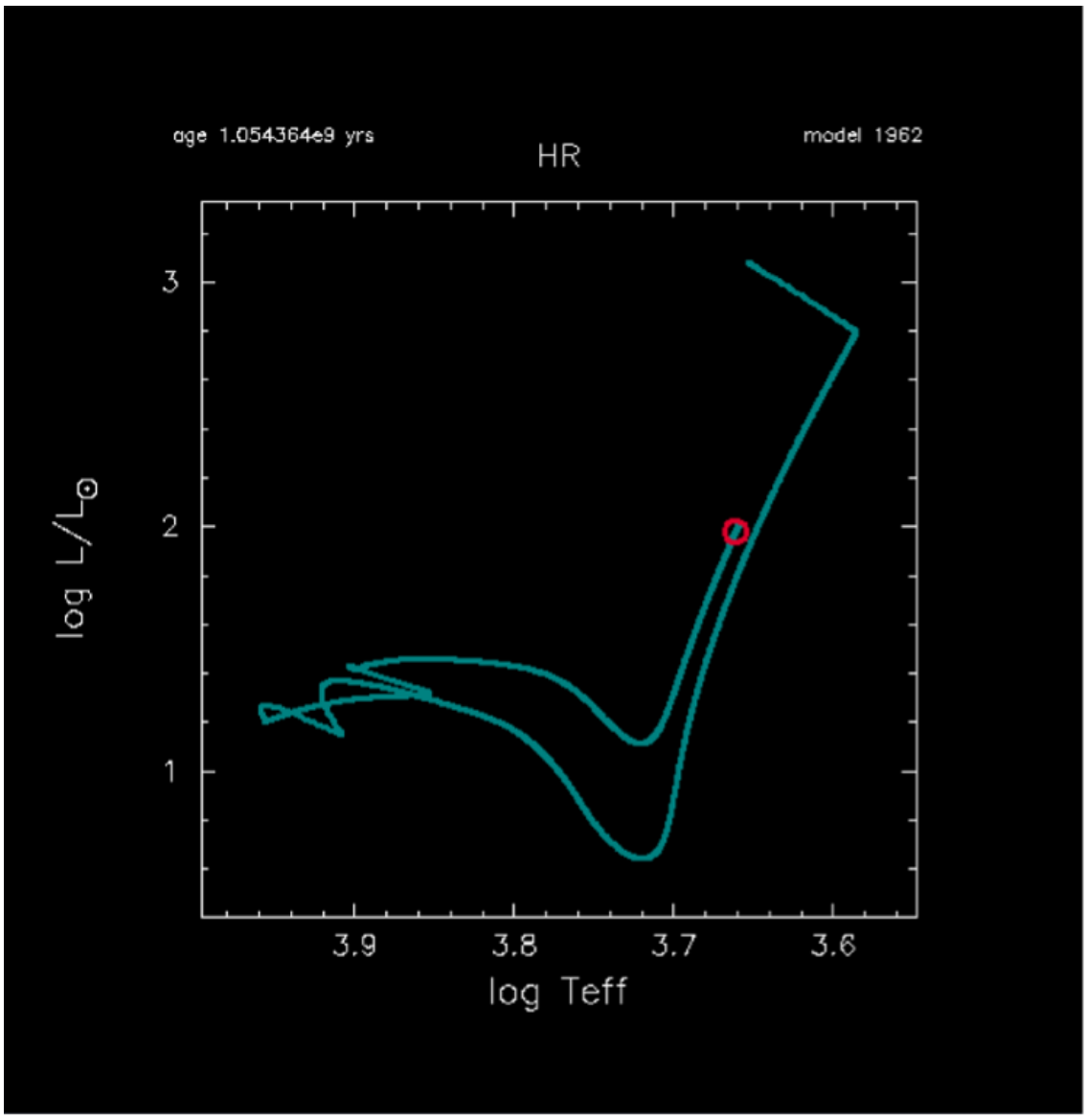

Figure 3.1: *An HR diagram showing the evolution of a simple 2.0 $M_\odot$ star from the pre-main sequence to ∼1 Gyr.*

a simple 2.0 $M_\odot$ star, except for the evolutions in § 3.1.4.1 for reasons which will become clear. Each evolution run included the bare-minimum stellar physics required by MESA — this ensured that the effect each parameter has on model star's evolution was exaggerated. This strategy was suitable for the objective of this Sub-Section, but the evolutions here *are not* representative of real stars.

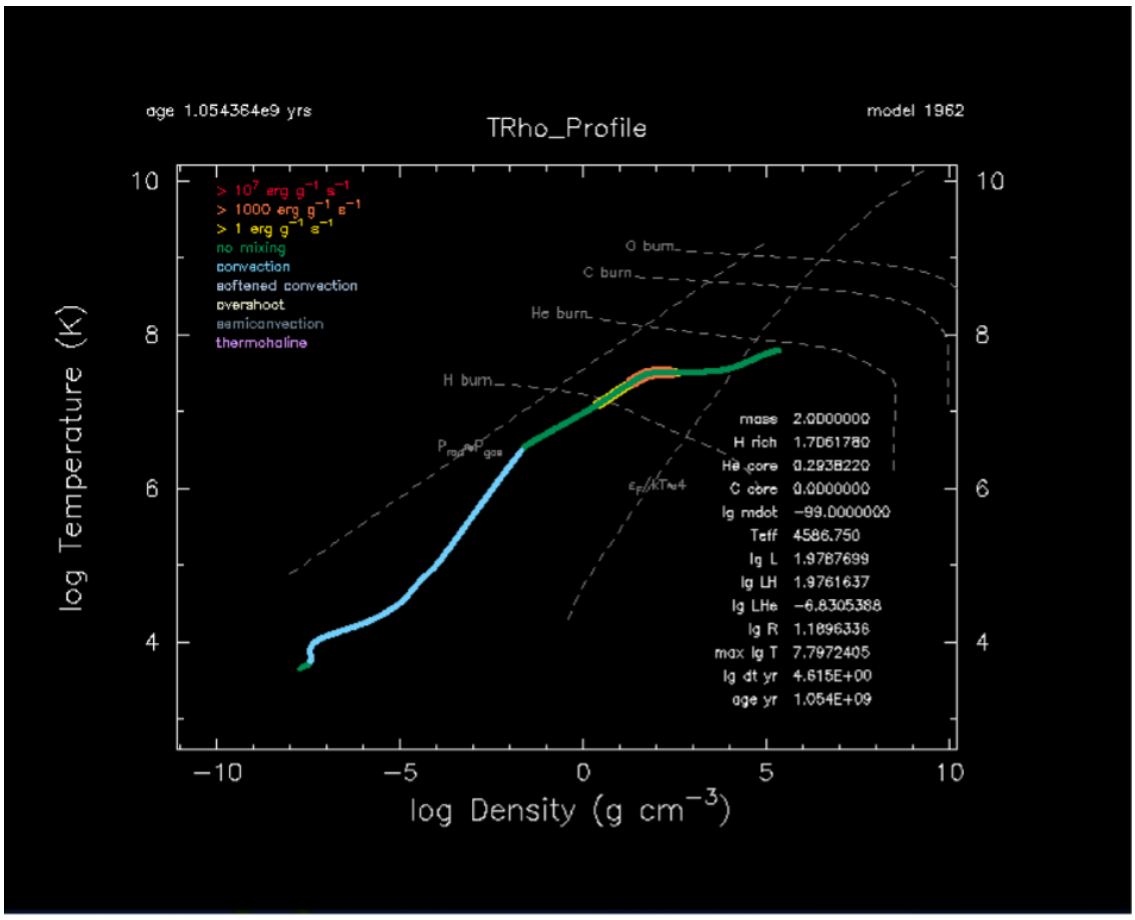

Figure 3.2: *The temperature-density profile of the evolution of the same 2.0 $M_\odot$ star from Figure 3.1, plotted from the pre-main sequence to ∼1 Gyr. On the right hand side lie parameter values for the specific snapshot in time of the model, and on the left is the colour-coordinated key of the currently-dominant internal process, corresponding to the colour of plotted track. Fixed-dashed lines in the plot provide boundaries to illustrate when different shells begin burning.*

3.1.4.1 Mass

The mass of a host star is one of the most valuable parameters required for fully characterising an exoplanetary system. Implementing Kepler's 3$^{\text{rd}}$ Law reveals the total mass of the system, but knowledge of the host star's mass can further reveal the mass of the companion (for single-companion systems at least), without needing inclination data required for RV mass-determinations. Figure 3.3 is an HR diagram displaying the evolution of 10 model stars with masses between 0.05 – 100 $M_\odot$. All

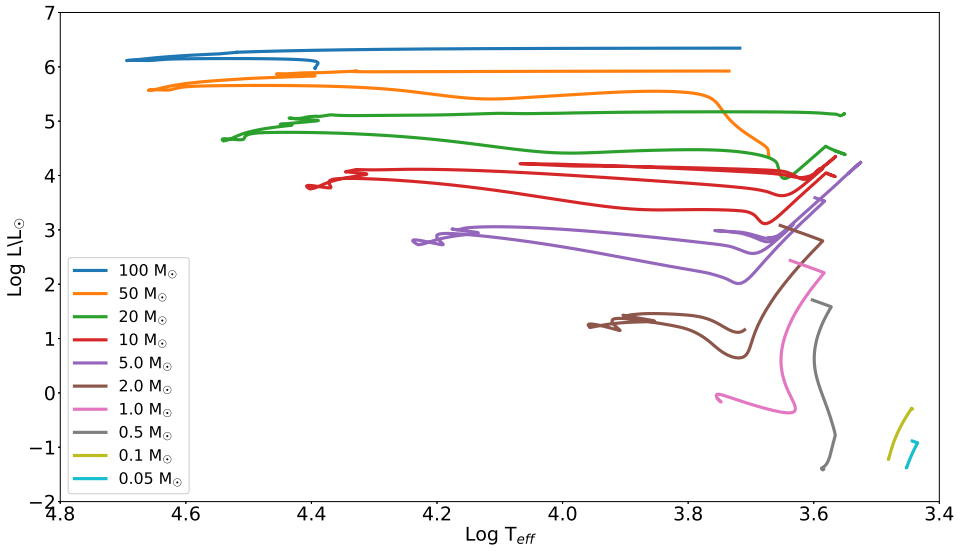

Figure 3.3: *An HR diagram showing the evolution tracks of 10 different-mass model stars. The 1.0 $M_\odot$ and 2.0 $M_\odot$ models reached the implemented 1 Gyr age threshold, but the lower mass models became computationally expensive at ages of $\sim 5 \times 10^5$ yr at the pre-main sequence; likewise, the higher mass models became computationally expensive at ages of $\sim 5 \times 10^6$ yr (prior to their core collapse stages). The expected positive correlation between luminosity, $T_{\rm eff}$ and stellar mass across the main sequence can clearly be seen, as well as different length evolution tracks for different starting masses: the lowest mass stars hardly evolve across the pre-main sequence; the intermediate mass stars have evolved onto-and-beyond the main sequence and are in their respective RBG phases; and the highest mass stars have evolved beyond their giant phase and are heading towards their core collapse stages. A full main sequence track can be imagined as a curve joining the left most points of each evolution track.*

models started from the pre-main sequence up to a maximum-age threshold of 1 Gyr to improve the comparability of the different models. However, this age-boundary was only reached by the 1.0 $M_\odot$ and 2.0 $M_\odot$ model stars: the lower-mass models became computationally expensive before they even reached the main sequence ($\sim 5 \times 10^5$ yr), and the higher-mass models became computationally expensive prior to their core collapse stages ($\sim 5 \times 10^6$ yr). This result provides an excellent demonstration of the effect the mass of a star has on its evolution: lower mass stars evolve

many orders of magnitudes slower than higher mass stars, reflected in the computation time. In addition, Figure 3.3 portrays the different $T_{\rm eff}$ and luminosities that the different mass model stars exhibited during identical epochs in their evolutions: particularly the main sequence "*dance*"[5] all increase in $T_{\rm eff}$ and luminosity with increasing mass. A full main sequence track for the HR diagram can be imagined as a curve joining the left most points of each evolution track.

3.1.4.2 Rotation

Rotation plays an important role during the evolution of a star. It physically alters a star's shape: the faster a star rotates, the more oblate it becomes. This oblateness causes a lower equatorial $\log g$ and $T_{\rm eff}$ (the gas is more diffuse), "gravity-darkening" the same region (and vice versa at the poles; von Zeipel, 1924). Therefore, measuring a star's rotation is paramount to designating the correct classification, correcting for discrepancies in $T_{\rm eff}$ and luminosity (von Zeipel, 1924; Paxton et al., 2019).

Eqn. [B4] of Paxton et al. (2013), given here as Equation 3.13, describes how angular momentum is transported within a model star:

$$\left(\frac{\delta\omega}{\delta}\right)_m = \frac{1}{i}\left(\frac{\delta}{\delta m}\right)_t \left[(4\pi r^2\rho)^2 i\nu \left(\frac{\delta\omega}{\delta m}\right)_t\right] - \frac{2\omega}{r}\left(\frac{\delta r}{\delta t}\right)_m \left(\frac{1}{2}\frac{d\,ln\,i}{d\,ln\,r}\right) \tag{3.13}$$

- where ν is the turbulent viscosity, defined as sum of the diffusion coefficients from Thoul, Bahcall & Loeb (1994) combined with rotationally induced instabilities, all implemented into a convection module.

Furthermore, a user-defined surface equatorial rotation speed, $v_{\rm eq}$, set in the model inlist file, is transformed to a rotational frequency, Ω, then combined with

[5] a self-coined term for the slanted figure-of-eight pattern that intermediate-mass stars create on a HR diagram during their main-sequence phase

the Newtonian potential, Φ, and polar angle, θ, to describe the Roche potential, Ψ: a measure of how gravitationally bound the stellar material is, given as Equation 3.14 (Eqn [34]; Paxton et al., 2019):

$$\Psi(r,\theta) = \Phi(r,\theta) - \frac{r^2\Omega^2\sin^2\theta}{2} \tag{3.14}$$

As mentioned above, flags for differential rotation and internal mixing can be introduced; but for the purposes of this Sub-Section the model stars have been thought of as solid rotators, so differential rotation and internal mixing have been neglected. Figure 3.4 is a HR diagram displaying the stellar evolution tracks of seven $2.0\,\mathrm{M}_{\odot}$ model stars, from the pre-main sequence to 1 Gyr, with different rotation rates ranging from $v_{\mathrm{eq}} = 1 - 300\,\mathrm{km\,s^{-1}}$. It can be seen that the model stars with increasing rotation rates become cooler and dimmer during identical epochs in their evolutions, illustrating the phenomenon of gravity darkening. The faster-rotating model stars underwent a decrease in surface gravity at their equators, which in turn decreased their temperatures and luminosities. MESA allows a rotation rate within the above-used range, but within the software rotation only has an effect on stellar evolution once a model star reaches the ZAMS: MESA-pre-main sequence stars all evolve identically regardless of the stellar rotation rate implemented.

3.1.4.3 Metallicity

It is known that more metal-rich stars host more planets (Wang et al., 2015; Zhu, Wang & Huang, 2016). Furthermore, the degree of metallicity correlates with the type of planet a star hosts (gas giant, rocky, gas dwarf etc — a higher metallicity provides heavier elements that favour the formation of rocky planets, for example Wang & Fischer, 2015). Therefore, if the metallicity of a host star is known, then assumptions on the nature of its exoplanet(s) can be made. The user can define the initial metallicity, Z, of a stellar model via the flag `initial_z`, which MESA allows

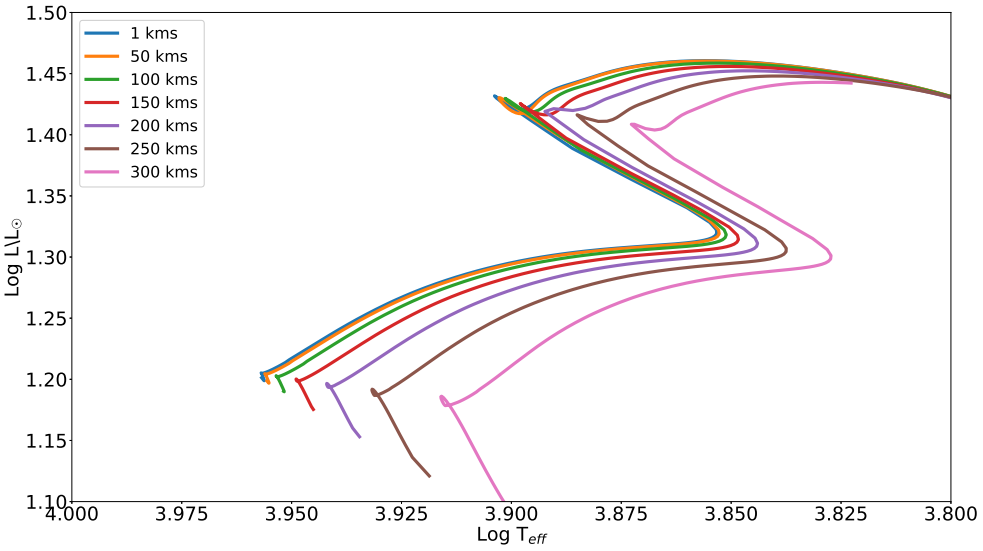

Figure 3.4: *A HR diagram showing the evolution of seven 2.0 $M_\odot$ stars, from the ZAMS to 1 Gyr, with equatorial rotation rates varying from $v_{\rm eq} = 1 - 300\,km\,s^{-1}$.*

to have a value between $Z = 0.00$ – 0.04; for reference, MESA defines the metallicity of the Sun as $Z = 0.02$. Figure 3.5 is a HR diagram displaying the stellar evolution tracks of five 2.0 $M_\odot$ model stars. All models started from the pre-main sequence; the $Z = 0.02$, $Z = 0.03$ and $Z = 0.04$ models all hit the age threshold of 1 Gyr, and the $Z = 0.00$ and $Z = 0.01$ models reached ages of 7.0×10^8 yr and 9.0×10^8 yr, respectively, before becoming too computationally-expensive. This provides a clear correlation between stellar evolution rate and metallicity which can be seen by the decreasing length of the post-main sequence sections of the evolution tracks with increasing metallicity. Furthermore, this correlation simultaneously negatively correlates with the $T_{\rm eff}$ and luminosity of the model stars at identical epochs in their evolutions. Finally, there is a large distinction between zero and non-zero metallicity, providing evidence that all-known stars have *some* metallicity (absolute zero-metallicity stars are the theoretical Population III stars; Tominaga, Umeda & Nomoto, 2007).

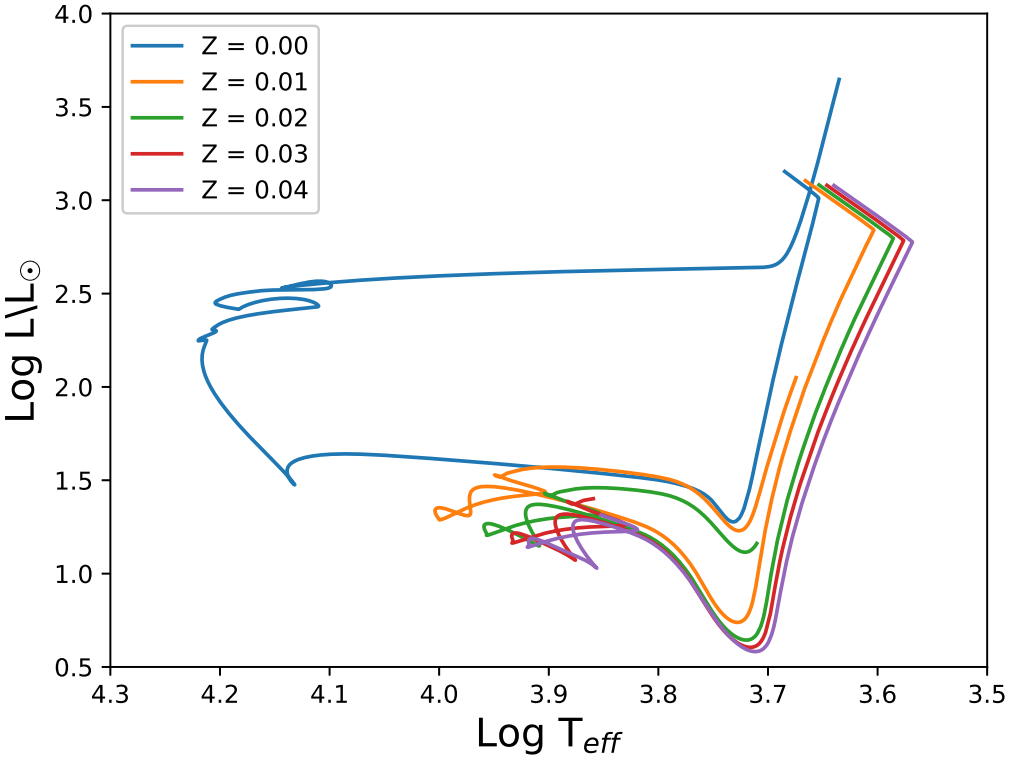

Figure 3.5: *A HR diagram showing the evolution of five 2.0 $M_\odot$ stars with metallicities ranging from Z = 0.00 – 0.04. The Z = 0.00 and Z = 0.01 models reached ages of 7.0×10^8 yr and 9.0×10^8 yr, respectively, before becoming too computationally-expensive; the remaining models all reached the age threshold of 1 Gyr. There is a large distinction between zero and non-zero metallicity, providing evidence that all-known stars have some metallicity (absolute zero-metallicity stars are the theoretical Population III stars; Tominaga, Umeda & Nomoto, 2007).*

3.1.4.4 Mixing Length Alpha

A quantitive value for the *mixing length* helps describe how much convective material moves within a star, giving insight to temperature and velocity gradients (see § 3.1.1.1). This value can be refined using the `mixing_length_alpha` flag, which changes the value of $\boldsymbol{\alpha_{\mathrm{MLT}}}$ in Equation 3.1 — $\boldsymbol{\alpha_{\mathrm{MLT}}}$ cannot be negative, and when set equal to zero forces the model star to be purely radiative. Figure 3.6 is a HR diagram displaying the stellar evolution tracks of seven 2.0 $M_\odot$ model stars, from the pre-main sequence to 1 Gyr, with $\boldsymbol{\alpha_{\mathrm{MLT}}} = 0.1 - 5.0$. The $\boldsymbol{\alpha_{\mathrm{MLT}}} = 0.1$ model

achieved so little of its evolution during 1 Gyr — and it is so dissimilar from the other evolutions — that it can be disregarded from being astrophysical (the model star was almost completely radiative): all of the other evolutions positively-correlated with increasing $\boldsymbol{\alpha_{\mathrm{MLT}}}$, increasing temperature, and luminosity. Additionally, the higher the $\boldsymbol{\alpha_{\mathrm{MLT}}}$ value the slightly further along the post-main sequence track the evolution reached by 1 Gyr. What is interesting is that no matter the value of $\boldsymbol{\alpha_{\mathrm{MLT}}}$, the main sequence "dance" of all stars was identical: this suggests that the *mixing length* of material within a star is a function of mass. Hence, it contributes greatly to a star's position on the HR diagram pre- and post-main sequence, due to mass accretion and mass ejection, respectively, but as the mass of a star effectively remains unchanged during the main sequence epoch of its evolution, all main-sequence evolution tracks remain identical. But this claim is only due to the bias of the stellar evolutions in Figure 3.6 with $\boldsymbol{\alpha_{\mathrm{MLT}}}$ as the only variable, and indeed with the MESA software itself. Bonaca et al. (2012) found a positive correlation between $\boldsymbol{\alpha_{\mathrm{MLT}}}$ and metallicity, as well as it being a function of other stellar parameters such as T_{eff}, $\log g$ and luminosity. Since it has a reliance on other parameters, the flag `mixing_length_alpha` was still implemented in the models used in this work.

3.1.4.5 Convective Overshoot

Convection within stars is described by the MLT, so the MESA software models convective overshoot closely with the Mixing Length Alpha parameter seen above. Figure 3.7 is a HR diagram displaying 11 2.0 $\mathrm{M}_{\odot}$ model stars that have been evolved to an age of 1 Gyr from the pre-main sequence, each with a different convective overshoot value ranging from $\boldsymbol{f_{\mathrm{ov}}}$ = -0.05 – 0.1. More-negative values were attempted, but the models appeared identical to that of $\boldsymbol{f_{\mathrm{ov}}}$ = -0.5, and as such have been assumed to be non-astrophysical (or at least have hit the computational limit of

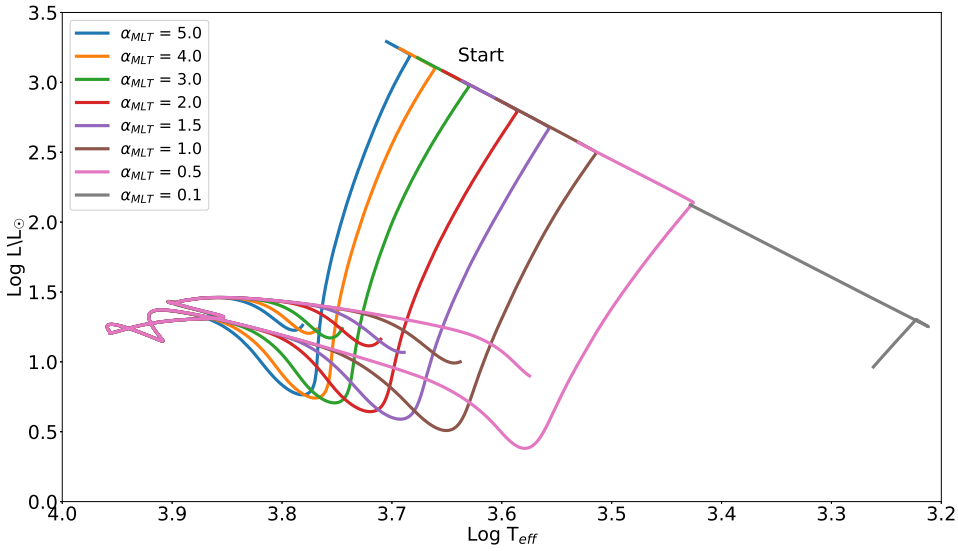

Figure 3.6: *A HR diagram showing the evolution of seven 2.0 $M_\odot$ stars, from the pre-main sequence to 1 Gyr, with* $\boldsymbol{\alpha_{\mathrm{MLT}}}$ *= 0.1 – 5.0.*

MESA). The negative value of $\boldsymbol{f_{\mathrm{ov}}}$ would suggest a negative buoyancy of the overshooting mass, which could arise from the mass being cooled quickly enough from the surrounding material that it still existed as its own identity (Spruit, 1997). It is of note that the pre-main sequence tracks of every model are indistinguishable, suggesting that convective overshoot does not occur — or at least has negligible effects — during the pre-main sequence epoch of stellar evolution. However, it *does* become an altering factor during the main sequence "dance", however, as the zoomed in view in Figure 3.8 reveals. Here, it can be seen that an increasing convective overshoot positively correlates with the temperature and luminosity of the model stars at identical points during their main sequence epochs. However, this negatively correlates with the model stars' evolution rates, suggesting that more internal mixing extends the life time of a star (more hydrogen-to-core accretion); this effect can be seen by the smaller post-main sequence tracks with increasing convective overshoot values.

Below shows an example of how to implement an overshoot value of $f_{\mathrm{ov}} = 0.030$ into MESA. Following the syntax of MESA, the value f_{ov} is defined by subtracting

`overshoot_f0` from `overshoot_f` (i.e., subtracting an upper scale height from a lower scale height). This is because MESA will break if the overshoot is set to occur exactly on a boundary (at `overshoot_f0 = 0.000`), so it requires a small offset.

```
overshoot_f = 0.033
overshoot_f0 = 0.003
```

Below shows further flags that the user can change. The `overshoot_scheme` can alter between an exponential or step equation (Equation 3.2 is the exponential option). The `overshoot_zone_type` below is set to *hydrogen burning*, but can change to *helium* or other metals for stars that have evolved off the main sequence (this is beyond the scope of this work). The `overshoot_zone_loc` below is set to the stellar *core*, but can be changed to other shells. The `overshoot_bdy_loc` below is set to the *top* of the boundary here — the boundary being the core in this case, as defined by `overshoot_zone_loc` — so the region is between the core of the star and its convective zone, but `overshoot_bdy_loc` can also be set as *below*. The offset value of 0.003 for `overshoot_f0`, and the options implemented in the four flags below, were chosen following the methods of Khalack et al. (2019); the other options were not related to the work in this thesis. The context of these flags can be seen in the full inlist file example in Appendix B.

```
overshoot_scheme = 'exponential'
overshoot_zone_type = 'burn_H'
overshoot_zone_loc = 'core'
overshoot_bdy_loc = 'top'
```

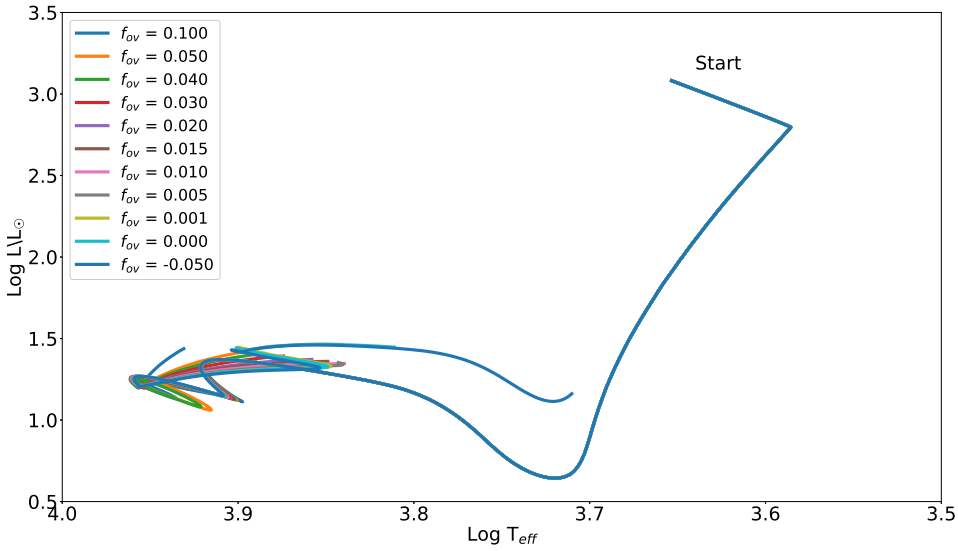

Figure 3.7: *A HR diagram showing the evolution of 11 2.0 $M_\odot$ stars, from the pre-main sequence to 1 Gyr, with convective overshoot values varying from* $\boldsymbol{f_{ov}}$ *= -0.05 – 0.1.*

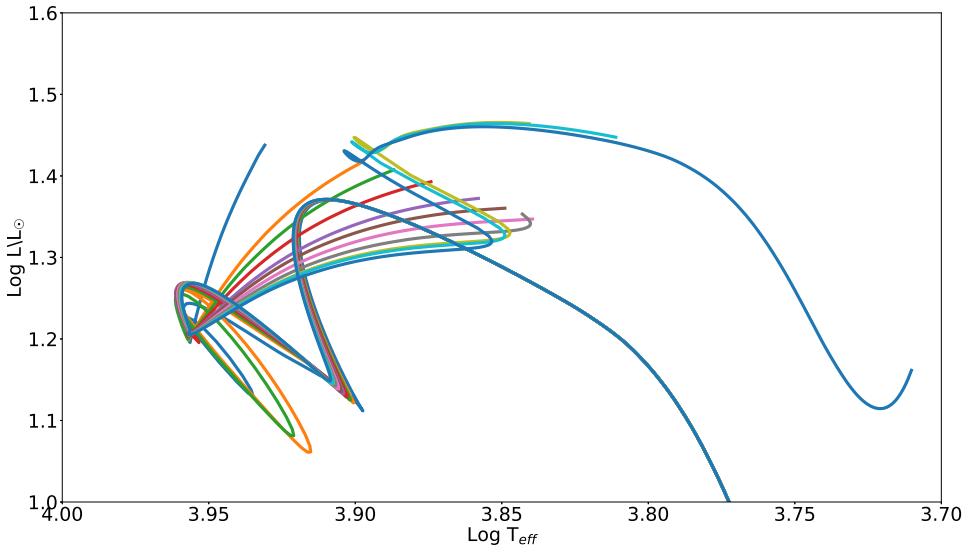

Figure 3.8: *A zoomed in view of the HR diagram in Figure 3.7, providing a clearer view of the main sequence "dance" of the model stars. The colour coding is the same as before, but the key has been omitted for clarity.*

3.2 The Stellar Pulsation-Modelling Software: GYRE 7.0

3.2.1 An Introduction to GYRE

GYRE (7.0; Townsend & Teitler, 2013) is a FORTRAN 08-based asteroseismic modelling software that solves adiabatic and non-adiabatic stellar pulsation equations to model oscillating stars. The software can analytically build model stars, or read-in pre-made models from other softwares (such as MESA). Hence, it is possible to unite both softwares to create the most robust and complete models of pulsating stars.

GYRE runs using the Magnus Multiple Shooting (MMS) scheme, devised by Townsend & Teitler (2013). The "Multiple Shooting" aspect of the MMS is an addendum to the standard "single" and "double" shooting schemes found in the literature. All shooting schemes split a so-called boundary value problem (BVP) into separate initial value problems (IVPs) — BVPs themselves are composed of first-order, linear ordinary differential equations (ODEs) that describe the non-radial and small-amplitude stellar oscillations of a star with respect to a background equilibrium: $\frac{d\boldsymbol{y}}{dx} = \boldsymbol{A}(x)\boldsymbol{y}$ (Eqn. [1], Townsend & Teitler (2013); here, an oscillation frequency is defined as an *eigen*frequency to the ODEs). The IVPs are placed at a boundary (algebraically-defined in the BVP, see Eqn. [2] of Townsend & Teitler (2013)) and integrated to a "fitting point" determined by the boundary conditions. The difference between all solutions is calculated as the "discriminant function" of the shooting scheme, and should equal zero once all integrations agree.

Single shooting is when one IVP integration is performed (Scuflaire, 1974), double shooting is for two IVPs together (Hurley, Roberts & Wright, 1966; Smeyers, 1966, 1967). The latter is more common, and is implemented in earlier stellar oscillation codes, but both schemes suffer from the weakness of "exponential dichotomies": potential oscillation solutions that "grow" and "decay" exponentially, but in both

directions — this is likely to happen in evanescent regions where oscillations cannot propagate. Hence, the "Multiple Shooting" scheme was developed to avoid any exponential dichotomies from occurring by keeping solutions independent.

The MMS scheme numerically solves BVPs as linear ODEs, but calculates them matrically using "Magnus Integrators", given as Equation 3.15 (Eqn. [29], Townsend & Teitler (2013)), to determine the best fitting eigenfrequencies (to the MESA-inputted models). The reader is directed to Townsend & Teitler (2013) for comprehensive description of the internal workings of GYRE.

$$\boldsymbol{Y}^{k+1;k} = \boldsymbol{M}_{\Omega}^{(\boldsymbol{\Lambda}_{\Omega})\boldsymbol{M}_{\Omega}^{-1}} \tag{3.15}$$

- Where $\boldsymbol{\Lambda}_{\Omega}$ and $\boldsymbol{M}_{\Omega}$ are the eigenvalue and eigenvector matrices, respectively, of $\boldsymbol{\Omega}(x^{k+1}; x^{k})$, the Magnus matrix seen in Equation 3.16 (see below).

GYRE runs from just one input file, which in this work reads in the MESA models and perturbs the model stars based off the user-defined flags of frequency ranges, and degree and order of ℓ and m, respectively (see § 1.1.3 for a definition of these two quantum numbers); furthermore, GYRE allows the user to choose what parameters will appear in its output file (see the GYRE inlist file example in Appendix D).

3.2.2 Inlist

Like MESA, GYRE requires an inlist to run, but this time only one per model (no master inlist, and no live plotting software).

3.2.2.1 Model Inlist

As before, the model inlist file contains all the physics flags and variable parameters for each specific MESA model star. An example GYRE inlist file, used to model the star TIC 409934330 in Chapter 5, can be found in Appendix D.

The GYRE model inlist file is split into nine sections, with the headings of `&constants`, `&model`, `&mode`, `&osc`, `&num`, `&scan`, `&grid`, `&ad_output` and `&nad_output`. A lot of these are based on their namesake MESA modules described in § 3.1.1.2.

&`constants`

The user can globally define constants in this area if they wish to, such as $M_\odot$, $R_\odot$, $L_\odot$, G, c, etc, overriding the default values from the MESA module `const` (see § 3.1.1.2). For this work, the default values were used and this area was left blank.

&`model`

This section is one of the more administrative sections, and is where the user defines what type of model GYRE will read in (such as, in this case, a stellar evolutionary model). Furthermore, this section is used to tell GYRE the evolution model's file-name, and what format it is in (such as in a MESA format).

&`mode`

Here is where the user can decided what harmonic degree, ℓ, and azimuthal order, m, the GYRE model will have (see § 1.1.3 for a definition of each).

&`osc`

Next reside some of the flags involved with the core workings of GYRE, where the user can define if a model star is pulsating in a vacuum with no external pressure forces, and whether GYRE should calculate adiabatic or non-adiabatic frequencies.

&`num`

Again, another flag for the internal workings of GYRE: the user can define what order they wish for the Magnus Integrator equations to be when solving numerical solutions to the implemented ODEs from Hairer & Wanner (1996). This is the Gauss–Legendre quadrature equation, usually taken in the 4^{th}-order — Eqn. [B1] in

Townsend & Teitler (2013), given here as Equation 3.16:

$$\boldsymbol{\Omega}(x^{k+1}; x^k) \approx \alpha_{4,1} - \frac{1}{12}[\alpha_{4,1}, \alpha_{4,2}] + \mathcal{O}[(\Delta x^k)^5], \tag{3.16}$$

Where:

$$\alpha_{4,1} = \frac{\Delta x^k}{2}(\boldsymbol{A}_1 + \boldsymbol{A}_2),$$

And:

$$\alpha_{4,2} = \Delta x^k \sqrt{3}(\boldsymbol{A}_2 - \boldsymbol{A}_1),$$

And the Jacobian matrices are:

$$\boldsymbol{A}_i \equiv \boldsymbol{A}(x_i^k) \text{ for } (i = 1, 2),$$

Where:

$$x_1^k = x^k + \left(\frac{1}{2} - \frac{\sqrt{3}}{6}\right)\Delta x^k,$$

And:

$$x_2^k = x^k + \left(\frac{1}{2} + \frac{\sqrt{3}}{6}\right)\Delta x^k.$$

&**scan**

This area is administrative as well, allowing the user to define what units they would like the frequencies to be in (such as Hz or c/d), whilst also configuring the resolution of the GYRE models, and, by extension, how computationally expensive each GYRE model may be. The user can define the frequency range to scan between, and the increment size between each scan, thus dictating the frequency bin size.

&**grid**

Here the user can define a minimum number of points per frequency scanned during the models, and specifically the minimum number in certain regions of Fourier

space. For example, the user can define more points per frequency to be scanned in regions where the pulsations can propagate well, and fewer points at frequencies where the pulsations cannot propagate and would have reduced amplitudes.

&`ad_output`

More administrative flags are found here, allowing the user to define what format the GYRE output files can be in (such as `.txt` files), as well as what resulting parameters from the GYRE models the user wishes to be in those files (such as mass and radius of the model star, and the list of frequencies of pulsations and their respective values of ℓ and m). These flags are here in the example GYRE inlist file in Appendix D as the models used in the work in this thesis had their frequencies calculated adiabatically (the "`ad`"' in "`ad_output`").

&`nad_output`

Here would be the same administrative flags as found above in the "`ad_output`" section if the user required non-adiabatically-calculated frequencies, but since this was not implemented in the work in this thesis, this section was left blank (and is omitted from the example GYRE inlist file in Appendix D).

3.3 The Exoplanet Transit-Modelling Software: EXOFASTv2

3.3.1 An Introduction to EXOFASTv2

EXOFASTv2 [6] (Eastman et al., 2019) is the second generation of the IDL-based exoplanet-fitting software `EXOFAST` (Eastman, Gaudi & Agol, 2013). The software fits single- or multi-system transit, radial velocity (RV) and astrometric models to

[6] *https://github.com/jdeast/*EXOFAST*v*2

single- or multi-wavelength observation data, from any number of different sources, simultaneously. Additionally, it provides an independent model of the system host star, but the key outputs are the mass and radius of the exoplanet(s). Both of these parameters ultimately rely on the mass and radius of the host star, which is fit simultaneously with the planet. The user can manually input literature or self-derived stellar parameter values into a "priors" file as starting points for the models, but note that if this is not done, solar-like values are assumed (see § 3.3.2).

To determine unknown stellar parameters, EXOFASTv2 employs the provided priors of $T_{\rm eff}$, [Fe}H] and combines them with the Torres, Andersen & Giménez (2010) equations that relate the aforementioned to stellar mass and radius (see 3.3.1.1 for more detail).

When running, EXOFASTv2 first utilises `AMOEBA`: a routine used to detect local minima in non-linear data (of which transits and RVs are examples) by modelling them via the downhill simplex method of Nelder & Mead (1965). The objective of `AMOEBA` is to numerically reduce the value of a chi-squared analysis between a data set and its model by iteratively stepping throughout parameter space, employing the result of the previous chi-squared to guide its next step, searching for a global minimum. Once a best fit has been achieved, its quality is inspected via a variety of cases that could be held accountable for a bad fit: there might exist a transit — un-modelled — for a second planet; model uncertainties may have been unsuccessfully approximated; or large, anomalous data-outliers have skewed the results.

Next, EXOFASTv2 employs a Markov Chain Monte Carlo (MCMC) routine which sets up chains of "walkers" that explore parameter space, to hone in on the best fit values. The size of the steps in the chains are essential: if they are too large, multiple model rejections will alternate with jumps to far-flung reaches of unnecessary parameter space, inducing irrelevant calculations and inefficiently using up time that

could otherwise be hosting a convergence on the best parameter values. Contrarily, steps sizes too small will cause — once a model has been accepted — adjacent MCMC best-fit steps to be continually accepted as they will appear almost identical in parameter space, causing the whole process to be computationally expensive. The addition of a small deviate to each step was added as an initiative from Ter Braak (2006) that guarantees the full exploitation of all parameter space, removing the risk of the MCMC steps becoming locked in a revolving manner around an area of parameter space that fits the data equally-well at all locations.

3.3.1.1 Stellar Parameters

Eastman et al. (2019) defines four methods for EXOFASTv2's stellar parameters:

Method 1 — the software default — utilises the MESA Isochrones and Stellar Tracks (MIST) evolution models from Dotter (2016) and Choi et al. (2016).

Method 2 requires the flag `YY` to deploy the Yonsei Yale (YY) stellar evolutionary models from Yi et al. (2001) (the flag `NOMIST` is also required to stop EXOFASTv2 running the default method).

Method 3 fits a spectral energy distribution (SED) on user-supplied broadbrand photometry of the host star, with parallax and extinction priors (see § 3.3.2).

Method 4 The user can set the flag `NOMIST` to prevent the default method from running (as seen in **Method 2**), and instead can provide a direct Gaussian, or uniform prior, on stellar mass and/or stellar radius.

As mentioned above, the default method used by EXOFASTv2 to constrain stellar mass and radius incorporates the Dotter (2016) and Choi et al. (2016) MESA Isochrones and Stellar Tracks (MIST) evolution models (for MESA see § 3.1; Paxton et al., 2011, 2013, 2015, 2018, 2019), and it was this method (**Method 1**) that was used for the work in this thesis. Dotter (2016) and Choi et al. (2016) computed many hundreds of stellar tracks for almost every conceivable star: those within a

mass range of 0.1 – 300 $M_\odot$, a radius range of 0.008 – 1432 $R_\odot$, a $T_{\rm eff}$ range of 2200 – 400,000 K, a metallicity range of Z = -4.0 – 0.5, and an age range of 0.1 Myr up to the age of the universe (and beyond, but an upper-limit exists for obvious reasons); they achieved complete evolutions from the pre-main sequence to white-dwarf.

A grid was populated with every initial parameter mentioned above, along with Equivalent Evolutionary Phases (EEPs): a set of numbers that correspond to certain epochs of stellar evolution (Dotter, 2016). EEPs are used instead of stellar ages as they are defined such that the evolution track at any EEP value appears to be the same, regardless of the star. Two EEP examples are 202 and 454, which represent zero age main sequence (ZAMS) and terminal age main sequence (TAMS), respectively. It was from this grid that the MIST stellar tracks were calculated.

EEPs replace the fitted stellar age parameter in MIST models. However, it was found that this caused stars to advance along their evolution tracks too quickly, so the model steps were weighted by the interpolated age gradient, $\partial(EEP)/\partial(Age)$, to rectify this (NB: This is not a *stellar age gradient*). The metallicity of each MIST model at each EEP is converted into surface iron abundance using Equation 3.17 (Eqn. [1], Eastman et al., 2019), calibrated by $\left(\frac{Z}{X}\right)_\odot = 0.0181$ — the metal fraction of the Sun (Asplund et al., 2009).

$$[\mathrm{Fe/H}] = \log_{10}\left(\frac{Z}{X}\right) - \log_{10}\left(\frac{Z}{X}\right)_\odot \tag{3.17}$$

- Where Z and X are the surface metallicity fraction, and the surface hydrogen (^{1}H) fraction, provided for each stellar age in the MIST EEP file, respectively.

The initial stellar masses in the parameter grid represent the current stellar masses of models: the mass-loss of stars during their planet-hosting epoch is comfortably inferior to their mass measurement error. However, Eastman et al. (2019) highlights that this assumption fails for very high mass stars ($\sim$10 $M_\odot$+), and that

such stars should not be fitted with MIST. This should not cause much concern for the user for two reasons: a) The currently-known highest-mass host star is μ^2 Scorpii (HD 151985), with a mass of $9.1 \pm 0.3\,M_\odot$ (Tetzlaff, Neuhäuser & Hohle, 2011; Squicciarini et al., 2022); b) Stars with masses beyond the aforementioned threshold do not have lifetimes long enough to harbour planet formation (or even host protoplanetary disks; Williams & Cieza, 2011), so EXOFASTv2 will never be required to model such systems. In parallel with the preceding, caution should be exercised when fitting stars with $T_{\rm eff} < 3500\,K$ or $T_{\rm eff} > 10{,}000\,K$ as well.

The MIST EEP models are incorporated into the EXOFASTv2 IDL package in parallel with the stellar age, $R_\odot$ and $T_{\rm eff}$, as well as the above derived [Fe/H] and $\partial(EEP)/\partial(Age)$, for each initial mass, M_*, and initial metallicity, Z. During a model run, IDL's `INTERPOLATE` function performs a trilinear interpolation[7] in the three parameters of EEP, initial metallicity and initial mass, which derives another set of $T_{\rm eff}$, $R_\odot$ and [Fe/H] at each MCMC step.

In addition, some assumptions are made by EXOFASTv2:

The star is non-rotating. This constructs the star symmetrically in the model, inducing a uniform density, temperature, pressure and magnetic field.

The star has solar-scaled abundances, such as [α/Fe]. This sets the α abundance as $[\alpha/Fe] = 0$, which permits its use as a proxy for stellar age when compared to that of the Sun (Casamiquela et al., 2018) — however, there is a caveat with this as younger stars (such as those studied in this thesis) will be alpha-enhanced more than a solar-age star due to the younger stars forming in a naturally more-enriched interstellar medium (Delgado Mena et al., 2019).

The star is limited to [Fe/H] $\leq$ 0.5. This limits the maximum metallicity of the model star to be approximately three times than that of the Sun. Feltzing & Gonzalez (2001) state the the generally accepted upper-limit for very metal-rich stars is [Fe/H] > 0.2, and, with even with a few known stars marginally higher than

[7] three interpolations over a 3D grid

0.2, all stars' iron abundances are well within the [Fe/H] $\leq$ 0.5 limit.

EXOFASTv2 **assumes Sun-like parameters for any value not supplied in the priors file** (See §3.3.2 for this).

3.3.2 The Stellar Priors File

To ensure EXOFASTv2 produces the most accurate results, the user can append a *priors* file. This file — populated with either self-derived or literature-based stellar parameters — is read-in and exploited by EXOFASTv2 during model runs.

A modicum of parameters can include EEP, from grids found in Dotter (2016); stellar age, estimated via gyrochronology (for Solar- and later-type stars; Barnes, 2003, 2007); stellar mass and radius, both revealed by ascertaining stellar density through asteroseismology (Aerts, Christensen-Dalsgaard & Kurtz, 2010), with help from the methods of Mann et al. (2015) which also calculate $T_{\rm eff}$; initial and current metallicity, determined from chemical abundance ratios; time of conjunction and orbital period, both evaluated from studying the time series data; and parallax, acquired from the most recent Gaia data release, DR3 (Gaia Collaboration et al., 2021; Gaia Collaboration, 2022). One would suggest that this parameter configuration in a priors file is the bare minimum required, and that these methods are to be used if any parameter values do not already exist in the literature. Note that if time of conjunction is acquired from the literature, a good practice is to propagate it to the same epoch as the data set being fitted (appendix K shows an example of a priors file, with each parameter explained, used for the star TIC 409934330 in Chapter 5). The reader is advised to study Table [3] from Eastman et al. (2019), which describes an extensive list of parameters available to add to the priors file, alongside their respective values and their numeric limits within EXOFASTv2 .

By default, EXOFASTv2 pre-emptively applies solar values to all parameters not provided in the priors file. Poor results will prevail if the user does not change these

starting values consistently: the model may obtain a satisfactory local solution rather than a correct global solution, or EXOFASTv2 may reject the model entirely. If the user only modifies stellar mass and radius, then all derived quantities (such as the equilibrium temperature of the planet) should be ignored.

3.3.2.1 Stellar Limb Darkening

It is known generally that the non-linear limb darkening law is superior, but for the precision of most of the data used in EXOFASTv2 , and as a compromise for efficiency, the quadratic limb darkening law is implement within the software.

The limb darkening models of Claret & Bloemen (2011) (and Claret (2017), updated for TESS) are based on the ATLAS atmospheres (Kurucz, 1979) which can be applied to wide ranges of $\log g$, $T_{\rm eff}$ and [Fe/H], each being interposed as priors for the EXOFASTv2 limb darkening at each step of a Markov chain. The tables of limb darkening coefficients in Claret & Bloemen (2011) and Claret (2017) supply the following bandpass filters allowed in EXOFASTv2: the Johnson/Cousins U, B, V, R, I, J, H and K; the Sloan u', g', r', i' and z'; the Strömgren u, b, v and y; the *Spitzer* 3.6 μm, 4.5 μm, 5.8 μm and 8.0 μm; CoRoT; *Kepler*; and TESS.

3.3.3 Modelling Exoplanet Transits

EXOFASTv2 is capable of fitting several planets around the *same* star — implementing Kepler's 3$^{\rm rd}$ Law with knowledge of the radius of the host star — the mass of the whole system, and each planet's orbital period, to derive the ratio of semi-major axis and stellar radius, a/R_*, for each planet at each step of the Markov chain. EXOFASTv2 can read-in and fit any combination of data sets simultaneously: RV data, photometric data, astrometry data, Doppler Tomography data, and SEDs; furthermore, useful fragments of out-of-transit data can be injected as well.

If RV data cannot be supplied, EXOFASTv2 has built within it the Chen & Kipping (2017) exoplanet mass-radius relations. These relations can be deployed to derive their namesake parameters with respect to observational photmetric data if it is the only data input: the relations can be used to generate ball-park approximations that can then be reiterated over to constrain the best fit (but all derived quantities will inherit the uncertainties from Chen & Kipping (2017), propagating further with additional calculations).

The user can enable Transit Timing Variations (TTVs), Transit Depth Variations (TδVs), and/or Transit Duration Variation (TDVs) within the software. Obtaining astrometry data, Doppler Tomography data and SEDs, were beyond the scope of the work in this thesis but previously-determined values were extracted from SIMBAD (where found) to provide further constraints. The reader is directed to Eastman, Gaudi & Agol (2013) and Eastman et al. (2019) for further discussions, and to study § [16] of the paper for full derivations of the transit models.

3.3.4 Calling EXOFASTv2

EXOFASTv2 is executed in IDL, using a file setup as shown in Appendix E, which brings together all inputted photometric data, RV data, and the required "priors" file (see § 3.3.2 and Appendix K), for a model star.

3.4 Output

In the form of results, the user will procure a collection of plots and a table from EXOFASTv2 . The results table is substantial, providing numerical values for every conceivable parameter for both the star and planet(s) that the user could require.

For every model implemented in EXOFASTv2, three plots at different epochs of the model run are manufactured: at the very start of the run, the best-fit from

`AMOEBA`, and the best-fit from the MCMC technique (Eastman et al. (2019) advise only the latter to be published). Furthermore, plots of chain, covariance and Probability Distribution Function (PDF) diagnostic plots are produced.

The reader should see Eastman et al. (2019) for examples of all plots if desired, as well as plots for different stellar evolution models such as the `YY` tracks.

3.5 The Time Series Analysis Tool: PERIOD04

PERIOD04 (Lenz & Breger, 2004) is a Java/C++ -based time series data manipulation tool expanded from a combination of PERIOD98 (Sperl, 1998) and `PERIOD/PERDET` (Breger, 1990) that specialises in analysing non-continuous astronomical time series data. Frequency analysis can be performed on periodic time series data via discrete Fourier transforms (not fast Fourier transforms due to potential gaps in the data), and the data can be exploited in phase space to visualise the accuracy of determined frequencies of planetary orbital periods or stellar oscillations.

The user is able to manually extract pulsational frequency peaks from the PERIOD04-calculated Fourier transforms. The extracted frequencies are appended to a list, where the amplitude and phase of each can be calculated using Equation 3.18, as well as propagating respective errors via a least-squares fit from Montgomery & O'Donoghue (1999), given as Equations 3.19, 3.20 & 3.21. Furthermore, harmonics of any extracted frequencies can be computed and added to this list as well.

$$f(t) = Z + \sum_{i=0} A_i \sin\left(2\pi(\omega_i t + \phi_i)\right) \tag{3.18}$$

- Where Z is the zero point, A_i is the amplitude, ω_i is the angular frequency, and ϕ_i is the phase.

$$\sigma(f) = \sqrt{\frac{6}{N}} \frac{1}{\pi T} \frac{\sigma(m)}{a} \tag{3.19}$$

$$\sigma(a) = \sqrt{\frac{2}{N}} \sigma(m) \tag{3.20}$$

$$\sigma(\phi) = \frac{1}{2\pi} \sqrt{\frac{2}{N}} \frac{\sigma(m)}{a} \tag{3.21}$$

- Where N is the number of time data points, T is the timebase of the data, $\sigma(m)$ is the residuals, and a is the frequency amplitude.

The now-fitted peaks can be removed from the original Fourier transform — and hence the respective variability from the light curve — to calculate a new Fourier transform from the residuals, to search for any additional pulsational activity. This practice is known as pre-whitening and can be repeated ad infinitum, but frequency peaks below S/N < 4 should be ignored as it then becomes impossible to tell whether the peak is astrophysical or generated from effects such as white noise (from a Gaussian distribution), red noise (from random patterns in the data), or a non-uniformly-spaced cadence in the data (Koen, 2010).

Chapter 4

MOSES: MHT Optical Star and Exoplanet Survey

4.1 Praefatio

The MHT is one of the largest-working-teaching telescopes, associated with a university, in the UK. As mentioned in § 2.2 the MHT's first light was in 2016, so between then and the time of writing it had successfully imaged Near-Earth Objects, Supernovae, Galaxies, Nebulae, and even Pluto[1]. Further, the MHT had captured a transit of the known-exoplanet WASP-11 b. It made sense, then, that the MHT's next venture should be one of discovery, primarily with the planet-transit capability in mind.

So-called "fishing exercises" — observing random points in the sky and hoping for something new to appear — do occasionally yield new discoveries, but, for the sake of time and efficiency, initiating a new survey to observe thousands of stars simultaneously was the best strategy if new exoplanets were to be discovered. This led to the establishment of **MOSES**: **M**HT **O**ptical **S**tar and **E**xoplanet **S**urvey, the first large stellar-and-exoplanet survey using exclusively UK-based observations.

[1]We believe this is the first time Pluto has been photographed from Lancashire.

4.2 Observing Strategy

During the initial phases of MOSES the MHT's field-of-view was deemed too small for the survey to be a single-aperture affair, so a grid-based approach built of multiple pointings was implemented. Hence, the MOSES field was formed of a 4×4 tiled array covering a 7 square degrees region of the sky, in the constellation of Cassiopeia. There are over 3500 stars per MOSES frame (per $40.2' \times 40.2'$ field-of-view), so with every iteration across the MOSES field more than 56,000 stars are observed.

The reasons for choosing this observing region were three-fold: the region is circumpolar with respect to Alston Observatory, permitting year-round observability; the region is near to the Galactic plane, a region of high stellar density (but not too close to the Galactic plane that dust lanes obscure stars); the region is in an area that had not been surveyed for exoplanets prior, and there were no known transiting exoplanets in the field. Additionally, the MOSES field had not yet been observed by TESS during its primary mission; therefore, any transiting exoplanet candidates detected in MOSES data had a higher chance of being new discoveries.

Each of the 16 tiles of the MOSES field underwent a 60-s exposure in the Johnson V-band, following a pre-written script that automatically slewed the telescope between tiles in succession. Once all 16 tiles had been observed the MHT slewed back to the first pointing and the procedure repeated, producing data with a $\sim$24-min cadence. This cycle was sustained for 10 months — weather permitting — forming the primary MOSES survey.

In addition to the target images, the MHT took the dark, bias and sky flat-field frames required for data reduction. No images of any kind were taken, however, until the CCD had cooled to -35°C. For this work, notable findings within the MOSES data sets will be designated as MOIs: MOSES Objects of Interest.

4.3 Data Reduction

4.3.1 Dark Images

During an exposure, pixels on a CCD chip can accumulate thermally-excited electrons. This is called dark *current*, and the accumulation occurs over time (linearly) such that longer exposures accrue more (sensor temperature causes an exponential increase as well, hence they are cooled down as much as possible). To try and remove this phenomena, dark *images* are created: here an exposure is taken without opening the shutter of the CCD, therefore capturing *only* the dark current portion a science image (no photon-excited pixels). Multiple dark images are combined to form a master dark image, which is then *subtracted* from each science image.

4.3.2 Bias Frames

Unlike dark images and sky flat-field images, bias images are taken with zero exposure. They remove the artificially-induced electronic offset applied by the CCD to ensure the Analogue-to-Digital Converter (ADC) always receives a positive signal. Hence, all frames captured by a CCD gain this offset, so it must be removed to make certain the counts recorded per pixel are genuine. The bias is contained within dark images, so is subtracted from the science image with the master dark frame. Hence, the master bias frame is subtracted from *only* the flat-field images.

4.3.3 Sky Flat-Field Images

Sky flat-field images are taken during twilight (sometimes at dusk too), when the sky is clear and uniformly bright. Unlike dark and bias frames, sky flat-field images need to be taken with the same filter(s) as the science images. Every sky flat-field image taken has a different pointing, such that any stars or other artefacts that may appear in the images do not line up on the CCD chip, but they do not require

the same exposure as they science images as the twilight sky could cause saturation. The multiple sky flat-field images are combined to form a master sky flat-field image, which is normalised to the median number of counts in the flat. The science images are then *divided* by this normalised flat field, removing any pixel-to-pixel variation in the detector. This helps to alleviate non-uniform illumination caused by effects such as vignetting, which arises from light reflecting between the front and back of the CCD sensor: this process averages out the less photon-sensitive pixels.

4.4 The MOSES Pipeline

4.4.1 What are Data Pipelines?

Data pipelines are coded routines designed to reduce observational data sets and prepare them for scientific analysis. For example: raw data from space telescopes are unusable in such form, so pipelines are employed to correct for effects such as spacecraft drift, thruster firings and other events that may cause non-astrophysical trends in observational data, as well as reducing the data using the methods described in § 4.3. Other pipelines may go further and perform analyses on newly-processed data. In short: pipelines automate work that would otherwise be done by hand, increasing both productivity and efficiency.

4.4.2 A Brief Summary of the MOSES Pipeline

The MOSES pipeline is fed data via four flavours of observational FITS file: raw science images, dark frames, sky flat-field images and bias frames. It reduces the science images, extracts the flux data for every star detected in each science image, converts the fluxes to magnitudes, then plots this photometric data against their respective time stamps, thus creating unique light curves for every star detected all whilst keeping a master "database" of every star observed. This approach allows

all observation data to be appropriately appended to all respective time series files automatically, regardless of observation date.

4.4.3 An In-depth Guide into the Internal Workings of the MOSES Pipeline

Before any science can be undertaken, the user is required to split up the four sets of data taken from an observation run — the science, dark, flat-field and bias frames — into four namesake directories, respectively, all within a directory containing the MOSES pipeline code: this allows a *master* dark, flat-field and bias frame to be created, from combining each respective set of the aforementioned reduction frames and taking the median of each. It is of paramount importance that new sets of dark, bias and sky-flat frames are taken with every observing run; they should not be reused with science images taken on different nights as observing conditions vary (both internally and externally to the telescope) and as such require different levels of correction.

Dark and bias frames can be taken each night without hindrance, but flat-field frames are sometimes not captured. This did occur during the primary MOSES survey, and on such nights the raw science frames were used to engineer a master flat-field frame, ensuring no change to the observing conditions. This master flat-field image was created by stacking all raw science images into one frame, subtracting the master dark frame, removing outlying stars from each "column" of stars in the stack, taking the median count value of each pixel, before the entire frame becoming normalised by dividing it by the median value of the stacked frame. The flat-field frames produced from the science frames with lots of exposures (200 or more for the same area of sky) are more accurate than their alternatives because they are produced from the actual science data, so the light in both sets of images has traversed the exact same light path (for targets with not many separate exposures

we used standard flat-field images made from sky flats instead).

A second phenomena exists within the science images that needs to be accounted for: barrel distortion. This is the effect of the MHT's curved primary inducing a curved focal plane on all observations, which is amplified by the MHT's focal reducer (see § 2.2) when increasing to a larger field-of-view: the curved focal plane becomes distorted when recorded by a flat CCD chip. This has no major effect on the central ∼75% of the image, but it does has a very significant effect on stars towards the edges and particularly the corners of the science frames (known as "barrel distortion"): edge- and corner-star's celestial coordinates are up to several arcseconds different to true values, and hence the world coordinate system (WCS) of each science image is wrong. This problem must be accounted for, but it cannot be done with the WCS software that the MHT uses during observations.

When observing, the MHT utilises the MAXIM DL [MaxIm DL, 2021] WCS software for its science images (standard for PlaneWave™instruments), but this software treats the science frames as being flat and linear: that is, it does not recognise the curved focal plane injected from the MHT's primary mirror (and hence produces the progressively-inaccurate celestial coordinates of stars towards a science frame's corners).

The barrel-distortion correction begins via a formatting routine publicly available on *astrometry.net*, which takes the science images taken with the MHT and catalogue images of the same areas of the sky, and searches for the same star patterns in both to compare their celestial coordinates. After finding identical star patterns in both images, the routine fits a Single Image (5^{th}-order) Polynomial (SIP) to correct the coordinates of the stars in the science images and assign them their true celestial coordinates. *astrometry.net* then outputs the corrected data as new SIP FITS images, saving an updated WCS in each.

Next, the SIP images are converted from a "standard" WCS to the "Tangent

Plane Projection with Velocity (TPV)" WCS of Calabretta & Greisen (2000) and Greisen & Calabretta (2002), which allows the SIP images to be analysed using software such as Source-Extractor (*SExtractor* Bertin & Arnouts, 1996).

SExtractor is fed all the updated and corrected FITS files and identifies stars in each, before a time series file for each unique star is created. The time series files are numerically named in succession, and contain the respective time stamps, magnitudes, magnitude errors, and celestial coordinates for each star. If the celestial coordinates of two stars match within $1''$, they are assumed to be the same star and the data are combined in the same time series file: this stragergy allows all observation data to be appended to all respective time series files automatically. In parallel with this, a master catalogue of all observed stars is continually appended too: each entry consists of a star's catalogue name, its coordinates, its magnitude, the error in its magnitude, its magnitude standard deviation, and the number of observations.

4.5 MOSES Capabilities

It has already been proven that the MHT can successfully detect exoplanet transits: in 2017 it observed a transit of WASP-11 b, a $0.53\,\mathrm{M_{Jup}}$ gas giant orbiting a $0.81\,\mathrm{M_{\odot}}$ K-type star (West et al., 2009; Bakos et al., 2009). The light curve from this observation contained transit dip with a depth of $\sim$25 mmag and duration of $\sim$2.5 hours (with a 3 mmag standard deviation), both of which are in good agreement with the literature values of a $\sim$20 mmag transit depth and a $2.556^{+0.029}_{-0.007}$-hour duration (West et al., 2009). This delivers confidence that MOSES is highly capable of detecting short-period hot Jupiters around K and M dwarfs, either by detecting entire transits or multiple events of partial transits (to provide ample phase coverage). Any new exoplanet discoveries in the MOSES survey will most likely be made towards the red end of the main sequence, due to high planet-to-star radius ratios. Howard

et al. (2012) determined the occurrence rate of hot Jupiter's from *Kepler* to be one hot Jupiter per 250 stars, and with the *Kepler* field and MOSES field lying in close proximity in the sky — and if it is assumed that the MHT is one tenth as sensitive as *Kepler* — it can be inferred that MOSES could detect ∼20 hot Jupiters.

Given that the MOSES timebase is currently only 10 months long, the maximum period of an exoplanet that can be feasibly designated as a candidate is ∼ 100 d. Over 4000 confirmed and candidate *Kepler* transiting exoplanets with orbital periods <100 d are known[2], so accounting for the smaller survey region there could be ∼250 detectable transiting exoplanets in the MOSES field (however this is not accounting for the stellar density differences between the two regions). Further, a large fraction of planets in the MOSES field-of-view may only be detected once; and even more will not be detected at all. Thus, it is reasonable to assume MOSES will not discover an Earth-like planet. As mentioned above, MOSES will favour detecting hot Jupiters orbiting close to their host stars (P<10 d).

MOSES is sensitive to variable stars, too, and is more likely to be successful with stellar discoveries. However, the seeing at Alston Observatory is poor (∼2.5″ at best), which restricts the MHT from achieving the high S/N required to confidently detect low-amplitude variability, and distinguish low-amplitude pulsations from the noise in Fourier transforms. But for high-amplitude and/or long-period variable stars, it *is* possible. Another hindrance is that MOSES does not achieve the continuous regular coverage required to observe several pulsation cycles.

The work discussed above was presented via a poster at the 2019 UK Exoplanet Meeting at Imperial University in London, and at the TESS Science Conference 1 at MIT in Boston later that year.

[2] *http://exoplanets.org*

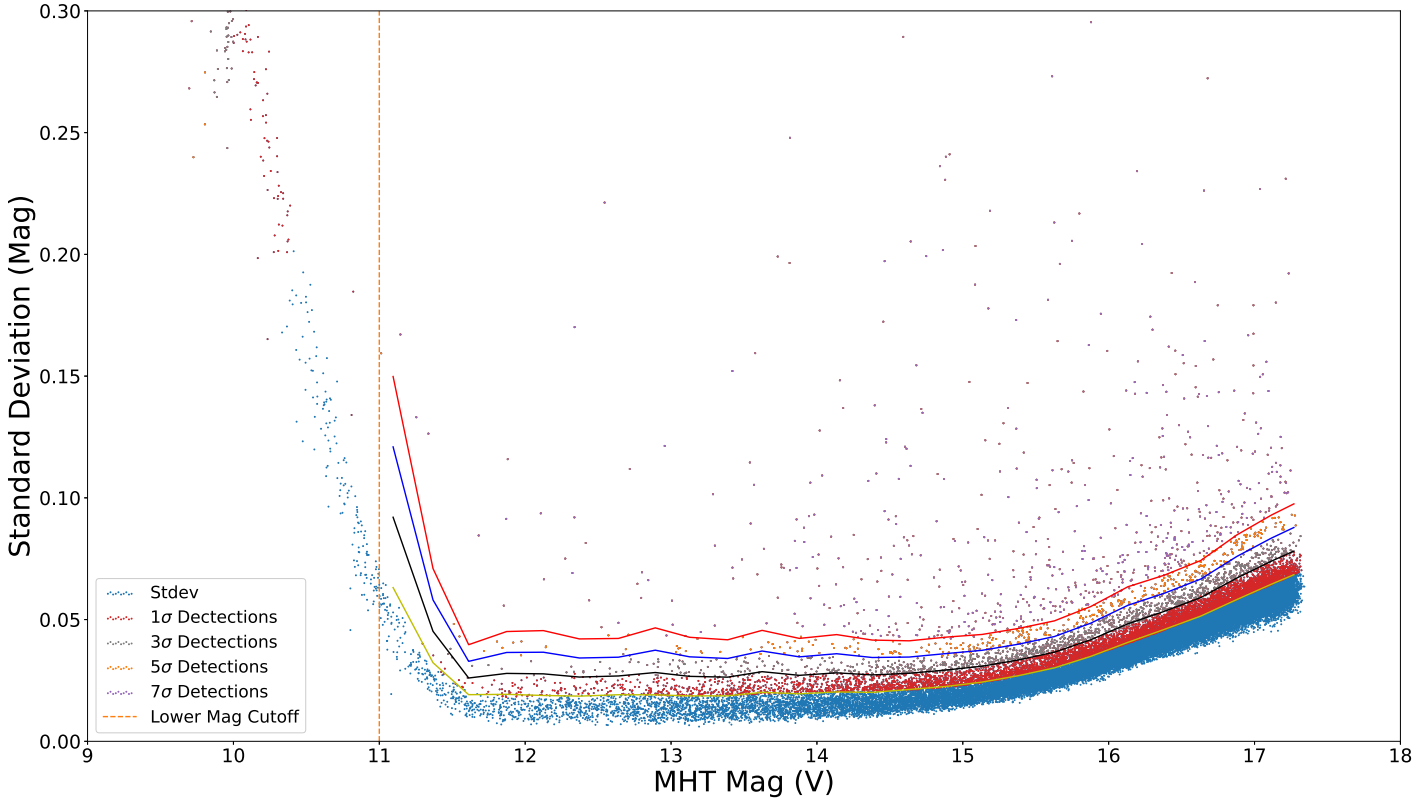

Figure 4.1: *The average magnitude of each MOSES star plotted against its respective standard deviation (blue points), with an average magnitude and standard deviation of 0.125 mag-sized bins over-plotted as the yellow line. The black, blue and red lines are the profiles of 3σ, 5σ and 7σ standard deviations, respectively, with the corresponding σ data points (grey, orange and purple) lying above each. The data points brighter than* 11^{th} *mag were rejected due to non-linearalities in their standard deviation values.*

4.6 Results

The maiden observing season of MOSES yielded 3998 individual FITS images from 28 nights of observations over a 10-month run, from which the MOSES pipeline produced 98,580 unique time series data files that were ready for science. Only targets between 11^{th} and 17.5^{th} mag were used in this work, removing all objects too bright and too faint that non-linearalities in their standard deviations were being produced. Furthermore, any time series files containing fewer than 100 observation points were disregarded as well (249 observations points was the highest number of measurements any star could have).

It would have been an arduous task to plot and manually-inspect all light curves for signs of variability, so a small addendum script was written to try and locate which stars *may* be variable. Here, the master catalogue was employed.

First, all magnitude values in the master catalogue were binned into 0.125 mag bin-width bins. Then, the median magnitude of each bin was plotted against the median standard deviation of all stars contained within that bin, as can be seen overlaid as the black profile in Figure 4.1 — a plot of magnitude and standard deviations of all MOSES stars. Plotting these two parameters revealed an expected SNR trend (the fainter the target star the higher the relative noise), but outliers to the trend — stars which are not uniformly bright over their observation timebase and hence variable — will have a greater standard deviation than the average for its magnitude, and the more extensive the variability the higher that data point will lie above average: this is how potentially-variable stars could be identified.

Next, all the standard deviation values from the black profile were listed in ascending order and a cut was made at the 16^{th} percentile. Between this cut, and the median of the entire black profile, lay a standard deviation width of 1σ. This 1σ-width was then mirrored across the black profile median line to better estimate the non-astrophysical variability induced by photometric errors. If the 16^{th} percentile

cut had been made at the high end of the total distribution, there would be a bias injected from the most-variable stars which would lead to a underestimate of the title number of variables, and the magnitude of variability within the final sample. Hence, by applying the formula "Median + [$x \times$ (Median $-$ 16$^{\text{th}}$percentile)]" the cut above the mirrored 1σ for $x\sigma$ can be determined. Figure 4.1 shows the 3σ, 5σ and 7σ detection profiles overlaid on the MOSES data: this is how the *most* potentially variable stars *were* identified.

Within Figure 4.1, any data points that lay above the three different σ profiles were stars with a variability potentially greater than the σ profile they lie above. It was discovered that 1191 stars lie between the 3σ and 5σ profile, 1140 lie between the 5σ and 7σ profile, and 754 lie above the 7σ profile (in total, 3085 stars that have at least a 3σ detection for variability). For this work, we concentrated on only the $>$7σ detections. A catalogue was produced containing the light curves of the 754 $>$7σ stars.

For every light curve in this catalogue, a Fourier transform was created and the python module `gatspy.periodic` was exploited to find the best-fitting period of variability from the Fourier transform. Then, a script automatically plotted a phase-curve for each star using this information, and each were manually inspected for variability. Scores of variable stars were discovered — some unknown to databases such as SIMBAD — but for the purposes of this work only phase curves showing transit events were sought.

Table 4.1 lists the $>$7σ transit-candidate objects — now designated as MHT Objects of Interest (MOIs) — along with their MOSES catalogue entry, respective coordinates, MHT magnitude, a comment on any previously known nature of the MOIs, and references to previous work if applicable. Table 4.1 hence forms an MOI list for the primary MOSES survey.

Figures 4.2 to 4.17 show phase curves of the MOIs in Table 4.1.

Table 4.1: *The list of all >7σ transiting MOIs and their corresponding MOSES catalogue entry, along with respective co-ordinates, MHT magnitude, a comment on any previously known nature of the MOIs, and references to previous work if applicable.*

MOI Designation	MHT Designation	Target Coordinates	Magnitude (MHT V)	Period (days)	Transit Depth (Mag)
MOI 1	MHT 0006336	02 29 17 +62 45 56	16.20	1.41	0.58
MOI 2	MHT 0010201	02 07 38 +63 26 42	13.98	3.52	0.27
MOI 3	MHT 0011261	02 17 30 +63 21 43	15.70	2.52	0.59
MOI 4†	MHT 0012088	02 15 57 +63 08 08	12.83	1.62	0.35
MOI 5	MHT 0015294	02 21 20 +63 18 38	15.87	1.15	0.47
MOI 6	MHT 0016107	02 19 00 +63 03 00	14.27	1.38	0.30
MOI 7††	MHT 0017194	02 29 16 +63 00 59	15.81	40.3	0.55
MOI 8	MHT 0018303	02 24 46 +62 52 06	16.46	3.94	0.90
MOI 9	MHT 0019039	02 26 34 +63 09 46	15.01	2.78	0.29
MOI 10	MHT 0020176	02 10 04 +63 53 01	14.99	3.80	0.53
MOI 11	MHT 0027171	02 20 13 +64 01 53	16.52	1.37	0.53
MOI 12	MHT 0034016	02 14 42 +64 44 32	16.24	1.50	0.58
MOI 13	MHT 0036135	02 18 51 +64 19 57	16.38	2.66	0.41
MOI 14	MHT 0037054	02 20 48 +64 19 54	16.72	0.99	0.59
MOI 15	MHT 0037080	02 20 55 +64 15 13	16.25	1.95	0.62
MOI 16	MHT 0055161	02 06 53 +64 50 06	15.90	0.39	0.23

† MOI 4 also has the designation TYC 4037-1309-1, but it is classified as a star and no previous variability work has been published

†† MOI 7 also has the designation 2MASS J02291632+6300587, and is a Long Period Variable candidate (Lebzelter et al., 2023).

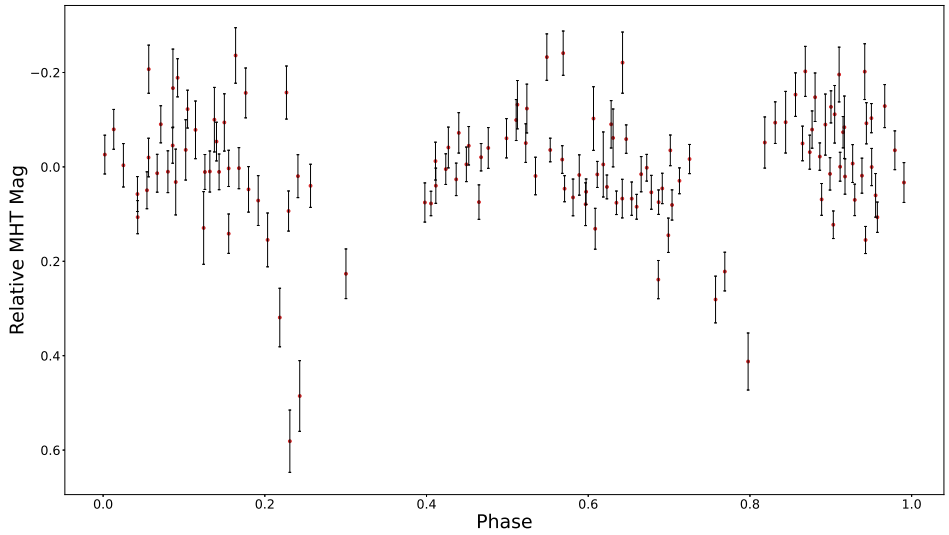

Figure 4.2: *The phase curve of MHT 0006336 (MOI 1), phased over its transiting period of 1.41 d and displaying a primary transit depth of 0.58 mag.*

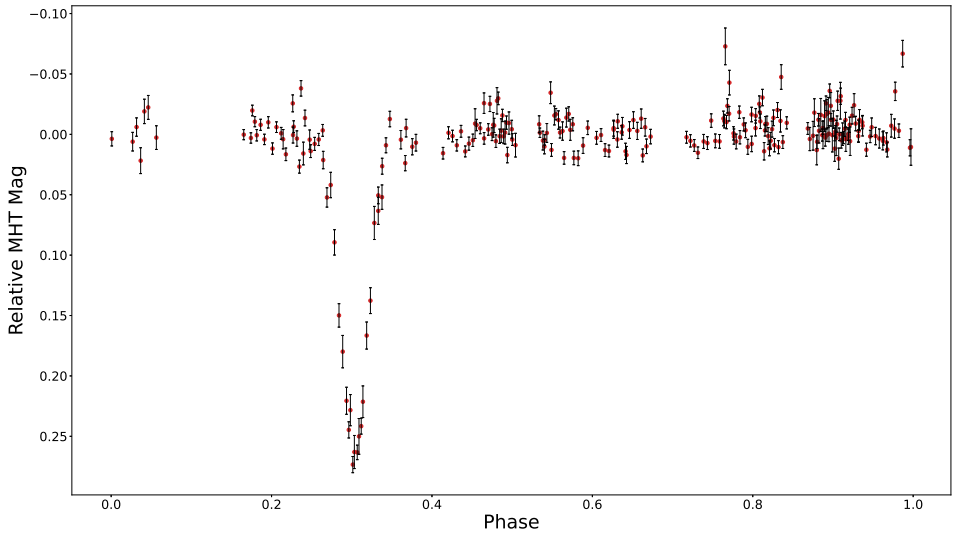

Figure 4.3: *The phase curve of MHT 0010201 (MOI 2), phased over its transiting period of 3.52 d and displaying a primary transit depth of 0.27 mag.*

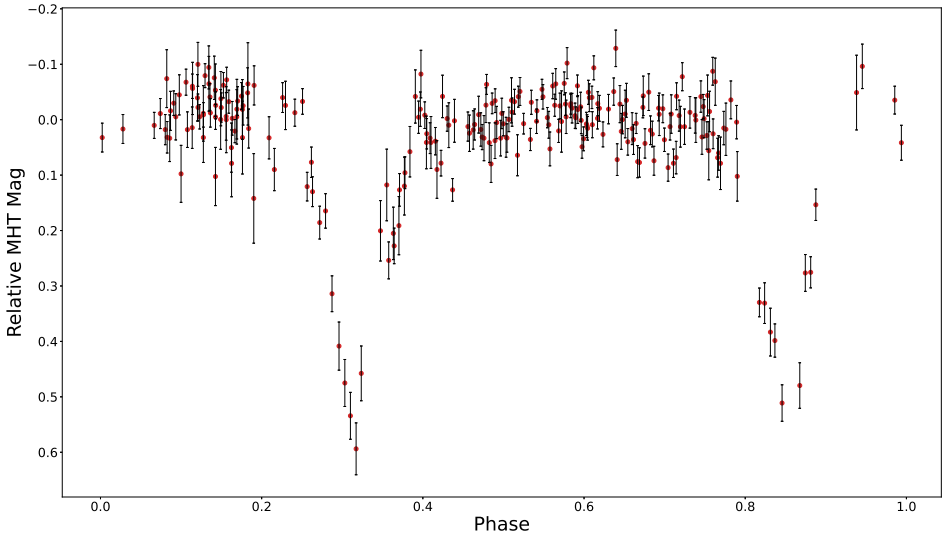

Figure 4.4: *The phase curve of MHT 0011261 (MOI 3), phased over its transiting period of 2.52 d and displaying a primary transit depth of 0.59 mag.*

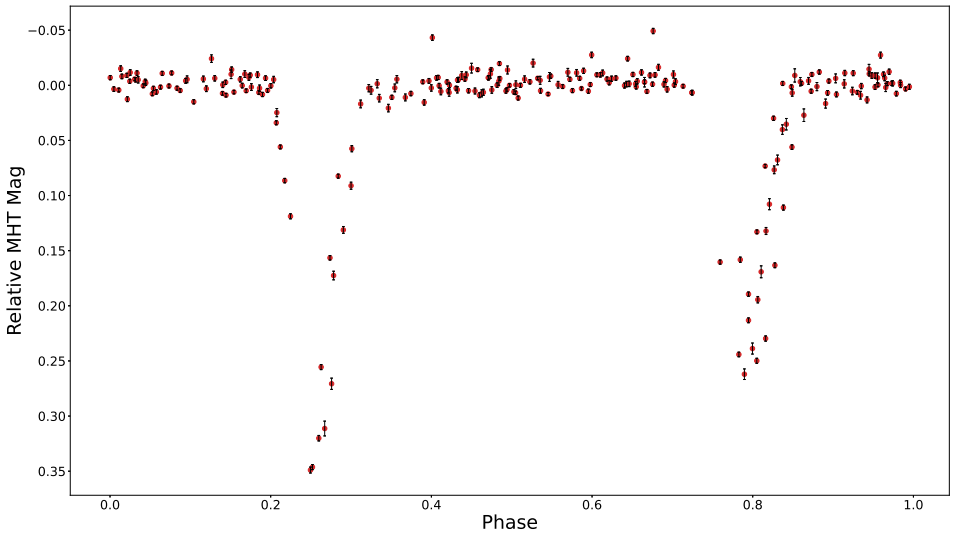

Figure 4.5: *The phase curve of MHT 0012088 (MOI 4), phased over its transiting period of 1.62 d and displaying a primary transit depth of 0.35 mag.*

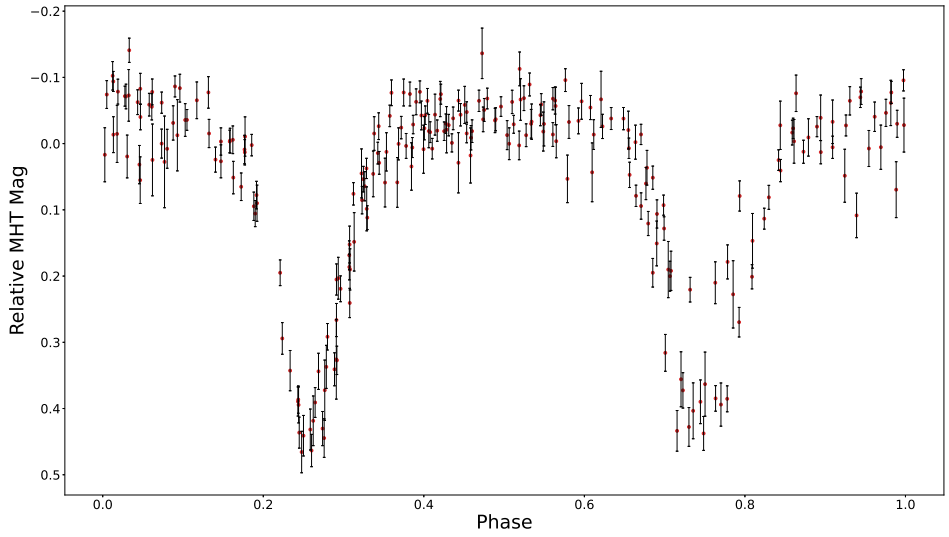

Figure 4.6: *The phase curve of MHT 0015294 (MOI 5), phased over its transiting period of 1.15 d and displaying a primary transit depth of 0.47 mag.*

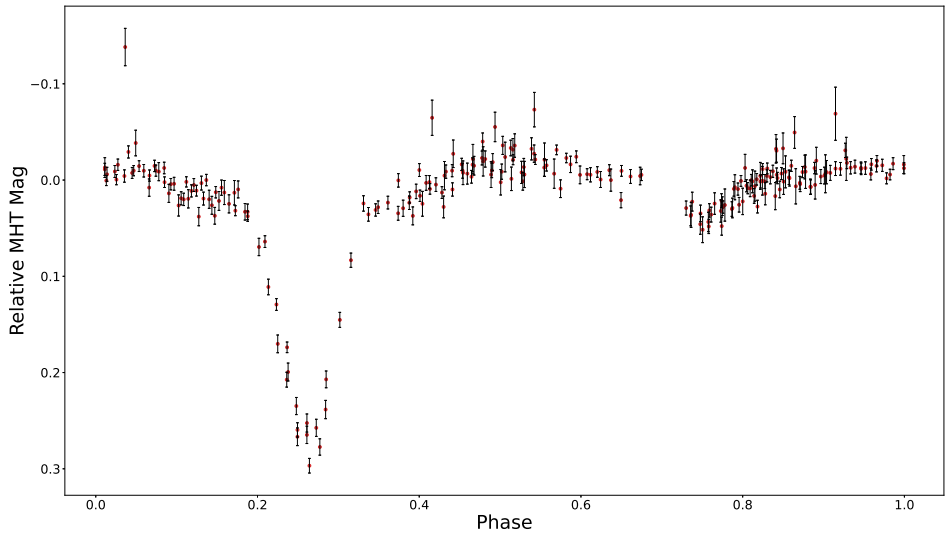

Figure 4.7: *The phase curve of MHT 0015294 (MOI 6), phased over its transiting period of 1.38 d and displaying a primary transit depth of 0.30 mag.*

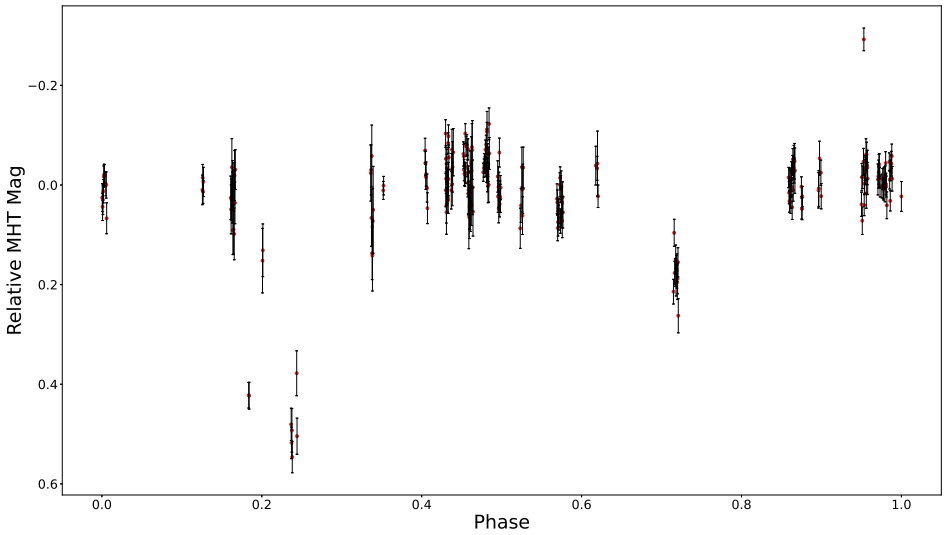

Figure 4.8: *The phase curve of MHT 0017194 (MOI 7), phased over its transiting period of 40.3 d and displaying a primary transit depth of 0.55 mag.*

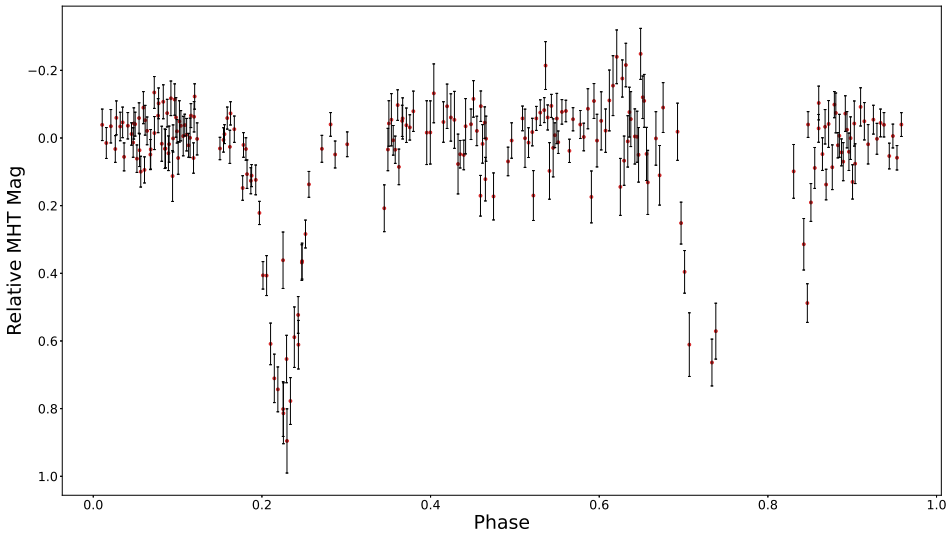

Figure 4.9: *The phase curve of MHT 0018303 (MOI 8), phased over its transiting period of 3.94 d and displaying a primary transit depth of 0.90 mag.*

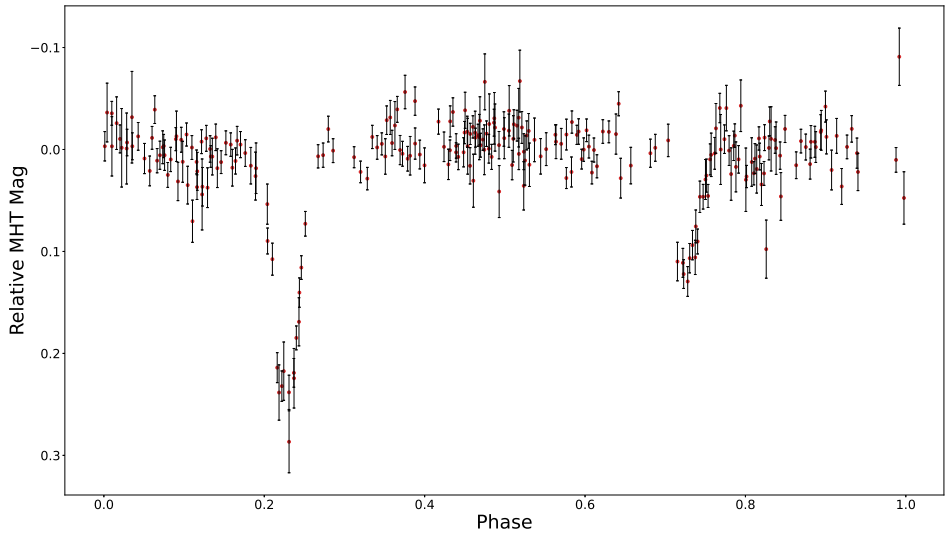

Figure 4.10: *The phase curve of MHT 0019039 (MOI 9), phased over its transiting period of 2.78 d and displaying a primary transit depth of 0.29 mag.*

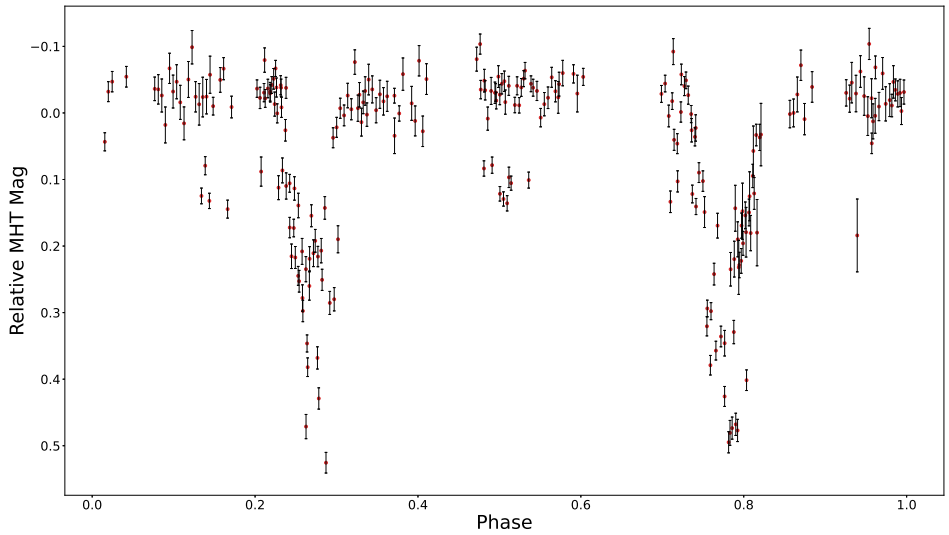

Figure 4.11: *The phase curve of MHT 0020176 (MOI 10), phased over its transiting period of 1.37 d and displaying a primary transit depth of 0.53 mag.*

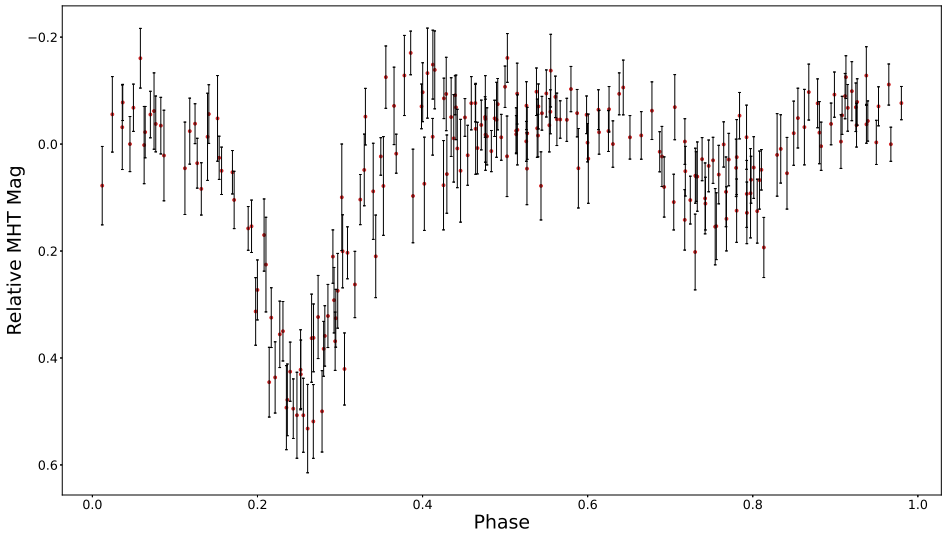

Figure 4.12: *The phase curve of MHT 0027171 (MOI 11), phased over its transiting period of 1.37 d and displaying a primary transit depth of 0.53 mag.*

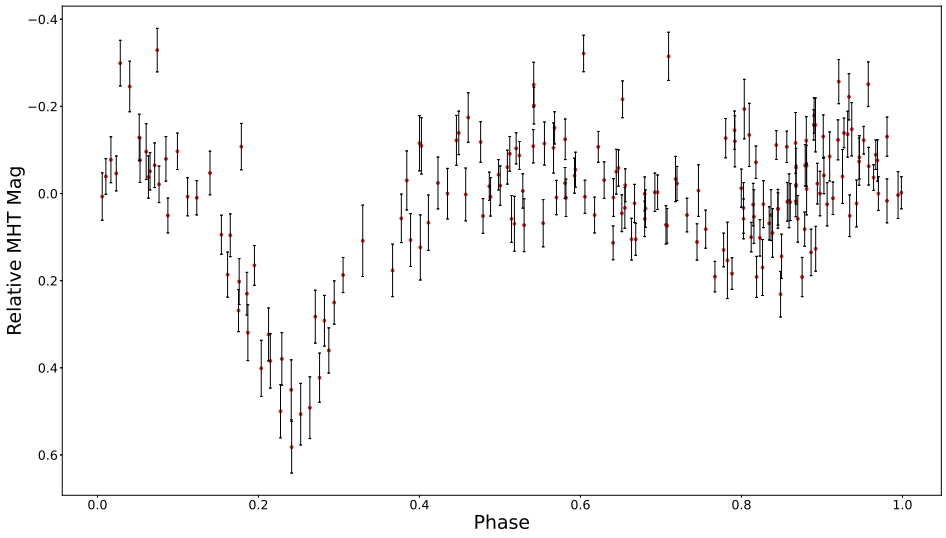

Figure 4.13: *The phase curve of MHT 0034016 (MOI 12), phased over its transiting period of 1.50 d and displaying a primary transit depth of 0.58 mag.*

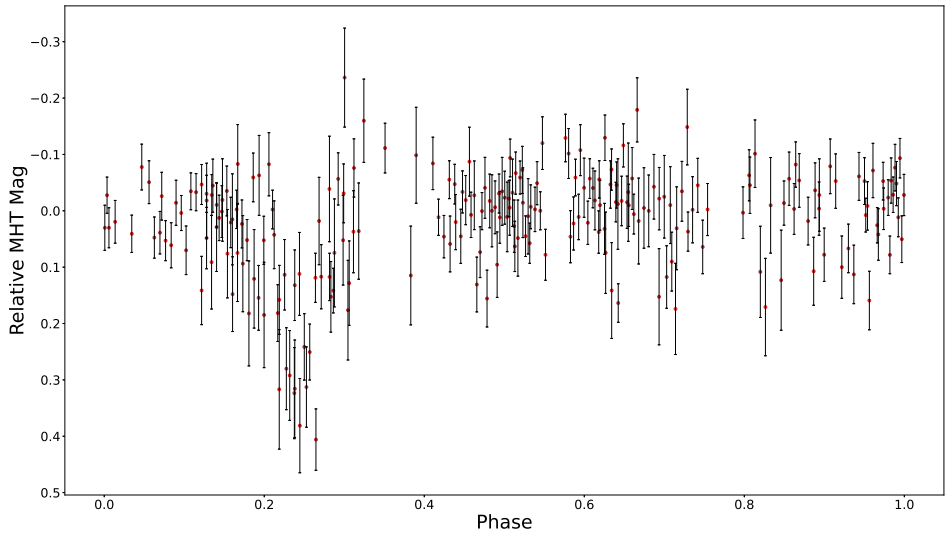

Figure 4.14: *The phase curve of MHT 0036135 (MOI 13), phased over its transiting period of 2.66 d and displaying a primary transit depth of 0.41 mag.*

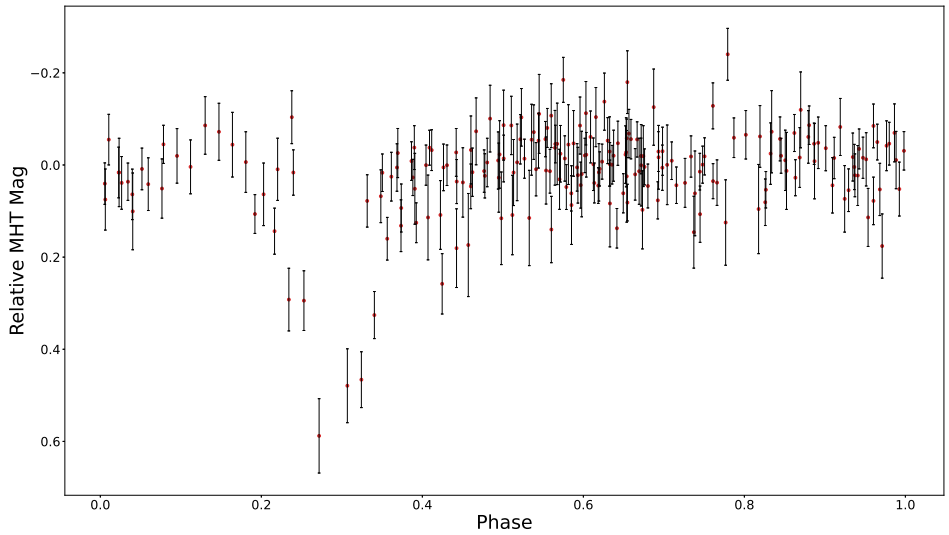

Figure 4.15: *The phase curve of MHT 0037054 (MOI 14), phased over its transiting period of 0.99 d and displaying a primary transit depth of 0.59 mag.*

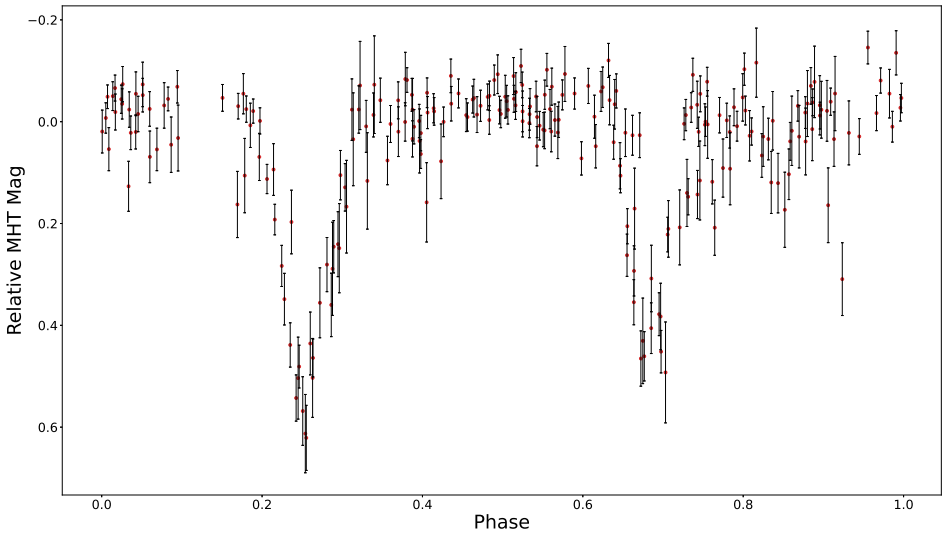

Figure 4.16: *The phase curve of MHT 0037080 (MOI 15), phased over its transiting period of 1.95 d and displaying a primary transit depth of 0.62 mag.*

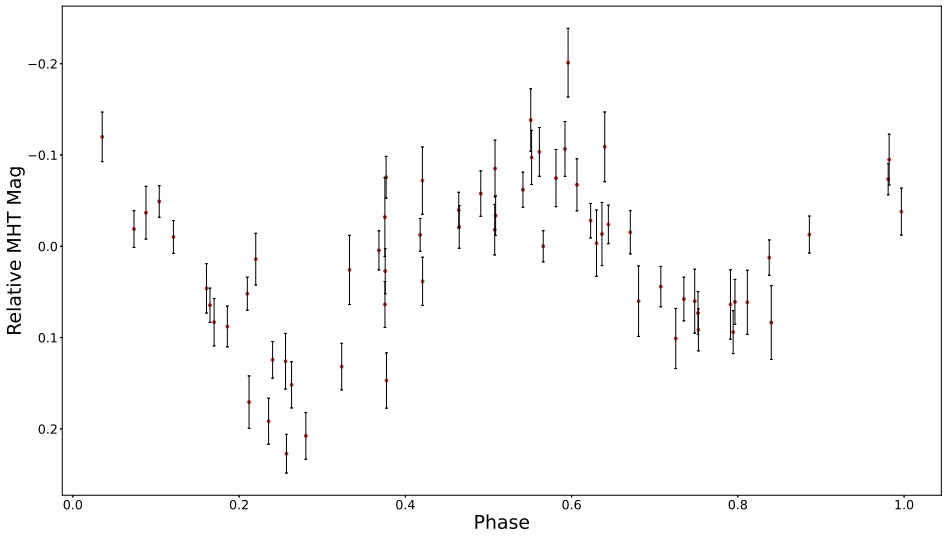

Figure 4.17: *The phase curve of MHT 0055161 (MOI 16), phased over its transiting period of 0.39 d and displaying a primary transit depth of 0.23 mag.*

4.7 Discussion

Figures 4.2 to 4.17 illustrate that transiting objects can easily be observed by the MHT. Table 4.1 reveals that only two of the MOIs have SIMBAD entries, with just one categorised as variable-candidate: hence, all transit events listed have to potential to be new discoveries. The MOIs were then cross-referenced against TESS data, for a comparison between the TESS light curves and the MOSES light curves now that TESS has observed the MOSES field. However, no short cadence data are available yet (only the 1800 s FFIs).

When inspecting the depth of the transits of all the MOIs, all exhibit much deeper depths than would be expected from companions of a planetary nature — orders of magnitude deeper. Therefore, it must be suspected that all companions are stellar: all MOI systems are most likely to be binary star systems, with either fainter companions where shallower secondary transits exists, or identical companions for systems with identically-deep transit depths. However, this result is not unexpected: the approach we took would *only* be sensitive to brown dwarf-esque transits as we were looking for $>7\sigma$ detections. Planet-sized transit are far, far smaller and are lost in the scatter of the data. It was not known at the beginning of this work what quality the data would have.

The stellar-nature conclusion can be drawn when studying the transit widths of several of the MOIs as well: in Figure 4.8, for example, the transit widths are up to days-long — much wider than would be expected for anything of a planetary size, which transit on average between three and four hours. However it must be noted that some extreme systems do exist, with the longest exoplanet transit lasting $\sim$12 hours (Hébrard et al., 2010), but such cases are rare. Furthermore, whilst there is an overlap between the widest transits and shortest-period intrinsically-variable stars (widest transit is over one day and shortest pulsation period is 6.5 hours), there is a dichotomy between the two classes of object: the short-period variables show

sinusoidal and saw-tooth shapes in their phase curves, opposed to the characteristic transit shapes that are sought after in this work. Thus, they can be easily separated apart.

The shape of the transits in Figures 4.2 to 4.17 are more akin to stellar transits too, with distinct "V"-shaped transits visible throughout. Yet, one MOI appears to be a mono-transit: MOI 2 (Figure 4.3). With the lack of a secondary transit visible in this phase curve, two inferences can be made: it could be that the transiting companion is much dimmer than the primary star, so potentially of brown-dwarf nature — but with a 0.27 mag transit depth, far larger than anything planetary; or the companion could be on a highly eccentric orbit, with the orientation such that we do not see the secondary eclipse.

Hence: the MHT data is good; it shows transiting objects clearly, but the data is not of the precision required to extract high-quality information about the MOI systems.

4.7.1 Future Upgrades

In Figure 4.1, a colour-coding or numbered-labelling system routine could be to included, to identify each of the MOIs above a certain σ profile and allow them to be cross-referenced in a table such as Tables 4.1.

A future upgrade that *is* happening is that Alston Observatory has installed a dedicated planet-hunter telescope: a PlaneWave™ Instruments DeltaRho350: the Isabella Holden Telescope (IHT). It is slightly smaller than the MHT — 35 cm (14 in) aperture — but is accessible via remote observing.

The current cadence of observations is too poor and not well-suited for finding short-term variability. In addition, there was a random nature of observing nights and lengths due to weather limitations, and the 16-tile cycle rather than hammering 1 tile per-night reduced cadences further. With a fully robotic dome and the IHT,

future campaigns of MOSES will yield data with a higher cadence of observations that will lead to better sampling over an ever increasing timebase.

4.8 Conclusions

Out of 98,580 stars observed during the initial campaign of MOSES, 754 were flagged to be of a variable nature with a confidence of $>7\sigma$. A manual search extracted only the transiting objects — rather than the intrinsically-variable stars — and designated each as a unique MOI. This list was compiled in Table 4.1, which now forms the standard naming convention for these stars that should be used in all future studies.

As evidence to support the claim made in § 4.7 — that: "*The MHT data is good; it shows transiting objects clearly, but the data is not of the precision required to extract high-quality information about the MOI systems.*" — a non-$>7\sigma$ transiting object that *did* have short-cadence TESS data was studied.

Figure 4.18 displays the phase curve of MHT 0004464 (between a 3σ and 4σ detection), and Figure 4.19 is the corresponding TESS data for this star (TIC 458879750) — this star also has the designation TYC 4050-2830-1, but no previous variability work has been published. Overlaying the two in phase provides evidence that the MOSES data is capable of detecting transiting objects, but emphasises that the quality of said data is not nearly at the standard required for this work. As mentioned above (due to the approach taken in this work) all detected-transits are of stellar nature, and MHT 0004464 proves that transits in lower-sigma detections get lost in the scatter and noise of the data. As such, we ruled out a ground-based observing approach: we left MOSES and turned to space-based observing with TESS.

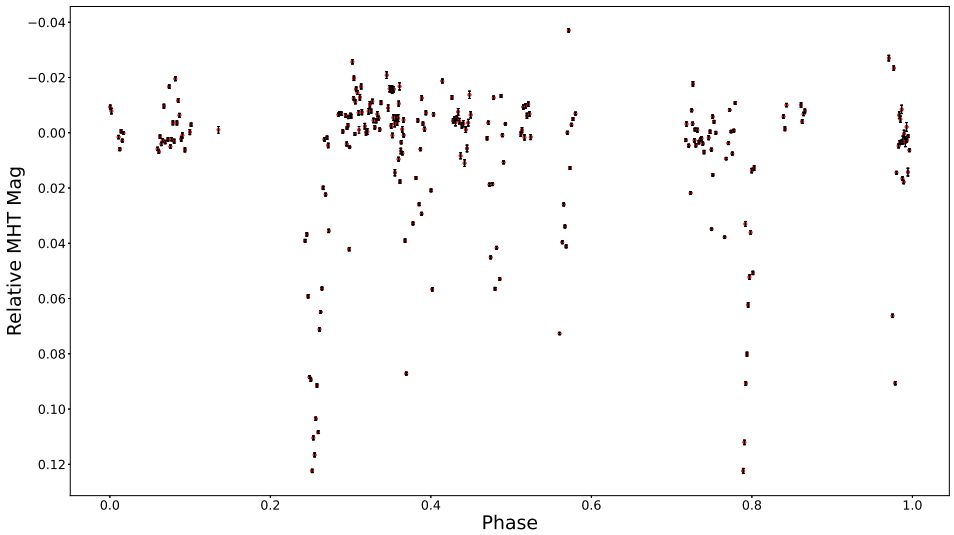

Figure 4.18: *The MHT phase curve of MHT 0004462.*

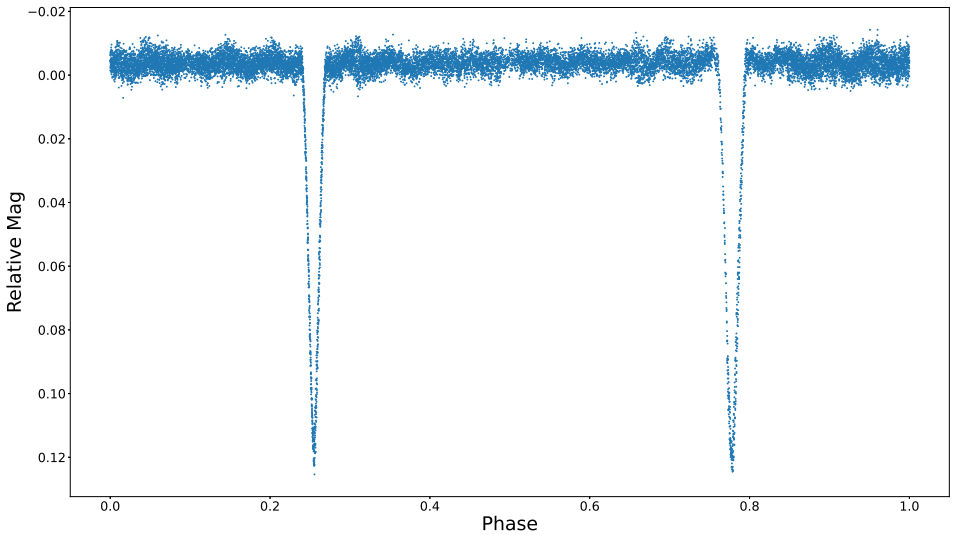

Figure 4.19: *The TESS phase curve of the same star, here designated TIC 458879750.*

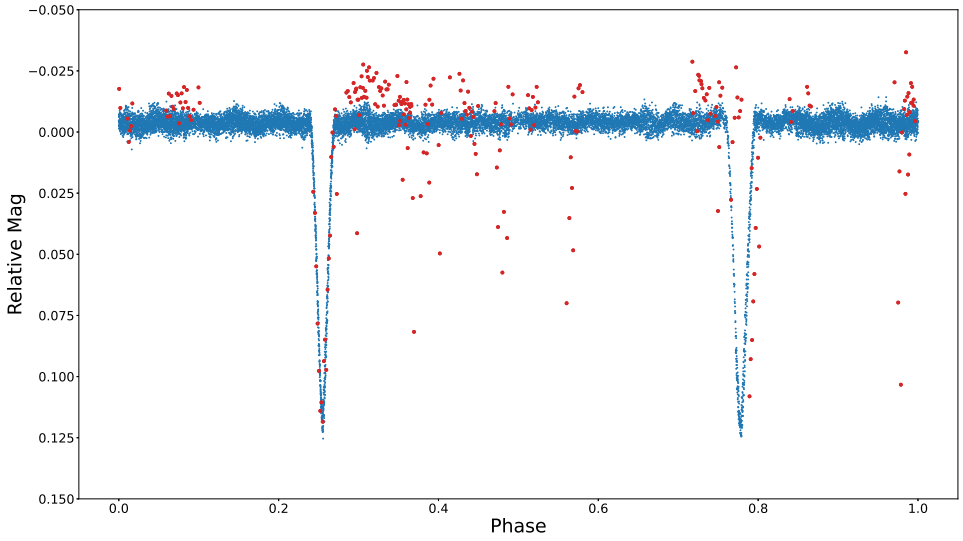

Figure 4.20: *The MHT and TESS phase curves from Figures 4.18 and 4.19 overlaid (without MHT error bars for clarity), showing the two curves match up exactly and highlighting the difference in the quality between the two data sets.*

Chapter 5

The TIC 409934330 (HD 189995) System

5.1 Introduction: Nomenclature

This Chapter contains in-depth scientific analysis of a star observed during the TESS primary mission, flagged as TOI 1114.01. Its TESS designation is TIC 409934330, which will be used throughout this Chapter. It must be stressed that even though TIC 409934330 has been observed historically, the star has not been previously targeted, studied, or published with any exoplanetary or asteroseismic themes. That is to say: TIC 409934330 is a known star so is not a new discovery here, but the work done in this Chapter and to be published in Ebo et al. (a) (in prep) is entirely new and contains wholly original contributions to the aforementioned fields.

5.2 Previous Observations of TIC 409934330

TIC 409934330 was first catalogued by Henry Draper over 130 years ago, receiving its maiden designation of HD 189995 (Pickering, 1890; Maury & Pickering, 1897),

followed closely by observations from Cordoba Observatory (The Argentine National Observatory) by Thome (1892) who gave the designation CD-71 1603. But TIC 409934330 was not observed scientifically until 1975 (Houk & Cowley, 1975), which produced the star's still-accepted spectral type of A2mA4. In 1991, Renson, Gerbaldi & Catalano (1991) first classified TIC 409934330 as both an A-Type and Am star, designated "Renson 52720" — and it was later catalogued as binary, by Hartkopf et al. (1993), with further double star work added by Fabricius & Makarov (2000) and Horch et al. (2001) a decade later. This epoch also gave the accepted values of the Johnson B and V magnitudes of 8.17 ± 0.01 and 8.00 ± 0.01, respectively (Høg et al., 2000), followed by the accepted values of the J, H and K magnitudes as 7.575 ± 0.023, 7.532 ± 0.024 and 7.523 ± 0.018, respectively, in 2003 (Cutri et al., 2003). Four years later, the accepted values for parallax, proper motion and ICRS coordinates of 4.14 ± 0.99 mas, 4.50 ± 0.84 mas N 11.39 ± 0.72 mas E, and 20:08:35.44 ($\pm$ 00:00:00.01) -71:33:08.95 ($\pm$ 00:00:00.06), respectively (van Leeuwen, 2007). In 2007, Renson & Manfroid (2009) once again included TIC 409934330 in their updated A-Type and Am star catalogue, and in 2012 the star was studied during a revisit to the Hipparcos survey, earning it another designation: HIP 99227 (McDonald, Zijlstra & Boyer, 2012). Most recently, the star's binarity was studied by *Gaia* (Kervella et al., 2019), and after being flagged from TESS mission data as a Tess Object of Interest (TOI 1114.01) by the NASA Ames Research Centre's Science Processing Operations Center (SPOC) pipeline in that same year (see Appendix F), it was further vetted as a TOI by the **TRICERATOPS**[1] team in 2021 (Giacalone et al., 2021). The most recent works are by Kervella, Arenou & Thévenin (2022) and Paunzen (2022), who investigated TIC 409934330's stellar parameters.

Table 5.1 contains the complete list of all different designations for TIC 409934330, invested from all previous surveys. All stellar parameters can be found in Table 5.3.

[1]**T**ool for **R**ating **I**nteresting **C**andidate **E**xoplanets and **R**eliability **A**nalysis of **T**ransits **O**riginating from **P**roximate **S**tars

Table 5.1: *All designations for TIC 409934330 from historic observations.*

Survey	Designation	Reference(s)
Catalogue of Components of Double and Multiple Stars (CCDM)	CCDM J20086-7133AB	(Dommanget, 1983) (Dommanget & Nys, 1994)
SIMBAD Class "**"	** I 1042	URL: cds.unistra.fr
—"—	** I 1042AB	—"—
Cordoba Observatory, Durchmusterung (CD)	CD-71 1603	(Thome, 1892) (Thome, 1894) (Thome, 1900) (Thome, 1914) (Perrine, 1932)
Cape Observatory, Photographic catalogue (CPC)	CPC 21.1 3895	(Jackson & Stoy, 1954) (Jackson & Stoy, 1955a) (Jackson & Stoy, 1955b) (Jackson & Stoy, 1958) (Stoy, 1966) (Stoy, 1968)
Cape Observatory, Photographic Durchmusterung (CPD)	CPD-7 2537	(Gill & Kapteyn, 1896) (Gill & Kapteyn, 1897) (Gill & Kapteyn, 1900) (Gill, 1903)
—"—	CPD-71 2537A	—"—
General catalogue (GC)	GC 27874	(Boss, 1937)
Guide Star catalogue (GSC)	GSC 09315-01865	(Lasker et al., 1990) (Russell et al., 1990) (Jenkner et al., 1990) (Lasker & et al., 1990) (Morrison et al., 2001)

Henry Draper (HD)	HD 189995	(Pickering, 1890) (Maury & Pickering, 1897) (Cannon & Pickering, 1918) (Cannon, 1925a) (Cannon, 1925b) (Cannon, 1927) (Cannon, 1928) (Cannon, 1931) (Cannon, 1936) (Cannon & Mayall, 1949) (Roeser, Bastian & Wiese, 1991) (Nesterov et al., 1995)
Hipparcos Input Catalogue (HIC)	HIC 99227	(Turon et al., 1992) (Turon et al., 1993)
Hipparcos Catalogue (HIP)	HIP 99227	(van Leeuwen, 2007)
Index catalogue of Double Stars (IDS)	IDS 19577-7150 AB	(Jeffers, van den Bos & Greeby, 1963)
2Micron All-Sky Survey (2MASS)	2MASS J20083548-7133088	(Cutri et al., 2003)
Position and Proper Motion (PPM)	PPM 374515	(Röeser & Bastian, 1988) (Röser, Bastian & Kuzmin, 1994)
Renson	Renson 52720	(Renson, Gerbaldi & Catalano, 1991) (Renson & Manfroid, 2009)
Smithsonian Astrophysical Observatory (SAO)	SAO 257778	(Haramundanis, 1967)
TESS Input catalogue (TIC)	TIC 409934330	(Stassun et al., 2018) (Stassun et al., 2019)
Tycho mission (TYC)	TYC 9315-1865-1	(ESA, 1997) (Høg et al., 2000)
Washington University, Double Stars (WDS)	WDS J20086-7133AB	(Worley & Douglass, 1997) (Mason et al., 2001)

5.3 TESS Observations of TIC 409934330

TIC 409934330 has been observed twice by TESS, with one future observation planned for July 2023. Table 5.2 lists the Sectors that TIC 409934330 was observed in — with the respective dates — alongside which Camera and CCD the star appeared in, and what cadence of data is available. Table 5.3 lists the initial parameters known for TIC 409934330; the information in Table 5.2 was extracted from the TESS Asteroseismic Science Operations Center (TASOC)[2], and the data populating Table 5.3 were taken from the TESS Input Catalogue (TIC; Guerrero et al., 2021) and the SIMBAD database.

Table 5.2: *The TESS observations of TIC 409934330, listing the Sectors, Cameras and CCDs that the star appeared in, alongside the respective dates of each observation and the available cadences of the data. The information in this Table was retrieved from the TASOC.*

Sector	Start (UTC)	End (UTC)	Camera	CCD	Available Cadences (sec)
13	19/06/19	18/07/19	2	2	120
27	04/07/20	30/07/20	2	1	20, 120
67	01/07/23	29/07/23	2	1	—

Figure 5.1 shows the light curve of TIC 409934330 created from the data taken during Sector 13. It was not the raw data used in the light curve, but the publicly-available reduced data that had been processed through the TESS SPOC pipeline (see Appendix F). When studying Figure 5.1 it becomes apparent that TIC 409934330 hosts a transiting object: across the 27-d timebase, 10 equally-spaced periodic dips in the light curve can be seen. The cause of equally-spaced dips in a star's light curve is due to the presence of a companion blocking out a fraction of star light as it transits across the star from an observer's point-of-view, repeating once per orbit. The 10 dips in Figure 5.1 are very clearly equally spaced, and hence TIC 409934330

[2]https://tasoc.dk

Table 5.3: *Prior-known stellar properties and parameters of TIC 409934330, gathered from the TIC and the SIMBAD database, indicated by* † *and* ††*, respectively. Data marked with* ‡ *were identical in both databases. References from the SIMBAD-retrieved data can be found in § 5.2. The parameters log(g), [Fe/H] and U Mag are omitted as no such data could be retrieved. For the two values of B and V Mag, the more recent TIC values were used in this work.*

Parameter	Value
Right Ascension	20 08 35.441‡
Declination	-71 33 08.99‡
Spectral Type	A2mA4‡
Star Classification	(Not previously known)
T_{eff} (K)	$8050 \pm 160^{\dagger}$
B Mag	$8.02^{\dagger}$ / $8.17^{\dagger\dagger}$
V Mag	$7.89^{\dagger}$ / $8.00^{\dagger\dagger}$
R Mag	$7.91^{\dagger\dagger}$
I Mag	$7.97^{\dagger\dagger}$
J Mag	7.58‡
H Mag	7.53‡
K Mag	7.52‡
Gaia Mag	$8.21^{\dagger}$
T Mag	$8.11^{\dagger}$
Parallax (mas)	$4.02 \pm 1.41^{\dagger}$

was entered into the TOI catalogue as TOI-1114, and the newly flagged planet-candidate was designated TOI-1114.01.

By studying the equal spacing of the dips, one can making an assumption of there being an extra dip in the centre of the light curve (at JD ≈2458668), visible were the data-download gap not there. From this visual information, a first approximation of the orbital period of this planet-candidate can be made by dividing the *11* transits by the 27-day timebase: $P \approx (27/11) \approx 2.5\,\text{d}$.

There is more to TIC 409934330 than it just being a potential host star, however. Conventionally, the depth of a transit-induced dip in a light curve remains constant over time. This is intelligible, as the depth of the dip is a direct measurement of the ratio between the radius of the companion and the radius of the host star, both

of which typically remain constant. Yet, when studying the transit depths in Figure 5.1, no two are the same. This indicates that either the radius of the companion is changing over time, or the radius of the star. A companion can lose or gain mass throughout its lifetime, but it is very unrealistic for this to be occurring by so much on this time scale. Furthermore, the out-of-transit sections of the light curve show variance over time, rather than a smooth "constant" signal. In consequence, it must be that TIC 409934330 itself is varying in size over short time periods, and is therefore a pulsating star. Not only this, but a pulsating-host star, therefore both star and companion exist as an example of a rare type of system.

To discover the pulsational nature of TIC 409934330, a Fourier transform of the light curve in Figure 5.1 was generated — shown in Figure 5.2 — revealing the frequencies of pulsation that TIC 409934330 exhibits (see § 1.1.2 for discussions on Fourier transforms of light curves). The lowest-frequency peak is frequency of the orbital period of the companion, and the following equally-spaced cascade of peaks are its harmonics. The remaining central "block" (18-35 c/d) of high-amplitude peaks are signatures of δ Scuti pulsations, so we conclude that TIC 409934330 is a δ Scuti star: Figure 5.3 shows only δ Scuti pulsations once the orbital frequency and harmonics has been removed.

The 1st harmonic exhibits a higher amplitude than that of the orbital period frequency due to the combination of the primary and secondary transits constructively interfering, hence it appears at exactly twice the frequency of the orbital period. This occurs for all harmonics, but with reduced power and hence lower amplitudes with increasing frequency.

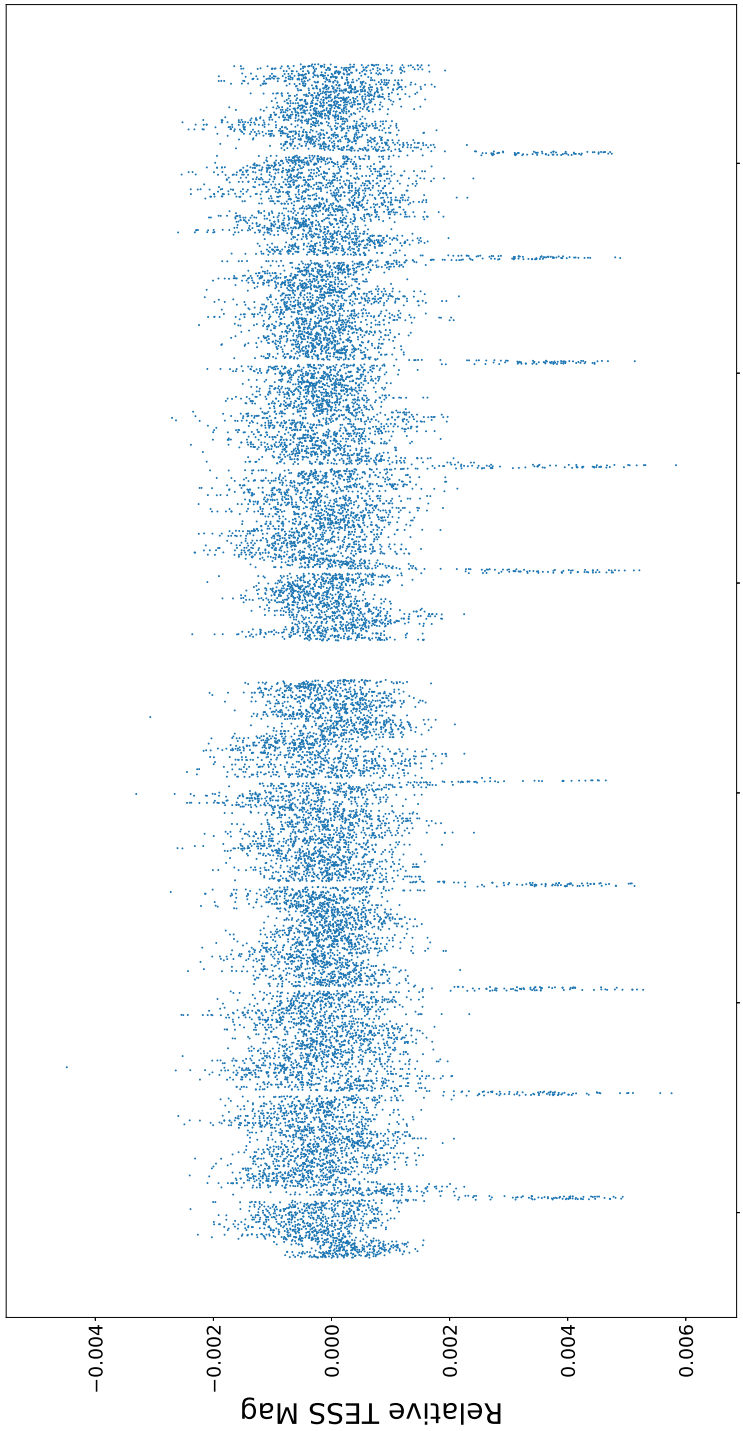

Figure 5.1: *The light curve of TIC 409934330, constructed using data taken from TESS observations during Sector 13.*

Figure 5.2: *The Fourier transform of the light curve in Figure 5.1. The orbital frequency of the companion and following cascade of harmonics are the low-frequency peaks at <10 c/d. Classical δ Scuti pulsations can be see between 18-35 c/d.*

Figure 5.3: *The same Fourier transform as Figure 5.2, but with the orbital frequency and its harmonics removed revealing only δ Scuti pulsations.*

5.4 Modelling the Host Star

5.4.1 Pre-Main Sequence Models

The software MESA (see § 3.1 Paxton et al., 2011, 2013, 2015, 2018, 2019) was used to build a grid of stellar models. There were two sections of evolution for each model star: a pre-main sequence evolution up to the ZAMS, and a main sequence evolution tending towards the TAMS. The reason for separating each evolutionary run across the ZAMS was that MESA cannot incorporate stellar rotation across one complete evolution, leading to incorrect models (see § 3.1.4.2 for a more empirical example and explanation of this). The pre-main sequence models were constructed first: within the inlists of each the flags for the necessary evolution physics were planted, such as the '`dedt`' energy equations (see § 3.1), and the "stop" flag that ensured the model star would not cross the ZAMS. Altering these pre-main sequence inlists is rather limited, due to the evolution being almost fully hard-coded into MESA itself. However, the one parameter that it was necessary to change was mass.

It would have been inefficient to create pre-main sequence models for the entire stellar mass range of the HR diagram. Furthermore, most of the models would not have been useful due to the limited range of masses a star of this spectral type can have. Instead, a suitable mass range was calculated via several different iterations of calculation, based on the errors of some of TIC 409934330's parameters such as parallax and $T_{\rm eff}$. The mass-luminosity relationship was the crux of these calculations and was used to obtain two extreme values of stellar mass for TIC 409934330, and hence a mass range for the pre-main sequence models. Equation 5.1 states the generally-accepted mass-luminosity relationship (Duric, 2004; Salaris & Cassisi, 2005):

$$\frac{L}{\mathrm{L}_\odot} = x \left(\frac{M}{\mathrm{M}_\odot} \right)^a \tag{5.1}$$

The parameters $\boldsymbol{x}$ and $\boldsymbol{a}$ in Equation 5.1 change depending on stellar mass. Table 5.4 lists the values that $\boldsymbol{x}$ and $\boldsymbol{a}$ take, for given stellar mass ranges (Duric, 2004; Salaris & Cassisi, 2005).

Table 5.4: *The mass-luminosity relationship in Equation 5.1 changes form depending on stellar mass. This Table lists the different values that* $\boldsymbol{x}$ *and* $\boldsymbol{a}$ *take, and their respective stellar mass thresholds (Duric, 2004; Salaris & Cassisi, 2005).*

x value	a value	Mass Range
0.23	2.3	$M_* < 0.43\,\mathrm{M}_\odot$
1	4	$0.43\,\mathrm{M}_\odot < M_* < 2\,\mathrm{M}_\odot$
1.4	3.5	$2\,\mathrm{M}_\odot < M_* < 55\,\mathrm{M}_\odot$
32000	1	$M_* > 55\,\mathrm{M}_\odot$

It is known that the some A-type stars straddle the $2\,\mathrm{M}_\odot$ boundary (Pecaut & Mamajek, 2013), and with TIC 409934330 having a mixed spectral type of A2mA4 it is important that its mass is calculated correctly.

Following the work of Pecaut & Mamajek (2013), who tabulated the average mass and T_{eff} for stars of every spectral type, an average A2 star has a mass of $1.98\,\mathrm{M}_\odot$, and $1.93\,\mathrm{M}_\odot$ for an A4-type. But with the TIC-determined T_{eff} of 8050 ± 160 K (Guerrero et al., 2021), the spectral type of TIC 409934330 would be more on the order of ≈A5, suggesting a mass of $1.88\,\mathrm{M}_\odot$. However, it is important to remember that any or all of these database-retrieved parameters may be incorrect. Therefore, with the stellar mass of TIC 409934330 potentially lying so close to a boundary between two different forms of the mass-luminosity relationship, two different versions of Equation 5.1 were used in the following calculations, employing the parameters in rows 2 and 3 in Table 5.4, respectively. Equations 5.2 and 5.3 show these two versions of the mass-luminosity relationship, accounting for below and above the $2.0\,\mathrm{M}_\odot$ boundary, respectively (Duric, 2004; Salaris & Cassisi, 2005):

$$\frac{L}{\mathrm{L}_\odot} = \left(\frac{M}{\mathrm{M}_\odot}\right)^4 \qquad \text{for } M < 2\mathrm{M}_\odot \tag{5.2}$$

$$\frac{L}{\mathrm{L}_\odot} \approx 1.4\left(\frac{M}{\mathrm{M}_\odot}\right)^{3.5} \qquad \text{for } M \geq 2\mathrm{M}_\odot \tag{5.3}$$

The strategy for calculating the mass ranges also embodied the astrophysical thickness that the main sequence track exhibits across the HR diagram, from the works of Fernandes, Lebreton & Baglin (1996) and Lebreton et al. (1997). This hence lead to an error in magnitude for TIC 409934330.

All calculated mass ranges, using the various methods described above, had their respective errors propagated through the different versions of the mass-luminosity relationship (Equations 5.2 and 5.3) to determine the maximum and minimum value of stellar mass — and hence a mass range — for each method. All results are listed in Table 5.5. The calculations are shown in the following pages.

5.4.1.1 The Error in Parallax

Parallax was the first parameter used as its error leads to a change in the brightness of a star, and hence the determined luminosity.

Table 5.3 lists the value of parallax taken from the updated Hipparcos survey as 4.02 ± 1.41 mas (van Leeuwen, 2007); the two extremes of which were hence taken as 2.61 mas and 5.43 mas. With these two values, two sets of calculations were performed in parallel.

First, the inverse of the parallaxes (in arcsecs) were taken to obtain distances (in parsecs) using Equation 5.4:

$$d\,(\mathrm{pc}) = \frac{1}{\mathrm{parallax}\,('')} \tag{5.4}$$

The distance values were then used to calculate the two values for the absolute magnitude of TIC 409934330, M_*, utilising the visual TIC magnitude value of V Mag in Table 5.3, m, employing a slightly rearranged version of the distance modulus equation, with the Torres (2010) bolometric correction (BC_V) included, given as Equation 5.5:

$$M_* = m - 5\log(d) + 5 + BC_V \tag{5.5}$$

Following this, the calculated absolute magnitudes were transformed into luminosities (in terms of Solar luminosity), via Equation 5.6:

$$\frac{L}{\mathrm{L}_\odot} = 2.51^{\mathrm{M}_\odot - M_*} \tag{5.6}$$

Below shows the full workings, in two columns for both the minimum and maximum values of each term. The final mass values have been calculated twice, first employing Equation 5.2 and then Equation 5.3.

$\text{parallax}_{\text{min}} = 2.61 \times 10^{-3''}$

$$d_{\text{min}} = \frac{1}{5.43 \times 10^{-3''}}$$

$$\therefore d_{\text{min}} = 184.16\,\text{pc}$$

$$(M_V)_{\text{min}} = 7.89 - 5\log(184.16) + 5 - 0.02$$

$$\therefore (M_V)_{\text{min}} = 1.54$$

$\text{parallax}_{\text{max}} = 5.43 \times 10^{-3''}$

$$d_{\text{max}} = \frac{1}{2.61 \times 10^{-3''}}$$

$$\therefore d_{\text{min}} = 383.14\text{pc}$$

$$(M_V)_{\text{max}} = 7.89 - 5\log(383.14) + 5 - 0.02$$

$$\therefore (M_V)_{\text{max}} = -0.05$$

$$\left(\frac{L}{\mathrm{L}_\odot}\right)_{\min} = 2.51^{(4.83-1.54)} \qquad \left(\frac{L}{\mathrm{L}_\odot}\right)_{\max} = 2.51^{(4.83+0.05)}$$
$$\therefore \left(\frac{L}{\mathrm{L}_\odot}\right)_{\min} = 20.65\,\mathrm{L}_\odot \qquad \therefore \left(\frac{L}{\mathrm{L}_\odot}\right)_{\max} = 89.21\,\mathrm{L}_\odot$$

Equation 5.2 :

$$\left(\frac{M}{\mathrm{M}_\odot}\right)_{\min} = 20.65^{\frac{1}{4}} \qquad \left(\frac{M}{\mathrm{M}_\odot}\right)_{\max} = 89.21^{\frac{1}{4}}$$
$$\therefore \left(\frac{M}{\mathrm{M}_\odot}\right)_{\min} = 2.13\,\mathrm{M}_\odot \qquad \therefore \left(\frac{M}{\mathrm{M}_\odot}\right)_{\max} = \mathbf{3.07\,M_\odot}$$

Equation 5.3 :

$$\left(\frac{M}{\mathrm{M}_\odot}\right)_{\min} = \frac{1}{1.4}\,(20.65)^{\frac{1}{3.5}} \qquad \left(\frac{M}{\mathrm{M}_\odot}\right)_{\max} = \frac{1}{1.4}\,(89.21)^{\frac{1}{3.5}}$$
$$\therefore \left(\frac{M}{\mathrm{M}_\odot}\right)_{\min} = \mathbf{1.70\,M_\odot} \qquad \therefore \left(\frac{M}{\mathrm{M}_\odot}\right)_{\max} = 2.58\,\mathrm{M}_\odot$$

Hence we see that the two forms of the mass-luminosity relations produce an overall wider mass range than each would give separately. Therefore the total mass uncertainty from these causes is $1.69 \leq \mathrm{M}_\odot \leq 3.07$, emphasised in bold in the above calculations. These masses are listed with the other calculated mass ranges in Table 5.5.

5.4.1.2 The Effect of the Main Sequence Width

The track that the main sequence cuts across the HR diagram is not infinitesimally thin. It exhibits a physical width, inducing a small but non-trivial error on the brightness of main sequence stars: their position on the main sequence path is not an absolute position, but instead stars lie within a narrow window on the HR diagram, constrained by the thickness of the main sequence.

In a diagram of M_V vs. $B-V$, Fernandes, Lebreton & Baglin (1996) state a main sequence width of $M_V \approx 0.55$, hence an absolute magnitude error of approximately $M_V \pm 0.275$. In similar work to Fernandes, Lebreton & Baglin (1996), Lebreton et al. (1997) also state that in a M_V vs $B-V$ HR diagram, the main sequence has a physical width. They provide two estimates of the width size: $M_V \approx 0.25$ and $M_V \approx 0.45$, observationally and theoretically respectively. Both of the Lebreton et al. (1997) estimates will be used in the calculations, to make an argument on whether the observational or theoretical estimate is more likely to be astrophysically correct. The two error estimates can be taken as two respective absolute magnitude errors of approximately $M_V \pm 0.125$ and approximately $M_V \pm 0.225$.

To use the above absolute magnitude errors to find mass ranges, the same methods were followed as when calculating the mass range based on the parallax error in § 5.4.1.1, but this time including the error in M_V. Initial values of M_V were taken from § 5.4.1.1 to save recalculation. This time, with four sets of calculations, the iterations were labelled A, B, C, D until the final minimum and maximum values were known. The final mass calculations were also performed twice, accounting for the two versions of the mass-luminosity equations given as Equations 5.2 and 5.3.

Below shows all working, and the final mass range is listed with the other calculated mass ranges in Table 5.5.

(Fernandes, Lebreton & Baglin, 1996)

The same methods engaged when calculating the mass range based on the parallax error in § 5.4.1.1 were widened to include the above errors in M_V, and the initial values of M_V were taken from § 5.4.1.1, with bolometric correction included, to save recalculation. Below shows all working:

$$(M_V)_{\min} = 1.54 \qquad (M_V)_{\max} = -0.05$$

Employing an error bar of approximately $M_V \pm 0.275$:

$$\therefore (M_V)_{\mathrm{A}} = 1.265 \qquad \therefore (M_V)_{\mathrm{C}} = \mathbf{-0.325}$$
$$\therefore (M_V)_{\mathrm{B}} = \mathbf{1.815} \qquad \therefore (M_V)_{\mathrm{D}} = 0.225$$

Taking the two extremes in bold from above:

$$\left(\frac{L}{\mathrm{L}_\odot}\right)_{\mathrm{A}} = 2.51^{(4.83-1.815)} \qquad \left(\frac{L}{\mathrm{L}_\odot}\right)_{\mathrm{B}} = 2.51^{(4.83+0.325)}$$
$$\therefore \left(\frac{L}{\mathrm{L}_\odot}\right)_{\mathrm{A}} = 16.03\,\mathrm{L}_\odot \qquad \therefore \left(\frac{L}{\mathrm{L}_\odot}\right)_{\mathrm{B}} = 114.90\,\mathrm{L}_\odot$$

Equation 5.2:

$$\left(\frac{M}{\mathrm{M}_\odot}\right)_{\mathrm{A}} = 16.03^{\frac{1}{4}} \qquad \left(\frac{M}{\mathrm{M}_\odot}\right)_{\mathrm{B}} = 114.90^{\frac{1}{4}}$$
$$\therefore \left(\frac{M}{\mathrm{M}_\odot}\right)_{\mathrm{A}} = 2.00\,\mathrm{M}_\odot \qquad \therefore \left(\frac{M}{\mathrm{M}_\odot}\right)_{\mathrm{B}} = \mathbf{3.27\,M_\odot}$$

Equation 5.3:

$$\left(\frac{M}{\mathrm{M}_\odot}\right)_{\mathrm{C}} = \frac{1}{1.4}\,(16.03)^{\frac{1}{3.5}} \qquad \left(\frac{M}{\mathrm{M}_\odot}\right)_{\mathrm{D}} = \frac{1}{1.4}\,(114.90)^{\frac{1}{3.5}}$$
$$\therefore \left(\frac{M}{\mathrm{M}_\odot}\right)_{\mathrm{C}} = \mathbf{1.58\,M_\odot} \qquad \therefore \left(\frac{M}{\mathrm{M}_\odot}\right)_{\mathrm{D}} = 2.77\,\mathrm{M}_\odot$$

Hence — with their mass values amplified in bold — $\left(\frac{M}{\mathrm{M}_\odot}\right)_{\mathrm{B}}$ from the Equation 5.2 form of the mass-luminosity relation, and $\left(\frac{M}{\mathrm{M}_\odot}\right)_{\mathrm{C}}$ from the Equation 5.3 form of the mass-luminosity relation, are the $\left(\frac{M}{\mathrm{M}_\odot}\right)_{\mathrm{max}}$ and $\left(\frac{M}{\mathrm{M}_\odot}\right)_{\mathrm{min}}$ now-best mass values, respectively, and are listed with the other calculated mass ranges in Table 5.5.

(Lebreton et al., 1997)

Once again the same methods engaged when calculating the mass range based on the parallax error in § 5.4.1.1 were widened to include the above errors in M_V, and again the initial values of M_V were taken from § 5.4.1.1 to save recalculation. Below shows all working:

$$(M_V)_{\min} = 1.54 \qquad (M_V)_{\max} = -0.05$$

Employing an error bar of approximately $M_V \pm 0.125$:

$$\therefore (M_V)_{\mathrm{A}} = 1.415 \qquad \therefore (M_V)_{\mathrm{C}} = \mathbf{-0.175}$$
$$\therefore (M_V)_{\mathrm{B}} = \mathbf{1.665} \qquad \therefore (M_V)_{\mathrm{D}} = 0.075$$

Taking the two extremes in bold from above:

$$\left(\frac{L}{\mathrm{L}_\odot}\right)_{\mathrm{A}} = 2.51^{(4.83-1.665)} \qquad \left(\frac{L}{\mathrm{L}_\odot}\right)_{\mathrm{B}} = 2.51^{(4.83+0.175)}$$
$$\therefore \left(\frac{L}{\mathrm{L}_\odot}\right)_{\mathrm{A}} = 18.41\mathrm{L}_\odot \qquad \therefore \left(\frac{L}{\mathrm{L}_\odot}\right)_{\mathrm{B}} = 100.09\mathrm{L}_\odot$$

Equation 5.2:

$$\left(\frac{M}{\mathrm{M}_\odot}\right)_{\mathrm{A}} = 18.41^{\frac{1}{4}} \qquad \left(\frac{M}{\mathrm{M}_\odot}\right)_{\mathrm{B}} = 100.09^{\frac{1}{4}}$$
$$\therefore \left(\frac{M}{\mathrm{M}_\odot}\right)_{\mathrm{A}} = 2.07\,\mathrm{M}_\odot \qquad \therefore \left(\frac{M}{\mathrm{M}_\odot}\right)_{\mathrm{B}} = \mathbf{3.16\,M_\odot}$$

Equation 5.3:

$$\left(\frac{M}{\mathrm{M}_\odot}\right)_{\mathrm{C}} = \frac{1}{1.4}\,(18.41)^{\frac{1}{3.5}} \qquad \left(\frac{M}{\mathrm{M}_\odot}\right)_{\mathrm{D}} = \frac{1}{1.4}\,(100.09)^{\frac{1}{3.5}}$$
$$\therefore \left(\frac{M}{\mathrm{M}_\odot}\right)_{\mathrm{C}} = \mathbf{1.64\,M_\odot} \qquad \therefore \left(\frac{M}{\mathrm{M}_\odot}\right)_{\mathrm{D}} = 2.66\,\mathrm{M}_\odot$$

Hence — with their mass values amplified in bold — $\left(\frac{M}{\mathrm{M}_\odot}\right)_{\mathrm{B}}$ from the Equation 5.2 form of the mass-luminosity relation, and $\left(\frac{M}{\mathrm{M}_\odot}\right)_{\mathrm{C}}$ from the Equation 5.3 form of the mass-luminosity relation, are the $\left(\frac{M}{\mathrm{M}_\odot}\right)_{\mathrm{max}}$ and $\left(\frac{M}{\mathrm{M}_\odot}\right)_{\mathrm{min}}$ mass values, respectively, and are listed with the other calculated mass ranges in Table 5.5.

Employing an error bar of approximately $M_V \pm 0.225$:

$$\therefore (M_V)_{\mathrm{A}} = 1.315 \qquad \therefore (M_V)_{\mathrm{C}} = \mathbf{-0.275}$$
$$\therefore (M_V)_{\mathrm{B}} = \mathbf{1.765} \qquad \therefore (M_V)_{\mathrm{D}} = 0.175$$

Taking the two extremes in bold from above:

$$\left(\frac{L}{\mathrm{L}_\odot}\right)_{\mathrm{A}} = 2.51^{(4.83-1.765)} \qquad \left(\frac{L}{\mathrm{L}_\odot}\right)_{\mathrm{B}} = 2.51^{(4.83+0.275)}$$
$$\therefore \left(\frac{L}{\mathrm{L}_\odot}\right)_{\mathrm{A}} = 16.79\mathrm{L}_\odot \qquad \therefore \left(\frac{L}{\mathrm{L}_\odot}\right)_{\mathrm{B}} = 109.73\mathrm{L}_\odot$$

Equation 5.2:

$$\left(\frac{M}{\mathrm{M}_\odot}\right)_{\mathrm{A}} = 16.79^{\frac{1}{4}} \qquad \left(\frac{M}{\mathrm{M}_\odot}\right)_{\mathrm{B}} = 109.73^{\frac{1}{4}}$$
$$\therefore \left(\frac{M}{\mathrm{M}_\odot}\right)_{\mathrm{A}} = 2.02\,\mathrm{M}_\odot \qquad \therefore \left(\frac{M}{\mathrm{M}_\odot}\right)_{\mathrm{B}} = \mathbf{3.24\,M_\odot}$$

Equation 5.3:

$$\left(\frac{M}{\mathrm{M}_\odot}\right)_{\mathrm{C}} = \frac{1}{1.4}\,(16.79)^{\frac{1}{3.5}} \qquad \left(\frac{M}{\mathrm{M}_\odot}\right)_{\mathrm{D}} = \frac{1}{1.4}\,(109.73)^{\frac{1}{3.5}}$$

$$\therefore \left(\frac{M}{\mathrm{M}_\odot}\right)_{\mathrm{C}} = \mathbf{1.60\,M_\odot} \qquad \therefore \left(\frac{M}{\mathrm{M}_\odot}\right)_{\mathrm{D}} = 2.73\,\mathrm{M}_\odot$$

Hence — with their mass values amplified in bold — $\left(\frac{M}{\mathrm{M}_\odot}\right)_{\mathrm{B}}$ from the Equation 5.2 form of the mass-luminosity relation, and $\left(\frac{M}{\mathrm{M}_\odot}\right)_{\mathrm{C}}$ from the Equation 5.3 form of the mass-luminosity relation, are the $\left(\frac{M}{\mathrm{M}_\odot}\right)_{\mathrm{max}}$ and $\left(\frac{M}{\mathrm{M}_\odot}\right)_{\mathrm{min}}$ mass values, respectively, and are listed with the other calculated mass ranges in Table 5.5.

5.4.1.3 The Error in T_{eff}

However, T_{eff} also has an effect on stellar brightness. An increase in luminosity of a main sequence star is proportional to its T_{eff}, so the error in T_{eff} has a direct influence on a star's brightness as well; hence T_{eff} is required as a final parameter integrated into the mass-luminosity equation. As with the parallax value above, the value of T_{eff} listed in Table 5.3 for TIC 409934330, $T_{\mathrm{eff}} = 8050 \pm 160\,\mathrm{K}$, was taken from the TIC: the 160 K error was taken from Stassun et al. (2018), used to obtain two T_{eff} extremes: $T_{\mathrm{eff}} = 7890\,\mathrm{K}$ and $T_{\mathrm{eff}} = 8210\,\mathrm{K}$.

Wang & Zhong (2018) devised a mass estimation based on T_{eff}. which they derived from the mass-luminosity relation given as Equation 5.2. Instead of luminosity, their version of the relation was in terms of T_{eff} and stellar radius, given as Equation 5.7. However in some cases — such as currently in this work — the stellar radius might not be known. Therefore, Wang & Zhong (2018) modified the classical mass-luminosity relationship by reintroducing luminosity but additionally placing T_{eff} as its exponent. This slight modification allows T_{eff} to have more significance on the mass of the star. Equation 5.8 is the final form of this relation, and was used in

the calculations below (Wang & Zhong, 2018). Equation 5.3 was not used for this method as Wang & Zhong (2018) only used the form of Equation 5.2.

$$\left(\frac{M}{\mathrm{M}_\odot}\right) = \left(\frac{T_{\mathrm{eff}}}{T_\odot}\right)\left(\frac{R}{\mathrm{R}_\odot}\right)^{\frac{1}{2}} \tag{5.7}$$

$$\left(\frac{M}{\mathrm{M}_\odot}\right) = \left(\frac{L}{\mathrm{L}_\odot}\right)^{\frac{1}{4}}\left(\frac{1}{3}\right)^{\left(\frac{T_{\mathrm{eff}}}{T_\odot}\right)^{\frac{1}{3}}-1} \tag{5.8}$$

Values for stellar luminosity were taken from § 5.4.1.2, from each variant of the main sequence width, to save recalculation. As in § 5.4.1.1, two sets of calculations were performed in parallel. Below shows all working, with respective calculated masses each labeled A, B, C, D initially as it was not know which would be the minimum and maximum. A value of T_{eff} for the Sun was required, and taken to be $T_{\mathrm{eff}} = 5772\,K$ (Prša et al., 2016). The final mass range is listed with the other calculated mass ranges in Table 5.5.

$\underline{M_V \approx 0.55}$

$$\left(\frac{L}{\mathrm{L}_\odot}\right)_{\mathrm{min}} = 16.03\,\mathrm{L}_\odot \qquad \left(\frac{L}{\mathrm{L}_\odot}\right)_{\mathrm{max}} = 114.90\,\mathrm{L}_\odot$$

$$(T_{\mathrm{eff}})_{\mathrm{min}} = 7890\,\mathrm{K} \qquad (T_{\mathrm{eff}})_{\mathrm{max}} = 8210\,\mathrm{K}$$

$$\left(\frac{M}{\mathrm{M}_\odot}\right)_{\mathrm{A}} = (16.03)^{\frac{1}{4}} \times \left(\frac{1}{3}\right)^{\left(\frac{7890}{5772}\right)^{\frac{1}{3}}-1}$$

$$\therefore \left(\frac{M}{\mathrm{M}_\odot}\right)_{\mathrm{A}} = 1.77\,\mathrm{M}_\odot$$

$$\left(\frac{M}{\mathrm{M}_\odot}\right)_{\mathrm{C}} = (114.90)^{\frac{1}{4}} \times \left(\frac{1}{3}\right)^{\left(\frac{7890}{5772}\right)^{\frac{1}{3}}-1}$$

$$\therefore \left(\frac{M}{\mathrm{M}_\odot}\right)_{\mathrm{C}} = \mathbf{2.90\,M_\odot}$$

$$\left(\frac{M}{\mathrm{M}_\odot}\right)_{\mathrm{B}} = (16.03)^{\frac{1}{4}} \times \left(\frac{1}{3}\right)^{\left(\frac{8210}{5772}\right)^{\frac{1}{3}}-1}$$

$$\therefore \left(\frac{M}{\mathrm{M}_\odot}\right)_{\mathrm{B}} = \mathbf{1.75\,M_\odot}$$

$$\left(\frac{M}{\mathrm{M}_\odot}\right)_{\mathrm{D}} = (114.90)^{\frac{1}{4}} \times \left(\frac{1}{3}\right)^{\left(\frac{8210}{5772}\right)^{\frac{1}{3}}-1}$$

$$\therefore \left(\frac{M}{\mathrm{M}_\odot}\right)_{\mathrm{D}} = 2.86\,\mathrm{M}_\odot$$

$\underline{M_V \approx 0.25}$

$$\left(\frac{L}{\mathrm{L}_\odot}\right)_{\min} = 18.41\,\mathrm{L}_\odot \qquad \left(\frac{L}{\mathrm{L}_\odot}\right)_{\max} = 100.09\,\mathrm{L}_\odot$$

$$(T_{\mathrm{eff}})_{\min} = 7890\,\mathrm{K} \qquad (T_{\mathrm{eff}})_{\max} = 8210\,\mathrm{K}$$

$$\left(\frac{M}{\mathrm{M}_\odot}\right)_{\mathrm{A}} = (18.41)^{\frac{1}{4}} \times \left(\frac{1}{3}\right)^{\left(\frac{7890}{5772}\right)^{\frac{1}{3}}-1}$$

$$\therefore \left(\frac{M}{\mathrm{M}_\odot}\right)_{\mathrm{A}} = 1.84\,\mathrm{M}_\odot$$

$$\left(\frac{M}{\mathrm{M}_\odot}\right)_{\mathrm{C}} = (100.09)^{\frac{1}{4}} \times \left(\frac{1}{3}\right)^{\left(\frac{7890}{5772}\right)^{\frac{1}{3}}-1}$$

$$\therefore \left(\frac{M}{\mathrm{M}_\odot}\right)_{\mathrm{C}} = \mathbf{2.80\,M_\odot}$$

$$\left(\frac{M}{\mathrm{M}_\odot}\right)_{\mathrm{B}} = (18.41)^{\frac{1}{4}} \times \left(\frac{1}{3}\right)^{\left(\frac{8210}{5772}\right)^{\frac{1}{3}}-1}$$

$$\therefore \left(\frac{M}{\mathrm{M}_\odot}\right)_{\mathrm{B}} = \mathbf{1.81\,M_\odot}$$

$$\left(\frac{M}{\mathrm{M}_\odot}\right)_{\mathrm{D}} = (100.09)^{\frac{1}{4}} \times \left(\frac{1}{3}\right)^{\left(\frac{8210}{5772}\right)^{\frac{1}{3}}-1}$$

$$\therefore \left(\frac{M}{\mathrm{M}_\odot}\right)_{\mathrm{D}} = 2.76\,\mathrm{M}_\odot$$

***M_V* ≈ 0.45**

$$\left(\frac{L}{\mathrm{L}_\odot}\right)_{\min} = 16.79\,\mathrm{L}_\odot \qquad \left(\frac{L}{\mathrm{L}_\odot}\right)_{\max} = 109.73\,\mathrm{L}_\odot$$

$$(T_{\mathrm{eff}})_{\min} = 7890\,K \qquad (T_{\mathrm{eff}})_{\max} = 8210\,K$$

$$\left(\frac{M}{\mathrm{M}_\odot}\right)_{\mathrm{A}} = (16.79)^{\frac{1}{4}} \times \left(\frac{1}{3}\right)^{\left(\frac{7890}{5772}\right)^{\frac{1}{3}}-1} \qquad \left(\frac{M}{\mathrm{M}_\odot}\right)_{\mathrm{C}} = (109.73)^{\frac{1}{4}} \times \left(\frac{1}{3}\right)^{\left(\frac{7890}{5772}\right)^{\frac{1}{3}}-1}$$

$$\therefore \left(\frac{M}{\mathrm{M}_\odot}\right)_{\mathrm{A}} = 1.79\,\mathrm{M}_\odot \qquad \therefore \left(\frac{M}{\mathrm{M}_\odot}\right)_{\mathrm{C}} = \mathbf{2.87\,M_\odot}$$

$$\left(\frac{M}{\mathrm{M}_\odot}\right)_{\mathrm{B}} = (16.79)^{\frac{1}{4}} \times \left(\frac{1}{3}\right)^{\left(\frac{8210}{5772}\right)^{\frac{1}{3}}-1} \qquad \left(\frac{M}{\mathrm{M}_\odot}\right)_{\mathrm{D}} = (109.73)^{\frac{1}{4}} \times \left(\frac{1}{3}\right)^{\left(\frac{8210}{5772}\right)^{\frac{1}{3}}-1}$$

$$\therefore \left(\frac{M}{\mathrm{M}_\odot}\right)_{\mathrm{B}} = \mathbf{1.77\,M_\odot} \qquad \therefore \left(\frac{M}{\mathrm{M}_\odot}\right)_{\mathrm{D}} = 2.82\,\mathrm{M}_\odot$$

5.4.1.4 Error in Mass Results

Table 5.5 lists the results from all of the different methods used to calculate the mass ranges. These results are shown graphically as horizontal bars in Figure 5.4.

To ensure that the ranges would be appropriate to use for the pre-main sequence models, they were compared against literature values of masses of stars with similar spectral types to TIC 409934330 (A2mA4). As mentioned earlier, Pecaut & Mamajek (2013) specifically state that a typical mass of an A2-type star is 1.98 $\mathrm{M}_\odot$, and 1.93 $\mathrm{M}_\odot$ for an A4-type (relevant to TIC 409934330's spectral type). For completeness, Pecaut & Mamajek (2013) provide mass estimates across the full range of A-type stars, giving an upper and lower mass-boundary of 1.75 $\mathrm{M}_\odot$ and 2.18 $\mathrm{M}_\odot$ for A9 and A0 stars, respectively. Extending this boundary further, Pecaut & Mamajek (2013) state that a typical mass of an F0 star is 1.61 $\mathrm{M}_\odot$, and 2.75 $\mathrm{M}_\odot$ for a B9 star. Taking the midpoint in-between F0 – A9 and A0 – B9, a full mass range for

A-type stars can therefore be assumed as $1.680\,M_\odot - 2.465\,M_\odot$, rounded to $1.68\,M_\odot - 2.47\,M_\odot$: this is the blue region in Figure 5.4. For completeness, this process was repeated for B-type stars (only up to B5 due to a much larger mass range). This mass range was assumed as $1.68\,M_\odot - 2.47\,M_\odot$: this is the teal region in Figure 5.4.

Figure 5.4 shows that the combination of all three errors from the previous Sub-Sections provides the most appropriate and realistic error ranges, with the most succinct being the main sequence width of $M_V \pm 0.25$. Comparing the mass range of the main sequence width of $M_V \pm 0.25$ to the work of Pecaut & Mamajek (2013), I here make the argument that the main sequence width of $M_V \pm 0.25$ is the most astrophysical. Naturally, it was decided that the mass range should be taken as the length that the grey bar spans across the blue shaded area (the full A-type mass range since the observed data for the star does not support a tight range): $1.81\,M_\odot$ up to $2.47\,M_\odot$, and since the work of Pecaut & Mamajek (2013) was to two decimal places, the mass increase from model to model was to be $0.01\,M_\odot$. The final mass range is highlighted in Figure 5.4 as the orange region.

Table 5.5: *All sets of calculated mass ranges for the pre-main sequences models for TIC 409934330.*
†*(Pecaut & Mamajek, 2013),*
††*(Fernandes, Lebreton & Baglin, 1996),*
‡*(Lebreton et al., 1997).*

Source of Error	Calculated Stellar Mass Range
$T_{\rm eff}$ - Mass†	$1.83 \leq M_\odot \leq 1.93$
Parallax	$1.70 \leq M_\odot \leq 3.07$
Parallax & $M_V \approx 0.55^{\dagger\dagger}$	$1.58 \leq M_\odot \leq 3.27$
Parallax & $M_V \approx 0.25^\ddagger$	$1.64 \leq M_\odot \leq 3.16$
Parallax & $M_V \approx 0.45^\ddagger$	$1.60 \leq M_\odot \leq 3.24$
Parallax & $M_V \approx 0.55^{\dagger\dagger}$ & $T_{\rm eff}$	$1.75 \leq M_\odot \leq 2.90$
Parallax & $M_V \approx 0.25^\ddagger$ & $T_{\rm eff}$	$1.81 \leq M_\odot \leq 2.80$
Parallax & $M_V \approx 0.45^\ddagger$ & $T_{\rm eff}$	$1.77 \leq M_\odot \leq 2.87$

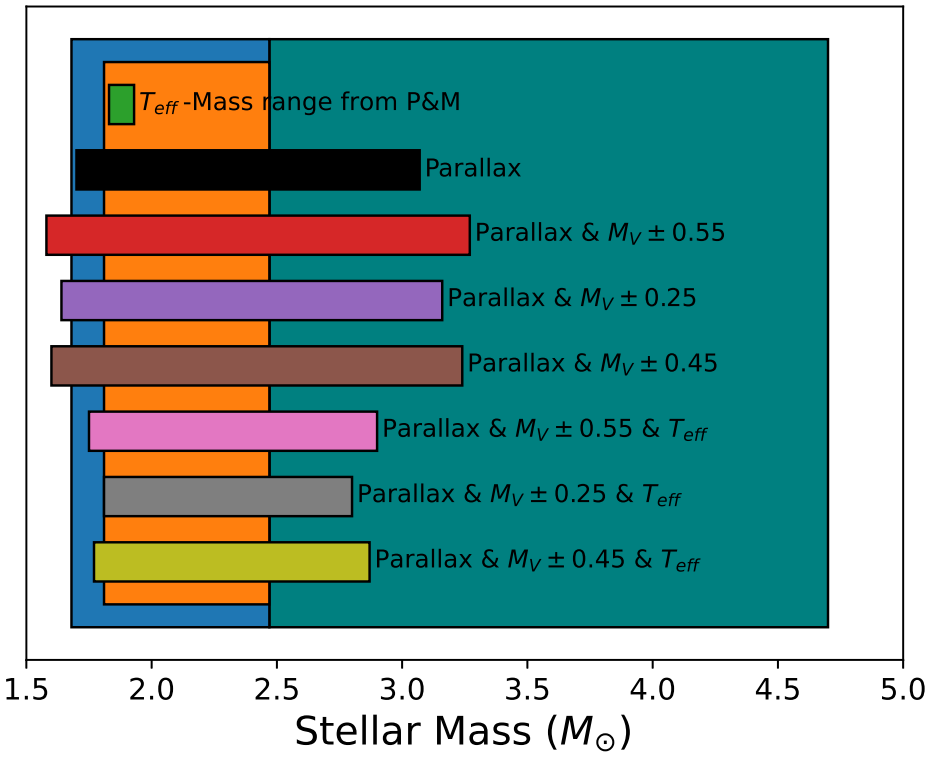

Figure 5.4: *All calculated mass ranges from Table 5.5 represented by the horizontal bars, each labelled with the respective source of error used to calculate its mass range. The blue-shaded region is the assumed full mass range of all A-type stars and the teal-shaded region is the assumed full mass range of all B-type stars up to B5, based on mass estimates given by Pecaut & Mamajek (2013). The orange shaded region is the final mass range that was used to create the pre-main sequence models,* $\boldsymbol{1.81\,M_\odot - 2.47\,M_\odot}$*, chosen from the length of the grey bar across the blue shaded region. It can be seen that the combination of all three errors provides the most realistic mass range for an A-type star.*

"P&M" = Pecaut & Mamajek (2013).

5.4.2 Main Sequence Models

The most prominent aspect of each model was the main sequence evolution. The inlists followed the work of Khalack et al. (2019), and a further two parameters became variables alongside stellar mass: stellar rotation, and convective overshoot.

5.4.2.1 Stellar Mass

As a quick summary of the previous Sub-Sections, the finalised stellar mass range was taken from a variety of mass ranges calculated from errors of parameters such as parallax, the main sequence width, and $T_{\rm eff}$. The final mass range is therefore $1.81\,\mathrm{M}_{\odot} - 2.47\,\mathrm{M}_{\odot}$, as shown in Table 5.6a (the subscript "a" is due to this Table being appended to in the following Sub-Sections).

Table 5.6a: *Parameters and respective ranges so far for the stellar models for TIC 409934330.*

Parameter	Range	Step Size
Mass	$1.81 \leq \mathrm{M}_{\odot} \leq 2.47$	$0.01\,\mathrm{M}_{\odot}$

5.4.2.2 Stellar Rotation

Another point to consider is that TIC 40993440 being an Am star has the effect of it rotating more slowly than chemically-normal A-type stars (see § 1.1.8.2). Fig. [1] of Reiners (2006) maps a sample of stars across $v \sin i$ vs. $B - V$ space. For TIC 409934330, $B - V = 0.13$[3]. Therefore, Reiners (2006) suggests TIC 409934330 would have a rotation rate between $v \sin i \approx 100 - 150\,\mathrm{km\,s^{-1}}$. But as discussed in § 1.1.8.2, $v \sin i \approx 100\,\mathrm{km\,s^{-1}}$ is the generally considered upper-limit of Am star rotation (with perhaps the one exception of $v \sin i \approx 120\,\mathrm{km\,s^{-1}}$), so we can confidently say that TIC 409934330 rotates more slowly than its $B - V$ implies.

[3]Using the B and V magnitude values listed in Table 5.3

The above discussion justified an upper limit for the rotation rate of $100\,\mathrm{km\,s^{-1}}$, but in the interests of CPU time a lower limit was still needed, and a suitable increment between different models. This issue was solved by Zorec & Royer (2012) who sampled the rotation rates of slow-rotating and fast-rotating chemically-normal and CP A-type stars. Several thousand stars comprised their sample, which they binned based on mass and estimated a rotation rate per bin. For the CP stars — most relevant to TIC 409934330 — the rotation estimates lay within the range of $28 \leq v\,\mathrm{km\,s^{-1}} \leq 58$ (extracted from their Table [5]).

Hence we based our rotation range on the above estimates from Zorec & Royer (2012) — expanding their lower-limit slightly to $20\,\mathrm{km\,s^{-1}}$ — increasing in integer increments of $1\,\mathrm{km\,s^{-1}}$ to the aforementioned generally-accepted upper-limit for Am stars, thus finalising an equatorial rotation range of $20 \leq v_{\mathrm{eq}}\,\mathrm{km\,s^{-1}} \leq 100$, as shown in Table 5.6b.

Table 5.6b: *Parameters and respective ranges so far for the stellar models for TIC 409934330.*

Parameter	Range	Step Size
Mass	$1.81 \leq \mathrm{M_\odot} \leq 2.47$	$0.01\,\mathrm{M_\odot}$
Rotation	$20 \leq v_{\mathrm{eq}}\,\mathrm{km\,s^{-1}} \leq 100$	$1\,\mathrm{km\,s^{-1}}$

5.4.2.3 Convective Overshoot

The astrophysical nature of this parameter is discussed in-depth in § 3.1.4.5, but in short it describes how far a parcel of gas within the convective zone of a star moves from a stable region to an unstable region, leading to effects such as star core masses being higher than predicted (Johnston, 2021).

Within the convective overshoot equation (Equation 3.2) the overshoot parameter is "f_{ov}". This was the variable that physically changed the amount of overshoot occurring within the model stars, but it was soon discovered that it was difficult

to justify a suitable range of values for it. We therefore turned once again to the methods within Khalack et al. (2019), noting that they had initially implemented an overshoot parameter range of $0.00 \leq f_{\rm ov} \leq 0.04$ with incremental changes of 0.01 per model, but found too many matching models within that resolution, so evolved their range to $0.01 \leq f_{\rm ov} \leq 0.03$ with incremental changes of 0.002 per model.

As with our rotation range above, we took the overshoot parameter range of Khalack et al. (2019) as the foundation for ours, but extended the lower boundary back to zero and increased the incremental resolution for absolute confidence. We therefore finalised an overshoot parameter range of $0.000 \leq f_{\rm ov} \leq 0.030$ with increment changes of 0.001 per model, as shown in Table 5.6c.

Table 5.6c: *The finalised parameters and respective ranges for the stellar models for TIC 409934330.*

Parameter	Range	Step Size
Mass	$1.81 \leq \mathrm{M}_{\odot} \leq 2.47$	$0.01\,\mathrm{M}_{\odot}$
Rotation	$20 \leq v_{\rm eq}\,\mathrm{km\,s^{-1}} \leq 100$	$1\,\mathrm{km\,s^{-1}}$
Overshoot	$0.000 \leq f_{\rm ov} \leq 0.030$	0.001

5.4.2.4 The Final MESA Models

Incorporating the parameter variables described above, and implementing appropriate physics flags following the work of Khalack et al. (2019) (full discussions of each can be found in § 3.1), a total of **170,748** MESA models were created. An example of the inlists used to create the MESA models can be seen in Appendix B. The next step was to set the models pulsating, by feeding each through GYRE.

5.5 Modelling the Stellar Pulsations

Figure 5.1 shows the light curve of TIC 409934330 produced from the Sector 6 data set. With the host star being pulsationally active as well as hosting a companion, the two sets of signals are here intertwined and as such need to be isolated, to allow independent analysis of each. Figure 5.5 — the same Fourier transform as seen in Figure 5.2 — shows the two sets of signals more clearly, with the *red* arrow signalling the frequency of the companion's orbital period and the following *black* arrows highlighting its harmonics (i.e., non-astrophysical signals). The *green* arrow shows a harmonic that at first may be mistaken as pulsational frequency. The unlabelled peaks are the astrophysical frequencies of TIC 409934330's pulsations.

Figure 5.3, shown again here Figure 5.6, is the Fourier transform TIC 409934330 with the orbital period and all its harmonic peaks removed such that only signals intrinsic to TIC 409934330 can be seen. A total of 250 harmonics were pulled out, ensuring higher-frequency harmonics were not mistaken as pulsational.

The SPOC pipeline — that initially flagged TIC 409934330 as TOI 1114.01 — previously determined the companion's orbital period to be 2.488885 ± 0.000142 d (Guerrero et al., 2021), which when inverted produces an orbital frequency of 0.401786 ± 0.000046 c/d (labelled in Figure 5.5 by the *red* arrow; this is very close to the period estimation made in § 5.3). This orbital frequency, as well as 250 of its harmonics, were removed from the Fourier transform using the program Period04 (Lenz & Breger, 2005) in a process called pre-whitening (see § 3.5). Only removing the orbital period frequency and the "obvious" harmonics would have isolated the stellar pulsational frequencies, but removing an appropriate number of higher-order harmonics as well ensured that any with locally-high amplitudes were not mistaken for stellar pulsational frequencies, and otherwise erroneously included in the modelling process. As can be seen in Figure 5.5, the harmonic indicated by the *green* arrow, for example, could easily have been mistaken as a stellar pulsation. Hence, this allowed

the transits to be excised from the light curve, leaving it to be purely pulsational.

Next, the stellar pulsational frequencies were manually extracted, again using PERIOD04 (Lenz & Breger, 2005). Included were all peaks with amplitudes higher than ≈ 0.02 mmag: a trade-off between a sufficient number of peaks to achieve the best stellar model possible and removing any chance of incorrectly incorporating high-amplitude noise. A total of 87 frequencies were extracted, and are listed in Table G.1 in Appendix G. The errors in frequency and amplitude were calculated by PERIOD04 using the methods within Montgomery & O'Donoghue (1999).

A final check was required before modelling the host star could take place. Any of the 87 frequencies extracted could be a so-called "combination frequency", a self-explanatory concept but importantly non-astrophysical. A self-written Python script cycled through each of the 87 frequencies, calculating the result of every combination of addition or subtraction, for all frequencies and multiples there of, up to the 5^{th} order following the strategy of Kurtz et al. (2016). A chi-squared analysis was then performed on all 387,645 resulting combinations against the original 87 frequencies, looking for matches that were exact to 1 PPM or more ($>6\sigma$). 17 were found and are listed in Table 5.7, alongside their determined combination relationship. The remaining 70 frequencies listed in Table G.2 in Appendix G were confidently believed to be the astrophysical stellar pulsation frequencies of TIC 409934330.

Figure 5.7 shows the Fourier transform of TIC 409934330 now with black arrows labelling the discovered combination frequencies. The frequencies ν_4, ν_{31} and ν_{86} were not obvious to the eye that they were not astrophysical, and would have caused the MESA and GYRE models to be incorrect: this highlights the importance of calculating combination frequencies. In the interests of computational expense, it was deemed unwise to try and fit all 70 remaining pulsational frequencies. Therefore, the cut-off amplitude was increased to include only the highest-amplitude frequencies, enough to achieve a good model fit. This cut-off point was chosen as 0.2 mmag,

and Table 5.8 lists the 11 frequencies that were used in the final analysis.

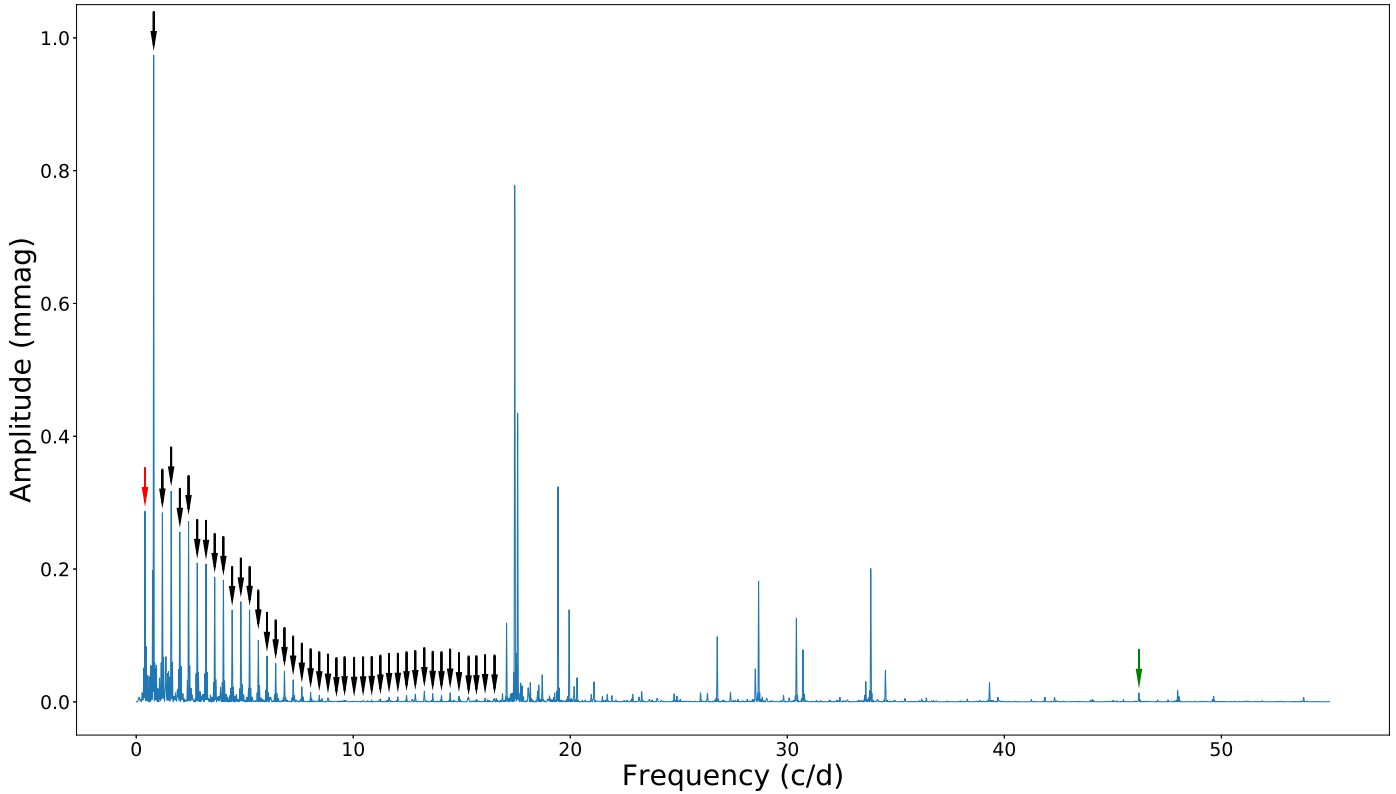

Figure 5.5: *The same Fourier transform as Figure 5.2, but with the orbital frequency of the companion, its harmonics, and an unrecognisable harmonic, labelled by the red, black and green arrows respectively. The presence of the green-arrowed harmonic signifies the importance of removing harmonics to avoid miss-identifying them as frequency peaks.*

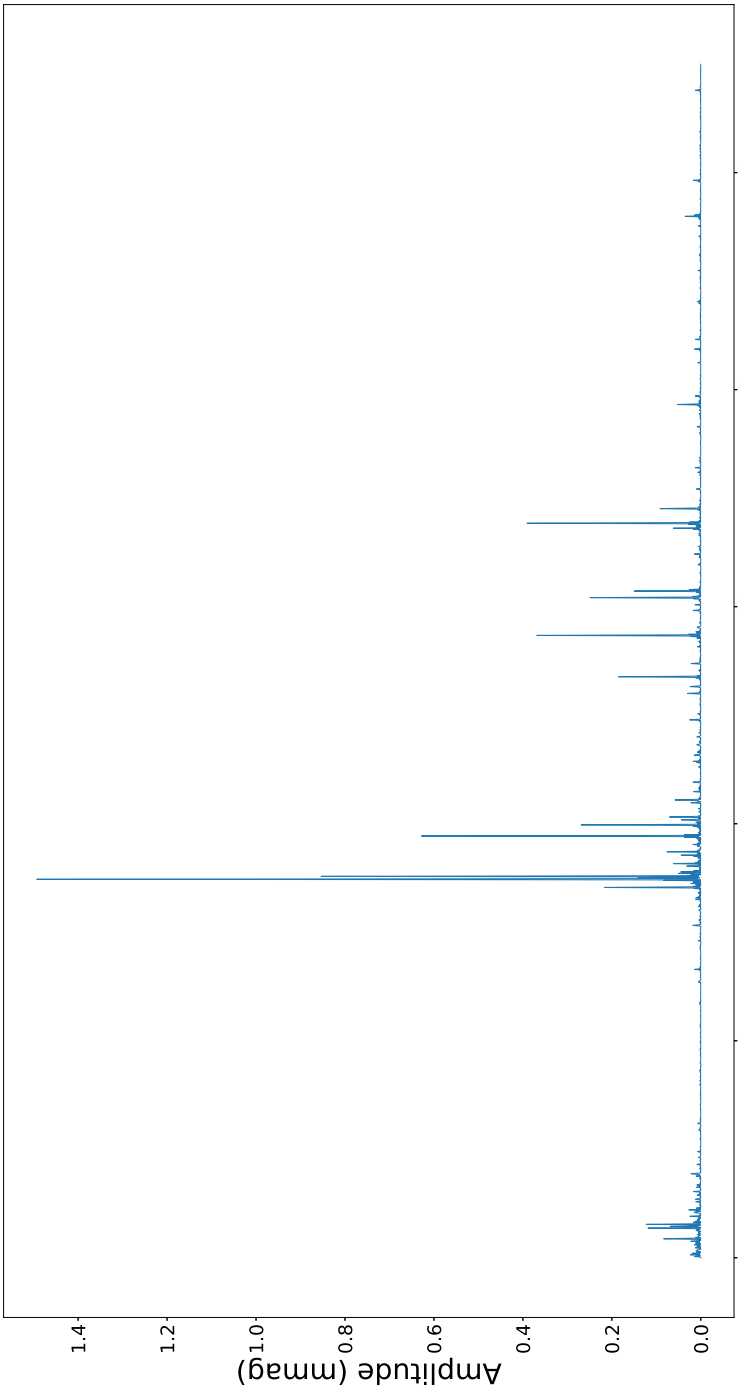

Figure 5.6: *The resultant Fourier transform after 250 harmonics were extracted.*

Table 5.7: *The 17 combination frequencies that each matched an extracted TESS frequency to 1 PPM or more (>6σ; this Table has a higher number of significant figures than other frequency tables in this Chapter and Appendices as proof of the combinations). These frequencies were removed from the list of TESS-extracted frequencies, which is where their errors in frequency and amplitude can be located too (Table G.1 in Appendix G). Figure 5.7 shows where these combination frequencies are in the Fourier transform of TIC 409934330.*

Numerical Combination	Combination Frequency (c/d)	Observed Frequency (c/d)	$\|\Delta(O-C)\|$ (c/d)	Amplitude (mmag)
$4\nu_6 - 5\nu_2 = \nu_4$	1.5385303	1.5385309	0.0000006	0.1126548
$4\nu_{18} - 1\nu_{25} = \nu_{11}$	3.0489299	3.0489293	0.0000005	0.0418422
$5\nu_{18} - 1\nu_{47} = \nu_{13}$	3.3548779	3.3548788	0.0000009	0.0294790
$1\nu_{49} - 1\nu_{37} = \nu_{15}$	3.8700590	3.8700594	0.0000004	0.0465555
$4\nu_{10} - 5\nu_4 = \nu_{15}$	3.8700590	3.8700594	0.0000003	0.0465555
$4\nu_{18} - 1\nu_{11} = \nu_{25}$	16.510632	16.510631	0.0000005	0.0355697
$5\nu_{75} - 5\nu_{72} = \nu_{25}$	16.510630	16.510631	0.0000008	0.0355697
$5\nu_{43} - 5\nu_{25} = \nu_{28}$	17.178792	17.178793	0.0000005	0.0347587
$4\nu_{82} - 5\nu_{69} = \nu_{31}$	17.576176	17.576175	0.0000007	0.2971066
$1\nu_{49} - 1\nu_{15} = \nu_{37}$	18.045648	18.045649	0.0000004	0.0559502
$5\nu_{18} - 1\nu_{13} = \nu_{47}$	21.094573	21.094573	0.0000009	0.0770272
$1\nu_{15} + 1\nu_{37} = \nu_{49}$	21.915708	21.915708	0.0000004	0.0419869
$1\nu_{86} - 2\nu_{24} = \nu_{51}$	23.160601	23.160602	0.0000009	0.0390397
$4\nu_8 + 5\nu_{10} = \nu_{54}$	24.785288	24.785289	0.0000007	0.0509330
$2\nu_4 + 2\nu_{32} = \nu_{73}$	38.289192	38.289193	0.0000008	0.0288923
$5\nu_{43} - 2\nu_{64} = \nu_{73}$	38.289192	38.289193	0.0000005	0.0288923
$1\nu_{51} + 2\nu_{24} = \nu_{86}$	53.794066	53.794065	0.0000009	0.0410269

Figure 5.7: *The Fourier transform of TIC 409934330 with black arrows now denoting the locations of the calculated combination frequencies listed in Table 5.7.*

Table 5.8: *The 11 highest-amplitude frequencies of pulsation extracted from the Fourier transform of TIC 4099434330 that were used in the final stellar modelling.*

Frequency Number	Frequency ν (c/d)	Amplitude (mmag)
ν_{27}	17.0645 ± 0.0010	0.1500 ± 0.0081
ν_{30}	17.4408 ± 0.0004	0.3935 ± 0.0081
ν_{42}	19.4330 ± 0.0006	0.2554 ± 0.0081
ν_{43}	19.9464 ± 0.0009	0.1669 ± 0.0081
ν_{57}	26.7704 ± 0.0012	0.1379 ± 0.0081
ν_{59}	28.6782 ± 0.0008	0.1960 ± 0.0081
ν_{63}	30.4154 ± 0.0010	0.1606 ± 0.0081
ν_{64}	30.7214 ± 0.0012	0.1239 ± 0.0081
ν_{68}	33.8459 ± 0.0008	0.2009 ± 0.0081
ν_{69}	34.5194 ± 0.0017	0.0964 ± 0.0081
ν_{74}	39.3161 ± 0.0020	0.0723 ± 0.0081

The software GYRE (see § 3.2; Townsend & Teitler, 2013) perturbed each fed-in MESA model star to set them pulsating. The harmonic degree, ℓ, changed with each GYRE model of the *same* MESA model, between zero and three, and the azimuthal order, m, varied from minus three to three, thereby creating 28 GYRE models for *each* of the 170,748 MESA models, hence **4,780,944** GYRE models in total.

Finally, a chi-squared analysis was performed between each set of 28 GYRE models and the extracted frequencies from the TESS data to find the best-fitting model star to the target. This method can be thought of as a nested chi-squared analysis: each *separate* GYRE model was compared to the observational data and its chi-squared was calculated, then all chi-squares for a full set of 28 GYRE models for a *single* MESA model star were summed to find the total chi-squared for each model. This summed value was used to find the globally best fitting model star, then within the set of 28 separate GYRE models, each was assigned to its best-fit observed pulsational frequency, such that the harmonic degree and azimuthal order, ℓ and m, for each frequency was classified — but making sure that no model or TESS frequencies were fit more than once.

5.6 MESA and GYRE Model Results

A chi-squared analysis was performed between each list of model pulsational frequencies generated from the MESA and GYRE models, and the 11 highest-amplitude extracted pulsational frequencies of TIC 409934330 from the TESS data (see Table 5.8). The best fitting model had a combined chi-squared value of 26.9869 (≈27.0; summed from each fitted frequency), and gave the stellar parameters of TIC 409934330 listed in Table 5.9.

Table 5.9: *Stellar parameter results from this work, compared against literature values.*

"K.A.T.22" = (Kervella, Arenou & Thévenin, 2022),
"P.22" = (Paunzen, 2022).

Parameter	Unit	This Work	K.A.T.22	P.22
M_*	$\mathrm{M}_\odot$	2.10 ± 0.19	2.30	2.44
R_*	$\mathrm{R}_\odot$	4.72 ± 0.44	2.77	2.77
v_{eq}	$\mathrm{km\,s^{-1}}$	60 ± 0.5	—	—
Overshoot	f_{ov}	0.028 ± 0.0005	—	—

The errors in mass and radius were propagated from the errors in the parameters used to determine the mass ranges in § 5.4, combined with half the interval used between consecutive MESA models; the errors in rotation and overshoot were only solely-determined from half the interval used. Figures H.1, H.2 and H.3 in Appendix H justify these errors, as they show the global minimum chi-squared value was found for each of the three parameters, within the interval resolution.

Table 5.10 lists the seven of the 11 TESS-extracted pulsational frequencies that were successfully fitted by GYRE, together with their "equivalent" frequencies from the best-fitting model (and the difference between the two), their harmonic degree, ℓ, and azimuthal order, m. Four TESS frequencies are missing due to their

Table 5.10: *A comparison between the TESS-extracted frequencies and the best-fitting model frequencies.*

TESS Frequency (c/d)	Best-fit Frequency (c/d)	$\lvert\Delta(\mathrm{B}-\mathrm{T})\rvert$ (c/d)	Harmonic Degree	Azimuthal Order
17.0645	14.9610	2.1035	2	0
26.7704	27.6832	0.9128	0	0
28.6782	29.0593	0.3811	0	0
30.4189	30.4387	0.0198	0	0
33.8459	33.2008	0.6451	0	0
34.5193	34.5814	0.0621	0	0
39.3125	39.1161	0.1964	2	0

closest-fitting frequencies from GYRE being better fits to one of the seven remaining frequencies. The ramifications of all this will be collated and discussed in § 5.9 below. First we turn to the remaining data we have for this star.

5.7 Ground-Based Observations

5.7.1 40″ Telescope at the SAAO

Between 06/08/20 and 06/08/21 — the dates of the first and last observing session — TIC 409934330 was observed via 24 separate multi-colour observing runs using the 40″ telescope and *UBVRI* filters at the SAAO (see § 2.4). Due to the COVID-19 pandemic, I was unfortunately unable to perform these observations in-person: I wrote observing instructions and created star charts for any proxy observers at the SAAO, so that observations could still be completed. Poor weather during most observation runs induced poor results (mostly only calibration frames were taken). The later 2021 observations were performed by my supervisor and myself remotely from Preston, as the SAAO had developed new technology allowing remote access to the 40″ telescope and dome controls.

During each telescope set up the CCD was cooled to -40°C, the Read-Out Rate was set to 1 MHz, the Pre-Amp Gain was set to 2.4, and the Output Amplifier was set to "Conventional". Each observation run started by taking sky Flat-field 10-image cubes in each of the *UBVRI* filters, with exposure times in each filter sufficient to achieve an ADU count of ∼20,000 (except U as this required very long exposure times which would have been an inefficient use of telescope time, so instead for this filter we aimed for an ADU count of ∼5000). The flat-field cubes were taken with both 2×2 and 4×4 binning as a precaution in-case poor weather forced the science frames to also be 4×4 binned; this ensured data reduction could still take place. 1×1 binning was neglected as the purely photometric nights required for it to be beneficial were rare, so 2×2 binning was chosen as the most opportune. Table 5.11 shows a typical set of Flat-field cubes taken.

When testing the exposure times for each filter, 20,000 - 30,000 ADU counts were targeted (but this was very much subject to change depending on weather). Not only this, but the exposure times themselves had to be multiples of each other such that shorter exposures could be binned to the same exposure time as longer exposures.

Several different observing strategies were tested during the observing runs, to see which arrangement of cycling over the different filters was most efficient. The first attempt started with just cycling in the order *UBVRI*, and then cycling in sets of *UBVRIIRVBU*, but it soon became apparent that there were far more U and B observations when the final data sets were binned, and that the R and I data sets were sparsely sampled. Therefore, the observation strategy that was settled on consisted of cycling through *UBVRI* as before, but now each filter had more observations taken depending on its exposure time ensuring that at the end of a *UBVRI* cycle, all filters had equal amounts of exposure when binned. Table 5.12 lists a typical set of exposure times for each filter for TIC 409934330, showing the

binning strategy.

Table 5.11: *A typical set of Flat-field cubes taken during twilight before an observing run.*

Cube	Filter	Exposure Time (s)	Counts (ADU)	No. of Exposures	Binning
0001	U	5	∼7,500	10	2×2
0002	B	5	∼22,000	10	2×2
0003	V	5	∼20,000	10	2×2
0004	R	4	∼19,000	10	2×2
0005	I	4	∼20,000	10	2×2
0006	U	6	∼6,000	10	4×4
0007	B	5	∼12,000	10	4×4
0008	V	5	∼12,000	10	4×4
0009	R	5	∼17,000	10	4×4
0010	I	3	∼10,000	10	4×4

Many thousands of frames were taken of TIC 4099344330, and at the end of each run, two bias cubes were taken (with 2×2 and 4×4 binning, respectively).

These ground-based photometric observations were performed not only to complement the TESS data, but to observe the transits in extra wavelengths extending the TESS bandpass of 600 – 1100 nm (RI). Not only will the shape of the transit be different in different filters, helping constrain the companion's radius, but mode-identification of the stellar pulsations may also be performed due to the colour-dependency of the pulsational amplitudes.

5.7.1.1 40″ Telescope Results

Figure 5.8 shows the data taken with the 40″ telescope at the SAAO over all observation nights, phased on the companion's orbital period of 2.488885 d, separated into the five filters of $UBVRI$, and binned to a suitable degree for each filter.

The centre of the light curve in each colour contains the transit of the companion, however little-to-no evidence of this transit dip can be seen. Our observing strategy may have hindered detecting this: rather than cycling through the filters continually,

Table 5.12: *A typical set of exposure times per filter for TIC 409934330, showing how multiples of each filter allowed for efficient binning. The number of exposures per filter was not known until the end of each run.*

Frame	Filter	Exposure Time	No. of Exposures	Binning
0011	U	$2 \times 10\,\mathrm{s}$	Total	2×2
0013	B	$5 \times 4\,\mathrm{s}$	Number	2×2
0018	V	$10 \times 2\,\mathrm{s}$	Determined	2×2
0028	R	$20 \times 1\,\mathrm{s}$	After	2×2
0048	I	$20 \times 1\,\mathrm{s}$	Run	2×2

observing one complete transit per filter would have increased the signal-to-noise. Furthermore, the weather conditions did not provide photometric nights, and the weather was often unstable: atmospheric noise, as well as the star physically pulsating, combined to inject noise that was greater in magnitude than the transit dip of the companion.

5.7.2 SALT

SALT spectroscopically observed TIC 409934330 for 600 s per exposure, in the blue and red beam, using the HRS in the HR mode with the Iodine Cell out and the ThAr cell in[4], yielding a minimum S/N of 100. In this work only the blue-arm spectra were analysed as the red-arm spectra were contaminated with telluric noise.

Before analysis, the spectra required barycentric correction to remove the motion of the Earth from the signal. The date and time stamp of each observation (in UTC) were extracted from the FITS headers, along with the mid-point exposure times, which were then added to their respective time stamp. The exposure times for each, as mentioned above, were 600 s, and so for most observations the exposure midpoint was at the 300 s mark. However, during some observations effects such as weather or intrinsic instrumental problems caused the midpoint of the time in

[4]The cells are used for wavelength calibration

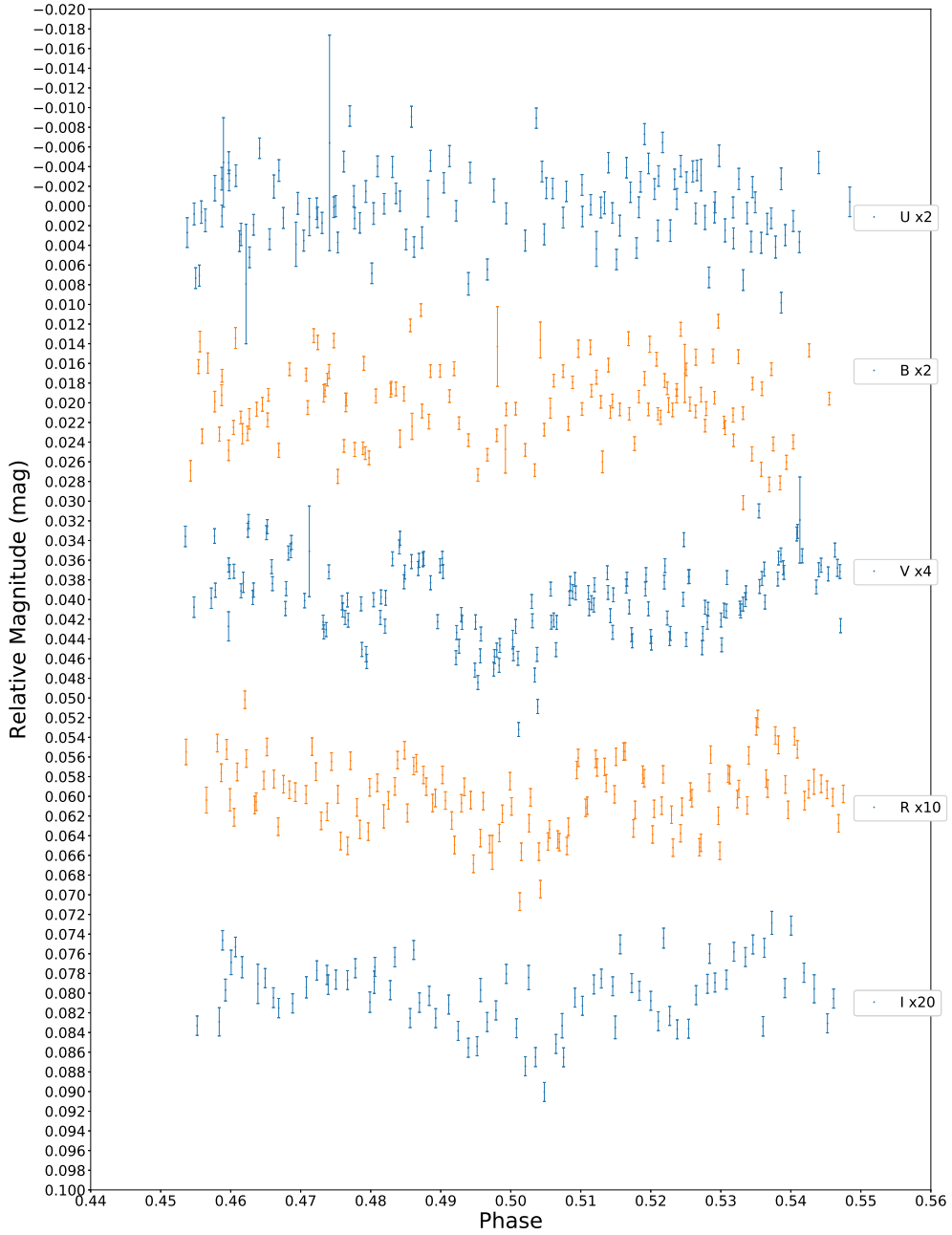

Figure 5.8: *The binned and phased UBVRI observations of TIC 409934330 taken with the 40″ telescope at the SAAO.*

which photons were collected to be different to the exposure midpoint. This was the *flux-weighted* exposure midpoint, which overwrote the standard exposure midpoint for observations where the mid-point was not equal to 300 s.

Next, the time stamp values plus the exposure midpoint or the flux-weighted exposure midpoint was converted from UTC to BJD using the Time Utilities tool[5] (Eastman, 2012), incorporating the celestial coordinates of TIC 409934330 and the geographical coordinates of SALT. The process was repeated to convert the BJD time stamps into JD, which were then fed into a barycentric velocity correction tool[6] that incorporates the `barycorr` code from Wright & Eastman (2014). This produced a list of barycentric correction velocities, each unique to respective observations.

After this process was complete, a synthetic spectrum of a similar star to TIC 409934330 was built in the software iSpec[7] (Blanco-Cuaresma et al., 2014; Blanco-Cuaresma, 2019), using the `SYNTHE` radiative transfer code within the `iSpec` software which incorporates the `ATLAS9.Castelli` model atmosphere, the `Grevesse.2007` Solar abundances, and the `VALD.300_1100nm` (Vienna Atomic Line Database) line list (Blanco-Cuaresma et al., 2014; Castelli & Kurucz, 2003; Grevesse, Asplund & Sauval, 2007; Kupka et al., 1999). Very rough estimates were inputted for the stellar parameters, such as $T_{\rm eff} = 8000\,{\rm K}$, $\log g = 4.00$, $[M/H] = 0$, and rotation $= 40\,{\rm km\,s^{-1}}$. This synthetic spectrum was then employed as a "zero-point" template against which all observational spectra were compared, thus determining an RV measurement for each observation. These were plotted to build an RV curve, illustrating the motion of TIC 409934330 over time. Furthermore: as a comparison RV curve, in case of an incorrectly-synthesised spectrum, by-chance one of the SALT observations occurred during a transit of the companion, so this too acted as a zero-point due to TIC 409934330 having a companion-induced RV of $0\,{\rm km\,s^{-1}}$ at that time (but of course it still had motion relative to the Sun). Once all RVs had

[5]https://astroutils.astronomy.osu.edu/time/
[6]https://astroutils.astronomy.osu.edu/exofast/barycorr.html
[7]https://www.blancocuaresma.com/s/iSpec

been determined, the earlier-calculated barycentric correction values were added to their respective RV values, thereby removing the motion of the Earth around the Sun from the observational data. This meant that any remaining signal of motion was purely from TIC 409934330.

The final RV curve, once phase-folded on the orbital period, would then have its best-fit over-plotted. The semi-amplitude of this is denoted by K, the final RV value. Equation 1.15, taken from Perryman (2018), shows the relation between K and the mass of the companion and was used to calculate the latter. Combining this with the calculated radius of the companion — deduced from the $\frac{R_P}{R_*}$ ratio of the transit depth, δ, and the determined radius from the stellar model — would allow the calculation of the companion's density, giving an immediate insight into whether it was of rocky or gaseous nature.

5.7.2.1 SALT Results

SALT performed 84 separate observations of TIC 409934330 over the course of 14 months. Table I.1 in Appendix I lists the RVs obtained via `iSpec`, which have additionally undergone barycentric correction.

Figure 5.9 shows the RV curve resulting from the 14 months worth of SALT observations of TIC 409934330. Phase-folding these data points over the orbital period of TIC 409934330's companion (2.488885 d) produced the RV phase curve shown by Figure 5.10, showing the motion of TIC 409934330 relative to the Earth. However upon inspection, it became apparent that the RV phase curve was not of the quality needed to deduce any parameters of the companion: there is no clear curve within the data points, and any motion of the star is lost within the noise (this work was pushing the precision limits of SALT). But, as TIC 409934330 is CP, chemical abundance analysis of the individual spectra themselves was still achievable.

Each spectrum was already barycentrically corrected from the above procedure,

and then each was further corrected for its respective RV. Once all spectra were at the same zero-point, they were co-added to form a *cumulative mean* spectrum. Similarly, as above, when creating a synthetic spectrum for the RV determination, iSpec was used to create a best-fitting model spectrum to the co-added SALT spectrum to obtain stellar parameters of TIC 409934330. Again, the `SYNTHE` spectrum, `ATLAS9.Castelli` model atmosphere, `Grevesse.2007` Solar abundances, and the `VALD.300_1100`nm line lists were used, and $T_{\rm eff}$ and $\log g$ were input as 8000 K and 4.00, respectively, but left as free parameters, allowing `iSpec` to iterate over varying values of both (hence why the input values were rounded). Once these parameters had been obtained, they were re-input and $v \sin i$ was left as the free parameter. This process itself was repeated a few times, until the reduced chi-squared value no longer decreased (`rchisq = 0.0008`). The results of this spectral analysis are listed with the MESA and GYRE results in Table 5.15.

The co-added spectra was additionally qualitatively analysed for chemical abundances: using the now best-fitting synthetic spectrum from above, the depth of certain lines in the SALT spectra were compared against the synthetic spectrum to check for abundance anomalies. We know that TIC 409934330 has previously been classified as an Am star (Renson, Gerbaldi & Catalano, 1991; Renson & Manfroid, 2009), hence it should exhibit chemical abundance anomalies in its spectra. Table 5.14 — a recreation of Table [3] from Conti (1970) that lists the species of the absorption lines where abundance anomalies are expected to occur — is identical to Table 1.1 but repeated here for convenience to the reader.

The lines of each of the species listed in Table 5.14 were investigated in the co-added spectra, and their abundance levels were qualitatively tabulated in Table 5.13 along side a reference to a respective Figure for each species, which show the co-added spectra overlaid with the synthetic spectra to illustrate each abundance-anomaly found (all Figures — J.1 to J.23 — can be found in Appendix J). Every

absorption line investigated, except for the species in bold (with their expected results in parentheses), exhibited the correct variance in chemical abundance as predicted when compared with the synthetic spectrum, so we can confidently confirm again that TIC 409934330 is an Am star (Ebo et al., (a) in prep).

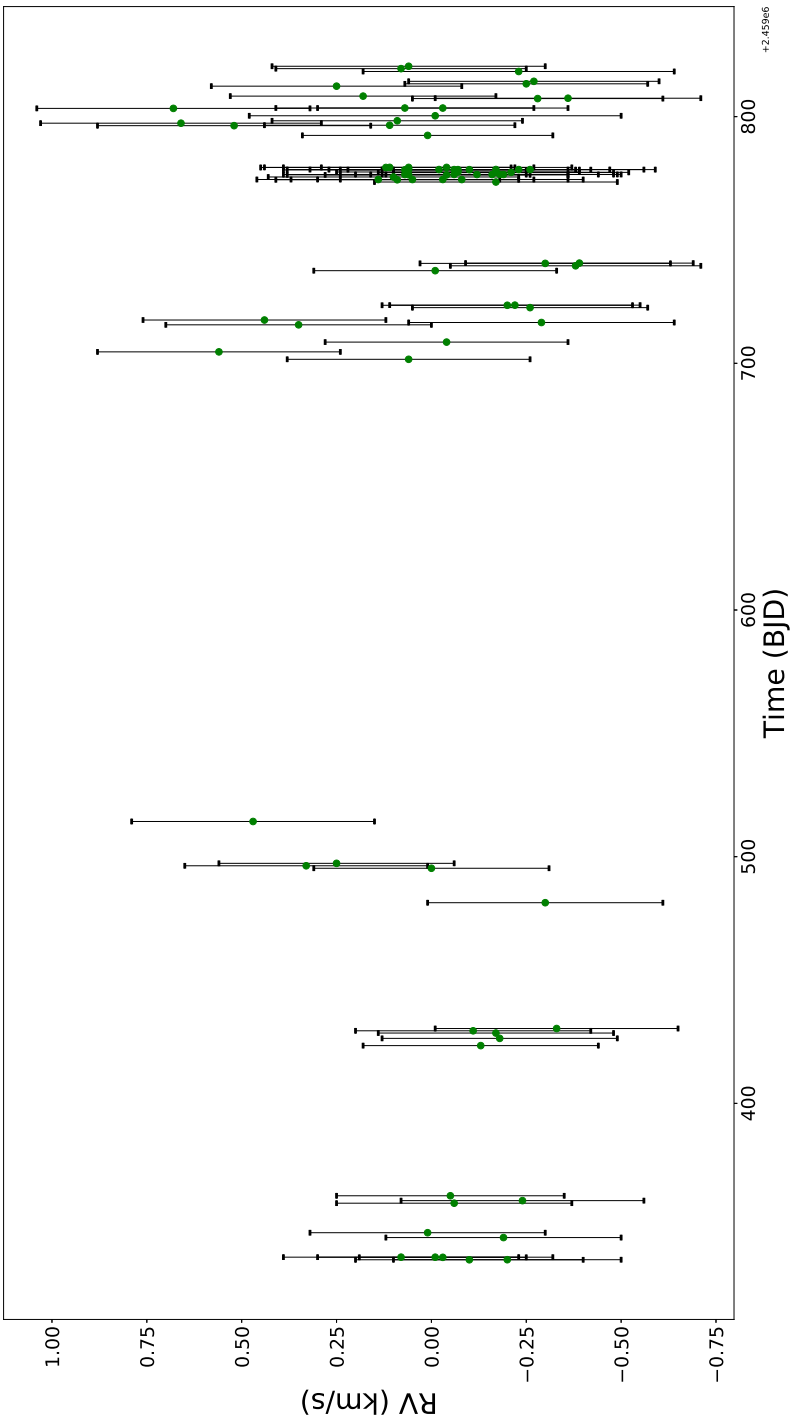

Figure 5.9: *A plot of all relative RVs of TIC 409934330 measured by SALT across the 14-month observation run.*

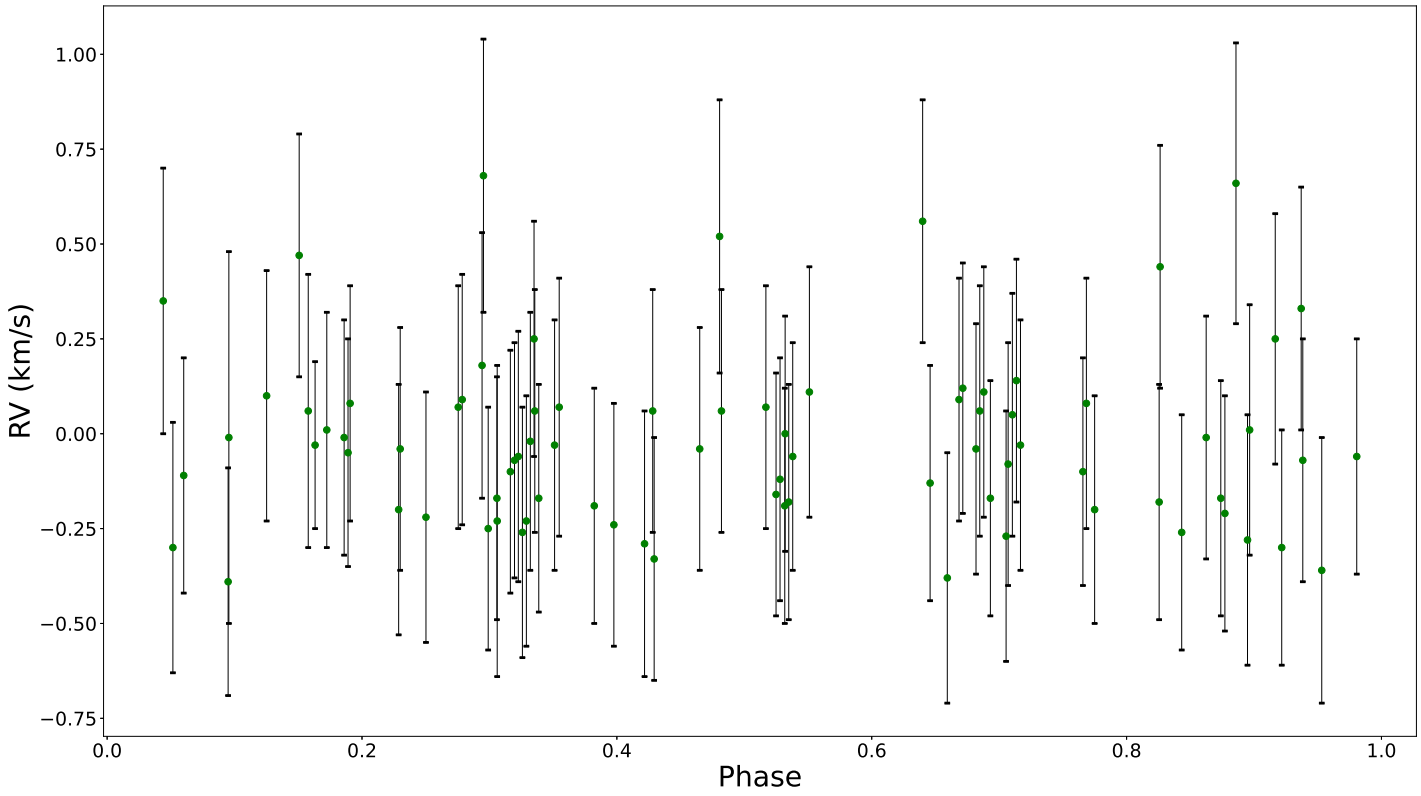

Figure 5.10: *The same RV curve as in Figure 5.9 but phased over the orbital period of TIC 409934330's companion (2.488885 d).*

Table 5.13: *The chemical abundance anomalies in the co-added spectra of TIC 409934330, were qualitatively investigated via the absorption lines of several species expected to exhibit signs of the star's Am nature. All lines investigated were correctly anomalous, except for the species in bold (with their expected results in parentheses), still proving that TIC 409934330 is indeed an Am star. The species with "N/A" entries have absorption lines with wavelengths longer than upper limit of the spectra used.*

Species	Absorption Line (nm)	Abundance	Figure
Carbon (C III)	465.1	Deficient	Figure J.1
Calcium (Ca I)	422.673	Deficient	Figure J.2
Copper (Cu II)	**505.1793**	**Deficient (Over)**	**Figure J.3**
Oxygen (O II)	430.281	Deficient	Figure J.4
Silicon (Sc II)	424.7	Deficient	Figure J.5
Potassium (K II)	500.5600	Possibly-Under	Figure J.6
Aluminium (Al III)	452.9	Normal	Figure J.7
Sulpher (S II)	425.4	Normal	Figure J.8
Nitrogen (N II)	462.139	Possibly-Over	Figure J.9
Barium (Ba II)	455.4	Over	Figure J.10
Chromium (Cr II)	461.9	Over	Figure J.11
Cobalt (Co I)	411.8774	Over	Figure J.12
Iron II (Fe II)	450.8	Over	Figure J.13
Magnesium II (Mg II)	448.113	**Over (Normal)**	**Figure J.14**
Manganese (Mn I)	403.1 – 403.6	Over	Figure J.15
Nickel (Ni I)	507.9/508.1	Over	Figure J.16
Rhenium (Re I)	435.869	Over	Figure J.17
Silicon (Si II)	504.1026	Over	Figure J.18
Strontium (Sr II)	407.771	Over	Figure J.19
Titanium II (Ti II)	**450.127**	**Over (Normal)**	**Figure J.20**
Yttrium (Y II)	417.7528	Over	Figure J.21
Zinc (Zn I)	472.21569	Over	Figure J.22
Zirconium (Zr II)	414.9	Over	Figure J.23
Sodium (Na I)	589.592	N/A	N/A
Vanadium (V I)	624.3	N/A	N/A

Table 5.14: *A recreation of Table 3 from Conti (1970), listing their full set of elemental species with abundance anomalies.*

	Well Determined	Not as Well Determined
Deficient	Ca, Sc	C, O
Normal	Mg, Ti	N, Na, K
Possibly overabundant	Si, V	Al, S, Co, Zr
Overabundant	Cr, Mn, Fe, Ni	Cu, Zn, Sr, Y, Ba, Re

Table 5.15: *Stellar parameter results from using the SALT observations, compared against literature values. iSpec determined these parameter values with a chi-squared result of 1.46, and a reduced chi-squared result of 0.0008.*

Parameter	Unit	This Work	Literature	Reference
$T_{\rm eff}$	K	8062 ± 29	8048 ± 160	(Canto Martins et al., 2020)
Fe/H	—	0.00 ± 0.20	—	—
$v \sin i$	$\mathrm{km\,s^{-1}}$	55 ± 3	—	—
$\log g$	$\log \mathrm{cm\,s^{-2}}$	3.86 ± 0.21	4.438	(Canto Martins et al., 2020)

5.8 Modelling the Planet Transit

With the RV curve in Figure 5.10 unable to determine a mass for the companion, M_P, using K, the mass was instead modelled. The software EXOFASTv2 (see § 3.3; Eastman, Gaudi & Agol, 2013; Eastman et al., 2019) was used to model the companion transiting TIC 409934330. The TESS data used to build the the light curve in Figure 5.1 was used in combination with additional observations of this star from Sector 27 as the transit input for EXOFASTv2 , but the RV results listed in Table I.1 in Appendix I were omitted as they are too poor quality for this work. M_P was determined by EXOFASTv2 using the mass-radius relationship of Chen & Kipping (2017) as only transit data was fitted (this method is standard procedure for the EXOFASTv2 software; Eastman et al., 2019). Finally, the "priors" file required by EXOFASTv2 contained the derived stellar parameters from the MESA and GYRE models in Table 5.9, several parameters obtained via iSpec in Table 5.15, and some archive-extracted parameters from Table 5.3 (this "priors" file can be seen in Appendix K).

5.8.1 Planet Transit Model Results

Figure 5.11 shows the phase-folded light curve seen in Figure 5.1 as the blue data points, with the black line of the EXOFASTv2 model overlaid. EXOFASTv2 has modelled the transit depth, δ, based on the average depth in the transit, and has excellently modelled the width and shape of the transit: hence, the planetary radius and transit duration are well constrained. The orange over-plotted points are a smoothed average of the phase curve that suggest the presence of ellipsoidal variability, most-likely arising from star light reflecting off the companion which peaks at phases of 0.25 and 0.75. This was not incorporated into the EXOFASTv2 modelling software as non-circular orbit modelling requires high-quality RV data: as no such data was achieved for this star, the companion's orbit was modelled as if it were circular. The

planetary parameters from this model are listed in Table 5.16. We now pull together all of the results listed in this Chapter, and discuss the consequences.

Table 5.16: *Stellar and Planetary parameters for TIC 409934330 and its companion, derived from the* MESA *and* GYRE *models using* EXOFAST*v*2 .

Parameter	Units	Values
Stellar Parameters:		
$\log g$	Surface gravity ($\log \mathrm{cm\,s^{-2}}$)	$3.348^{+0.13}_{-0.027}$
Age	Age (Myr)	580^{+190}_{-160}
Planetary Parameters:		
P	Period (d)	$2.48881^{+0.0010}_{-0.00082}$
R_P	Radius ($\mathrm{R_J}$)	$1.03^{+0.85}_{-0.49}$
M_P	Mass ($\mathrm{M_J}$)	$2.5^{+31}_{-2.1}$
a	Semi-major axis (au)	$0.0457^{+0.0020}_{-0.0016}$
i	Inclination (°)	$81.1^{+5.7}_{-12}$
T_{eq}	Equilibrium temperature (K)	4130^{+150}_{-210}
R_P/R_*	Radius of planet in stellar radii	$0.022^{+0.019}_{-0.011}$
a/R_*	Semi-major axis in stellar radii	$1.989^{+0.23}_{-0.074}$
δ	Transit depth (fraction)	$0.00048^{+0.0012}_{-0.00036}$
T_{14}	Total transit duration (d)	$0.377^{+0.050}_{-0.077}$
T_{FWHM}	FWHM transit duration (d)	$0.368^{+0.052}_{-0.088}$
b	Transit Impact parameter	$0.660^{+0.037}_{-0.53}$
ρ_P	Density ($\mathrm{g\,cm^{-3}}$)	$0.69^{+35}_{-0.27}$
$logg_P$	Surface gravity ($\log \mathrm{cm\,s^{-2}}$)	$3.41^{+1.5}_{-0.50}$
$M_P \sin i$	Minimum mass ($\mathrm{M_J}$)	$2.4^{+29}_{-2.1}$
M_P/M_*	Mass ratio	$0.0012^{+0.014}_{-0.0011}$
Wavelength Parameters:		
γ_1	linear limb-darkening coeff	$0.082^{+0.034}_{-0.029}$
γ_2	quadratic limb-darkening coeff	$0.30^{+0.30}_{-0.21}$

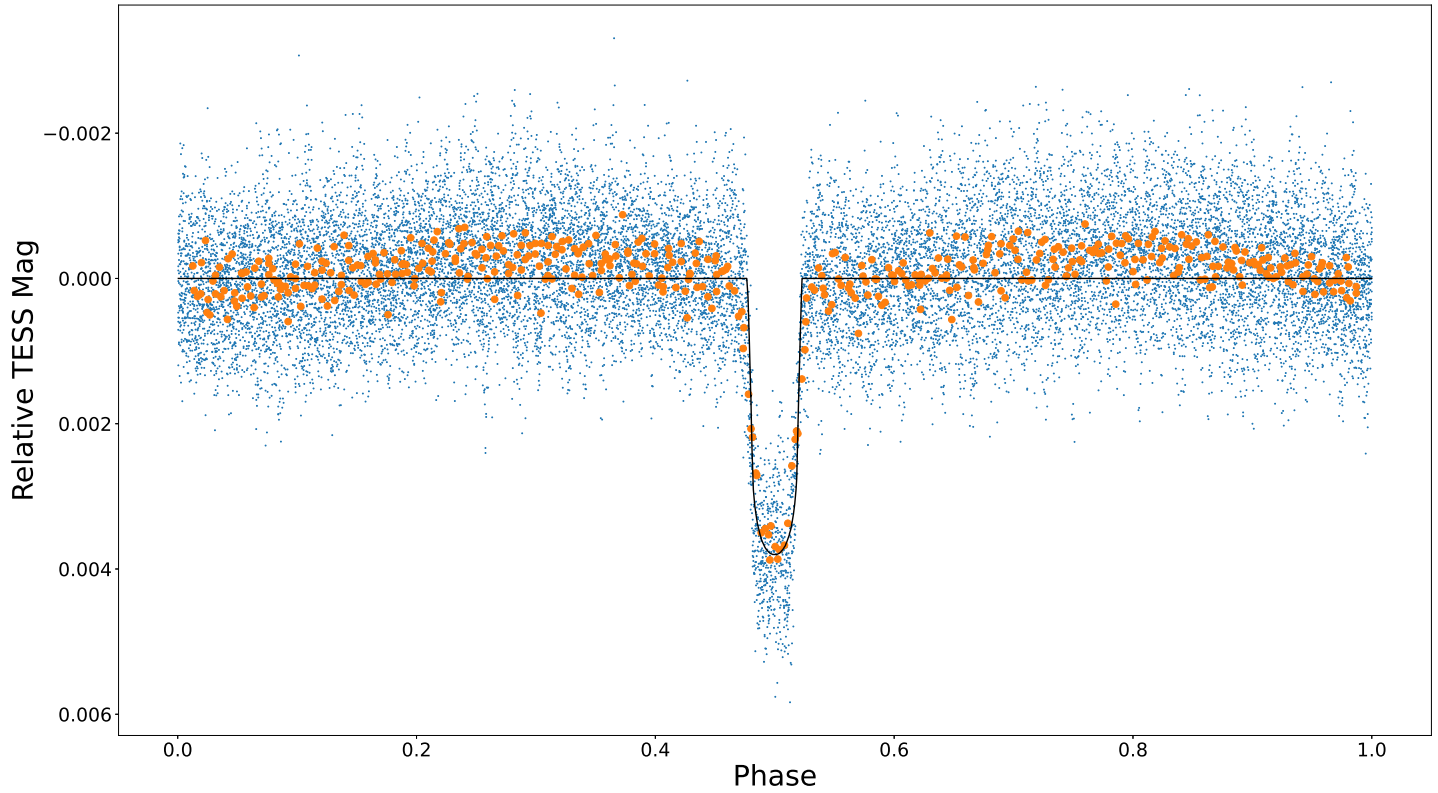

Figure 5.11: *A phase-folded version of the light curve in Figure 5.1, with the* EXOFAST*v*2 *model of the companion to TIC 409934330 overlaid as the black line. The orange over-plot is a smoothed average of the phase curve, which suggests the presence of ellipsoidal variability arising from star light reflecting off the companion, peaking at phases of 0.25 and 0.75.*

Table 5.17: *All results collected together from the* MESA *and* GYRE *models, the SALT observations, and the* EXOFAST*v*2 *models, compared against literature values where possible.*

"C.20" =(Canto Martins et al., 2020),
"K.A.T.22" = (Kervella, Arenou & Thévenin, 2022),
"P.22" = (Paunzen, 2022).

Software	Parameter	Unit	This Work	Literature	Reference
Stellar:					
MESA and GYRE:					
	M_*	$M_\odot$	2.10 ± 0.19	2.30/2.44	K.A.T.22/P.22
	R_*	$R_\odot$	4.72 ± 0.44	2.77/2.77	K.A.T.22/P.22
	$v_{\rm eq}$	$\mathrm{km\,s^{-1}}$	60 ± 0.5	—	—
	Rotation	d	3.98 ± 0.37	—	—
	Overshoot	$f_{\rm ov}$	0.028 ± 0.0005	—	—
iSpec:					
	$T_{\rm eff}$	K	8062 ± 29	8048 ± 160	C.20
	Fe/H	—	0.00 ± 0.20	—	—
	$v \sin i$	$\mathrm{km\,s^{-1}}$	55 ± 3	—	—
	Rotation	d	4.35 ± 0.47	—	—
	$\log g$	$\log \mathrm{cm\,s^{-2}}$	3.86 ± 0.21	4.438	C.20
EXOFASTv2:					
	$\log g$	$\log \mathrm{cm\,s^{-2}}$	$3.348^{+0.13}_{-0.027}$	4.438	C.20
	Age	Myr	580^{+190}_{-160}	—	—

	γ_1	—	$0.082^{+0.034}_{-0.029}$	—	—
	γ_2	—	$0.30^{+0.30}_{-0.21}$	—	—
Planetary:					
EXOFASTv2:					
	P	d	$2.48881^{+0.0010}_{-0.00082}$	—	—
	R_P	R_J	$1.03^{+0.85}_{-0.49}$	—	—
	M_P	M_J	$2.5^{+31}_{-2.1}$	—	—
	a	au	$0.0457^{+0.0020}_{-0.0016}$	—	—
	i	$^\circ$	$81.1^{+5.7}_{-12}$	—	—
	T_{eq}	K	4130^{+150}_{-210}	—	—
	R_P/R_*	—	$0.022^{+0.019}_{-0.011}$	—	—
	a/R_*	—	$1.989^{+0.23}_{-0.074}$	—	—
	b	—	$0.660^{+0.037}_{-0.53}$	—	—
	ρ_P	$\mathrm{g\,cm^{-3}}$	$0.69^{+35}_{-0.27}$	—	—
	$\log g_P$	$\log \mathrm{cm\,s^{-2}}$	$3.41^{+1.5}_{-0.50}$	—	—
	$M_P \sin i$	M_J	$2.4^{+29}_{-2.1}$	—	—
	M_P/M_*	—	$0.0012^{+0.014}_{-0.0011}$	—	—

5.9 Discussion

A chi-squared analysis was performed between the pulsation frequencies of each GYRE model and pulsations frequencies of TIC 409934330 to find the best fitting model to the TESS data, and hence a model of the star. Table 5.10 lists the best-fitting model frequencies to the real pulsation frequencies, and hence the best model of TIC 409934330 is a $2.10 \pm 0.19\,\mathrm{M}_{\odot}$ star with an equatorial rotational velocity, V_{eq}, of $60 \pm 0.5\,\mathrm{km\,s^{-1}}$ and an overshoot parameter value of $\mathrm{f}_{ov} = 0.028 \pm 0.0005$.

Table 5.17 lists all results determined from the MESA and GYRE models and SALT observations, compared to literature values for comparison where possible. The mass of TIC 409934330 produced by MESA and GYRE, $2.10 \pm 0.19\,\mathrm{M}_{\odot}$, agrees within error with the Kervella, Arenou & Thévenin (2022) literature value, but is a bit less than that of Paunzen (2022), all listed in Table 5.9. However, when considering the iSpec-obtained T_{eff} value of $8062 \pm 29\,\mathrm{K}$, and spectral type of A4mA2, the mass does not quite scale inline with the mass-T_{eff} relation given by Pecaut & Mamajek (2013). Instead, the Pecaut & Mamajek (2013) relation suggests that TIC 409934330 should have a mass of $\approx 1.88\,\mathrm{M}_{\odot}$, with $T_{\mathrm{eff}} = 8100 \pm 160\,\mathrm{K}$, for an A4 spectral type (the A2 portion was omitted as the T_{eff} is significantly lower than an A2-type [8800 K]). However, the iSpec-determined T_{eff} of $8062 \pm 29\,\mathrm{K}$ is very close in value to the literature T_{eff} of $8048 \pm 160\,\mathrm{K}$, and when examining the Pecaut & Mamajek (2013) mass-T_{eff} relation, such a star would have a mass of $\approx 1.85\,\mathrm{M}_{\odot}$, giving rise to the idea that the spectral type is incorrect and should instead be A5/A6.

Further to the above parameters, MESA and GYRE produced a model radius of TIC 409934330 of 4.72 ± 0.44. This does not agree with the literature values — but I argue that because this work is the first to study TIC 409934330 asteroseismically, the most accurate method of determining stellar radii, there is no reason to doubt this radius parameter; especially when it is noted that this star is not too dissimilar both in mass and radius to the prototype δ Scuti itself ($2.23^{+0.06}_{-0.05}\,\mathrm{M}_{\odot}$ and

$4.78 \pm 0.38\,\mathrm{R}_\odot$; Nordström et al., 2004; Gaia Collaboration et al., 2018). Yet, when contemplating the $\log g$ value of $3.86 \pm 0.21\,\log \mathrm{cm\,s^{-2}}$ obtained via the iSpec analysis of the SALT spectra (Table 5.15), the star cannot be as bloated as the $\log g$ value suggests.

Equation 5.9, a relation between $\log g$, mass and radius (both in terms of $\mathrm{M}_\odot$ and $\mathrm{R}_\odot$) from Smalley (2005):

$$\log g = \log M_* - 2\log R_* - 4.437 \tag{5.9}$$

was used as an additional method of calculating stellar parameters. Assuming a solar $\log g$ of $4.437\,\log \mathrm{cm\,s^{-2}}$ — as used by Smalley (2005) — then $\log g$ of TIC 409934330 comes out at $3.25 \pm 0.52\,\log \mathrm{cm\,s^{-2}}$. This value is slightly lower than the iSpec-determined $\log g$, more in agreement with the MESA radius. Reversing Equation 5.9 to determine a radius based on the iSpec-determined $\log g$ we get $R_* = 4.16 \pm 0.67\,\mathrm{R}_\odot$, which agrees with the MESA-determined radius within error.

The iSpec analysis produced a T_{eff} of $8062 \pm 29\,\mathrm{K}$, and a projected rotational velocity, $v \sin i$, of $55 \pm 3\,\mathrm{km\,s^{-1}}$ (both listed in Table 5.15). This T_{eff} value agrees very well with the literature: $8048 \pm 160\,\mathrm{K}$ (Canto Martins et al., 2020). And whilst a rotation velocity has not previously been calculated for TIC 409934330, ours confirms the Am nature of the star, as it is a slower rotation velocity than expected for its spectral type. $60 \pm 0.5\,\mathrm{km\,s^{-1}}$ translates to a stellar rotation period for TIC 409934330 of $3.98 \pm 0.37\,\mathrm{d}$, and $55 \pm 3\,\mathrm{km\,s^{-1}}$ translates to $4.35 \pm 0.47\,\mathrm{d}$.

But the $v \sin i$ is not the only Am star evidence in this work. § 5.7.2.1 consists of a qualitative spectral analysis of the absorption lines of the 25 separate species declared by Conti (1970) to have the chemical abundance anomalies found only in Am stars (and indeed how Am stars are explicitly defined). Apart from the two species that had lines at wavelengths beyond the analysed spectra, all but three species had the expected abundance anomalies found in their spectra — listed in

Table 5.13 — agree with those predicted by Conti (1970) in Table 5.14. Note that all of the well-determined species are in agreement, so this work can be used as further proof that TIC 409934330 is an Am star (Ebo et al., (a) in prep).

Unfortunately, the rest of the ground-based observations have produced data of a quality with too large error bars to be scientifically useful. The multicolour *UBVRI* observations of TIC 409934330 taken by the 40″ at the SAAO, that were used to construct the five phased light curves shown in Figure 5.8, had been performed with the idea of expanding the wavelength palette that TIC 409934330 had been observed with (UBV) as well as re-observing the star from the ground in wavelengths within the TESS bandpass (RI). It was hoped that each of the five light curves would show a different relative depth and shape of the transits, arising from the wavelength-dependant atmospheric absorption levels of the companion's atmosphere. However, with poor weather preventing observations on most of the nights awarded to observe TIC 409934330, an insufficient amount of data was gathered to show the wavelength-variance in the transit shapes.

The 82 SALT observations listed in Table I.1 in Appendix I were themselves successful, as initially only twelve observations were awarded as guaranteed time. When studying the "Δ RVs From Zero-Point" column it can be seen that most RV measurements are larger than their measurement error, proving a sufficient signal-to-noise per observation. However, in the phase curve (Figure 5.10) there is no clear RV motion of TIC 409934330 — the data are seemingly scattered and no clear sinusoidal curve can be seen — so the magnitude of the RV is too small to be detectable; less than the precision of SALT's HRS spectroscope. The range of Δ RV over this sample is $\approx$1.0 km s^{-1}, which is approximately the magnitude of the error of each data point (i.e: 1σ). Additionally, a larger-scale variation can be seen in Figure 5.9, the non-phased RV curve. This suggests that there is another companion to TIC 409934330, far more massive than the transiting companion, orbiting at a much larger radius.

Follow-up work of this second potential companion would be useful.

Due to the poor nature of the RV results, EXOFASTv2 could only use the TESS transit data to model the companion; but as mentioned above using transit only inputs for modelling exoplanets is standard procedure for the EXOFASTv2 software, as it employs the mass-radius relationship of Chen & Kipping (2017, (Eastman et al., 2019)). EXOFASTv2 produced a smooth model transit, overlaid on the TESS data as the black line in Figure 5.11. Whilst EXOFASTv2 has modelled the width and depth on the phased transit dip well, the base of the model dip is curved whereas it could be argued the the base of the TESS data dip is flat (implying a paucity of limb darkening, that is reflected by the low value of the linear limb darkening coefficient, γ_1, in Table 5.17). Furthermore, at phases 0 and/or 1 in Figure 5.11 a potential secondary transit occurs due to the occultation of TIC 409934330, and at phases of 0.25 and 0.75 there exists an over-abundance of flux from star light reflected off the companion's atmosphere. These two phenomena have not been modelled well by EXOFASTv2. EXOFASTv2 calculated a vast array of other parameters from its model transit too, the most relevant of which are listed in Table 5.16.

The EXOFASTv2-determined age of 580^{+190}_{-160} Myr for TIC 409934330 in Table 5.16 sits comfortably younger than the maximum age an A-type star of any kind can reach: 900-1000Myr (Freedman, Geller & Kaufmann, 2014) — the EXOFASTv2 age is already in agreement with TIC 409934330's spectral type. It is possible to see how this age range looks on the HR diagram by plotting it as an isochrone, with a thickness that of the error. Figure 5.12 shows an array of isochrones from VandenBerg & Clem (2003) plotted on the HR diagram, overlaid on the wide isochrone representing TIC 409934330 (light pink) plotted using the EXOFASTv2 age. The black circle on the HR diagram is the location of TIC 409934330 when plotting its luminosity, obtained from feeding the MESA- and GYRE-calculated mass back through Equation 5.3, and its iSpec-determined $T_{\rm eff}$. The MESA and GYRE mass and luminosity,

the EXOFASTv2 age, and the isochrones all agree within error. The orbital period listed in Table 5.16 for the companion is consistent with the value given by the TIC (Guerrero et al., 2021). EXOFASTv2 further-determined its mass and radius, giving a Jupiter-sized planet that is more dense than its Jovian namesake: $M_P = 2.5^{+31}_{-2.1}\,\mathrm{M_J}$, $1.03^{+0.85}_{-0.49}\,\mathrm{R_J}$. The large upper limit for the error on planetary mass arose from the mass-radius relationship of Chen & Kipping (2017) due to the lack of RV data used in the EXOFASTv2 analysis. If further RV data is taken of TIC 409934330 using a much higher resolution spectrograph — like HARPS, for example — then the mass errors will be constrained by over an order of magnitude more than currently.

The listed inclination of $81.1^{+5.7}_{-12}\,^\circ$ is similar to that of any transiting object: a low inclination would not allow an object to transit at all. Again, with large errors, one could be worried about the true inclination value, but when considering the aforementioned fact, and the upper limit of $5.7\,^\circ$, it can be said with 100% confidence that the inclination is correct within errors (otherwise no transits would appear in the light curve).

Now that a mass has been obtained for both TIC 409934330 and its companion, Equation 1.15 was exploited to predict an RV curve of the star and its semi-amplitude, K. Employing the EXOFASTv2-determined orbital period of $P = 2.48881^{+0.0010}_{-0.00082}\,\mathrm{d}$, the EXOFASTv2-determined companion minimum mass of $M_P \sin i = 2.5^{+31}_{-2.1}\,\mathrm{M_J}$, and the MESA and GYRE-determined stellar mass of $M_* = 2.10 \pm 0.19\,\mathrm{M_\odot}$, K was calculated as $228^{+2830}_{-183}\,\mathrm{m\,s^{-1}}$. A synthetic RV curve, with a semi-amplitude of the aforecalculated K, has been super-imposed on the RV data in Figure 5.13: it is impossible to seen any RV signal.

The transit impact parameter of $0.660^{+0.037}_{-0.53}$ is high, suggesting the transit may likely be grazing. This would produce a more V-shaped dip in the light curve, but as can be seen in Figure 5.11 this is not the case, alluding to the idea of a low impact parameter transit, which does fit within errors. Finally, the linear and quadratic

limb-darkening coefficients, γ_1 and γ_2, can be used to model the surface brightness profile of TIC 409934330 using the methods of Mandel & Agol (2002).

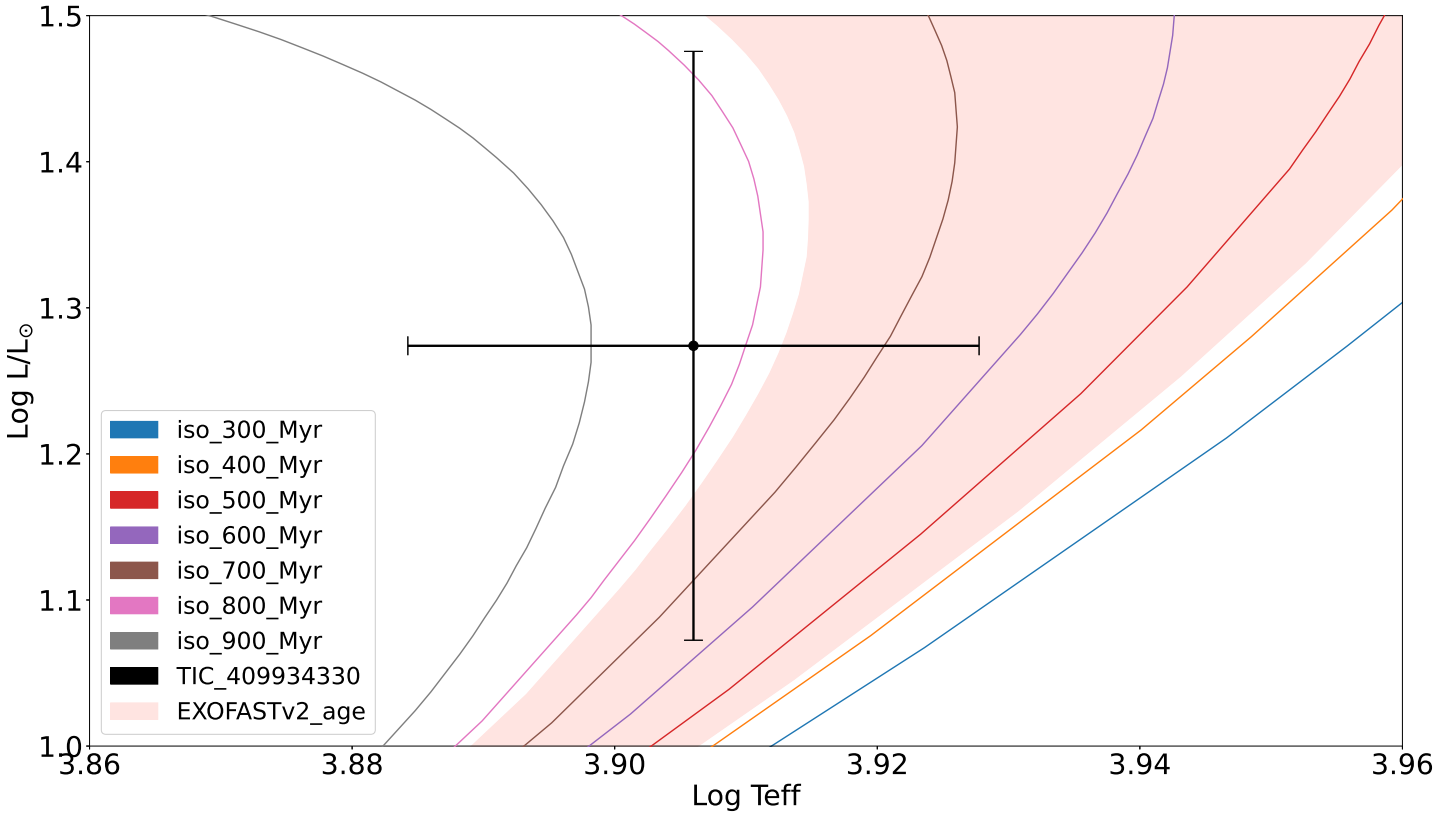

Figure 5.12: *An HR diagram showing the location of TIC 409934330 (black circle) plotted using the* MESA *and* GYRE *results, against the isochrone created from the* EXOFAST*v*2*-outputted age and error (light pink) with an array of other isochrones for reference (respective labels can be found in the key).*

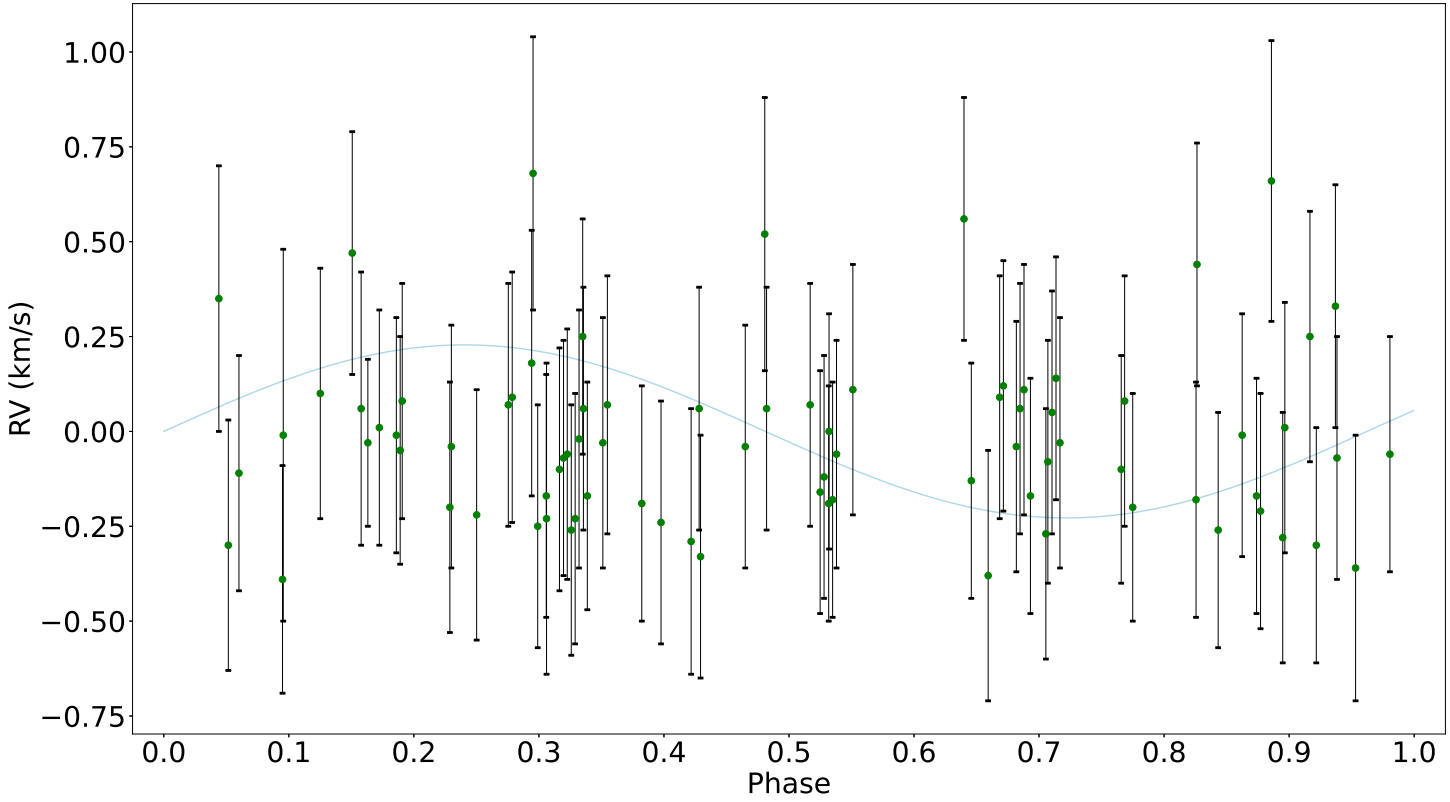

Figure 5.13: *The phased RV curve from Figure 5.10 with the expected RV curve over-plotted as the blue line ($K = 228\,m\,s^{-1}$).*

5.9.1 The δ Scuti Cone

I here hypothesise that there is a cone-shaped region inside the HR diagram, shown by Figure 5.14. This region of $T_{\rm eff} - \frac{\rm L}{\rm L_{\odot}}$ parameter space is a sub-region within which δ Scuti host stars do *only* exist, laying firm foundations for addressing the discrepancies between said δ Scuti host stars and standard, non-pulsating A-type hosts (and the dearth of the former). This small sample occupies only the lower-left region of the δ Scuti star population, and is clearly separated from the main spread of non-pulsating A-type hosts stars, inhabiting its own locality. All data points within Figure 5.14 have undergone the Flower (1996) bolometric corrections, with the Torres (2010) updated coefficients. The δ Scuti host star sample will be added to in future work, and with the target star in Chapter 6, constraining the δ Scuti cone further and evolving this hypothesis. For consistency, the same cut of stars only with $T_{\rm eff} > 6300\,{\rm K}$ were included in this plot, following the methods used earlier in this Chapter when identifying TESS targets.

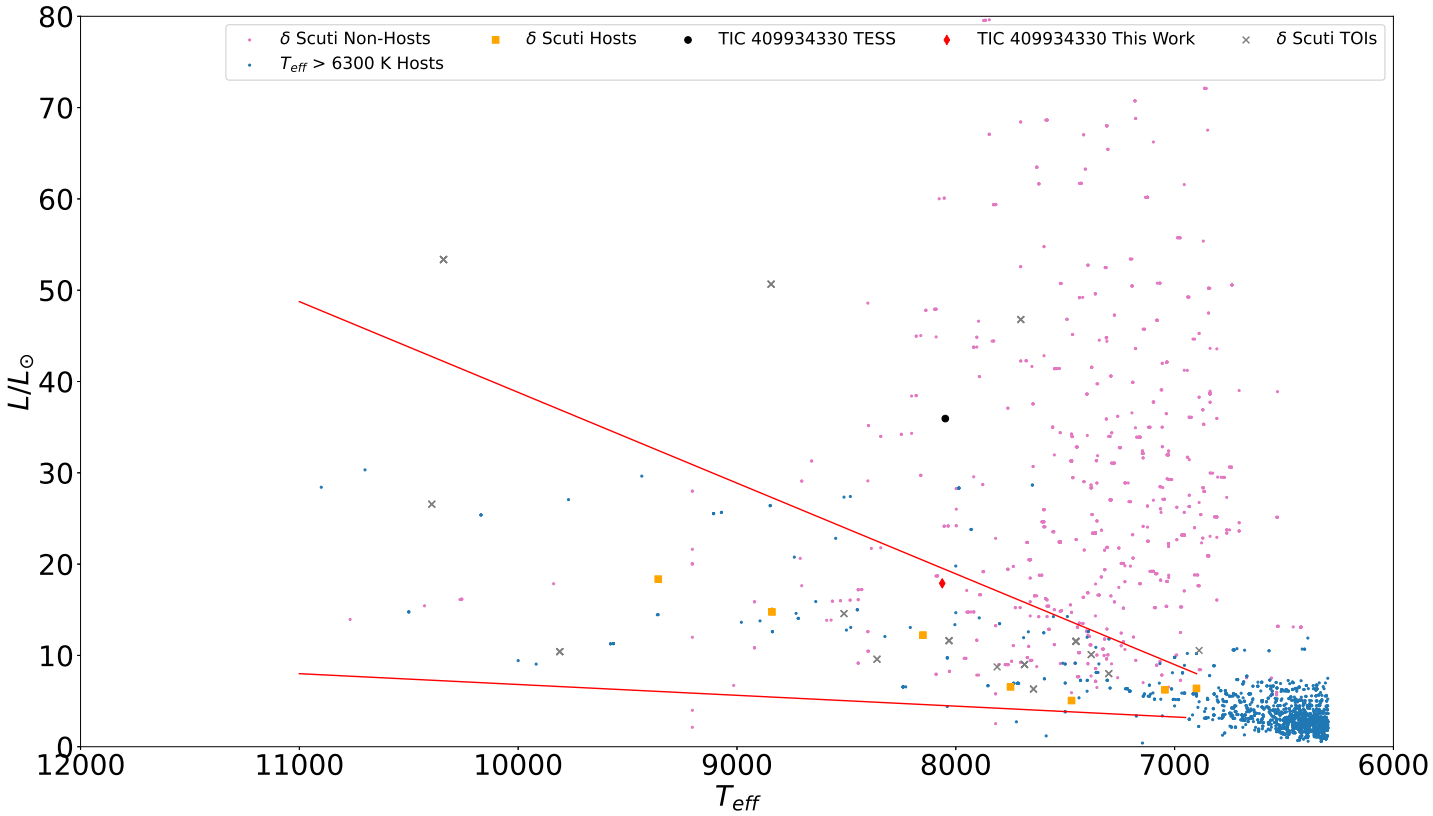

Figure 5.14: *An HR diagram showing the δ Scuti cone outlined by the red lines. The pink points are non-host δ Scuti stars, the blue points are all host stars with* $T_{\rm eff} > 6300\,{\rm K}$*, the orange squares are the known δ Scuti host stars, the black circle is TIC 409934330 (TESS), the red diamond is TIC 409934330 (this work), and the grey crosses are the δ Scuti TOIs yet to be confirmed as host stars. All data points have undergone the Flower (1996) bolometric corrections, with the Torres (2010) updated coefficients.*

5.10 Conclusions

A star — TIC 409934330 — was selected from the TOI catalogue of TESS data as it exhibited δ Scuti pulsations in its light curve, as well as luminosity dips caused from a transiting companion. Numerical ranges for the parameters of mass, equatorial rotation and convection overshoot were extensively calculated and used as initial constraints for a grid of models that was built using the software MESA. From here, each of the MESA models in the grid were put through the software GYRE, which perturbed the model stars such that the output files listed that frequencies of pulsations that such stars would have. In total, 4,780,944 individual models of pulsating stars were created, with each varying slightly in mass, rotational velocity and level of convective overshoot by the quantities listed in Table 5.6c, and between -3 and 3 — where applicable — in the quantum numbers ℓ and m. In parallel, PERIOD04 was used to extract astrophysical pulsational frequencies from the Fourier transform of the light curve of TIC 409934330 (combination frequencies were checked for and removed). This list of astrophysical frequencies was used as a comparison for frequencies within each of the GYRE models: a chi-squared analysis was performed to locate and determine the closest match between the GYRE model frequency lists and the TESS frequency list, and hence find the best-fitting MESA model star to the TESS data. There resulting best-fitting model is comprised of a $2.10 \pm 0.19\,\mathrm{M}_{\odot}$ star with a radius of $4.72 \pm 0.44\,\mathrm{R}_{\odot}$, an equatorial rotation velocity of $60 \pm 0.5\,\mathrm{km\,s^{-1}}$ and an overshoot parameter of $f_{\mathrm{ov}} = 0.028 \pm 0.0005$.

In addition to the above, ground-based observations were performed as a follow-up to the TESS observations. Using the 40″ telescope at the SAAO TIC 409934330 was observed in the *UBVRI* filters, extending the TESS *RI* bandpass into the shorter wavelengths: unfortunately, bad weather denied us data with a high enough quality for analysis. SALT, however, did provide some good quality data: it observed TIC 409934330 spectroscopically and allowed for spectral abundance analysis to be

performed with the software iSpec, which again-proved the star's Am-nature. Furthermore, iSpec was utilised to determine a projected rotation velocity rate for the star, $55 \pm 3\,\mathrm{km\,s^{-1}}$, a T_{eff} measurement of $8062 \pm 29\,\mathrm{K}$, and determined $\log g$ to be 3.86 ± 0.21. An attempt was made to observe the radial velocity of TIC 409934330 caused by the companion, but the RV was lower than SALT's precision.

Finally, EXOFASTv2 modelled the companion based off just the transit data and the model star parameters, and obtained a planetary mass value of $2.5^{+31}_{-2.1}\,\mathrm{M_J}$ and radius value of $1.03^{+0.85}_{-0.49}\,\mathrm{R_J}$, as well as a plethora of additional parameters listed in Table 5.16. From this we can say with confidence that the companion, now TIC 409934330 b, is of a hot-Jupiter nature, with a higher density than that of its namesake. As a consequence, TIC 409934330 forms an additional data point on the δ Scuti Cone (§ 5.9.1), and increases the number of known δ Scuti stars that host a planet from seven to eight (Ebo et al., (a) in prep).

The work discussed above was presented via posters and talks at the 2022 TASC Meeting at KU Leuven, the 2022 UKEXOM Meeting in Edinburgh, and 2023 National Astronomy Meeting in Cardiff.

Chapter 6

The TIC 156987351 (HD 47874) System

6.1 Introduction: Nomenclature

This Chapter contains in-depth scientific analysis of a star observed during the TESS primary mission, flagged as TOI 476.01. Its TESS designation is TIC 156987351, which will be used throughout this Chapter. It must be stressed that even though this star has been observed historically, it has not been previously targeted, studied, or published with any exoplanetary or asteroseismic themes. That is to say: TIC 156987351 is a known star so is not a new discovery here, but the work done in this Chapter and to be published in Ebo et al. (b) (in prep) is entirely new and contains wholly original contributions to the aforementioned fields.

6.2 Previous Observations of TIC 156987351

TIC 156987351 was first catalogued by Henry Draper over 130 years ago, receiving its maiden designation of HD 47874 (Pickering, 1890; Maury & Pickering, 1897),

followed closely by observations from Cordoba Observatory (The Argentine National Observatory) by Thome (1892) who gave the designation CD-47 2496. But TIC 156987351 was not observed scientifically until 1978, producing the star's still-accepted spectral type of F2 (Houk, 1978). In 1991, TIC 156987351 was used in a survey to determine interstellar reddening via uvbyβ observations due to its early F-type nature (Perry, 1991), and again five years later in the second such survey (Perry & Christodoulou, 1996): these works led TIC 156987351 to be published in a uvbyβ photoelectric photometric catalogue (Hauck & Mermilliod, 1998), and more recently in a Stroemgren-Crawford uvbyβ photometry catalogue (Paunzen, 2015). The turn of the new millennium yielded the accepted B and V magnitude measurements of 9.46 ± 0.02 and 9.17 ± 0.02, respectively (Høg et al., 2000), followed in 2003 with the accepted values of the J, H and K magnitude measurements as 8.534 ± 0.030, 8.432 ± 0.038 and 8.387 ± 0.023, respectively (Cutri et al., 2003). A further magnitude value, G Mag, was measured to be 9.102 ± 0.003 in 2020 by the *Gaia* Collaboration using DR3 data (Gaia Collaboration, 2020), who also measured the accepted International Celestial Reference System (ICRS) coordinates of 06:38:19.54 ($\pm$ 00:00:00.01) -47:36:49.90 ($\pm$ 00:00:00.01), proper motion of -0.24 ± 0.02 mas N -1.43 ± 0.02 mas E, and parallax of 4.17 ± 0.013 mas. The most recent works include TIC 156987351 being a member of a catalogue involving stellar diameters and mid-infrared interferometry (Cruzalèbes et al., 2019), and a survey by Zhou et al. (2019) who were investigating the occurrence rate of hot Jupiters around A-type stars in the TESS data. It was in that same year that TIC 156987351 was flagged from TESS mission data as a Tess Object of Interest (TOI 476.01) by the NASA Ames Research Centre's Science Processing Operations Center (SPOC) pipeline (See Appendix F).

Table 6.1 contains the complete list of all different designations for TIC 156987351, invested from all previous surveys. The above parameters, and more, can be found in Table 6.3.

Table 6.1: *All designations for TIC 156987351 from historic observations.*

Survey	Designation	Reference(s)
Cordoba Observatory, Durchmusterung (CD)	CD-47 2496	(Thome, 1892) (Thome, 1894) (Thome, 1900) (Thome, 1914) (Perrine, 1932)
Cape Observatory, Photographic catalogue (CPC)	CPC 0 3759	(Jackson & Stoy, 1954) (Jackson & Stoy, 1955a) (Jackson & Stoy, 1955b) (Jackson & Stoy, 1958) (Stoy, 1966) (Stoy, 1968)
Cape Observatory, Photographic Durchmusterung (CPD)	CPD-47 899	(Gill & Kapteyn, 1896) (Gill & Kapteyn, 1897) (Gill & Kapteyn, 1900) (Gill, 1903)
Gaia	DR1 5552450294824061568	(Gaia Collaboration et al., 2016a) (Gaia Collaboration et al., 2016b) (Gaia Collaboration et al., 2018) (Gaia Collaboration et al., 2021) (Panahi et al., 2022)
Gaia	DR2/DR3 5552450299121421696	(Gaia Collaboration et al., 2016a) (Gaia Collaboration et al., 2016b) (Gaia Collaboration et al., 2018) (Gaia Collaboration et al., 2021) (Panahi et al., 2022)
Geneva Identification System (GEN#)	GEN# +1.00047874	URL: cds.unistra.fr (Lasker et al., 1990)

Guide Star catalogue (GSC)	GSC GSC 08108-01867	(Russell et al., 1990) (Jenkner et al., 1990) (Lasker & et al., 1990) (Morrison et al., 2001)
Henry Draper (HD)	HD 189995	(Pickering, 1890) (Maury & Pickering, 1897) (Cannon & Pickering, 1918) (Cannon, 1925a) (Cannon, 1925b) (Cannon, 1927) (Cannon, 1928) (Cannon, 1931) (Cannon, 1936) (Cannon & Mayall, 1949) (Roeser, Bastian & Wiese, 1991) (Nesterov et al., 1995)
2Micron All-Sky Survey (2MASS)	2MASS J06381954-4736499	(Cutri et al., 2003)
Position and Proper Motion (PPM)	PPM 310966	(Röeser & Bastian, 1988) (Röser, Bastian & Kuzmin, 1994)
Smithsonian Astrophysical Observatory (SAO)	SAO 218082	(Haramundanis, 1967)
TESS Input catalogue (TIC)	TIC 156987351	(Stassun et al., 2018) (Stassun et al., 2019)
Tycho mission (TYC)	TYC 8108-1867-1	(ESA, 1997) (Høg et al., 2000)
uvbyβ Photoelectric Photometric Catalogue (uvby98)	uvby98 100047874	(Hauck & Mermilliod, 1998) (Mason et al., 2001)

6.3 TESS Observations of TIC 156987351

TIC 156987351 has been observed on seven occasions by TESS. Table 6.2 lists the Sectors that it was observed in — with the respective dates — alongside which Camera and CCD the star appeared in, and what cadence of data is available. Table 6.3 lists the initial parameters known for TIC 156987351; the information in Table 6.2 was extracted from the TASOC, and the data populating Table 6.3 were taken from the TIC (Guerrero et al., 2021) and the SIMBAD database.

Table 6.2: *The TESS observations of TIC 156987351, listing the Sectors, Cameras and CCDs that the star appeared in, alongside the respective dates of each observation and the available cadences of the data. The information in this table was retrieved from the TIC.*
† *These data exist in the TESS Full Frame Images (FFIs) which pipelines have yet to process.*

Sector	Start (UTC)	End (UTC)	Camera	CCD	Available Cadences (sec)
6	12/12/198	06/01/19	3	4	120, 1800
7	07/01/19	02/02/19	3	3	120
8	02/02/19	28/02/19	3	3	—†
32	19/11/20	17/12/20	3	4	—†
33	17/12/20	13/01/21	3	4	120
34	13/01/21	09/02/21	3	3	120
61	18/01/23	12/02/23	3	3	—†

Figure 6.1 shows the light curve of TIC 156987351 created from the data taken during Sector 6. It was not raw data used to create this light curve, but the publicly-available reduced data that had been processed through the TESS SPOC pipeline (see Appendix F).

When studying Figure 6.1 it becomes apparent that TIC 156987351 hosts a transiting object: across the 27-d timebase, seven equally-spaced periodic dips in the light curve can be seen. The cause of equally-spaced dips in a star's light curve is

Table 6.3: *Prior-known stellar properties and parameters of TIC 156987351, gathered from the TESS Input catalogue (TIC) and SIMBAD databases, indicated by* † *and* ††*, respectively. Data marked with* ‡ *were identical in both databases. References from the SIMBAD-retrieved data can be found in § 6.2. The parameters [Fe/H] and U Mag are omitted as no such data could be retrieved.*

Parameter	Value
Right Ascension	06 38 19.540‡
Declination	-47 36 49.898‡
Spectral Type	F2‡
Star Classification	EB††
$T_{\rm eff}$ (K)	$7450 \pm 160^{\dagger}$
$\log g$ (cgs)	4.05†
B Mag	9.46‡
V Mag	9.17‡
R Mag	8.86††
I Mag	8.76††
J Mag	8.53‡
H Mag	8.43‡
K Mag	8.39‡
Gaia Mag	9.10†
T Mag	8.87†
Parallax (mas)	$4.17 \pm 0.01^{\dagger}$

due to the presence of a companion blocking out a fraction of star light as it transits across the star from an observer's point-of-view, repeating once per orbit. The seven dips in Figure 6.1 are clearly equally spaced, and hence TIC 156987351 was entered into the TOI catalogue as TOI-476, and the newly flagged planet-candidate was designated TOI-476.01.

By studying the equal spacing of the dips, it can be said with confidence that the data-download gap at JD ≈2458477.5 does not omit another dip, therefore will not cause a problem in future calculations. From this visual information, a first approximation of the orbital period of this planet-candidate can be made by dividing the seven transits by the 27-day timebase: $P \approx (27/7) \approx 3.9\,\mathrm{d}$.

There is more to TIC 156987351 than it just being a potential host star, however.

Conventionally, the depth of a transit-induced dip in a light curve remains constant over time. This is intelligible, as the depth of the dip is a direct measurement of the ratio between the radius of the companion and the radius of the host star, both of which typically remain constant. Yet, when studying the transit depths in Figure 6.1, no two are the same. This indicates that either the radius of the companion is changing over time, or the radius of the star. A companion can lose or gain mass throughout its lifetime, but it is very unrealistic for this to be occurring by so much on this time scale. Furthermore, the out-of-transit sections of the light curve show variance over time, rather than a smooth "constant" signal. In consequence, it must be that TIC 156987351 itself is varying in size over short time periods, and is therefore another example of a pulsating star hosting a companion.

To discover the pulsational nature of TIC 156987351, a Fourier transform of the light curve in Figure 6.1 was generated — shown in Figure 6.2 — revealing the star's pulsational frequencies (see § 1.1.2 for discussions on Fourier transforms of light curves). The lowest-frequency peak is the frequency of the orbital period of the companion, and the following equally-spaced cascade of peaks are its harmonics. The remaining high-amplitude peaks (5-30 c/d) are signatures of δ Scuti pulsations, so we conclude that TIC 156987351 is a δ Scuti star: Figure 6.3 shows only δ Scuti pulsations once the orbital frequency and its harmonics have been removed.

The 1st harmonic exhibits a slightly higher amplitude than that of the orbital frequency due to the combination of the primary and secondary transits constructively interfering, hence it appears at exactly twice the frequency of the orbital period. This occurs for all harmonics, but with reduced power and hence lower amplitudes with increasing frequency.

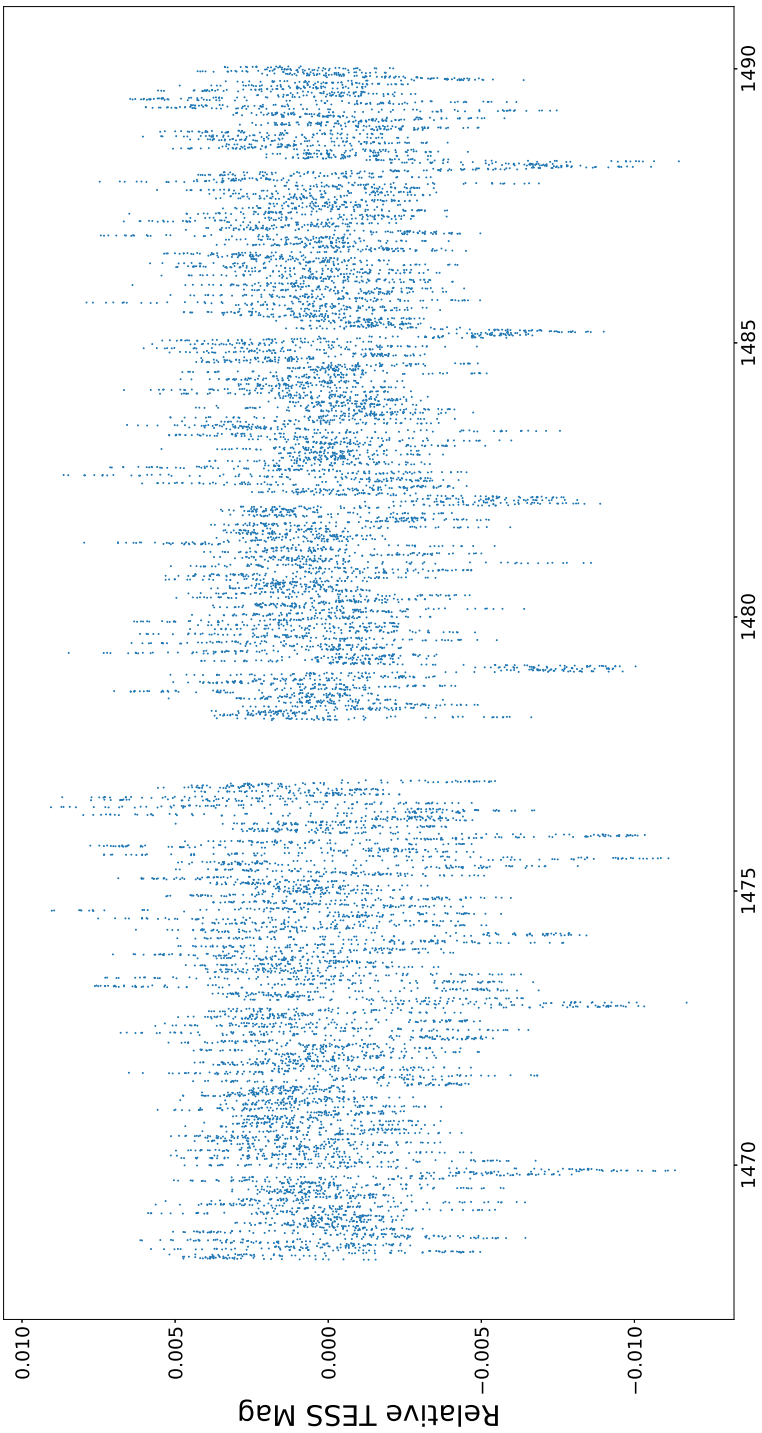

Figure 6.1: *The light curve of TIC 156987351, constructed using data taken from TESS observations during Sector 6.*

Figure 6.2: *The Fourier transform of the light curve in Figure 6.1. The orbital frequency of the companion and following cascade of harmonics are the low-frequency peaks at <5 c/d. Classical δ Scuti pulsations can be see between 5-30 c/d.*

Figure 6.3: *The same Fourier transform as Figure 6.2, but with the orbital frequency and its harmonics removed revealing only δ Scuti pulsations.*

6.4 Modelling the Host Star

6.4.1 Pre-Main Sequence Models

The software MESA (see § 3.1 Paxton et al., 2011, 2013, 2015, 2018, 2019) was used to build a plethora of stellar models. Following the methods used for TIC 409934330 in Chapter 5, the evolution for each model star was separated into two parts: a pre-main sequence evolution up to the ZAMS, and a main sequence evolution tending towards the TAMS. As before, the reason for separating each evolutionary run across the ZAMS was that MESA cannot incorporate stellar rotation across one complete evolution, leading to incorrect models (see § 3.1.4.2 for a more empirical example and explanation of this). The pre-main sequence models were constructed first, and again, the only changing parameter was the stellar mass. Again, suitable mass ranges were calculated for TIC 156987351 to save creating pre-main sequence models for the entire stellar mass range of the HR diagram, where only a small fraction of the models would be useful. Hence, as with TIC 409934330, several mass ranges were calculated via different iterations of calculation, based on the errors of some of TIC 156987351's parameters such as parallax and $T_{\rm eff}$.

As the mass-luminosity relationship is the crux of these calculations, it was used to obtain two extreme values of stellar mass for TIC 159687351 and hence a mass range for the pre-main sequence models. See Equation 5.1 for the generally-accepted mass-luminosity relationship (Duric, 2004; Salaris & Cassisi, 2005), and Table 5.4 for the values that $\boldsymbol{x}$ and $\boldsymbol{a}$ in Equation 5.1 take depending on stellar mass.

TIC 159687351 has its spectral type classified as F2 (Houk, 1978), and is therefore likely to have a mass under $2.0\,\mathrm{M}_{\odot}$. When studying the mass-$T_{\rm eff}$-spectral type table of Pecaut & Mamajek (2013), it can be seen that an average F2-type star has a mass of $1.46\,\mathrm{M}_{\odot}$, with $T_{\rm eff} = 6820\,\mathrm{K}$. However, the $T_{\rm eff}$ of TIC 156987351 from the TIC is strikingly hotter at 7450 K (Guerrero et al., 2021) which would put it inline with an

A9-type star with a mass of $1.75\,M_{\odot}$, according to Pecaut & Mamajek (2013)'s table. This 630 K-difference between the two values of T_{eff} may be due to TIC 159687351 straddling the boundary of sub-giant and main sequence star (its classification varies between IV – V), but this should not affect T_{eff} as across the HR diagram sub-giant stars are more luminous than their main sequence counterparts, but not hotter. Either way, with both aforementioned masses comfortably less than $2.0\,M_{\odot}$, only Equation 5.2 was needed to calculate the mass ranges.

As with TIC 409934330, the strategy for TIC 156987351 also took into account the astrophysical thickness that the main sequence track exhibits across the HR diagram, from the works of Fernandes, Lebreton & Baglin (1996) and Lebreton et al. (1997), which lead to an error in magnitude for TIC 156987351. To save space the calculations are not shown in the following sections, but they follow the workings seen in the respective Sections in Chapter 5.

6.4.1.1 The Error in Parallax

Parallax was the first parameter used as its error leads to a change in the brightness of a star, and hence its determined luminosity.

Table 6.3 lists the value of parallax taken from the TIC as 4.17 ± 0.01 mas; the two extremes of which were hence taken as 4.16 mas and 4.18 mas. With these two values, two sets of calculations were performed in parallel.

First, the inverse of the parallaxes (in arcsecs) were taken to obtain distances (in parsecs) using Equation 5.4, which were then used to calculate the two values for M_V of TIC 156987351, utilising the TIC value of V Mag in Table 6.3, employing a slightly rearranged version of the distance modulus equation, given as Equation 5.5. Following this, the calculated M_V values were transformed into luminosities (in terms of Solar luminosity), via Equation 5.6, and then into masses with the mass-luminosity equation given as Equation 5.2 (this time not using Equation 5.3 as TIC 156987351

is already known to be less than 2.0 $M_\odot$). As mentioned above, full workings here are omitted but the calculations followed their respective calculations in § 5.4.1.1.

Due to the very small error on the parallax, the total mass uncertainty from these causes is also very small: 1.8109... $\leq M_\odot \leq$ 1.8165..., and to three significant figures they are identical at $\mathbf{1.81\,M_\odot}$. Hence, distance uncertainty can be safely ignored. This mass is listed with the other calculated mass ranges in Table 6.4.

6.4.1.2 The Effect of the Main Sequence Width

The track that the main sequence cuts across the HR diagram is not infinitesimally thin. It exhibits a physical width, inducing a small but non-trivial error on the brightness of main sequence stars: their position on the main sequence path is not an absolute position, but instead stars lie within a narrow window on the HR diagram, constrained by the thickness of the main sequence.

Discussed in more detail in § 5.4.1.2, the same three main sequence width errors were used for TIC 156987351: $M_V \pm 0.275$ from a main sequence width of $M_V \approx 0.55$ according to Fernandes, Lebreton & Baglin (1996), and both $M_V \pm 0.125$ and $M_V \pm 0.225$ from the two different main sequence widths of $M_V \approx 0.25$ and $M_V \approx 0.45$, respectively, according to Lebreton et al. (1997).

To use the above absolute magnitude errors to find mass ranges, the same methods were followed as when calculating the mass range based on the parallax error in § 6.4.1.1, but this time including the error in M_V. Initial values of M_V were taken from § 6.4.1.1 to save recalculation. As previously, full workings here are omitted but the calculations followed their respective calculations in § 5.4.1.2.

(Fernandes, Lebreton & Baglin, 1996)

The two extremes of M_V used here were taken from the calculations used in

§ 6.4.1.1, and then the error of $M_V \pm 0.275$ was applied to each giving four values of M_V. The smallest and largest M_V values were then inputted into Equation 5.6 to transform them into luminosities, before being put through Equation 5.2 to calculate the stellar masses. The total mass uncertainty from these causes was $\mathbf{1.70 \leq M_{\odot} \leq 1.94}$. This mass range is listed with the other calculated mass ranges in Table 6.4.

(Lebreton et al., 1997)

Once again the two extremes of M_V used here were taken from the calculations used in § 6.4.1.1. With the two errors of $M_V \pm 0.125$ and $M_V \pm 0.225$ this time, the calculations were split into two parts.

1) Employing an error bar of approximately $M_V \pm 0.125$: again the smallest and largest M_V values were taken and put through Equation 5.6 to transform them into luminosities, before going through Equation 5.2 to obtain the stellar masses. The total mass uncertainty from these causes was $\mathbf{1.76 \leq M_{\odot} \leq 1.87}$. This mass range is listed with the other calculated mass ranges in Table 6.4.

2) Employing an error bar of approximately $M_V \pm 0.225$: again the smallest and largest M_V values were taken and put through Equation 5.6 to transform them into luminosities, before going through Equation 5.2 to obtain the stellar masses. The total mass uncertainty from these causes was $\mathbf{1.72 \leq M_{\odot} \leq 1.91}$. This mass range is listed with the other calculated mass ranges in Table 6.4.

6.4.1.3 The Error in T_{eff}

As above, the value of T_{eff} listed in Table 6.3 for TIC 156987351 — $T_{\text{eff}} = 7450 \pm 160\,\text{K}$ — was taken from the TIC. The 160 K error was taken from Stassun et al. (2018), and was used to obtain two T_{eff} extremes: $T_{\text{eff}} = 7290\,\text{K}$ and $T_{\text{eff}} = 7610\,\text{K}$.

Equation 5.8, derived by Wang & Zhong (2018) from the mass-luminosity relation in Equation 5.2, was modified by placing T_{eff} as an exponent to luminosity. This slight modification allows T_{eff} to have more significance on the mass of the star. Equation 5.8 was used in the calculations below, with values for stellar luminosity taken from § 6.4.1.2 — from each variant of the main sequence width — to save recalculation. As previously, full workings here are omitted but the calculations followed their respective calculations in § 5.4.1.3. Finally, a value of T_{eff} for the Sun was required, and taken to be $T_{\text{eff}} = 5772\,\text{K}$ (Prša et al., 2016).

$\underline{M_V \approx 0.55}$

The two extremes of luminosity and T_{eff} used here were taken from the main sequence width calculations above, and were used together with the main sequence width error of $M_V \pm 0.275$. The four configurations of luminosity and T_{eff} were inputted into Equation 5.8 to calculate the stellar masses. The total mass uncertainty from these causes was $\mathbf{1.53 \leq M_{\odot} \leq 1.77}$. This mass range is listed with the other calculated mass ranges in Table 6.4.

$\underline{M_V \approx 0.25}$

The two extremes of luminosity and T_{eff} used here were taken from the main sequence width calculations above, and were used together with the main sequence

width error of $M_V \pm 0.125$. The four configurations of luminosity and $T_{\rm eff}$ were inputted into Equation 5.8 to calculate the stellar masses. The total mass uncertainty from these causes was $\mathbf{1.58 \leq M_{\odot} \leq 1.71}$. This mass range is listed with the other calculated mass ranges in Table 6.4.

$M_V \approx 0.45$

The two extremes of luminosity and $T_{\rm eff}$ used here were taken from the main sequence width calculations above, and were used together with the main sequence width error of $M_V \pm 0.225$. The four configurations of luminosity and $T_{\rm eff}$ were inputted into Equation 5.8 to calculate the stellar masses. The total mass uncertainty from these causes was $\mathbf{1.55 \leq M_{\odot} \leq 1.75}$. This mass range is listed with the other calculated mass ranges in Table 6.4.

6.4.1.4 Error in Mass Results

Table 6.4 lists the results from all of the different methods used to calculate the mass ranges. These results are shown graphically as horizontal bars in Figure 6.4.

To ensure that the ranges would be appropriate to use for the pre-main sequence models, they were compared against literature values of masses of stars with similar spectral types to TIC 156987351 (F2). As mentioned earlier, Pecaut & Mamajek (2013) specifically state that a typical mass of an F2-type star is $1.46\,M_{\odot}$. For completeness, Pecaut & Mamajek (2013) provide mass estimates across the full range of F-type stars, giving an upper and lower mass-boundary of $1.08\,M_{\odot}$ and $1.61\,M_{\odot}$ for F9.5 and F0 stars, respectively. Extending this boundary further, Pecaut & Mamajek (2013) state that a typical mass of a G0 star is $1.06\,M_{\odot}$, and $1.75\,M_{\odot}$ for an A9 star. Taking the midpoint in-between G0 – F9.5 and F0 – A9, a full mass

Table 6.4: *All sets of calculated mass ranges for the pre-main sequences models for TIC 156987351.*
†*(Pecaut & Mamajek, 2013),*
††*(Fernandes, Lebreton & Baglin, 1996),*
‡*(Lebreton et al., 1997).*

Source of Error	Calculated Stellar Mass Range
T_{eff} - Mass†	$1.63 \leq \text{M}_{\odot} \leq 1.72$
Parallax	$1.81\,\text{M}_{\odot}$
Parallax & $M_V \approx 0.55$††	$1.70 \leq \text{M}_{\odot} \leq 1.94$
Parallax & $M_V \approx 0.25$‡	$1.76 \leq \text{M}_{\odot} \leq 1.87$
Parallax & $M_V \approx 0.45$‡	$1.72 \leq \text{M}_{\odot} \leq 1.91$
Parallax & $M_V \approx 0.55$†† & T_{eff}	$1.53 \leq \text{M}_{\odot} \leq 1.77$
Parallax & $M_V \approx 0.25$‡ & T_{eff}	$1.58 \leq \text{M}_{\odot} \leq 1.71$
Parallax & $M_V \approx 0.45$‡ & T_{eff}	$1.55 \leq \text{M}_{\odot} \leq 1.75$

range for F-type stars can therefore be assumed as $1.07\,\text{M}_{\odot} - 1.68\,\text{M}_{\odot}$: this is the cyan region in Figure 6.4. For completeness, the A-type star mass range was taken from § 5.4.1.4 as $1.68\,\text{M}_{\odot} - 2.47\,\text{M}_{\odot}$: this is the blue region in Figure 6.4.

In Figure 6.4 it can be seen not all mass ranges agree within error. Using the argument of $M_V \pm 0.25$ being the most likely astrophysical width of the main sequence (from § 5.4.1.4), it was decided that the mass range should be taken from the lower-bound of the grey bar, across the F-type/A-type boundary, and up to the upper-bound of the purple bar: $1.58\,\text{M}_{\odot}$ up to $1.87\,\text{M}_{\odot}$. And as before: since the work of Pecaut & Mamajek (2013) was to two decimal places, the mass increase from model to model was to be $0.01\,\text{M}_{\odot}$. The final mass range is highlighted in Figure 6.4 as the orange region.

6.4.2 Main Sequence Models

The most prominent aspect of each model was the main sequence evolution. The inlists of each were inspired by the work in Khalack et al. (2019), and a further two parameters became variables alongside stellar mass: stellar rotation, and convective

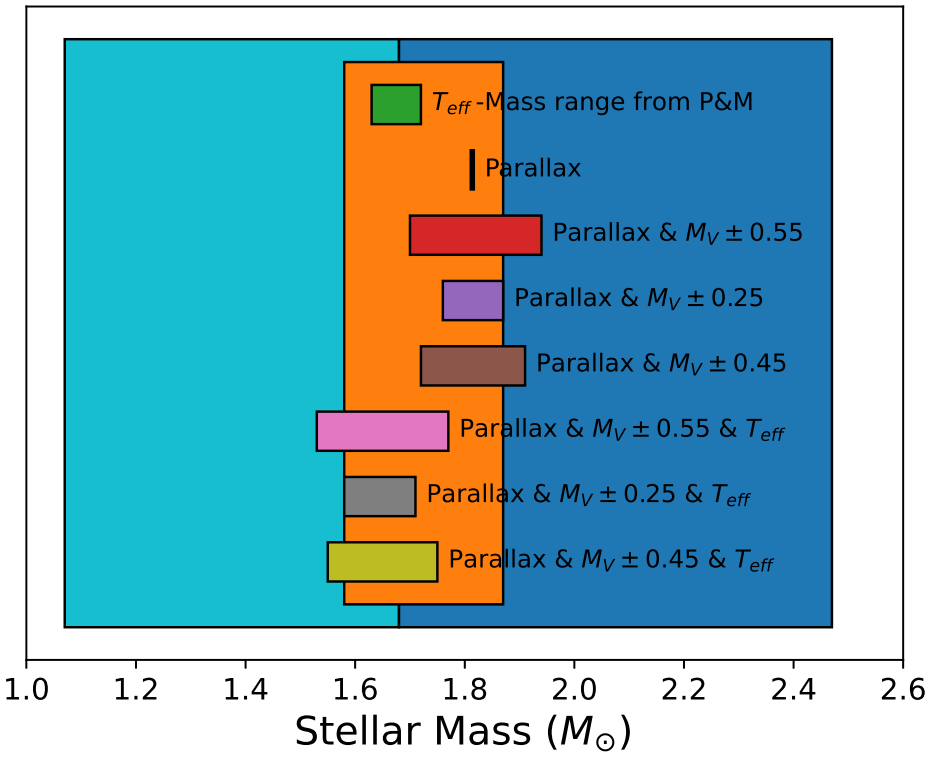

Figure 6.4: *All calculated mass ranges from Table 6.4 represented by the horizontal bars, each labelled with the respective source of error used to calculate its mass range. The cyan-shaded region is the assumed full mass range of all F-type stars and the blue-shaded region is the assumed full mass range of all A-type, based on mass estimates given by Pecaut & Mamajek (2013). The orange-shaded region is the final mass range that was used to create the pre-main sequence models,* $\boldsymbol{1.58\,M_\odot - 1.87\,M_\odot}$*, chosen from the lower-limit of the grey bar to the upper-limit of the purple bar. It can be seen that not all mass ranges agree within error, and that they straddle the crossover region between F-type and A-type stars.*

"P&M" = Pecaut & Mamajek (2013).

overshoot.

6.4.2.1 Stellar Mass

As a quick summary of the previous Sub-Sections, the finalised stellar mass range was taken from a variety of mass ranges calculated from errors of parameters such as parallax, the main sequence width, and $T_{\rm eff}$. The final mass range crosses the boundary between F-type and A-type stars, according to the work of Pecaut & Mamajek (2013), and is $1.58\,M_\odot - 1.87\,M_\odot$, as shown in Table 6.5a (the subscript "a" is due to this table being appended to in the following Sub-Sections).

Table 6.5a: *Parameters and respective ranges so far for the stellar models for TIC 156987351.*

Parameter	Range	Step Size
Mass ($M_\odot$)	$1.58 \leq M_\odot \leq 1.87$	$0.01\,M_\odot$

6.4.2.2 Stellar Rotation

Unlike TIC 409934330, TIC 156987351 is a chemically-normal F-type star and as such will not have such a strict rotation limit, nor will it rotate slower than expected as the Am stars do. Fig. [1] of Reiners (2006) maps a sample of stars across $v \sin i$ vs. $B\ V$ space. For TIC 156987351, $B - V = 0.29$[1]. Therefore, even without rotation limit restrictions, Reiners (2006) suggests TIC 156987351 would have a rotation rate between $v \sin i \approx 50 - 100\,\mathrm{km\,s^{-1}}$ — the same range as for TIC 409934330.

The above discussion justified an upper limit for the rotation rate of $100\,\mathrm{km\,s^{-1}}$ again, and the lower limit was implemented using the same methods as for TIC 409934330: Zorec & Royer (2012) sampled the rotation rates of several thousand slow-rotating and fast-rotating chemically-normal and CP A-type stars, which they binned based

[1]Using the B and V magnitude values listed in Table 6.3.

on mass and estimated a rotation rate per bin. Across all stars in their sample, their slowest rotation rate was $28\,\mathrm{km\,s^{-1}}$ (extracted from their Table [5]).

Hence we based our rotation range on the above estimates from Zorec & Royer (2012) — expanding their lower-limit slightly to $20\,\mathrm{km\,s^{-1}}$ — increasing in integer increments of $1\,\mathrm{km\,s^{-1}}$ to the aforementioned upper-limit of $100\,\mathrm{km\,s^{-1}}$, thus finalising an equatorial rotation range of $20 \leq v_{\mathrm{eq}}\,\mathrm{km\,s^{-1}} \leq 100$, as shown in Table 6.5b.

Table 6.5b: *Parameters and respective ranges so far for the stellar models for TIC 156987351.*

Parameter	Range	Step Size
Mass	$1.58 \leq \mathrm{M_{\odot}} \leq 1.87$	$0.01\,\mathrm{M_{\odot}}$
Rotation	$20 \leq v_{\mathrm{eq}}\,\mathrm{km\,s^{-1}} \leq 100$	$1\,\mathrm{km\,s^{-1}}$

6.4.2.3 Convective Overshoot

The astrophysical nature of this parameter is discussed in-depth in § 3.1.4.5, but in short it describes how far a parcel of gas within the convective zone of a star moves from a stable region to an unstable region, leading to effects such as star core masses being higher than predicted (Johnston, 2021).

As before, the "f_{ov}" parameter within the convective overshoot equation (Equation 3.2) was a variable that physically changed the amount of overshoot occurring within the model stars, and as with TIC 409934330 we turned once again to the methods within Khalack et al. (2019) and took their overshoot parameter range as the foundation for ours, but again extended the lower boundary to zero and increased the incremental resolution for absolute confidence. We therefore finalised an overshoot parameter range of $0.000 \leq f_{\mathrm{ov}} \leq 0.030$ with increment changes of 0.001 per model, as shown in Table 6.5c.

Table 6.5c: *The finalised parameters and respective ranges for the stellar models for TIC 156987351.*

Parameter	Range	Step Size
Mass	$1.58 \leq \mathrm{M}_{\odot} \leq 1.87$	$0.01\,\mathrm{M}_{\odot}$
Rotation	$20 \leq v_{\mathrm{eq}}\,\mathrm{km\,s^{-1}} \leq 100$	$1\,\mathrm{km\,s^{-1}}$
Overshoot	$0.000 \leq f_{\mathrm{ov}} \leq 0.030$	0.001

6.4.2.4 The Final MESA Models

Incorporating the parameter variables described in the previous Sub-Sections, and implementing appropriate physics flags following the work of Khalack et al. (2019, full discussions of each parameter can be found in § 3.1), a total of **72,819** MESA models were created. An example of the inlists used to create the MESA models can be seen in Appendix B. The next step was to set the models pulsating, by feeding each through GYRE.

6.5 Modelling the Stellar Pulsations

Figure 6.1 shows the light curve of TIC 156987351 produced from the Sector 13 data set. With the host star being pulsationally active as well as hosting a companion, the two sets of signals are here intertwined and as such need to be isolated, to allow independent analysis of each. Figure 6.5 — the same Fourier transform as seen in Figure 6.2 — shows the two sets of signals more clearly, with the *red* arrow signalling the frequency of the companion's orbital period and the following *black* arrows highlighting its harmonics (i.e., non-astrophysical signals). The *green* arrows show harmonics that may at first be mistaken as pulsational frequencies. The unlabelled peaks are the astrophysical frequencies of TIC 156987351's pulsations.

Figure 6.3, shown again here as Figure 6.6, is the Fourier transform TIC 156987351 with the orbital frequency and all its harmonic peaks removed such that only signals

intrinsic to TIC 156987351 can be seen. A total of 150 harmonics were removed, to ensure higher-frequency harmonics were not mistaken for pulsation frequencies.

The SPOC pipeline — that initially flagged TIC 156987351 as TOI 476.01 — previously determined the companion's orbital period to be 3.062987 ± 0.000004 d (Guerrero et al., 2021), which when inverted produces an orbital frequency of 0.326479 ± 0.00001 c/d (labelled in Figure 6.5 by the *red* arrow; interestingly this period is $\sim$25% shorter than the period estimation made in § 6.3). This orbital frequency, as well as 150 of its harmonics, were removed from the Fourier transform using the program Period04 (Lenz & Breger, 2005) in a process called pre-whitening (see § 3.5). Only removing the orbital frequency and the "obvious" harmonics would have isolated the stellar pulsational frequencies, but removing an appropriate number of higher-order harmonics as well ensured that any with locally-high amplitudes were not mistaken for stellar pulsational frequencies, and otherwise erroneously included in the modelling process. As can be seen in Figure 6.5, the harmonics indicated by the *green* arrows, for example, could easily have been mistaken as stellar pulsations. Hence, left only a purely-pulsational light curve.

Next, the stellar pulsational frequencies were manually extracted, again using Period04 (Lenz & Breger, 2005). Following the same strategy as with TIC 409934330: as a trade-off between a sufficient number of peaks to achieve the best stellar model possible, and removing any chance of incorrectly incorporating high-amplitude noise, a threshold of ≈ 0.1 mmag was implemented and only peaks with higher amplitudes than this threshold were included (**NB**: note how the noise level is $\sim 5\times$ higher in the data for TIC 159687351 compared with the TIC 409934330 data). A total of 71 frequencies were extracted, and are listed in Table L.1 in Appendix L. The errors in frequency and amplitude were calculated by Period04 using the methods within Montgomery & O'Donoghue (1999).

As with the extracted pulsational frequencies for TIC 409930433, any of the 71

frequencies extracted for TIC 159687351 could be combination frequencies. The same self-written Python script was employed again to cycle through each of the 71 frequencies, calculating the result of every combination of addition or subtraction, for all frequencies and multiples there of — up to the 5^{th} order — following the strategy of Kurtz et al. (2016, identically as with TIC 409934330). A chi-squared analysis was then performed on all 62,909 resulting combinations against the original 71 frequencies, looking for matches that were exact to 1 PPM or more ($>6\sigma$). This time only two were found, and are listed in Table 6.6 alongside their determined combination relationship. The remaining 69 frequencies listed in Table L.2 in Appendix L were confidently believed to be the astrophysical stellar pulsation frequencies of TIC 156987351. Figure 6.7 shows the Fourier transform of TIC 156987351 now with black arrows labelling the discovered combination frequencies. The frequency ν_{63} was not obvious to the eye that it was not astrophysical, and would have caused the MESA and GYRE models to be incorrect. This highlights the importance of calculating combination frequencies.

As with TIC 409934330: in the interests of computational expense, it was deemed unwise to try and fit all 69 remaining pulsational frequencies. Therefore, the cut-off amplitude was increased to include only the highest-amplitude frequencies, enough to achieve a good model fit. This cut-off point was chosen as 0.2 mmag to include only the highest amplitude peaks, and Table 6.7 lists the 8 frequencies that were used in the final analysis.

Figure 6.5: *The same Fourier transform as Figure 6.2, but with the orbital frequency of the companion, its harmonics, and the unrecognisable harmonics, labelled by the red, black and green arrows respectively. The presence of the green-arrowed harmonics signifies the importance of removing harmonics to avoid miss-identifying them as frequency peaks.*

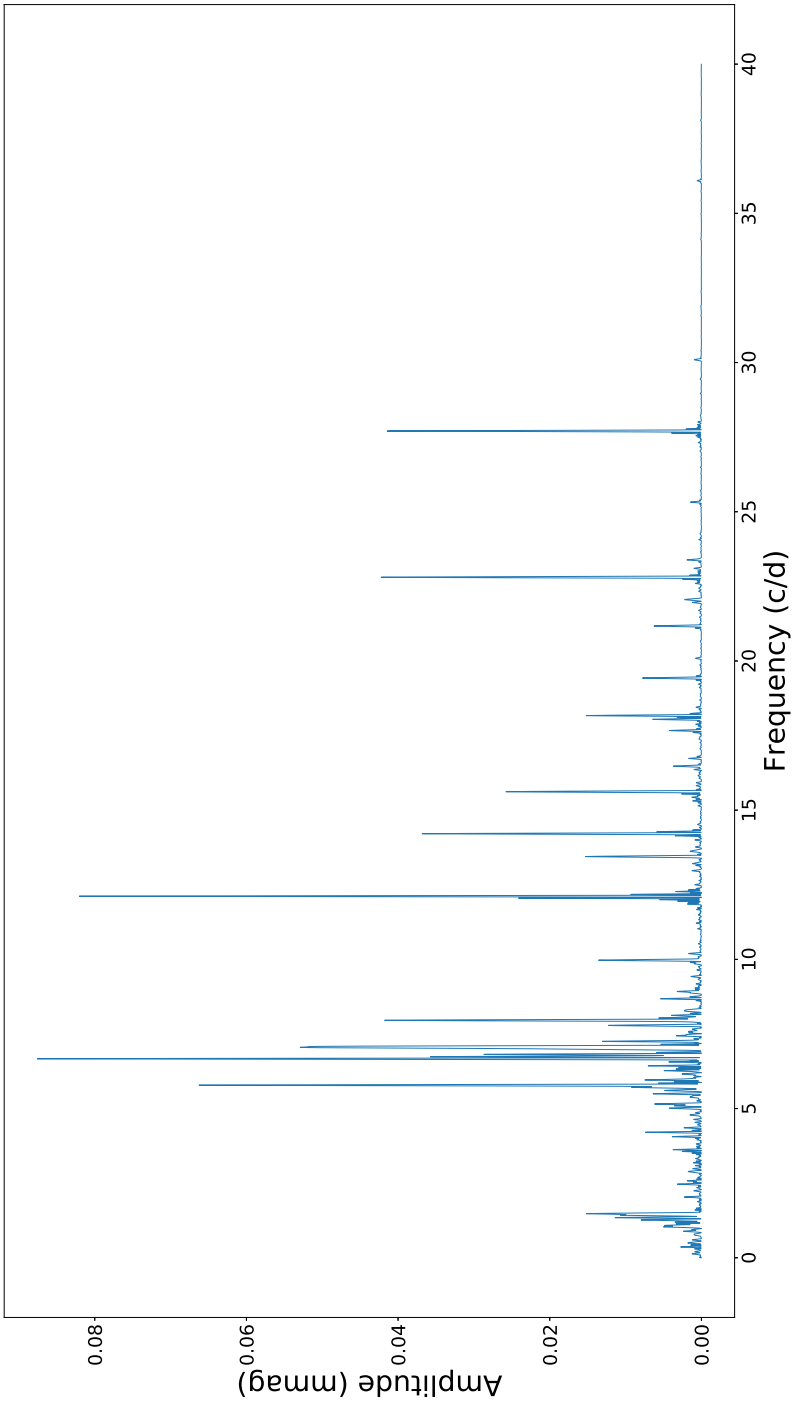

Figure 6.6: *The resultant Fourier transform after 150 harmonics were extracted.*

Table 6.6: *The two combination frequencies that each matched an extracted TESS frequency to 1 PPM or more (>6σ; this table has a higher number of significant figures than other frequency tables in this Chapter and Appendices as proof of the combinations). These frequencies were removed from the list of TESS-extracted frequencies, which is where their errors in frequency and amplitude can be located too (Table L.1 in Appendix L). Figure 6.7 shows where these combination frequencies are in the Fourier transform of TIC 156987351.*

Numerical Combination	Combination Frequency (c/d)	Observed Frequency (c/d)	$\|\Delta(\mathrm{O}-\mathrm{C})\|$ (c/d)	Amplitude (mmag)
$3\nu_3 - 2\nu_2 = \nu_5$	1.3432776	1.3432793	0.0000017	0.4665651
$2\nu_{46} - 2\nu_4 = \nu_{63}$	21.1710428	21.1710464	0.0000036	0.0990460

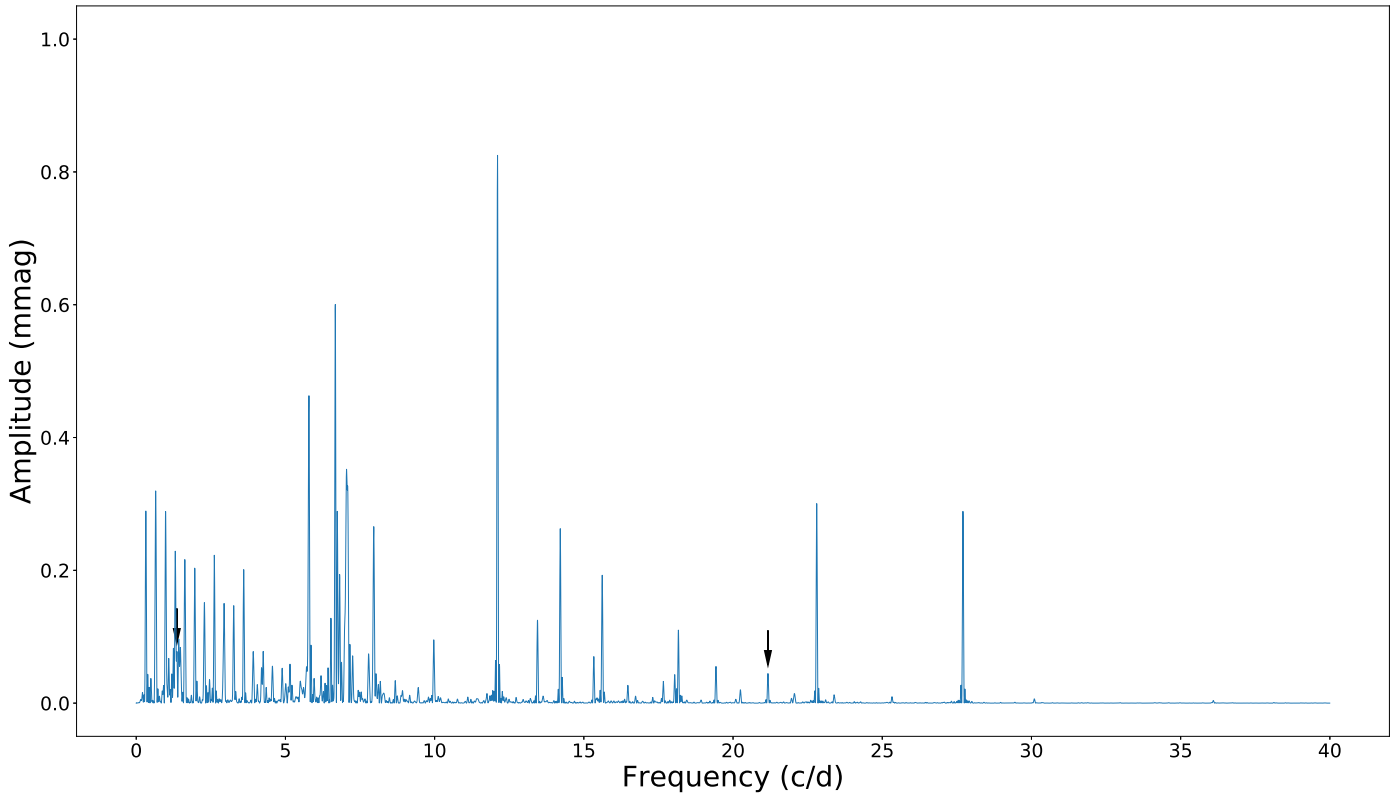

Figure 6.7: *The Fourier transform of TIC 156987351 with black arrows now denoting the locations of the calculated combination frequencies listed in Table 6.6.*

Table 6.7: *The eight highest-amplitude frequencies of pulsation extracted from the Fourier transform of TIC 156987351 that were used in the final stellar modelling.*

Frequency Number	Frequency ν (c/d)	Amplitude (mmag)
ν_{21}	5.7844 ± 0.0003	0.8539 ± 0.0112
ν_{27}	6.6688 ± 0.0003	0.8716 ± 0.0112
ν_{37}	7.9574 ± 0.0004	0.1505 ± 0.0112
ν_{48}	12.1159 ± 0.0002	0.0754 ± 0.0112
ν_{53}	14.2104 ± 0.0004	0.1597 ± 0.0112
ν_{55}	15.6180 ± 0.0005	0.2195 ± 0.0112
ν_{66}	22.8060 ± 0.0004	0.1589 ± 0.0112
ν_{69}	27.7047 ± 0.0004	0.0520 ± 0.0112

The software GYRE (see § 3.2; Townsend & Teitler, 2013) was once again employed to perturb each fed-in MESA model such that the model stars were set pulsating. The harmonic degree, ℓ, changed with each GYRE model of the *same* MESA model, between zero and three, and the azimuthal order, m, varied from minus three to three, thereby creating 28 GYRE models for *each* of the 72,819 MESA models, hence **2,038,932** GYRE models in total.

Finally, as before, a chi-squared analysis was performed between each set of 28 GYRE models and the extracted frequencies from the TESS data to find the best-fitting model star to the target. This method can be thought of as a nested chi-squared analysis: each *separate* GYRE model was compared to the observational data and its chi-squared was calculated, then all chi-squares for a full set of 28 GYRE models for a *single* MESA model star were summed to find the total chi-squared for each model. This summed value was used to find the globally best fitting model star, then within the set of 28 separate GYRE models, each was assigned to its best-fit observed pulsational frequency, such that the harmonic degree and azimuthal order, ℓ and m, for each frequency was classified — but making sure that no model or TESS frequencies were fitted more than once.

Table 6.8: *Stellar parameter results from this work, compared against literature values.*

"G.20" = (Gaia Collaboration et al., 2020),
"G.22" = (Gaia Collaboration, 2022).

Parameter	Unit	This Work	G.20	G.22
M_*	$\mathrm{M}_\odot$	1.63 ± 0.15	1.63	1.54
R_*	$\mathrm{R}_\odot$	3.05 ± 0.28	2.06	2.09
v_{eq}	$\mathrm{km\,s^{-1}}$	97 ± 0.5	—	—
Overshoot	f_{ov}	0.020 ± 0.0005	—	—

6.6 MESA and GYRE Model Results

A chi-squared analysis comapred each list of MESA and GYRE model pulsational frequencies and the eight highest-amplitude extracted pulsational frequencies of TIC 156987351 from the TESS data (see Table 6.7). The best fitting model had a combined chi-squared value of 28.6137 (≈29.0; summed from each fitted frequency), and gave the stellar parameters of TIC 156987351 listed in Table 6.8.

The errors in mass and radius were propagated from the errors in the parameters ranges in § 6.4, combined with half the interval used between consecutive MESA models. The errors in rotation and overshoot were solely determined from half the interval used between consecutive MESA models. Figures M.1, M.2 and M.3 in Appendix M justify these errors, as they show the global minimum chi-squared value was found for each of the three parameters, within the interval resolution.

Table 6.9 lists the seven of the eight TESS-extracted pulsational frequencies that were successfully fitted by GYRE, together with their "equivalent" frequencies from the best-fitting model (and the difference between the two), their harmonic degree, ℓ, and azimuthal order, m. One TESS frequency is missing due to its closest-fitting frequency from GYRE being a better fit to one of the seven remaining frequencies.

The ramifications of all this will be collated and discussed in § 6.9 below. First

Table 6.9: *A comparison between the TESS-extracted frequencies and the best-fitting model frequencies.*

TESS Frequency (c/d)	Best-fit Frequency (c/d)	$\|\Delta(\mathrm{B}-\mathrm{T})\|$ (c/d)	Harmonic Degree ℓ	Azimuthal Order m
5.7844	5.7826	0.0018	3	-2
6.6688	6.6676	0.0012	2	2
7.9574	8.0066	0.0492	2	0
12.1159	12.0916	0.0243	3	-1
14.2104	14.2401	0.0297	3	3
15.6180	15.6002	0.0178	3	3
27.7047	28.4454	0.7407	0	0

we turn to the remaining data we have for this star.

6.7 Ground-based Observations

6.7.1 40″ Telescope at the SAAO

Between 08/01/21 and 27/03/22 — the dates of the first and last observing session — TIC 156987351 was observed via nine separate multi-colour observing runs using the 40″ telescope and *UBVRI* filters at the SAAO (see § 2.4). Since these observation runs also took place during the COVID-19 pandemic, I was unfortunately unable to perform these observations in-person: again, having to write observing instructions and create star charts for proxy observers at the SAAO, so that observations could still be completed. Again, bad weather meant that some of the observation runs yielded poor results (only calibration frames were taken on certain nights). The 2022 observations were performed by my supervisor and myself remotely from Preston, as the SAAO had developed new technology allowing remote access to the 40″ telescope and dome controls.

The same telescope set-up and strategy used with TIC 409934330 was performed again here: the CCD was cooled to -40°C, the Read-Out Rate was set to 1 MHz, the

Pre-Amp Gain was set to 2.4, and the Output Amplifier was set to "Conventional".

As before, each observation run started by taking Flat-field 10-image cubes in each of the *UBVRI* filters, with exposure times in each filter sufficient to achieve an ADU count of ∼20,000 (except *U* as this required very long exposure times which would have been an inefficient use of telescope time, so instead for this filter we aimed for an ADU count of ∼5000). The flat-field cubes were taken with both 2×2 and 4×4 binning as a precaution in-case poor weather forced the science frames to also be 4×4 binned; this ensured data reduction could still take place. 1×1 binning was taken just once, on the night of 23/02/21, as the observing conditions were photometric. But for all the other nights, 2×2 binning was chosen as the most opportune. Table 5.11 shows a typical set of Flat-field cubes taken; it is not repeated here for TIC 156987351 as it would be identical.

When testing the exposure times for each filter, again 20,000 – 30,000 ADU counts were targeted (but this was very much subject to change depending on weather). Also as before, the exposure times themselves were set to be multiples of each other such that shorter exposures could be binned to the same exposure time as longer exposures.

Following the testing of observation strategies for TIC 409934330 — with regard to the number of exposures per filter — the observation strategy for TIC 156987351 consisted of cycling through *UBVRI* with each filter having a respective number of observations taken depending on its exposure time, ensuring that at the end of a *UBVRI* cycle all filters had equal amounts of exposure when binned. Table 6.10 lists a typical set of exposure times for each filter for TIC 156987351, showing the binning strategy.

Many thousands of frames were taken of TIC 156987351, and at the end of each run, two bias cubes were taken (with 2×2 and 4×4 binning, respectively, and a one-off 1×1 for the photometric night).

These ground-based photometric observations were performed not only to complement the TESS data, but to observe the transits in extra wavelengths, extending the TESS bandpass of 600 – 1100 nm (RI). As with TIC 409934330, this strategy was to observe the different shapes the transits would have in the different filters, which would help constrain the companion's radius. Furthermore, mode-identification of the stellar pulsations may also be performed due to the colour-dependency of the pulsation amplitudes.

Table 6.10: *An example of a typical set of exposure times per filter for TIC 156987351, showing how multiples of each filter allowed for efficient binning (and the adaptions to the exposure times made if the counts became too high or low during an observing run). The number of exposures per filter was not known until the end of each run.*

Frame	Filter	Exposure Time	No. of Exposures	Binning
0011	U	1×15 s	Total	2×2
0013	B	2×7.5 s/4×3.75 s	Number	2×2
0018	V	3×5 s/12×1.25 s	Determined	2×2
0028	R	6×2.5 s/20×0.75 s	After	2×2
0048	I	6×2.5 s/20×0.75 s	Run	2×2

6.7.1.1 40″ Telescope Results

Figure 6.8 shows the data taken with the 40″ telescope at the SAAO over all observation nights, phased on the companion's orbital period of 3.062987 d, separated into the five filters of $UBVRI$, and binned to a suitable degree for each filter.

The light curve is separated into three distinct groups of data for two reasons: one is due to an ephemeris miscalculation, and the other is where we attempted to "fill out" the light curve with more out-of-transit data. The central data group of the light curve in each colour contains the transit of the companion, however little-to-no evidence of this transit dip can be seen. As with TIC 409934330, our observing

strategy may have hindered detecting this and rather than cycling through the filters continually, observing one complete transit per filter would have increased the signal-to-noise. Furthermore, the weather conditions did not provide photometric nights (apart from one night), and the weather was again often unstable: atmospheric noise, as well as the star physically pulsating, combined to inject noise that was greater in magnitude than the transit dip of the companion.

6.7.2 SALT

SALT spectroscopically observed TIC 156987351 for 900 s per exposure, in the blue and red beam, using the HRS in the HR mode with the Iodine Cell out and the ThAr cell in[2], yielding a minimum S/N of 100. Only the blue arm spectra were analysed due to the red arm spectra being contaminated with telluric noise.

Before the spectra could be analysed, they required barycentric correction to remove the motion of the Earth from the signal. The date and time stamp of each observation (in UTC) were extracted from the FITS headers, along with the mid-point exposure times, which were then added to their respective time stamp. The exposure times for each, as mentioned above, were 900 s, and so for most observations the exposure midpoint was at the 450 s mark. However, during some observations effects such as weather caused the midpoint of the time in which photons were collected to be different to the exposure midpoint. This was the *flux-weighted* exposure midpoint, which overwrote the standard exposure midpoint when added to the time stamp for observations where the mid-point was not equal to 450 s.

Next, the time stamp values plus either the exposure midpoint or the flux-weighted exposure midpoint was converted from UTC to BJD using the Time Utilities tool[3] (Eastman, 2012), incorporating the celestial coordinates of TIC 156987351 and the geographical coordinates of SALT. The process was repeated to convert the

[2]The cells are used for wavelength calibration
[3]https://astroutils.astronomy.osu.edu/time/

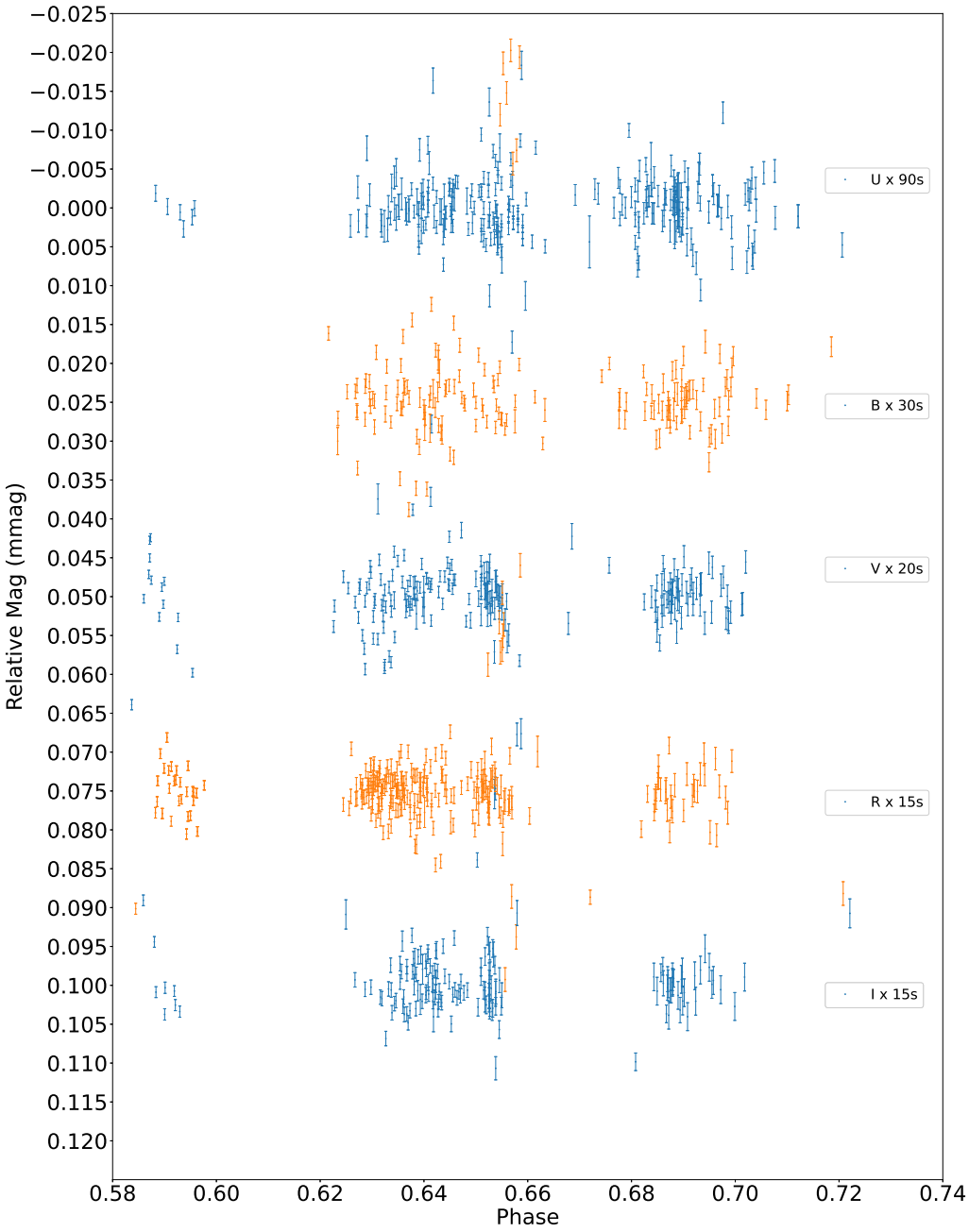

Figure 6.8: *The binned and phased UBVRI observations of TIC 156987351 taken with the 40″ telescope at the SAAO.*

BJD time stamps into JD, which were then fed into a barycentric velocity correction tool[4] that incorporates the `barycorr` code from Wright & Eastman (2014). This produced a list of barycentric correction velocities, each unique per observation.

After this process was complete, a synthetic spectrum of a similar star to TIC 156987351 was built in the software iSpec[5] (Blanco-Cuaresma et al., 2014; Blanco-Cuaresma, 2019). The synthetic spectrum was built using the `SYNTHE` radiative transfer code within the `iSpec` software, incorporating the `ATLAS9.Castelli` model atmosphere, the `Grevesse.2007` Solar abundances, and the `VALD.300_1100`nm (Vienna Atomic Line Database) line list (Blanco-Cuaresma et al., 2014; Castelli & Kurucz, 2003; Grevesse, Asplund & Sauval, 2007; Kupka et al., 1999). Very rough estimates were inputted for the stellar parameters, such as $T_{\rm eff} = 7500\,{\rm K}$, $\log g = 4.00$, $[M/H] = 0$, and rotation $= 40\,{\rm km\,s^{-1}}$. This synthetic spectrum was then employed as a "zero-point" template against which all observational spectra were compared, thus determining a radial velocity (RV) measurement for each observation. These RV data points built an RV curve, illustrating the motion of TIC 156987351 over time. As a comparison RV curve, by-chance one of the SALT observations occurred just after an occultation of the companion, so this too acted as a zero-point due to TIC 156987351 having an RV $\approx 0\,{\rm km\,s^1}$ at that time.

Once all RVs had been determined, the earlier-calculated barycentric correction values were added to their respective RV values, thereby removing the motion of the Earth around the Sun from the observational data. This meant that any remaining signal of motion was purely from TIC 156987351.

The final RV curve, once phase-folded on the orbital period, would then have its best-fit over-plotted. The semi-amplitude of this is denoted by K, the final RV value. Equation 1.15, taken from Perryman (2018), shows the relation between K and the mass of the companion and was used to calculate the latter. Combining

[4]https://astroutils.astronomy.osu.edu/exofast/barycorr.html
[5]https://www.blancocuaresma.com/s/iSpec

this with the calculated radius of the companion — deduced from the $\frac{R_P}{R_*}$ ratio of the transit depth, δ, and the determined radius from the stellar model — would allow the calculation of the companion's density, giving an immediate insight into whether it was of rocky or gaseous nature.

6.7.2.1 SALT Results

SALT performed 17 separate observations of TIC 156987351 over the course of 13 months. Table N.1 in Appendix N lists the RVs obtained via `iSpec`, which have additionally undergone barycentric correction.

Figure 6.9 shows the RV curve resulting from the 13 months worth of SALT observations of TIC 156987351. Phase-folding these data points over the orbital period of TIC 156987351's companion (3.062987 d) produced the RV phase curve shown by Figure 6.10, showing the motion of TIC 156987351 relative to the Earth. However upon inspection, it became apparent that the RV phase curve was not of the quality needed to deduce any parameters of the companion. It is noted that scatter of the data in Figure 6.10 is far larger than the error bars. This is because the RV signal of the companion is very small (which we discuss more in § 6.9 below). The wavelength solution of the MIDAS pipeline induces error into low-amplitude RV curves as the pipeline is unstable for RVs lower than 250 m/s (Kniazev et al., 2004; Kniazev, Gvaramadze & Berdnikov, 2016, 2017). This was not known when this work was first done, so we were searching for RVs well within the stability limit of HRS. In addition, iSpec will have induced systematic errors from difficulty finding the core of the spectral line, which were broadened due to its slow rotation. As an aside, TIC 156987351 is not an Am star so no chemical abundance work was required.

Each spectrum was already barycentrically corrected from the above procedure, and then each was further corrected for its respective RV. Once all spectra were at the same zero-point, they were co-added to form a *cumulative mean* spectrum.

Similarly, as above, when creating a synthetic spectrum for the RV determination, iSpec was used to create a best-fitting model spectrum to the co-added SALT spectrum to obtain stellar parameters of TIC 156987351. Again, the `SYNTHE` spectrum, `ATLAS9.Castelli` model atmosphere, `Grevesse.2007` Solar abundances, and the `VALD.300_1100`nm line lists were used, and the initial values of $T_{\rm eff}$ and $\log g$ were input as 7500 K and 4.00, respectively, but left as free parameters, allowing `iSpec` to iterate over varying values of both (hence why the input values were rounded). Once these parameters had been obtained, they were re-input and $v \sin i$ was left as the free parameter. This process itself was repeated a few times, until the reduced chi-squared value no longer decreased (`rchisq = 0.0008`). The results of this spectral analysis are listed with the MESA and GYRE results in Table 6.11.

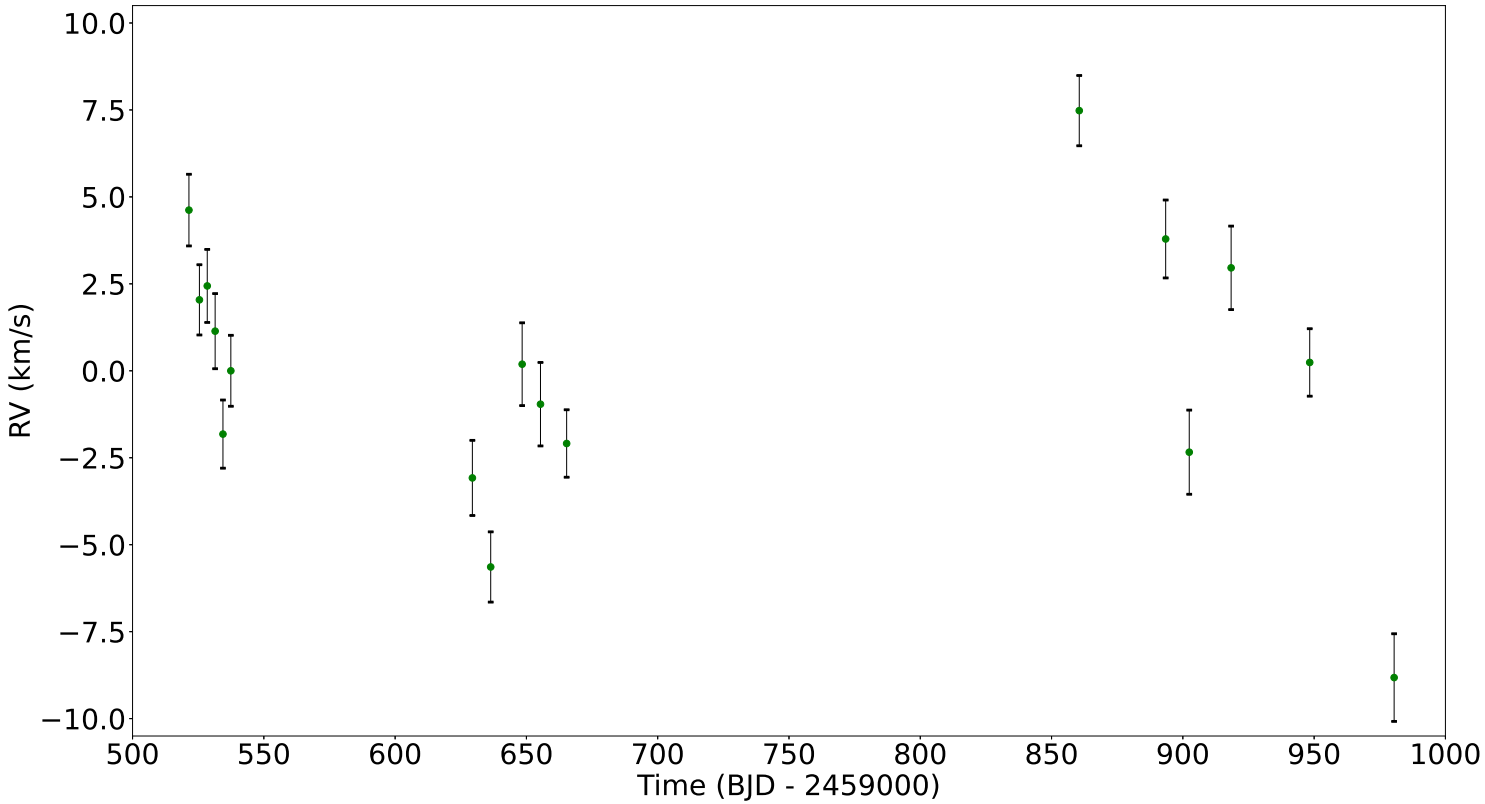

Figure 6.9: *A plot of all relative RVs of TIC 15698735 measured by SALT across the 13-month observation run.*

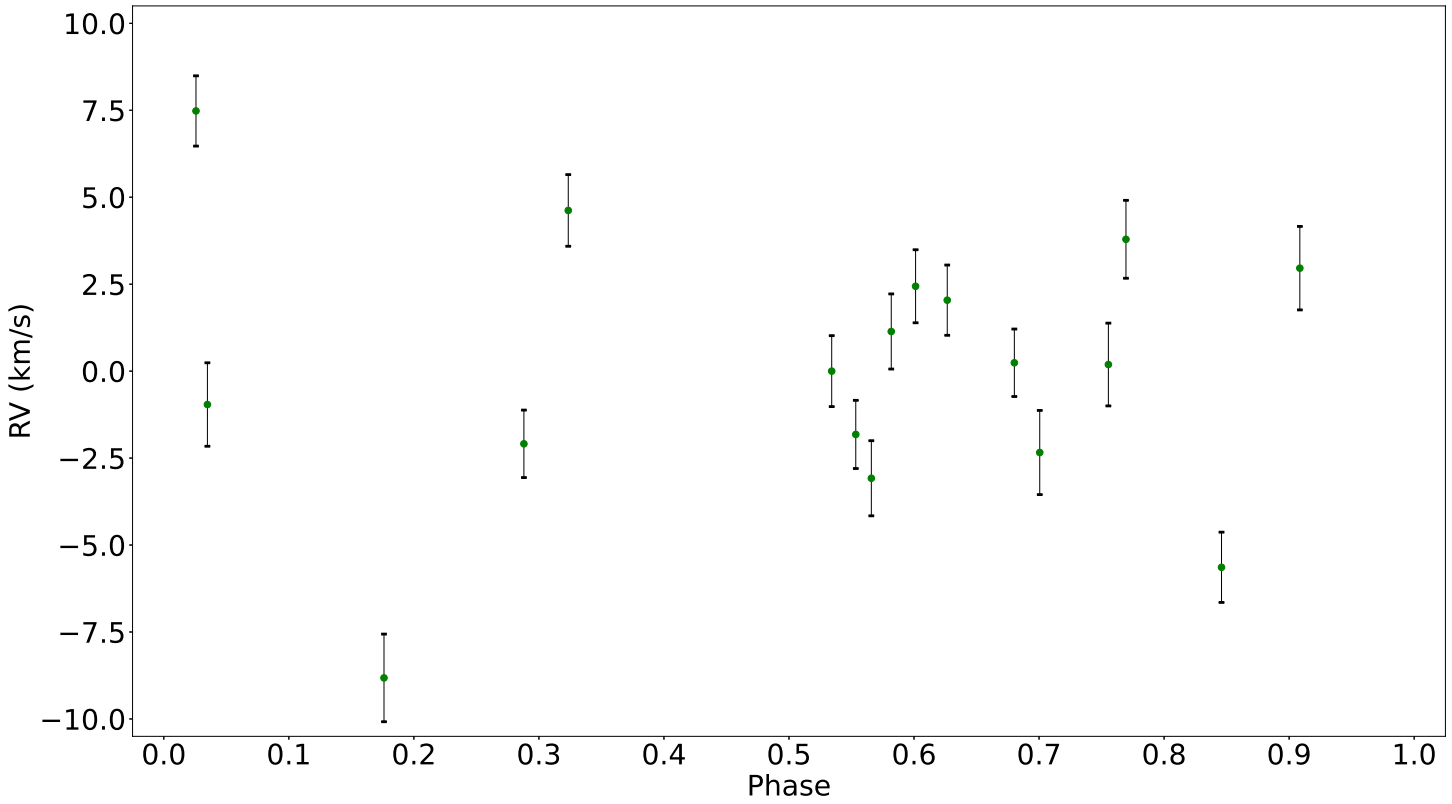

Figure 6.10: *The same RV curve as in Figure 6.9 but phased over the orbital period of TIC 156987351's companion (3.062987 d).*

Table 6.11: *Stellar parameter results from using the SALT observations, compared against literature values. iSpec determined these parameter values with a chi-squared result of 1.24, and a reduced chi-squared result of 0.0006.*

Parameter	Unit	This Work	Literature	Reference
$T_{\rm eff}$	K	7231 ± 63	7451 ± 160	(Stassun et al., 2019)
Fe/H	—	0.00 ± 0.20	—	—
$v \sin i$	$\mathrm{km\,s^{-1}}$	71 ± 9	—	—
$\log g$	$\log \mathrm{cm\,s^{-2}}$	4.02 ± 0.01	4.05 ± 0.08	(Stassun et al., 2019)

6.8 Modelling the Planet Transit

The RV curve in Figure 6.10 was unable to provide K, so calculating M_P, was unachievable: however, a mass could still be modelled.

The software EXOFASTv2 (see § 3.3; Eastman, Gaudi & Agol, 2013; Eastman et al., 2019) was used to model the companion transiting TIC 156987351. The TESS data used to build the the light curve in Figure 6.1 was used in combination with data from when this star was also observed during Sectors 7, 33 and 34 as the transit input for EXOFASTv2 , but the RV results listed in Table N.1 in Appendix N were omitted as they are too poor quality for this work. M_P was determined by EXOFASTv2 using the mass-radius relationship of Chen & Kipping (2017) as only transit data was fitted (this method is standard procedure for the EXOFASTv2 software; Eastman et al., 2019). Finally, the "priors" file required by EXOFASTv2 contained the derived stellar parameters from the MESA and GYRE models in Table 6.6, several parameters obtained via iSpec in Table 6.11, and some archive-extracted parameters from Table 6.3 (this "priors" file can be seen in Appendix O).

6.8.1 Planet Transit Model Results

Figure 6.11 shows the phase-folded light curve seen in Figure 6.1 as the blue data points, with the black line of the EXOFASTv2 model overlaid. EXOFASTv2 has modelled the transit depth, δ, based on the deepest data point in the transit, but it has overestimated the width and shape of the transit. The planetary radius, and transit duration, are not well constrained. The planetary parameters from this model are listed in Table 6.12. We now pull together all of the results listed in this Chapter, and discuss the consequences.

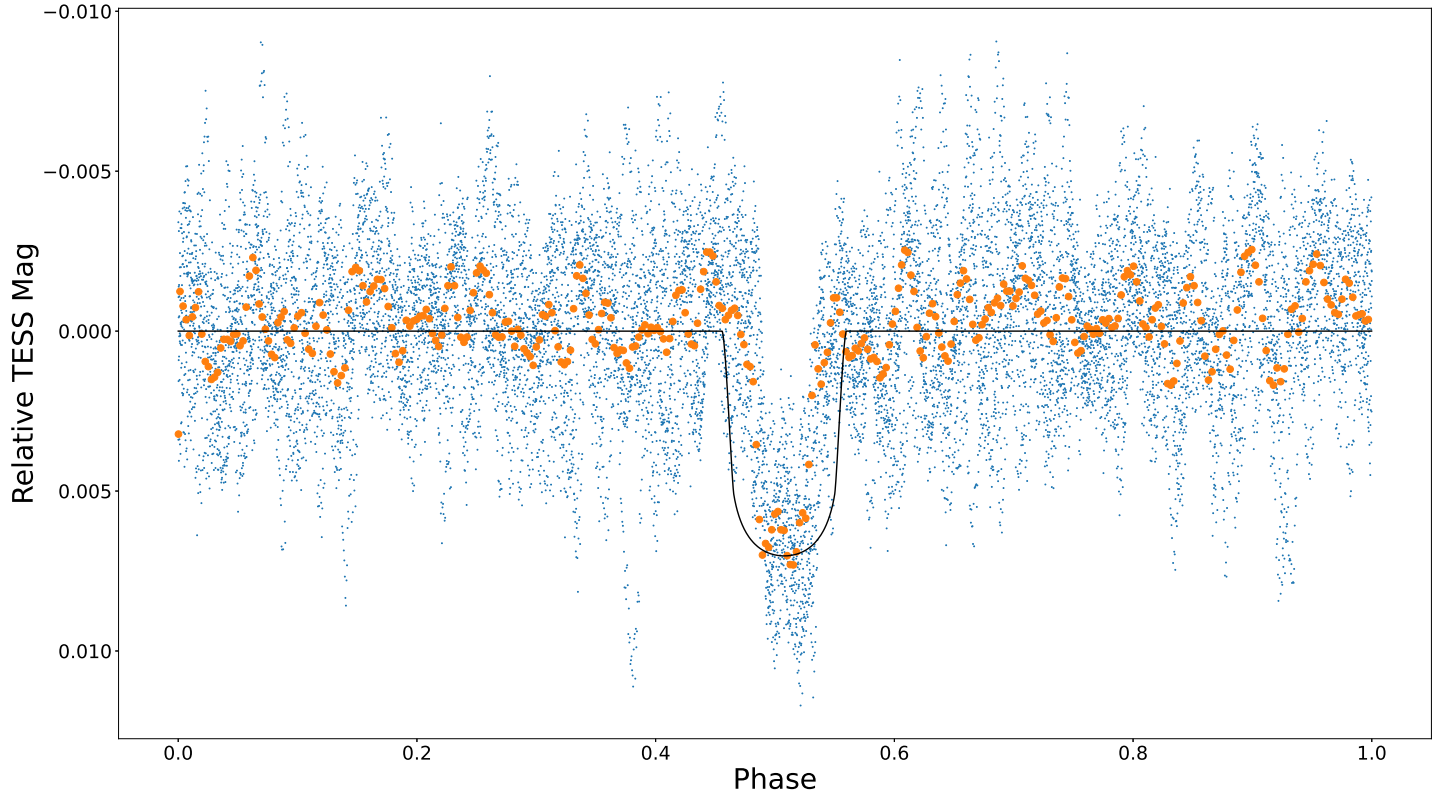

Figure 6.11: *A phase-folded version of the light curve in Figure 6.1, with the* EXOFAST*v*2 *model of the companion to TIC 156987351 overlaid as the black line. The orange over-plot is a smoothed average of the phase curve, the pulsations are obvious but there is no discernible trace of ellipsoidal variability. This could suggest inclination in the companion's orbit. The transit model is wider than the data would suggest, most likely arising from the pulsations injecting non-astrophysical "transits" that* EXOFAST*v*2 *is trying to fit.*

Table 6.12: *Stellar and Planetary parameters for TIC 156987351 and its companion, derived from the* MESA *and* GYRE *models using* EXOFAST*v*2 .

Parameter	Units	Values
Stellar Parameters:		
$\log g$	Surface gravity ($\log \mathrm{cm\,s^{-2}}$)	$3.91^{+0.19}_{-0.32}$
Age	Age (Gyr)	$1.46^{+0.67}_{-0.61}$
Planetary Parameters:		
P	Period (d)	$3.062988^{+0.000017}_{-0.000022}$
R_P	Radius ($\mathrm{R_J}$)	$0.97^{+0.56}_{-0.67}$
M_P	Mass ($\mathrm{M_J}$)	$0.39^{+7.9}_{-0.33}$
a	Semi-major axis (au)	$0.0483^{+0.0026}_{-0.0056}$
i	Inclination (°)	$83.4^{+4.2}_{-6.9}$
T_{eq}	Equilibrium temperature (K)	2470^{+430}_{-450}
R_P/R_*	Radius of planet in stellar radii	$0.040^{+0.054}_{-0.028}$
a/R_*	Semi-major axis in stellar radii	$4.4^{+1.6}_{-1.4}$
δ	Transit depth (fraction)	$0.0016^{+0.0072}_{-0.0015}$
T_{14}	Total transit duration (d)	$0.179^{+0.096}_{-0.087}$
T_{FWHM}	FWHM transit duration (d)	$0.17^{+0.10}_{-0.11}$
b	Transit Impact parameter	$0.50^{+0.39}_{-0.29}$
ρ_P	Density ($\mathrm{g\,cm^{-3}}$)	$1.7^{+13}_{-1.5}$
$\log g_P$	Surface gravity ($\log \mathrm{cm\,s^{-2}}$)	$3.22^{+1.1}_{-0.66}$
$M_P \sin i$	Minimum mass ($\mathrm{M_J}$)	$0.38^{+7.90}_{-0.33}$
M_P/M_*	Mass ratio	$0.00027^{+0.0043}_{-0.00024}$
Wavelength Parameters:		
γ_1	linear limb-darkening coeff	$0.29^{+0.27}_{-0.18}$
γ_2	quadratic limb-darkening coeff	$0.28^{+0.14}_{-0.15}$

Table 6.13: *All results collected together from the* MESA *and* GYRE *models, the SALT observations, and the* EXOFAST*v*2 *models, compared against literature values where possible.*

"G.20" = (Gaia Collaboration et al., 2020),
"G.22" = (Gaia Collaboration, 2022),
"S.19" = (Stassun et al., 2019),
"G.21" = (Guerrero et al., 2021).

Software	Parameter	Unit	This Work	Literature	Reference
Stellar:					
MESA and GYRE:					
	M_*	$M_\odot$	1.63 ± 0.15	1.63/1.54	G.20/G.22
	R_*	$R_\odot$	3.05 ± 0.28	2.06/2.09	G.20/G.22
	$v_{\rm eq}$	$\rm km\,s^{-1}$	97 ± 0.5	—	—
	Rotation	d	1.59 ± 0.20	—	—
	Overshoot	$f_{\rm ov}$	0.020 ± 0.0005	—	—
	iSpec:				
	$T_{\rm eff}$	K	7231 ± 63	7451 ± 160	S.19
	Fe/H	—	0.00 ± 0.20	—	—
	$v \sin i$S.19	$\rm km\,s^{-1}$	71 ± 9	—	—
	Rotation	d	2.18 ± 0.34	—	—
	$\log g$	$\log \rm cm\,s^{-2}$	4.02 ± 0.01	4.05 ± 0.08	S.19
	EXOFASTv2:				
	$\log g$	$\log \rm cm\,s^{-2}$	$3.91^{+0.19}_{-0.32}$	4.05 ± 0.08	S.19

Age	Gyr	$1.46^{+0.67}_{-0.61}$	—	—
γ_1	—	$0.29^{+0.27}_{-0.18}$	—	—
γ_2	—	$0.28^{+0.14}_{-0.15}$	—	—

Planetary:

EXOFASTv2:

P	d	$3.062988^{+0.000017}_{-0.000022}$	3.062987 ± 0.000004	G.21
R_P	R_J	$0.97^{+0.56}_{-0.67}$	—	—
M_P	M_J	$0.39^{+7.90}_{-0.33}$	—	—
a	au	$0.0483^{+0.0026}_{-0.0056}$	—	—
i	°	$83.4^{+4.2}_{-6.9}$	—	—
T_{eq}	K	2470^{+430}_{-450}	—	—
R_P/R_*	—	$0.040^{+0.054}_{-0.028}$	—	—
a/R_*	—	$4.4^{+1.6}_{-1.4}$	—	—
b	—	$0.50^{+0.39}_{-0.29}$	—	—
ρ_P	$\mathrm{g\,cm^{-3}}$	$1.7^{+13.0}_{-1.5}$	—	—
$\log g_P$	$\log \mathrm{cm\,s^{-2}}$	$3.22^{+1.10}_{-0.66}$	—	—
$M_P \sin i$	M_J	$0.38^{+7.90}_{-0.33}$	—	—
M_P/M_*	—	$0.00027^{+0.00430}_{-0.00024}$	—	—

6.9 Discussion

A chi-squared analysis was performed comparing the frequencies of the pulsations in each model with the frequencies of pulsations of TIC 156987351 to find the best fitting model to the TESS data, and hence a model of the star. Table 6.9 lists the best-fitting model frequencies to the real pulsation frequencies, and hence the best model of TIC 156987351 is a $1.63 \pm 0.15\,\mathrm{M}_{\odot}$ star with an equatorial rotational velocity, V_{eq}, of $97 \pm 0.5\,\mathrm{km\,s^{-1}}$ and an overshoot parameter value of $\mathrm{f}_{ov} = 0.020 \pm 0.0005$. Table 6.13 lists all results determined from the MESA and GYRE models and the SALT observations, and literature values for comparison where possible. The mass of TIC 156987351 produced by the MESA and GYRE models — $1.63 \pm 0.15\,\mathrm{M}_{\odot}$ — agrees exactly with the Gaia Collaboration et al. (2020) literature value, listed in Table 6.6. However, considering the iSpec-obtained T_{eff} value of $7231 \pm 63\,\mathrm{K}$ and a spectral type of F2, the mass does not scale inline with the mass-T_{eff} relation given by Pecaut & Mamajek (2013). Instead, the Pecaut & Mamajek (2013) relation suggests that TIC 156987351 should have a mass of $\approx 1.46\,\mathrm{M}_{\odot}$, with $T_{\mathrm{eff}} = 6820 \pm 160\,\mathrm{K}$, for an F2 spectral type. However, the iSpec-determined T_{eff} of $7231 \pm 63\,\mathrm{K}$ is close in value to the literature T_{eff} of $7451 \pm 160\,\mathrm{K}$, and examining the Pecaut & Mamajek (2013) mass-T_{eff} relation such a star would have a mass of $\approx 1.61\,\mathrm{M}_{\odot}$, giving rise to the idea that the spectral type is incorrect and should instead be F0.

Further to the above parameters, MESA and GYRE produced a model radius of TIC 156987351 of $3.05 \pm 0.28\,\mathrm{R}_{\odot}$. This does not agree with the literature values — but I argue that because this work is the first to study TIC 156987351 asteroseismically, and because asteroseismology is the most accurate method of determining stellar radii, there is no reason to doubt this radius parameter. Yet, when contemplating the $\log g$ value of $4.02 \pm 0.14\,\log \mathrm{cm\,s^{-2}}$ obtained via the iSpec analysis of the SALT spectra (Table 6.11), the star cannot be as bloated as the $\log g$ value suggests.

Equation 5.9, the same relation between $\log g$, mass and radius from Smalley

(2005) was again employed as an additional method of calculating stellar parameters. Assuming a solar $\log g$ of $4.437 \log \mathrm{cm\,s^{-2}}$ — as used by Smalley (2005) — then $\log g$ of TIC 156987351 comes out at $\log g = 3.87 \pm 0.62 \log \mathrm{cm\,s^{-2}}$. This value is slightly lower than the iSpec-determined $\log g$, more in agreement with the MESA radius. Reversing Equation 5.9 to determine a radius based on the iSpec-determined $\log g$ we get $R_* = 2.99 \pm 0.48\,\mathrm{R_\odot}$, agreeing with the MESA-determined radius within error.

The iSpec analysis also produced a T_{eff} of 7231 ± 63 K, and a projected rotational velocity, $v \sin i$, of $71 \pm 9\,\mathrm{km\,s^{-1}}$ (both listed in Table 6.11). The T_{eff} value agrees very well with the literature value of 7351 ± 160 K (Stassun et al., 2019), and whilst a rotation velocity has not previously been calculated for TIC 156987351, this value of $v \sin i$ agrees with the $B - V$ table of Reiners (2006). $97 \pm 0.5\,\mathrm{km\,s^{-1}}$ translates to a stellar rotation period for TIC 156987351 of 1.59 ± 0.15 d, and $71 \pm 9\,\mathrm{km\,s^{-1}}$ translates to 2.18 ± 0.34 d.

Unfortunately, the rest of the ground-based observations have produced data of a quality with too large error bars to be scientifically useful. The multicolour *UB-VRI* observations of TIC 156987351 taken by the 40″ at the SAAO, that were used to construct the five phased light curves shown in Figure 6.8, had been performed with the idea of expanding the wavelength palette that TIC 156987351 had been observed with (UBV) as well as re-observing the star from the ground in wavelengths within the TESS bandpass (RI). It was hoped that each of the five light curves would show a different relative depth and shape of the transits, arising from the wavelength-dependant atmospheric absorption levels of the companion's atmosphere. However, with poor weather preventing observations on 11 of the 14 nights awarded to observe TIC 156987351, an insufficient amount of data was gathered to show the wavelength-variance in the transit shapes.

The 17 SALT observations listed in Table N.1 in Appendix N were themselves successful, as initially only six observations were awarded as guaranteed time. When

studying the "Δ RVs From Zero-Point" column it can be seen that most RV measurements are larger than their measurement error, proving a sufficient signal-to-noise per observation. However, in the phase curve (Figure 6.10) there is no clear RV motion of TIC 156987351 — the data are seemingly scattered and no clear sinusoidal curve can be seen — so the magnitude of the RV is too small to be detectable; less than the precision of SALT's HRS spectroscope. The range of Δ RV over this sample is $16.3\,\mathrm{km\,s^{-1}}$, which is approximately $16\times$ the magnitude of the error of each data point ($\sim$$1.0\,\mathrm{km\,s^{-1}}$, i.e: up to 16σ RV measurements). Additionally, a larger-scale variation can be seen in Figure 6.9, the non-phased RV curve. This suggests that there is another companion to TIC 156987351, far more massive than the transiting companion, orbiting at a much larger radius. Follow-up work of this second companion would be useful.

Due to the poor nature of the RV results, EXOFASTv2 could only use the TESS transit data to model the companion; but as mentioned above using transit only inputs for modelling exoplanets is standard procedure for the EXOFASTv2 software, as it employs the mass-radius relationship of Chen & Kipping (2017, (Eastman et al., 2019)). EXOFASTv2 produced a smooth model transit, overlaid on the TESS data as the black line in Figure 6.11. EXOFASTv2 has modelled the transit depth, δ, based on the deepest data point in the transit, but it has overestimated the width and shape of the transit: hence, the planetary radius and transit duration are not well constrained, and future work is required to resolve this. EXOFASTv2 calculated a vast array of other parameters from its model transit too, the most relevant of which are listed in Table 6.12.

The EXOFASTv2-determined age of $1.46^{+0.67}_{-0.61}$ Gyr for TIC 156987351 in Table 6.12 sits comfortably in the age range of F-type stars: $\sim$4 Gyr for F9 stars and $\sim$1 Gyr for F0 stars (Sato et al., 2014) — the EXOFASTv2 age is already in agreement with TIC 156987351's spectral type. It is possible to see how this age range looks on the

HR diagram by plotting it as an isochrone, with a thickness that of the error. Figure 6.12 shows an array of isochrones plotted on the HR diagram, obtained from VandenBerg & Clem (2003), overlaid on the wide isochrone representing TIC 156987351 (light pink) plotted using the EXOFASTv2 age. The black circle on the HR diagram is the location of TIC 156987351 when plotting its luminosity, obtained from feeding the MESA- and GYRE-calculated mass back through Equation 5.3, and its iSpec-determined T_{eff}. The MESA and GYRE mass and luminosity results agree with the EXOFASTv2 age, all of which agree with the isochrones.

The orbital period listed in Table 6.12 for the companion is consistent with the value given by the TIC (Guerrero et al., 2021). EXOFASTv2 further determined its mass and radius, giving a Jupiter-sized planet that is less dense than its Jovian namesake: $M_P = 0.39^{+7.9}_{-0.33}\,\mathrm{M_J}$, $R_P = 0.97^{+0.56}_{-0.67}\,\mathrm{R_J}$. The large upper limit for the error on planetary mass arose from the mass-radius relationship of Chen & Kipping (2017) due to the lack of RV data used in the EXOFASTv2 analysis. If further RV data is taken of TIC 156987351 using a much higher resolution spectrograph — like HARPS, for example — then the mass errors will be constrained by over an order of magnitude more than currently.

The listed inclination of $i = 83.4^{+4.2}_{-6.9}\,^\circ$ is similar to that of any transiting object: a low inclination would not allow an object to transit at all. Again, with large errors, one could be worried about the true inclination value, but when considering the aforementioned fact, and that transits do appear in the light curve, this value of inclination can be considered correct and the errors could be constrained further.

Now that a mass has been obtained for both TIC 156987351 and its companion, Equation 1.15 was exploited to predict an RV curve of the star and its semi-amplitude, K. Employing the EXOFASTv2-determined orbital period of

$P = 3.062988^{+0.000017}_{-0.000022}\,\mathrm{d}$, the EXOFASTv2-determined companion minimum mass of $M_P \sin i = 0.38^{+7.90}_{-0.33}\,\mathrm{M_J}$, and the MESA and GYRE-determined stellar mass of

$M = 1.63 \pm 0.15\,M_\odot$, K was calculated as $38^{+797}_{-32}\,m\,s^{-1}$. A synthetic RV curve with K that of above has been super-imposed on the data in Figure 6.13, with a zoomed in view in Figure 6.14: it is impossible to see any RV signal.

The transit impact parameter of $b = 0.50^{+0.39}_{-0.29}$ is high, suggesting the transit may likely be grazing. This would produce a more V-shaped dip in the light curve, but as can be seen in Figure 6.11 this is not the case, alluding to the idea of a low impact parameter transit, which does fit within errors. Finally, the linear and quadratic limb-darkening coefficients, γ_1 and γ_2, can be used to model the surface brightness profile of TIC 156987351 using the methods of Mandel & Agol (2002).

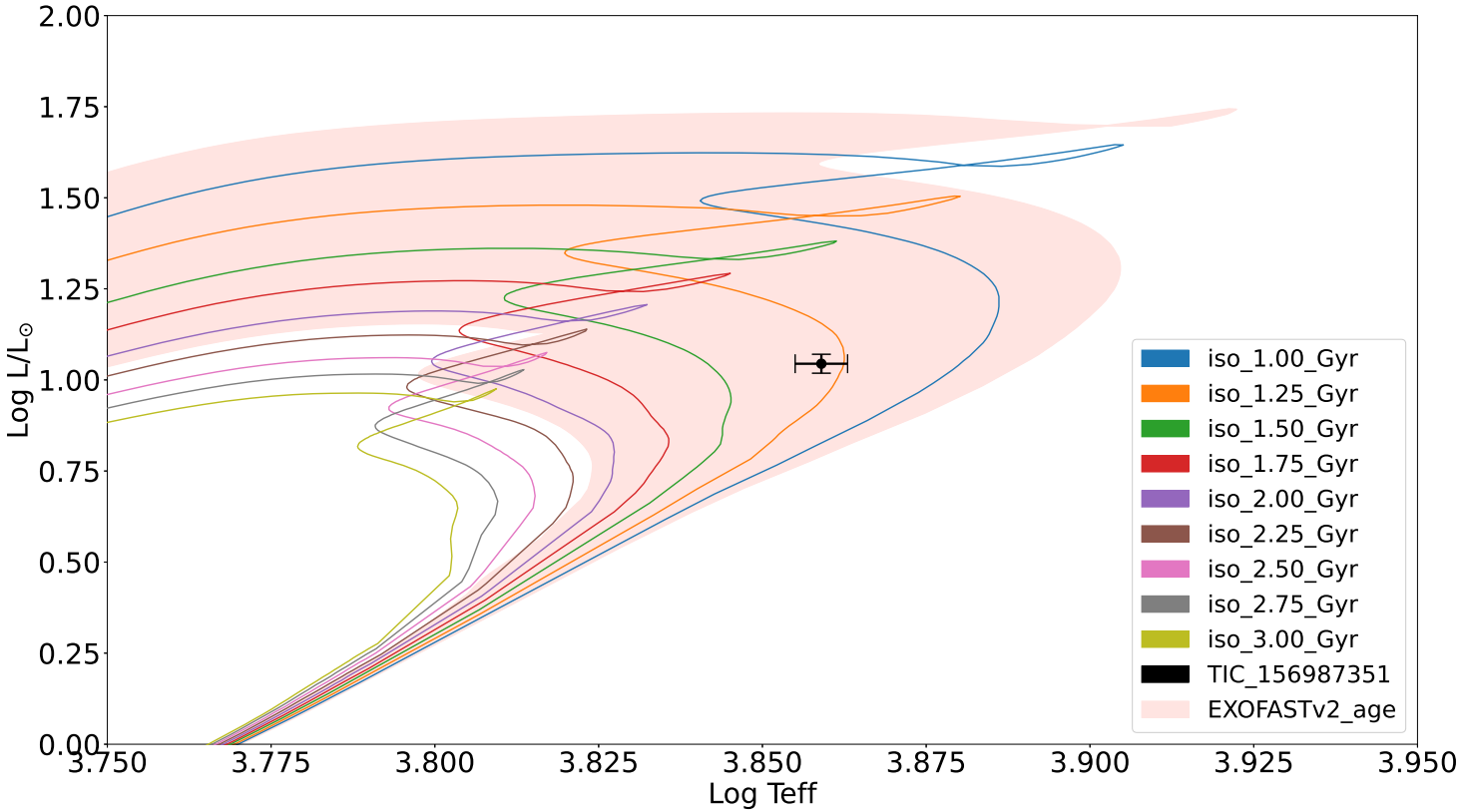

Figure 6.12: *An HR diagram showing the location of TIC 156987351 (black circle) plotted using the* MESA *and* GYRE *results, against the isochrone created from the* EXOFAST*v*2*-outputted age and error (light pink) with an array of other isochrones for reference (respective labels can be found in the key).*

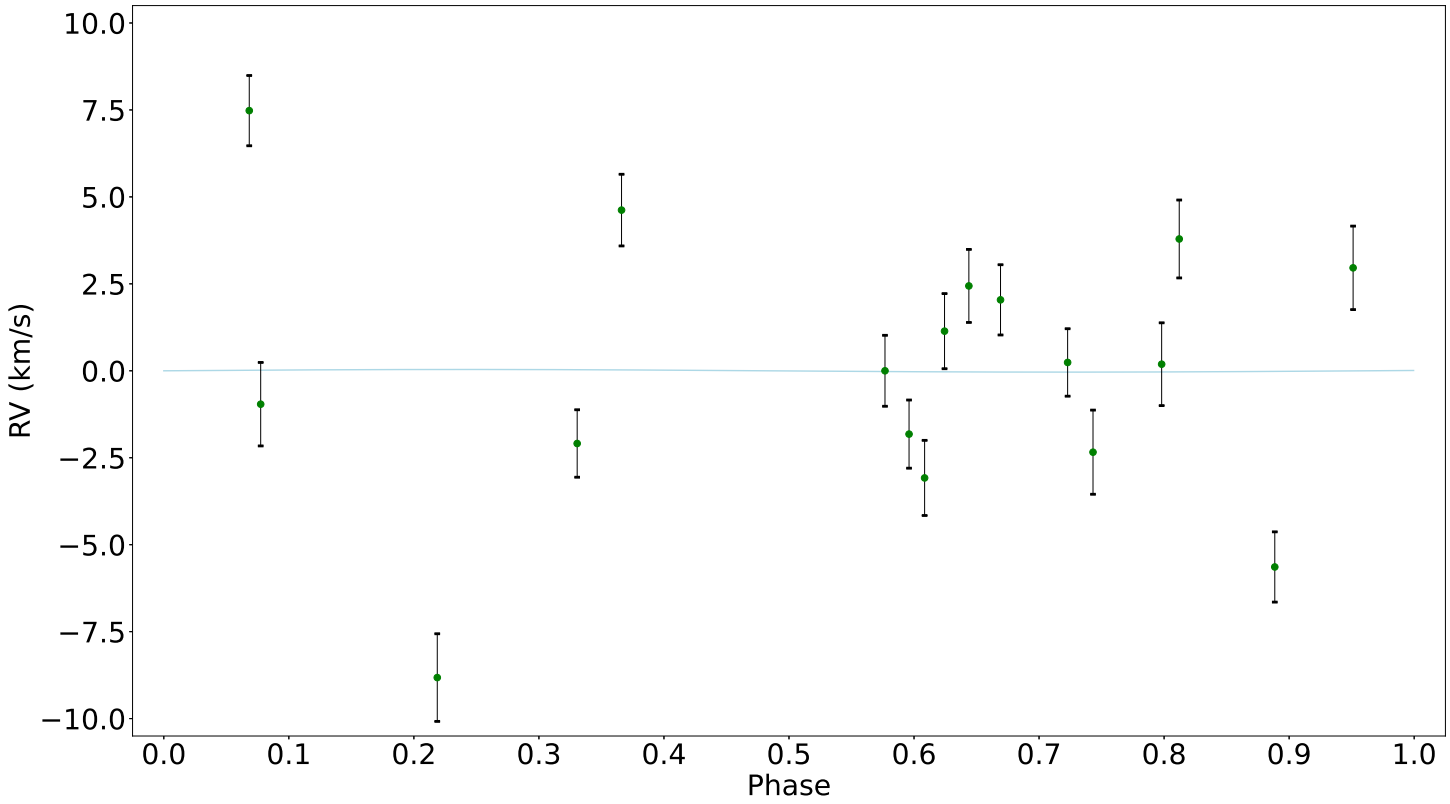

Figure 6.13: *The phased RV curve from Figure 6.10 with the expected RV curve over-plotted as the blue line ($K = 38\,m\,s^{-1}$).*

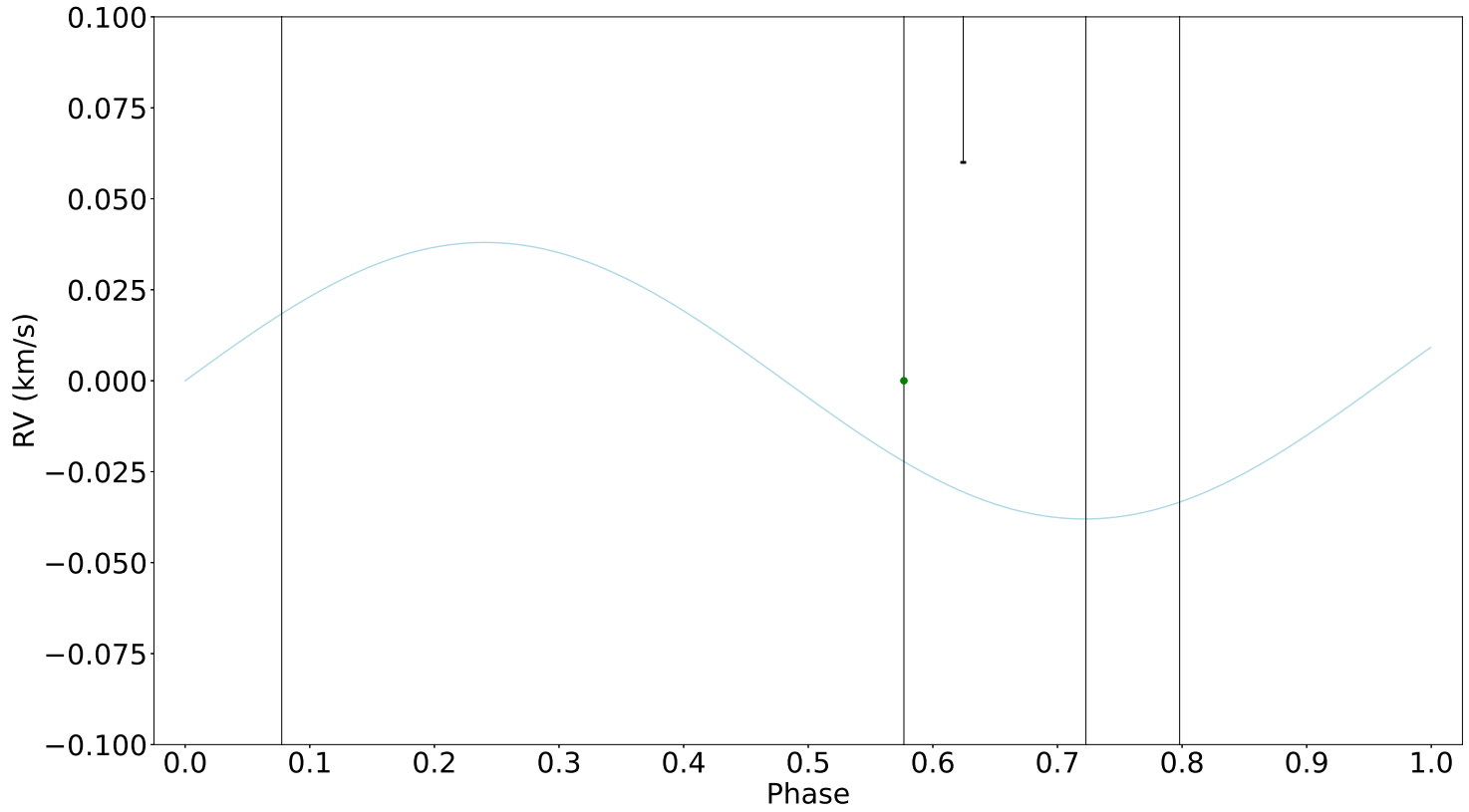

Figure 6.14: *The phased RV curve from Figure 6.10 with the expected RV curve over-plotted as the blue line ($K = 38\,m\,s^{-1}$), now zoomed in.*

6.9.1 The δ Scuti Cone

In § 5.9.1 I hypothesised a cone-shaped region inside the HR diagram that is a sub-region within which δ Scuti host stars do *only* exist, addressing the discrepancies between said δ Scuti host stars and standard, non-pulsating A-type hosts (and the dearth of the former) mentioned in previous Chapters. Figure 6.15 shows this region of $T_{\rm eff} - \frac{\rm L}{\rm L_{\odot}}$ parameter space, complete with a sample of δ Scuti star, non-pulsating A-type stars, the previously known δ Scuti hosts, and the two δ Scuti host stars from the work in this thesis. This small sample occupies only the lower-left region of the δ Scuti star population, and is clearly separated from the main spread of non-pulsating A-type hosts stars, inhabiting its own locality. All data points within Figure 6.15 have undergone the Flower (1996) bolometric corrections, with the Torres (2010) updated coefficients. The δ Scuti host star sample will be added to in future work, constraining the δ Scuti cone further and evolving this hypothesis. For consistency, the same cut of stars only with $T_{\rm eff} > 6300$ K were included in this plot, following the methods used earlier in this Chapter when identifying TESS targets.

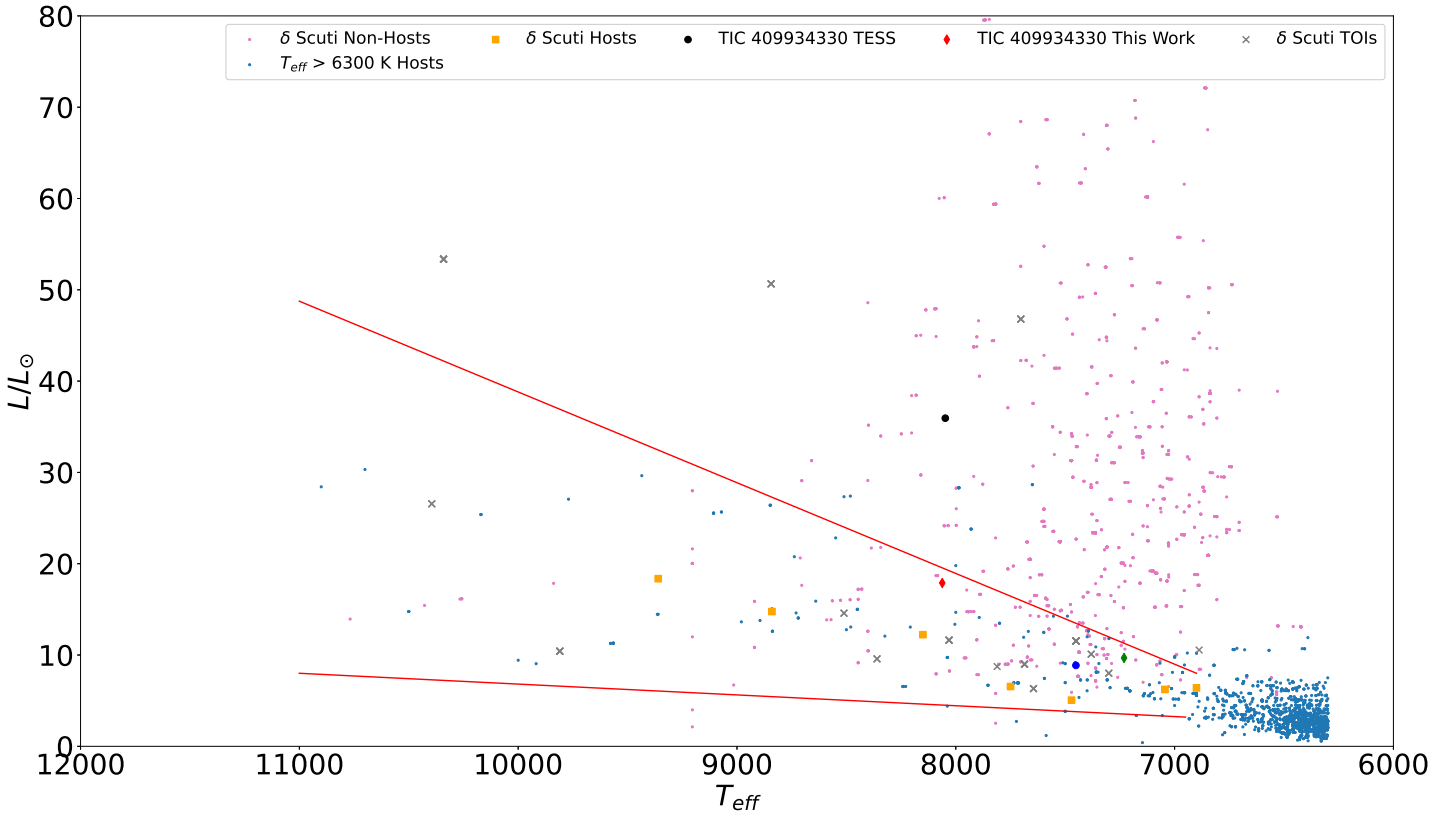

Figure 6.15: *An HR diagram showing the δ Scuti cone outlined by the red lines. The pink points are non-host δ Scuti stars, the blue points are all host stars with* $T_{\rm eff} > 6300\,{\rm K}$*, the orange squares are the known δ Scuti host stars, the black circle is TIC 409934330 (TESS), the red diamond is TIC 409934330 (this work), the blue circle is TIC 156987351 (TESS), the green diamond is TIC 156987351 (this work), and the grey crosses are the δ Scuti TOIs yet to be confirmed as host stars. All data points have undergone the Flower (1996) bolometric corrections, with the Torres (2010) updated coefficients.*

6.10 Conclusions

A star — TIC 156987351 — was selected from the TOI catalogue of TESS data as it exhibited δ Scuti pulsations in its light curve, as well as luminosity dips caused from a transiting companion. Numerical ranges for the parameters of mass, equatorial rotation and convection overshoot were extensively calculated and used as initial constraints for a grid of models that was built using the software MESA. From here, each of the MESA models in the grid were put through the software GYRE, which perturbed the model stars such that the output files listed the frequencies of pulsations that such stars would have. In total, 2,038,932 individual models of pulsating stars were created, with each varying slightly in mass, rotational velocity and level of convective overshoot by the quantities listed in Table 5.6c, and between -3 and 3 — where applicable — in the quantum numbers ℓ and m. In parallel, PERIOD04 was used to extract astrophysical pulsational frequencies from the Fourier transform of the light curve of TIC 156987351 (combination frequencies were checked for and removed). This list of astrophysical frequencies was used as a comparison for frequencies within each of the GYRE models: a chi-squared analysis was performed to locate and determine the closest match between the GYRE model frequency lists and the TESS frequency list, and hence find the best-fitting MESA model star to the TESS data. The resulting best-fitting model is comprised of a $1.63 \pm 0.15\,\mathrm{M}_{\odot}$ star with a radius of $3.05 \pm 0.28\,\mathrm{R}_{\odot}$, an equatorial rotation velocity of $97 \pm 0.5\,\mathrm{km\,s^{-1}}$ (1.59 ± 0.20 d) and an overshoot parameter of $f_{\mathrm{ov}} = 0.020 \pm 0.0005$.

In addition to the above, ground-based observations were performed as a follow-up to the TESS observations. Using the $40''$ telescope at the SAAO TIC 156987351 was observed in the *UBVRI* filters, extending the TESS *RI* bandpass into shorter wavelengths: unfortunately, bad weather prevented data with a high enough quality for analysis. SALT, however, did provide some good quality data: it observed TIC 156987351 spectroscopically and allowed for spectral analysis with the software

iSpec, which was utilised to determine a projected rotation velocity for the star, $71 \pm 9\,\mathrm{km\,s^{-1}}$ ($2.18 \pm 0.34\,\mathrm{d}$), a T_{eff} measurement of $7321 \pm 63\,\mathrm{K}$, and determined $\log g$ to be $4.02 \pm 0.014\,\log \mathrm{cm\,s^{-2}}$. An attempt was made to observe the radial velocity of TIC 156987351 caused by the companion, but the RV was lower than SALT's precision and as such was lost in the noise.

The MESA and GYRE-generated mass and radius value of this star that we generated from the software does not appear to be consistent that that generated by other analytical and numerical methods (i.e., the Gaia Collaboration et al. (2020) & Gaia Collaboration (2022) values listed in Table 6.6). We will feed all of this information back to the software writers, as this may be of assistance to them in potentially refining their software.

Finally, EXOFASTv2 modelled the companion based off just the transit data and the model star parameters, and obtained a planetary mass value of $M_P = 0.39^{+7.9}_{-0.33}\mathrm{M_J}$ and radius value of $R_P = 0.97^{+0.56}_{-0.67}\mathrm{R_J}$, as well as a plethora of additional parameters listed in Table 6.12. From this we can say with confidence that the companion, now TIC 156987351 b, is of a hot-Jupiter nature, with a lower density than that of its namesake. As a consequence, TIC 156987351 forms an additional data point on the δ Scuti Cone (§ 6.9.1), and increases the number of known δ Scuti stars that host a planet from eight to nine (Ebo et al., (b) in prep).

Chapter 7

Conclusions and Future Work

7.1 Conclusions

When this work first began, we decided to marry together the two fields of asteroseismology and exoplanets. It was noticed that there was a sparsity of planetary systems with host stars hotter than the Sun, and even fewer systems consisting of exoplanets orbiting classical pulsators. Thus, it was decided that δ Scuti host stars would be suitable targets as their signature pulsation frequencies allow them to be well-modelled, and since asteroseismic analysis of stars enables the most precise determination of stellar properties, modelling planets around pulsators offers the opportunity for the most precise exoplanet studies. When the work commenced there were only seven examples in the literature of exoplanet – δ Scuti systems. This number was remarkably low: we wanted to find more examples to increase the population of these rare systems, to constrain system properties to try and theorise what makes these systems rare; how the pulsations affect the properties of the exoplanets; to see what (if any) characteristics the host stars and their companions have in common.

We studied two new systems, TIC 409934330 and TIC 156987351, and all determined parameters from the work in this thesis are listed in Table 7.1. The aforementioned δ Scuti host stars are compared with the known literature δ Scuti host stars in Table 7.2, and the two new companions are compared with the known literature companions to δ Scuti stars in Table 7.3.

The TIC 409934330 System:

The δ Scuti star TIC 409934330 is a $2.10 \pm 0.19\,M_\odot$ star hosting a $2.5^{+31.0}_{-2.1}\,M_J$ companion, in a close-in orbit with a period of $2.48881^{+0.00100}_{-0.00082}$ d, which translates to a semi-major axis of $0.0457^{+0.0020}_{-0.0016}$ au ($6.837^{+0.299}_{-0.239} \times 10^6$ km). The star has a radius of $4.72 \pm 0.44\,R_\odot$, so in both mass and radius TIC 409934330 is not too dissimilar to the namesake δ Scuti itself ($2.23^{+0.06}_{-0.05}\,M_\odot$ and $4.78 \pm 0.38\,R_\odot$; Nordström et al., 2004; Gaia Collaboration et al., 2018). The companion has a radius of $1.03^{+0.85}_{-0.49}\,R_J$ so is comparable in size to the planet Jupiter, but is more dense. Hence, we can confidently claim the nature of this companion to be a gas giant exoplanet, and due to its proximity to its host star, further claim that the exoplanet is a hot-Jupiter (which is the nomenclature that will be used for this object from now on).

The TIC 156987351 System:

The δ Scuti star TIC 156987351 is a $1.63 \pm 0.15\,M_\odot$ star hosting a $0.39^{+7.90}_{-0.33}\,M_J$ companion, in a close-in orbit with a period of $3.062988^{+0.000017}_{-0.000022}$ d, which translates to a semi-major axis of $0.0483^{+0.0026}_{-0.0056}$ au ($7.226^{+0.389}_{-0.838} \times 10^6$ km). The star has a radius of $3.05 \pm 0.28\,R_\odot$, and the companion has a radius of $0.97^{+0.56}_{-0.67}\,R_J$. This companion is less massive than Jupiter, more similar in mass to Saturn ($0.30\,M_J$; Baines et al., 2018), but with a radius 97% that of Jupiter's it is approximately two Saturn-densities. Hence, we can confidently claim the nature of this companion to be a gas

Table 7.1: *All results collated together for TIC 409934330 and TIC 156987351.*

Software	Parameter	Unit	TIC 409934330	TIC 156987351
Stellar:				
MESA and GYRE:				
	M_*	$\mathrm{M}_\odot$	2.10 ± 0.19	1.63 ± 0.15
	R_*	$\mathrm{R}_\odot$	4.72 ± 0.44	3.05 ± 0.28
	v_{eq}	$\mathrm{km\,s^{-1}}$	60 ± 0.5	97 ± 0.5
	Rotation	d	3.98 ± 0.37	1.59 ± 0.15
	Overshoot	f_{ov}	0.028 ± 0.0005	0.020 ± 0.0005
iSpec:				
	T_{eff}	K	8062 ± 29	7231 ± 63
	Fe/H	—	0.00 ± 0.20	0.00 ± 0.20
	$v \sin i$	$\mathrm{km\,s^{-1}}$	55 ± 3	71 ± 9
	Rotation	d	4.35 ± 0.47	2.18 ± 0.34
	$\log g$	$\log \mathrm{cm\,s^{-2}}$	3.86 ± 0.21	$4.020f \pm 0.014$
EXOFASTv2:				
	$\log g$	$\log \mathrm{cm\,s^{-2}}$	$3.348^{+0.13}_{-0.027}$	$3.91^{+0.19}_{-0.32}$
	Age	Gyr	$0.58^{+0.19}_{-0.16}$	$1.46^{+0.67}_{-0.61}$
	γ_1	—	$0.082^{+0.034}_{-0.029}$	$0.29^{+0.27}_{-0.18}$
	γ_2	—	$0.30^{+0.30}_{-0.21}$	$0.28^{+0.14}_{-0.15}$
Planetary:				
EXOFASTv2:				
	P	d	$2.48881^{+0.00100}_{-0.00082}$	$3.062988^{+0.000017}_{-0.000022}$
	R_P	$\mathrm{R_J}$	$1.03^{+0.85}_{-0.49}$	$0.97^{+0.56}_{-0.67}$
	M_P	$\mathrm{M_J}$	$2.5^{+31.0}_{-2.1}$	$0.39^{+7.90}_{-0.33}$
	a	au	$0.0457^{+0.0020}_{-0.0016}$	$0.0483^{+0.0026}_{-0.0056}$
	i	$^\circ$	$81.1^{+5.7}_{-12.0}$	$83.4^{+4.2}_{-6.9}$
	T_{eq}	K	4130^{+150}_{-210}	2470^{+430}_{-450}
	R_P/R_*	—	$0.022^{+0.019}_{-0.011}$	$0.040^{+0.054}_{-0.028}$
	a/R_*	—	$1.989^{+0.230}_{-0.074}$	$4.4^{+1.6}_{-1.4}$
	b	—	$0.660^{+0.037}_{-0.530}$	$0.50^{+0.39}_{-0.29}$
	ρ_P	$\mathrm{g\,cm^{-3}}$	$0.69^{+35.00}_{-0.27}$	$1.7^{+13.0}_{-1.5}$
	$\log g_P$	$\log \mathrm{cm\,s^{-2}}$	$3.41^{+1.50}_{-0.50}$	$3.22^{+1.10}_{-0.66}$
	$M_P \sin i$	$\mathrm{M_J}$	$2.4^{+29.0}_{-2.1}$	$0.38^{+7.90}_{-0.33}$
	M_P/M_*	—	$0.0012^{+0.0140}_{-0.0011}$	$0.00027^{+0.00430}_{-0.00024}$

giant exoplanet, and due to its proximity to its host star, further claim that the exoplanet is a hot-Saturn (which is the nomenclature that will be used for this object from now on). Note that for this system, and for TIC 409934300 above, M_P was determined by EXOFASTv2 using the mass-radius relationship of Chen & Kipping (2017) as in the case of both systems only transit data was fitted (this method is standard procedure for the EXOFASTv2 software; Eastman et al., 2019).

Comparing the TIC 409934330 System and the TIC 156987351 System:

TIC 409934330 is a more massive star than TIC 156987351 ($2.10 \pm 0.19\,M_\odot$ vs. $1.63 \pm 0.15\,M_\odot$), with a higher $T_{\rm eff}$ (8062 ± 29 K vs. 7231 ± 63 K) and spectral type (A2mA4 vs. F2). TIC 409934330 has a larger radius than TIC 156987351 ($4.72 \pm 0.44\,R_\odot$ vs $3.05 \pm 0.28\,R_\odot$), but a lower density (calculated to be $0.034 \pm 0.004\,\mathrm{g\,cm^{-3}}$ vs. $0.081 \pm 0.011\,\mathrm{g\,cm^{-3}}$ — for reference, average Solar density is $1.408\,\mathrm{g\,cm^{-3}}$; Ko, 1999) as revealed by both stars' surface gravities ($\log g$; $3.348^{+0.13}_{-0.027}\,\log \mathrm{cm\,s^{-2}}$ vs. $3.91^{+0.19}_{-0.32}\,\log \mathrm{cm\,s^{-2}}$). TIC 409934330 is the younger star of the pair ($0.58^{+0.19}_{-0.16}$ Gyr vs. $1.46^{+0.67}_{-0.61}$ Gyr), but both are main sequence stars (each are well below the maximum age for each spectral type and have not evolved beyond the TAMS). Furthermore, the Fourier transform of TIC 156986351 (Figure 6.3) reveals its δ Scuti pulsations to be generally lower in frequency than that of TIC 409934330 (Figure 5.3): TIC 409934330 has its δ Scuti frequencies between 15 – 40 c/d, whereas for TIC 156986351 they are between 5 – 30 c/d. This suggests that TIC 156987351 is more evolved than TIC 409934330, as an oscillating stars' frequencies of pulsation become lower frequency with increasing age (Bedding et al., 2020) — this is also consistent with the different densities of the two stars.

Next, we look at the limb darkening coefficients. The values of the quadratic limb darkening coefficients, γ_2, for the two stars are almost identical ($0.30^{+0.30}_{-0.21}$ vs. $0.28^{+0.14}_{-0.15}$, respectively), but the linear limb darkening coefficient, γ_1, for TIC 409934330

is much lower than for TIC 156987351 ($0.082^{+0.034}_{-0.029}$ vs. $0.29^{+0.27}_{-0.18}$). A smaller limb darkening coefficient represents a less-pronounced decrease in brightness towards the limb of a star, suggesting TIC 409934330 has a lower opacity than TIC 156987351 — this is as expected as TIC 409934330 is the hotter star, and stellar temperature is inversely proportional to opacity (Iglesias & Rogers, 1996).

Finally, TIC 409934330 has a slower equatorial velocity ($v_{\rm eq}$) than TIC 156987351 ($60 \pm 0.5\,{\rm km\,s^{-1}}$ vs. $97 \pm 0.5\,{\rm km\,s^{-1}}$), but this is expected as TIC 409934330 is an Am star and hence a slow rotator for its spectral type. When considering the projected velocity ($v \sin i$) values of both stars from Table 7.1 as well, the inclination angle of each star's rotation axis (with respect to the line of sight) can be determined: 66.44° for TIC 409934330 and 47.05° for TIC 156987351. Hence, when comparing the stars' rotation axis inclinations with the respective exoplanet's orbital inclinations (66.44° vs. $81.1^{+5.7}_{-12.0}$° for TIC 409934330, and 47.05° vs. $83.4^{+4.2}_{-6.9}$° for TIC 156987351), both systems are revealed to be spin-orbit misaligned, since $|\lambda|$ — the difference between the axis and orbital inclinations — is >10° for both stars (Zhou et al., 2016). This is in agreement with the work of Zhou et al. (2016) who suggest that it is very common for exoplanets that orbit hot host stars (>6300 K), and exoplanets that are hot-Jupiters, to exist in spin-orbit-misaligned systems.

Due to the physical properties of the systems, TIC 40993440 has a larger planet-to-star mass ratio (M_P/M_*; $0.0012^{+0.0140}_{-0.0011}$ vs. $0.00027^{+0.00430}_{-0.00024}$) but a smaller planet-to-star radius ratio (R_P/R_*; $0.022^{+0.019}_{-0.011}$ vs. $0.040^{+0.054}_{-0.028}$), highlighting that no mass – radius relations exist between the two systems. The two planets were dubbed earlier as a hot-Jupiter and hot-Saturn, respectively, due to their masses being comparable to their namesakes. But the hot-Jupiter is less than half the density of the hot-Saturn ($0.69^{+35.00}_{-0.27}\,{\rm g\,cm^{-3}}$ vs. $1.7^{+13.0}_{-1.5}\,{\rm g\,cm^{-3}}$). Hence, the hot-Jupiter has a density more-akin to Saturn and the hot-Saturn has a density is very close that of Neptune's ($0.687\,{\rm g\,cm^{-3}}$ and $1.64\,{\rm g\,cm^{-3}}$, respecitvely; Perryman, 2018).

Table 7.2: *The seven known δ Scuti host stars, now with TIC 409934330 and TIC 156987351 included (in bold), along with their parameters and respective references, listed in order of discovery.*
† *Whilst there is no formal mention in the literature of these stars being δ Scuti stars, they exhibit δ Scuti pulsations in their TESS light curves.*

C.C.10, H.11, G.18 = (Collier Cameron et al., 2010; Herrero et al., 2011; Goyal et al., 2018),
R.13, G.14, C.18 = (Rameau et al., 2013; Galicher et al., 2014; Chauvin et al., 2018),
R.14, M.19, H.21 = (Rowe et al., 2014; Murphy et al., 2019; Hey et al., 2021),
M.16 = (Morton et al., 2016),
C.17 = (Chauvin et al., 2017),
T.17 = (Temple et al., 2017),
H.19 = (Hellier et al., 2019),
E.23 (a) = (Ebo et al., (a) in prep),
E.23 (b) = (Ebo et al., (b) in prep).

Star Designation	Spectral Type	$T_{\rm eff}$ (K)	$\log g$ ($\log \mathrm{cm\,s^{-2}}$)	$v \sin i$ ($\mathrm{km\,s^{-1}}$)	M_* ($\mathrm{M_\odot}$)	R_* ($\mathrm{R_\odot}$)	Reference
HD 15082	kA5hA8mF4	7471 ± 63	4.35 ± 0.07	90 ± 10	1.495 ± 0.031	1.444 ± 0.034	C.C.10, H.11, G.18
HD 95086†	A8	7750 ± 250	4.0 ± 0.5	20 ± 10	1.6 ± 0.1	—	R.13, G.14, C.18
Kepler-340	F6	8150 ± 376	$4.3772400^{+0.0914693}_{-0.1062500}$	—	$1.870000^{+0.383933}_{-0.226349}$	$1.4666800^{+0.0871834}_{-0.0841834}$	R.14, M.19, H.21
Kepler-1171†	—	$7044.000^{+277.693}_{-199.093}$	$4.38^{+0.17}_{-0.09}$	—	$1.580^{+0.179}_{-0.168}$	$1.950^{+0.513}_{-0.384}$	M.16
HD 116434†	A2	8840 ± 200	—	299 ± 9	1.96 ± 0.04	1.77 ± 0.05	C.17
CD-34 8618	F1	6900 ± 150	—	52 ± 8	1.59 ± 0.08	1.79 ± 0.05	T.17
HD 134004†	A1	9360 ± 50	4.31 ± 0.04	8.2 ± 0.6	2.07 ± 0.11	1.67 ± 0.07	H.19
HD 189995†	**A2mA4**	$\mathbf{8062 \pm 29}$	$\mathbf{3.348^{+0.13}_{-0.027}}$	$\mathbf{55 \pm 3}$	$\mathbf{2.10 \pm 0.19}$	$\mathbf{4.72 \pm 0.44}$	**E.23 (a)**
HD 47874†	**F2**	$\mathbf{7231 \pm 63}$	$\mathbf{3.91^{+0.19}_{-0.32}}$	$\mathbf{71 \pm 9}$	$\mathbf{1.63 \pm 0.15}$	$\mathbf{3.05 \pm 0.28}$	**E.23 (b)**

Table 7.3: *The eight known exoplanets orbiting δ Scuti host stars, now with the hot-Jupiter and hot-Saturn orbiting TIC 409934330 and TIC 156987351, respectively, included (in bold), along with their parameters and respective references, listed in order of discovery.*

C.C.10, H.11, G.18 = (Collier Cameron et al., 2010; Herrero et al., 2011; Goyal et al., 2018),
R.13, G.14, C.18 = (Rameau et al., 2013; Galicher et al., 2014; Chauvin et al., 2018),
R.14, M.19, H.21 = (Rowe et al., 2014; Murphy et al., 2019; Hey et al., 2021),
M.16 = (Morton et al., 2016),
C.17 = (Chauvin et al., 2017),
T.17 = (Temple et al., 2017),
H.19 = (Hellier et al., 2019),
E.23 (a) = (Ebo et al., (a) in prep),
E.23 (b) = (Ebo et al., (b) in prep).

Exoplanet	P (d)	M_p (M_J)	R_p (R_J)	a au	Reference
WASP-33 b	1.2198669 ± 0.0000012	<4.1	1.497 ± 0.045	0.02555 ± 0.00017	C.C.10, H.11, G.18
HD 95086 b	$288.6^{+11.5}_{-176.5}$ yr	4.5 ± 0.5	—	$52.0^{+12.8}_{-24.3}$	R.13, G.14, C.18
Kepler-340 b	14.844387 ± 0.000473	—	0.226 ± 0.054	0.1340	R.14, M.19, H.21
Kepler-340 c	22.824669 ± 0.000481	—	0.301 ± 0.069	0.1780	R.14, M.19, H.21
Kepler-1171 b	$1.44259224 \pm 0.00000219$	—	$0.228^{+0.061}_{-0.045}$	—	M.16
HIP 65426 b	$\sim$600 yr	9.0 ± 3.0	1.5 ± 0.1	$\sim$92	C.17
WASP-167 b	2.0219596 ± 0.0000006	<8	1.58 ± 0.05	0.0365 ± 0.0006	T.17
WASP-178 b	3.3448285 ± 0.0000012	1.66 ± 0.12	1.81 ± 0.09	0.0558 ± 0.0010	H.19
Hot-Jupiter	$\mathbf{2.48881^{+0.00100}_{-0.00082}}$	$\mathbf{2.5^{+31.0}_{-2.1}}$	$\mathbf{1.03^{+0.85}_{-0.49}}$	$\mathbf{0.0457^{+0.0020}_{-0.0016}}$	**E.23 (a)**
Hot-Saturn	$\mathbf{3.062988^{+0.000017}_{-0.000022}}$	$\mathbf{0.39^{+7.90}_{-0.33}}$	$\mathbf{0.97^{+0.56}_{-0.67}}$	$\mathbf{0.0483^{+0.0026}_{-0.0056}}$	**E.23 (b)**

Comparing the Studied Systems to the Known Systems:

Table 7.2 is a repeat of Table 1.3, which lists all known δ Scuti host stars from the literature, but now-included are TIC 409934330 and TIC 156987351 for comparison. Likewise, Figure 7.1 is a repeat of the data from Figure 6.15, but now only includes the known δ Scuti host stars from the literature as well as the two new stars from this work. Also included is β Pictoris — see discussion below.

The spectral types and $T_{\rm eff}$ of TIC 409934330 and TIC 156987351 lie comfortably within the respective ranges of the known δ Scuti host stars, as expected given our initial search criteria, but their $\log g$ values are the lowest in the table. However, note that several of the stars have a $\log g$ close to that of the Sun, because some authors take $\log g_{\odot}$ as a proxy if the true $\log g$ value is unknown (Canto Martins et al., 2020). The masses of the two stars studied in this work fit in line with those of the known δ Scuti hosts, but when comparing the radii of all the stars, that of TIC 409934330 and TIC 156987351 are larger. There is no reason to doubt these radius values — as mentioned above: note that the mass and radius of TIC 409934330 is very similar to that of the star δ Scuti itself — but future work will look into repeating measurements to check these values.

Table 7.3 is a repeat of Table 1.4, which lists all known exoplanets from the literature that orbit δ Scuti stars, but now-included are the hot-Jupiter and hot-Saturn that orbit TIC 409934330 and TIC 156987351, respectively, for comparison.

All values deduced for the exoplanets studied in this work fit in well with literature values of the known populations, but note that the orbital periods and semi-major axes of HD 95086 b and HIP 65426 b are larger than the rest: this could be due to a selection effect since these exoplanets were discovered via the direct imaging method (Rameau et al., 2013; Galicher et al., 2014; Chauvin et al., 2018, 2017).

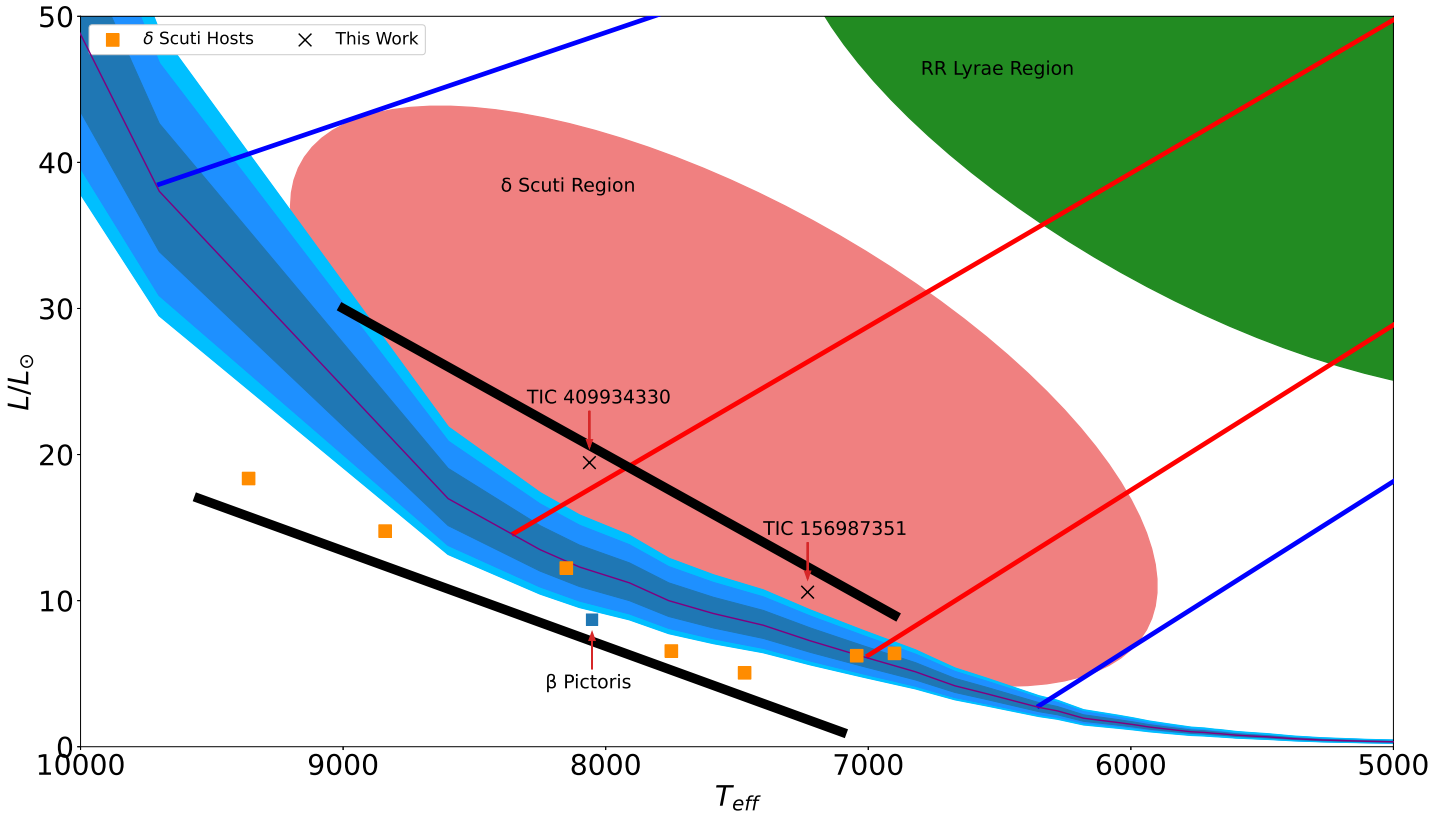

Figure 7.1: *An HR diagram showing The δ Scuti Cone (black lines), within which all lie: the known δ Scuti host stars (orange squares), TIC 409934330 and TIC 156987351 (the two crosses; both labelled), and β Pictoris (blue square). The blue streak is the main sequence track, built using star data from Pecaut & Mamajek (2013), showing a range of thicknesses represented by different shades of blue, each a main sequence width errors according to Fernandes, Lebreton & Baglin (1996) and Lebreton et al. (1997). The two perpendicular blue lines outline the classical instability strip, encompassing the δ Scuti star (red) and the RR Lyrae star (green) regions, mirroring the colour schemed used in the pulsational HR diagram in Figure 1.7. The two reds lines parallel to the blue lines enclose the theoretical δ Scuti instability strip according to Dupret et al. (2004).*

All systems also have another common attribute: they all lie in a confined region on the HR diagram that this work has labelled "The δ Scuti Cone".

First let us look at observational bias: the more luminous a star is the less starlight a certain sized companion will block during a transit, causing smaller dips to appear in a light curve. And with all the known exoplanets orbiting δ Scuti stars having luminosities of $\lesssim$20 $L_{\odot}$, we do not know whether more luminous δ Scuti stars host companions that have signals too small to detect. However, note that more luminous stars have stronger stellar winds than fainter stars, which would accelerate the dispersal of their proto-planetary discs and stop planets forming at all (Conti & McCray, 1980) — there is no empirical relation between stellar mass and winds in the literature, so it is difficult to discuss this theory quantitively.

Close-in to the Sun (used here as a proxy for all G-type stars), at an orbit with a semi-major axis of $\approx$1 $R_{\odot}$ ($\approx$7.0$\times$10^6 km; consistent with the semi-major axes of the exoplanets orbiting TIC 409934330 and TIC 156987351) the magnetised-corona drives the Solar wind up to speeds of 750 km s^{-1} (Geller et al., 2002). F-type stars have faster winds from a similar mechanism, of up to 1000 km s^{-1} (Seach et al., 2022), and stellar winds are faster still for the hottest stars on the main sequence, at 1500 km s^{-1}+ for the O- and B-type stars (although here the stellar winds are driven by radiation pressure; Castor, Abbott & Klein, 1975). Hence a dependance of wind speed on spectral type can be seen, so we assume that A-type stars have stellar winds between that of the F-type, and O- and B-types — this is true, at least, for main sequence stars. For stars that evolve off the main sequence, and increase in luminosity as they travel up the red giant branch, their stellar winds contrarily become enormously reduced down to 10 – 100 km s^{-1} (Mattsson & Höfner, 2011). However, in the case of these more-luminous evolved stars, *slower* winds do not mean *weaker* winds: the mechanism driving stellar winds in these post-main sequence stars is still radiation pressure, but now coupled with mass-ejection, which

increases the density (and hence momentum) of the stellar winds by up to three orders of magnitude (Sandin & Höfner, 2004). And with the intermediate mass stars (A- and F-type) having respective main sequence lifetimes of 2 – 20 Myr (on the order of the dispersion time of proto-planetary discs; Laughlin, Bodenheimer & Adams, 1997; Hansen, Kawaler & Trimble, 2012; Li & Xiao, 2016) this phenomenon is one reason that we hypothesis why δ Scuti – exoplanet systems are so rare.

As mentioned in § 1.1.7.1, the intrinsic stellar instabilities of the classical δ Scuti stars cause visual brightness changes of up to 0.3 mag (and up to 1.0 mag for the HADS stars), dependant on the amplitudes of pulsations (Sun et al., 2021). Let us use Kepler-1171 as a first example, sitting right on the main sequence track in Figure 7.1, with an average luminosity of 6.12 $L_\odot$. It has an absolute magnitude (from the its distance modulus) of 2.86 mag, and hence if it had a $\pm$0.3 mag variability its luminosity would constantly vary by $\pm$3.64 $L_\odot$ — this is fine as its luminosity remains relatively low, hence its proto-planetary disc does not undergo sufficient disruption that it gets blown away in its entirety. Let us now look at the most luminous δ Scuti star in the sample: TIC 409934330, with an average luminosity of 19.45 $L_\odot$. From its distance modulus (*not* accounting for the parallax error as otherwise done in Chapter 5), the star has an absolute magnitude of 0.91. And once again, if it had the $\pm$0.3 mag brightness fluctuations, its luminosity would change by $\pm$10.31 $L_\odot$ — now we are in the range where stars become too luminous to allow planet formation from their stellar wind momentum. Of course, the two aforementioned stars do not have $\pm$0.3 mag brightness fluctuations, which could well be why they *are* exoplanet hosts. But many δ Scuti stars *do* have such brightness fluctuations — and much more for the HADS stars. Yet, with its larger mass playing a role too, it can be considered that TIC 409934330 is on the limit of what parameters δ Scuti stars can have and still host exoplanets, and even this limit could cause disruptions to their proto-planetary discs from their periodically-changing stellar winds blowing

away material, and causing grain erosion of planetesimals. Hence, only the more massive proto-planets survive — which is why all known exoplanets orbiting δ Scuti stars are gas giants — and this phenomena is the second reason that we hypothesis why δ Scuti – exoplanet systems are so rare: the most luminous and/or the highest amplitude δ Scuti stars do not have to evolve off the main sequence before their luminosities induce stellar winds fast enough to have the same momentum as the winds of the post-main sequence stars, preventing the chance of planet formation. We therefore additionally hypothesise that the reason the population of all known δ Scuti host stars in Table 7.2 lie in the same region on the HR diagram is because they all share another common attribute: they all have low-amplitude pulsations.

Figure 7.1 shows a zoomed-in view of The δ Scuti Cone from Figure 6.15. The Cone itself illustrates the narrow band of parameter space along which the δ Scuti host stars in Table 7.2 all lie, flanked by the black lines, which border both sides of the main sequence track drawn from a full spectrum of star data from Pecaut & Mamajek (2013): the main sequence track is in various shades of blue due to all three sets of main sequence width errors from Fernandes, Lebreton & Baglin (1996) and Lebreton et al. (1997). The two blue lines perpendicular to the main sequence track outline the classical instability strip, its width based on the temperature ranges different varieties of pulsating star can be. This area hence encompasses the δ Scuti and RR Lyrae star regions, in red and green, respectively, mirroring the colour schemed used in the pulsational HR diagram in Figure 1.7. The two red lines also perpendicular to the main sequence track outline the theoretical δ Scuti instability strip according to Dupret et al. (2004). The two crosses represent TIC 4090344330 and TIC 156987351, both individually labelled in the Figure. The orange squares are the positions of the previously-known δ Scuti host stars, and the blue square is a new addition of β Pictoris. This star was omitted from the original sample as at $<$25 Myr it is pre-main sequence (Mamajek & Bell, 2014), but the star has been

included for comparison here as it exhibits δ Scuti pulsations, and is known to host two exoplanets (Koen, 2003; Lagrange et al., 2009, 2019) — β Pictoris is in very good agreement with the rest of the sample.

It can be seen that four of the known δ Scuti host stars lie below the main sequence track, but this is consistent with the case of β Pictoris mentioned above. Three of the δ Scuti host stars lie on the main sequence track, as expected, but the two stars studied in this thesis lie above it. This reflects those stars having the two largest masses of all the δ Scuti host stars listed in Table 7.2, and hence greater luminosities due to the mass-luminosity relationship (Equation 5.1).

We note that only 60% of the δ Scuti host stars in Figure 7.1 lie within the boundaries of the theoretical δ Scuti instability strip (red lines) of Dupret et al. (2004). The width of this theoretical δ Scuti instability strip is specifically based on stars that pulsate non-radially (ℓ>0; as do TIC 409934330 and TIC 15698735), and Dupret et al. (2004) state that the $T_{\rm eff}$ of the boundaries of the theoretical δ Scuti instability strip increase with increasing degree, ℓ, so in Figure 7.1 the star lying on the outside of the cooler edge of the the theoretical δ Scuti instability strip boundary might well be a radial pulsator, and would otherwise exist within the $\ell = 0$ theoretical δ Scuti instability strip limits (lower $T_{\rm eff}$ boundaries). However, the same argument cannot be made for TIC 40993430, as this star does display non-radial pulsations and so should exist within the red boundary lines of the theoretical δ Scuti instability strip.

Furthermore, of the pre-main sequence δ Scuti host star population, two of the stars lie hotter than the red boundary lines as well. And since the hotter boundary of the theoretical δ Scuti instability strip cuts right through the middle of the entire δ Scuti accepted $T_{\rm eff}$ range, we argue that the theoretical δ Scuti instability strip according to Dupret et al. (2004) is too narrow.

Murphy et al. (2019) calculated an empirical δ Scuti instability strip based on *Gaia*-derived luminosities of *Kepler* stars, and found its boundaries to be wider

than the theoretical δ Scuti instability strip according to Dupret et al. (2004). We based our instability strip width on the maximum $T_{\rm eff}$ ranges of the different types of pulsating stars that populate it: the fact that the boundaries of Murphy et al. (2019) are wider than those of Dupret et al. (2004) allows us to have confidence that the width of our classical instability strip (blue lines in Figure 7.1) encompasses all δ Scuti pulsators.

There is an absence of δ Scuti host stars in a large fraction of the δ Scuti (red) region in Figure 7.1, with none lying above the black line of The δ Scuti Cone's upper boundary. This is consistent with our above hypothesis: that δ Scuti stars lying above this line are too luminous to permit planet formation. All of the known δ Scuti host stars lie in a restricted $T_{\rm eff}$ – luminosity parameter space, not far from the main sequence track.

So, in summary:

1) We have found that δ Scuti stars that host planetary systems only populate the lower part of the "δ Scuti" region of the HR diagram, as shown in Figure 7.1.

2) We have hypothesised that the more luminous δ Scuti stars disrupt planet formation from their stellar winds: either via short main sequence lifetimes increasing the density of the winds from red giant branch mass ejections, or from high amplitude pulsations fuelling large fluctuations in luminosity, proportionally increasing the speed of the winds.

3) We have argued that β Pictoris should be included in this sample, despite its pre-main sequence nature, since it lies in the same part of the HR diagram as four of the previously-known δ Scuti planet hosts do, slightly below the main sequence.

4) We have shown that the the parameter constraints of the theoretical δ Scuti instability strip according to Dupret et al. (2004) are too narrow: the wider classical instability strip used in this work (blue lines in Figure 7.1), based off the maximum $T_{\rm eff}$ ranges of the different types of pulsating stars that populate it, agree with the wider boundaries of the *Kepler*-based empirical δ Scuti instability strip of Murphy et al. (2019)).

5) We have theorised that only the most massive exoplanets can form around δ Scuti stars, as the known sample are all gas giants, and that these planets only survived the still-turbulent planet formation as their host stars exhibit only low-amplitude pulsations.

6) The known population of δ Scuti stars hosting exoplanets is now 10, and this sample can be used for further study to investigate the remaining planet candidates that lie in the vicinity of The δ Scuti Cone, to ascertain their physical properties and environments and that of the Cone, to determine if it is astrophysical: such results could lead to defining a new sub-region on the classical instability strip.

Table 7.4: *The remaining 15 TOIs that are δ Scuti candidate host stars, with $T_{\rm eff}$ > 6300 K, listed in increasing TOI designation. Data were extracted from SIMBAD, the TASOC and the TIC (Guerrero et al., 2021).*

TOI	TIC	Spectral Type	V Mag	Coordinates	$T_{\rm eff}$ (K)	Companion Orbital Period (d)
522	19451711	A6	7.580	08:18:24.7 -07:34:16.6	7381 ± 160	0.397853 ± 0.000022
610	80275202	—	10.600	08:06:06.3 -44:22:30.4	8360 ± 160	3.664953 ± 0.000009
861	372913430	B8.5	8.380	07:58:08.1 -60:46:50.0	10341 ± 160	6.739160 ± 0.000024
877	255704097	—	10.780	06:36:27.6 -50:17:50.8	7686 ± 160	6.014943 ± 0.000659
884	167031605	B8	9.910	06:15:41.0 +11:49:57.5	11246 ± 160	2.780900 ± 0.000610
886	120269103	A0	8.330	06:46:46.5 -06:08:41.2	8844 ± 160	20.42767 ± 0.002103
986	320536216	—	10.260	08:00:25.3 +10:20:38.0	8031 ± 160	0.547669 ± 0.000000
1019	341420329	—	10.890	08:00:35.5 -54:52:42.8	7645 ± 160	5.234096 ± 0.000027
1032	146589986	A0	9.762	10:36:53.2 -42:32:30.0	10395 ± 160	5.664473 ± 0.000769
1034	400595342	A2	9.880	08:57:46.0 -49:00:02.1	9810 ± 160	3.634469 ± 0.000977
1120	143257766	A8/9	10.397	19:33:33.4 -45:53:33.7	7301 ± 160	1.66226 ± 0.00000
1888	459997997	A	10.520	10:25:00.1 -60:34:30.7	8511 ± 160	5.547485 ± 0.000025
2001	118084044	A5	9.200	08:32:43.5 -58:34:31.9	7703 ± 160	2.743456 ± 0.000124
2554	144043410	—	10.750	08:27:01.2 -20:40:48.5	6888 ± 160	6.263650 ± 0.001046
2633	386131764	—	11.910	07:26:21.7 -13:55:32.3	7811 ± 160	18.196049 ± 0.003232

7.2 Future Work

Figure 6.15, the HR diagram showing The δ Scuti Cone at the end of Chapter 6, contains within it 15 grey crosses that represent the remaining TOIs that matched the criteria of being δ Scuti stars with $T_{\rm eff} > 6300\,{\rm K}$ — these TOIs may also host companions due to the stars exhibiting transit signatures in their light curves. I could work through these TOIs, modelling the stars, companions, and obtain spectra as with the two stars in this thesis, to make The δ Scuti Cone more complete — note the trend that almost all of the δ Scuti TOIs lie amongst the known δ Scuti host star population already, suggesting good agreement to the known population. The 15 remaining TOIs are listed in Table 7.4, and Appendix P contains Figures P.1 to P.45: their respective light curves, phased curves and Fourier transforms, created from TESS observations.

Simon J. Ebo, 2024

Bibliography

, 1997, ESA Special Publication, Vol. 1200, The HIPPARCOS and TYCHO catalogues. Astrometric and photometric star catalogues derived from the ESA HIPPARCOS Space Astrometry Mission

Abt H., 1961, AJ, 70, 277

Abt H. A., 1979, AJ, 84, 1591

—, 2000, ApJ, 544, 933

—, 2009, AJ, 138, 28

Abt H. A., Levy S. G., 1985, ApJS, 59, 229

Abt H. A., Moyd K. I., 1973, ApJ, 182, 809

Adams J. C., 1846, MNRAS, 7, 149

Aerts C., Christensen-Dalsgaard J., Kurtz D. W., 2010, Asteroseismology. Springer

Agol E., Steffen J., Sari R., Clarkson W., 2005, MNRAS, 359, 567

Ahmed S., Warren S. J., 2019, A&A, 623, A127

Akima H., 1996, ACM Trans. Math. Softw., 22, 357–361

Amado P. J., Moya A., Suárez J. C., Martín-Ruiz S., Garrido R., Rodríguez E., Catala C., Goupil M. J., 2004, MNRAS, 352, L11

Anglada-Escudé G. et al., 2016, Nature, 536, 437

Angulo C., 1999, in American Institute of Physics Conference Series, Vol. 495, Experimental Nuclear Physics in europe: Facing the next millennium, pp. 365–366

Arimoto N., 2005, in From Lithium to Uranium: Elemental Tracers of Early Cosmic Evolution, Hill V., Francois P., Primas F., eds., Vol. 228, pp. 503–512

Artigau É. et al., 2022, AJ, 164, 84

Asplund M., Grevesse N., Sauval A. J., Scott P., 2009, ARA&A, 47, 481

Baglin A. et al., 2006, in 36th COSPAR Scientific Assembly, Vol. 36, p. 3749

Bahcall J. N., Basu S., Pinsonneault M., Serenelli A. M., 2005, ApJ, 618, 1049

Bailey S. I., 1902, Annals of Harvard College Observatory, 38, 1

Baines K. H., Flasar F. M., Krupp N., Stallard T., 2018, Saturn in the 21st Century

Baker N., Kippenhahn R., 1965, ApJ, 142, 868

Bakos G. Á. et al., 2009, ApJ, 696, 1950

Balmer J. J., 1885, Annalen der Physik, 261, 80

Balona L. A., 2016, MNRAS, 459, 1097

Balona L. A., Catanzaro G., Abedigamba O. P., Ripepi V., Smalley B., 2015, MNRAS, 448, 1378

Balona L. A., Krisciunas K., Cousins A. W. J., 1994, MNRAS, 270, 905

Barclay T. et al., 2013, Nature, 494, 452

Barnes S. A., 2003, ApJ, 586, 464

—, 2007, ApJ, 669, 1167

Barnes S. I. et al., 2008, in Society of Photo-Optical Instrumentation Engineers (SPIE) Conference Series, Vol. 7014, Ground-based and Airborne Instrumentation for Astronomy II, McLean I. S., Casali M. M., eds., p. 70140K

Basri G., Borucki W. J., Koch D., 2005, New Astronomy Reviews, 49, 478

Bateman H., 1915, Monthly Weather Review, 43, 163

Bedding T. R. et al., 2020, Nature, 581, 147

Berdyugina S. V., Berdyugin A. V., Fluri D. M., Piirola V., 2008, ApJL, 673, L83

Bertin E., Arnouts S., 1996, A&AS, 117, 393

Bhardwaj A., Kanbur S. M., Rejkuba M., Marconi M., Catelan M., Ripepi V., Singh H. P., 2022, A&A, 668, A59

Blanco-Cuaresma S., 2019, MNRAS, 486, 2075

Blanco-Cuaresma S., Soubiran C., Heiter U., Jofré P., 2014, A&A, 569, A111

Bohn A. J. et al., 2020, ApJL, 898, L16

Bonaca A. et al., 2012, ApJL, 755, L12

Bond I. A. et al., 2004, ApJL, 606, L155

Borkovits T., Csizmadia S., Forgács-Dajka E., Hegedüs T., 2011, A&A, 528, A53

Borucki W. et al., 2008, in IAU Symposium, Vol. 249, Exoplanets: Detection, Formation and Dynamics, Sun Y.-S., Ferraz-Mello S., Zhou J.-L., eds., pp. 17–24

—, 2009, in IAU Symposium, Vol. 253, Transiting Planets, Pont F., Sasselov D., Holman M. J., eds., pp. 289–299

Borucki W. J. et al., 2010, Science, 327, 977

—, 2011, ApJ, 736, 19

—, 2003, in Proc. SPIE, Vol. 4854, Future EUV/UV and Visible Space Astrophysics Missions and Instrumentation., Blades J. C., Siegmund O. H. W., eds., pp. 129–140

Boss B., 1937, General Catalogue of 33342 stars for the epoch 1950. Vol.1: Introduction and explanatory tables; Right Ascension 6h - 12h; Right Ascension 12h - 18h; Vol.5: Right Ascension 18h - 24h

Box G. E., 1979, Robustness in the strategy of scientific model building. Elsevier, pp. 201–236

Bramall D. G. et al., 2012, in Society of Photo-Optical Instrumentation Engineers (SPIE) Conference Series, Vol. 8446, Ground-based and Airborne Instrumentation for Astronomy IV, McLean I. S., Ramsay S. K., Takami H., eds., p. 84460A

—, 2010, in Society of Photo-Optical Instrumentation Engineers (SPIE) Conference Series, Vol. 7735, Ground-based and Airborne Instrumentation for Astronomy III, McLean I. S., Ramsay S. K., Takami H., eds., p. 77354F

Breger M., 1990, Delta Scuti Star Newsletter, 2, 21

Breton S. N., Brun A. S., García R. A., 2022, A&A, 667, A43

Brooks T., Stahl H. P., Arnold W. R., 2015, in Society of Photo-Optical Instrumentation Engineers (SPIE) Conference Series, Vol. 9577, Optical Modeling and Performance Predictions VII, Kahan M. A., Levine-West M. B., eds., p. E3

Brown T. M., Ferguson H. C., Smith E., Kimble R. A., Sweigart A. V., Renzini A., Rich R. M., 2004, AJ, 127, 2738

Buckley D. A. H., Stobie R. S., 2001, in Astronomical Society of the Pacific Conference Series, Vol. 232, The New Era of Wide Field Astronomy, Clowes R., Adamson A., Bromage G., eds., p. 380

Burgers J., 1948, in , Elsevier, pp. 171–199

Burkhart C., 1979, A&A, 74, 38

Burnham R., 1978, Burnham's celestial handbook. an observers guide to the universe beyond the solar system, Vol. 445

Calabretta M., Greisen E. W., 2000, in Astronomical Society of the Pacific Conference Series, Vol. 216, Astronomical Data Analysis Software and Systems IX, Manset N., Veillet C., Crabtree D., eds., p. 571

Campbell B., Walker G. A. H., Yang S., 1988, ApJ, 331, 902

Cannon A. J., 1925a, Annals of Harvard College Observatory, 100, 17

—, 1925b, Annals of Harvard College Observatory, 100, 1

—, 1927, Annals of Harvard College Observatory, 100, 33

—, 1928, Annals of Harvard College Observatory, 100, 49

—, 1931, Annals of Harvard College Observatory, 100, 61

—, 1936, Annals of Harvard College Observatory, 100, 205

Cannon A. J., Mayall M. W., 1949, Annals of Harvard College Observatory, 112, 1

Cannon A. J., Pickering E. C., 1918, Annals of Harvard College Observatory, 91, 1

Canto Martins B. L. et al., 2020, ApJS, 250, 20

Carson J. et al., 2013, ApJL, 763, L32

Casamiquela L. et al., 2018, A&A, 610, A66

Cassan A. et al., 2012, Nature, 481, 167

Castelli F., Kurucz R. L., 2003, in Modelling of Stellar Atmospheres, Piskunov N., Weiss W. W., Gray D. F., eds., Vol. 210, p. A20

Castor J. I., Abbott D. C., Klein R. I., 1975, ApJ, 195, 157

Caughlan G. R., Fowler W. A., 1988, Atomic Data and Nuclear Data Tables, 40, 283

Charbonneau D. et al., 2009, Nature, 462, 891

Charpinet S. et al., 2011, Nature, 480, 496

Chauvin G. et al., 2017, A&A, 605, L9

—, 2018, A&A, 617, A76

Chauvin G., Lagrange A. M., Dumas C., Zuckerman B., Mouillet D., Song I., Beuzit J. L., Lowrance P., 2004, A&A, 425, L29

Chen J., Kipping D., 2017, ApJ, 834, 17

Choi J., Dotter A., Conroy C., Cantiello M., Paxton B., Johnson B. D., 2016, ApJ, 823, 102

Christensen-Dalsgaard J., Gough D. O., 2001, MNRAS, 326, 1115

Christie G., 2006, Society for Astronomical Sciences Annual Symposium, 25, 97

Claret A., 2017, A&A, 600, A30

Claret A., Bloemen S., 2011, A&A, 529, A75

Collier Cameron A. et al., 2007, MNRAS, 375, 951

—, 2010, MNRAS, 407, 507

Conti P. S., 1970, PASP, 82, 781

Conti P. S., McCray R., 1980, Science, 208, 9

Coppejans R. et al., 2013, PASP, 125, 976

Cowling T. G., 1941, MNRAS, 101, 367

Cox J. P., Giuli R. T., 1968, Principles of stellar structure

Crause L. A. et al., 2014, in Society of Photo-Optical Instrumentation Engineers (SPIE) Conference Series, Vol. 9147, Ground-based and Airborne Instrumentation for Astronomy V, Ramsay S. K., McLean I. S., Takami H., eds., p. 91476T

Crook A. C., Huchra J. P., Martimbeau N., Masters K. L., Jarrett T., Macri L. M., 2007, ApJ, 655, 790

Cruzalèbes P. et al., 2019, MNRAS, 490, 3158

Cunha M. S. et al., 2007, A&A Rev., 14, 217

Currie T. et al., 2023, Science, 380, 198

Cutri R. M. et al., 2003, VizieR Online Data Catalog, II/246

Danielski C., Baudino J.-L., Lagage P.-O., Boccaletti A., Gastaud R., Coulais A., Bézard B., 2018, AJ, 156, 276

de Boer K., Seggewiss W., 2008, Stars and Stellar Evolution

de Wit J. et al., 2017, ApJL, 836, L17

Debernardi Y., Mermilliod J. C., Carquillat J. M., Ginestet N., 2000, A&A, 354, 881

Deeg H. J., Garrido R., Claret A., 2001, NewA, 6, 51

Delgado Mena E. et al., 2019, A&A, 624, A78

Di Stefano R., Berndtsson J., Urquhart R., Soria R., Kashyap V. L., Carmichael T. W., Imara N., 2020, arXiv e-prints, arXiv:2009.08987

Dommanget J., 1983, Bulletin d'Information du Centre de Donnees Stellaires, 24, 83

Dommanget J., Nys O., 1994, Communications de l'Observatoire Royal de Belgique, 115, 1

Dotter A., 2016, ApJS, 222, 8

Doyle L. R. et al., 2011, Science, 333, 1602

Dupret M. A., Grigahcène A., Garrido R., Gabriel M., Scuflaire R., 2004, A&A, 414, L17

—, 2005, A&A, 435, 927

Duric N., 2004, Advanced astrophysics

Eastman J., 2012, Time Utilities. Astrophysics Source Code Library, record ascl:1206.012

Eastman J., Gaudi B. S., Agol E., 2013, PASP, 125, 83

Eastman J. D. et al., 2019, arXiv e-prints, arXiv:1907.09480

Eddington A. S., 1917, The Observatory, 40, 290

—, 1926, The Internal Constitution of the Stars

Eggleton P. P., 1971, MNRAS, 151, 351

Emilio M., Kuhn J. R., Bush R. I., Scholl I. F., 2012, ApJ, 750, 135

Epstein C. R. et al., 2014, ApJL, 785, L28

Fabricius C., Makarov V. V., 2000, A&A, 356, 141

Faigler S., Tal-Or L., Mazeh T., Latham D. W., Buchhave L. A., 2013, ApJ, 771, 26

Faria J. P. et al., 2022, A&A, 658, A115

Fath E. A., 1937, Lick Observatory Bulletin, 487, 77

Feltzing S., Gonzalez G., 2001, A&A, 367, 253

Ferguson J. W., Alexander D. R., Allard F., Barman T., Bodnarik J. G., Hauschildt P. H., Heffner-Wong A., Tamanai A., 2005, ApJ, 623, 585

Fernandes J., Lebreton Y., Baglin A., 1996, A&A, 311, 127

Fischer D. A. et al., 2012, MNRAS, 419, 2900

Fischer D. A., Valenti J., 2005, ApJ, 622, 1102

Flower P. J., 1996, ApJ, 469, 355

Freedman R. A., Geller R. M., Kaufmann W. J., 2014, Universe: stars and galaxies, 5th Edition

Gaia Collaboration, 2020, VizieR Online Data Catalog, I/350

—, 2022, VizieR Online Data Catalog, I/355

Gaia Collaboration et al., 2018, A&A, 616, A1

Gaia Collaboration, Brown A. G. A., Vallenari A., Prusti T., de Bruijne J. H. J., Babusiaux C., Biermann M., 2020, arXiv e-prints, arXiv:2012.01533

Gaia Collaboration et al., 2021, A&A, 649, A1

—, 2016a, A&A, 595, A2

—, 2016b, A&A, 595, A1

Galicher R. et al., 2014, A&A, 565, L4

Galle J. G., 1846, MNRAS, 7, 153

García R. A., Ballot J., 2019, Living Reviews in Solar Physics, 16, 4

Gaudi B. S. et al., 2017, Nature, 546, 514

Gautschy A., Saio H., 1996, ARA&A, 34, 551

Geller E., et al., 2002, McGraw-Hill Encyclopedia of Science & Technology. McGraw-Hill Professional

Giacalone S. et al., 2021, AJ, 161, 24

Gill D., 1903, Annals of the Cape Observatory, 9, 1

Gill D., Kapteyn J. C., 1896, Annals of the Cape Observatory, 3, 1

—, 1897, Annals of the Cape Observatory, 4, 1

—, 1900, Annals of the Cape Observatory, 5, 1

Gillon M., Jehin E., Magain P., Chantry V., Hutsemékers D., Manfroid J., Queloz D., Udry S., 2011, in European Physical Journal Web of Conferences, Vol. 11, European Physical Journal Web of Conferences, p. 06002

Gillon M. et al., 2017, Nature, 542, 456

Girardi L., Groenewegen M. A. T., Hatziminaoglou E., da Costa L., 2005, A&A, 436, 895

Goodricke J., 1786, Philosophical Transactions of the Royal Society of London Series I, 76, 48

Goyal J. M. et al., 2018, MNRAS, 474, 5158

Gray D. F., 2014, AJ, 147, 81

Greisen E. W., Calabretta M. R., 2002, A&A, 395, 1061

Grevesse N., Asplund M., Sauval A. J., 2007, Space Sci. Rev., 130, 105

Grevesse N., Noels A., 1993, Physica Scripta Volume T, 47, 133

Grimm S. L. et al., 2018, A&A, 613, A68

Guerrero N. M. et al., 2021, ApJS, 254, 39

Guzik J. A., Kaye A. B., Bradley P. A., Cox A. N., Neuforge C., 2000, ApJL, 542, L57

Haas M. R. et al., 2014, in American Astronomical Society Meeting Abstracts, Vol. 223, American Astronomical Society Meeting Abstracts #223, p. 228.01

Hairer E., Wanner G., 1996, Solving Ordinary Differential Equations II. Stiff and Differential-Algebraic Problems. Springer, Berlin, iD: unige:12344

Hambleton K. et al., 2018, MNRAS, 473, 5165

Handler G., 2009, in American Institute of Physics Conference Series, Vol. 1170, Stellar Pulsation: Challenges for Theory and Observation, Guzik J. A., Bradley P. A., eds., pp. 403–409

Handler G. et al., 2020, Nature Astronomy, 4, 684

Hansen C. J., Kawaler S. D., Trimble V., 2012, Stellar interiors: physical principles, structure, and evolution. Springer Science & Business Media

Haramundanis K., 1967, AJ, 72, 588

Harris H. C., Welch D. L., 1989, AJ, 98, 981

Hartkopf W. I., Mason B. D., Barry D. J., McAlister H. A., Bagnuolo W. G., Prieto C. M., 1993, AJ, 106, 352

Hatzes A., Cochran W., Endl M., Paulson D., McArthur B., Walker G., 2002, in Astronomische Gesellschaft Abstract Series, Vol. 19, Astronomische Gesellschaft Abstract Series, pp. 6–6

Hatzes A. P., Cochran W. D., Endl M., McArthur B., Paulson D. B., Walker G. A. H., Campbell B., Yang S., 2003, ApJ, 599, 1383

Hauck B., Mermilliod M., 1998, A&AS, 129, 431

Hauschildt P. H., Allard F., Baron E., 1999, ApJ, 512, 377

Hauschildt P. H., Allard F., Ferguson J., Baron E., Alexander D. R., 1999, ApJ, 525, 871

Hébrard G. et al., 2010, A&A, 516, A95

Hellier C. et al., 2019, MNRAS, 490, 1479

—, 2012, MNRAS, 426, 739

Henyey L., Vardya M. S., Bodenheimer P., 1965, ApJ, 142, 841

Herrero E., Morales J. C., Ribas I., Naves R., 2011, A&A, 526, L10

Herschel W., Watson D., 1781, Philosophical Transactions of the Royal Society of London Series I, 71, 492

Herwig F., 2000, A&A, 360, 952

Hey D. R., Montet B. T., Pope B. J. S., Murphy S. J., Bedding T. R., 2021, AJ, 162, 204

Hill G. M., Landstreet J. D., 1993, A&A, 276, 142

Høg E. et al., 2000, A&A, 355, L27

Holman M. J., Murray N. W., 2005, Science, 307, 1288

Horch E., van Altena W. F., Girard T. M., Franz O. G., López C. E., Timothy J. G., 2001, AJ, 121, 1597

Houk N., 1978, Michigan catalogue of two-dimensional spectral types for the HD stars

Houk N., Cowley A. P., 1975, University of Michigan Catalogue of two-dimensional spectral types for the HD stars. Volume I. Declinations -90_ to -53_f0.

Howard A. W. et al., 2012, ApJS, 201, 15

Howell S. B. et al., 2014, PASP, 126, 398

Hoyle F., 1946, MNRAS, 106, 343

—, 1954, ApJS, 1, 121

Huang X. et al., 2017, in American Astronomical Society Meeting Abstracts, Vol. 230, American Astronomical Society Meeting Abstracts #230, p. 102.09

Hurley M., Roberts P. H., Wright K., 1966, ApJ, 143, 535

Iglesias C. A., Rogers F. J., 1993, ApJ, 412, 752

—, 1996, ApJ, 464, 943

Iglesias C. A., Rogers F. J., Wilson B. G., 1987, ApJL, 322, L45

Iliadis C., 2007, Nuclear Physics of Stars

Iliev I. K., Budaj J., Feňovčík M., Stateva I., Richards M. T., 2006, MNRAS, 370, 819

Jackson J., Stoy R. H., 1954, Cape Photographic Catalogue for 1950.0. Vol.17: Zone -30 deg. to -35 deg.

—, 1955a, Annals of the Cape Observatory, 18, 0

—, 1955b, Annals of the Cape Observatory, 19, 0

—, 1958, Annals of the Cape Observatory, 20, 0

Janson M. et al., 2021, Nature, 600, 231

Jeffers H. M., van den Bos W. H., Greeby F. M., 1963, Index Catalogue of Visual Double Stars, 1961.0

Jenkins J. M. et al., 2021, in Posters from the TESS Science Conference II (TSC2), p. 183

—, 2016, in Society of Photo-Optical Instrumentation Engineers (SPIE) Conference Series, Vol. 9913, Software and Cyberinfrastructure for Astronomy IV, Chiozzi G., Guzman J. C., eds., p. 99133E

Jenkner H., Lasker B. M., Sturch C. R., McLean B. J., Shara M. M., Russel J. L., 1990, AJ, 99, 2082

Jha S., Charbonneau D., Garnavich P. M., Sullivan D. J., Sullivan T., Brown T. M., Tonry J. L., 2000, ApJL, 540, L45

Johnston C., 2021, A&A, 655, A29

Jurcsik J., Kovacs G., 1996, A&A, 312, 111

Jurcsik J. et al., 2015, ApJS, 219, 25

Jurkovic M. I., 2021, in Astronomical Society of the Pacific Conference Series, Vol. 529, RR Lyrae/Cepheid 2019: Frontiers of Classical Pulsators, Kinemuchi K., Lovekin C., Neilson H., Vivas K., eds., p. 305

Kepler J., 1619, Ioannis Keppleri harmonices mundi libri V : quorum primus harmonicus ... quartus metaphysicus, psychologicus et astrologicus geometricus ... secundus architectonicus ... tertius proprie ... quintus astronomicus & metaphysicus ... : appendix habet comparationem huius operis cum harmonices Cl. Ptolemaei libro III cumque Roberti de Fluctibus ... speculationibus harmonicis, operi de macrocosmo & microcosmo insertis

Kervella P., Arenou F., Mignard F., Thévenin F., 2019, A&A, 623, A72

Kervella P., Arenou F., Thévenin F., 2022, A&A, 657, A7

Kervella P., Thévenin F., Morel P., Bordé P., Di Folco E., 2003, A&A, 408, 681

Khalack V. et al., 2019, MNRAS, 490, 2102

Kite E. S., Fegley, Bruce J., Schaefer L., Ford E. B., 2019, ApJL, 887, L33

Kjeldsen H., Bedding T. R., 1995, A&A, 293, 87

Kniazev A. Y., Gvaramadze V. V., Berdnikov L. N., 2016, MNRAS, 459, 3068

—, 2017, in Astronomical Society of the Pacific Conference Series, Vol. 510, Stars: From Collapse to Collapse, Balega Y. Y., Kudryavtsev D. O., Romanyuk I. I., Yakunin I. A., eds., p. 480

Kniazev A. Y., Pustilnik S. A., Grebel E. K., Lee H., Pramskij A. G., 2004, ApJS, 153, 429

Ko M., 1999, Density of the Sun

Koch D. G. et al., 2010, ApJL, 713, L79

Koen C., 2003, MNRAS, 341, 1385

—, 2010, Ap&SS, 329, 267

Kohl K., 1964, ZAp, 60, 115

Konacki M., Torres G., Sasselov D. D., Jha S., 2003, ApJ, 597, 1076

Krimm H. A. et al., 2007, ApJL, 668, L147

Krisciunas K., 1993, in American Astronomical Society Meeting Abstracts, Vol. 183, American Astronomical Society Meeting Abstracts, p. 84.02

Krishna Swamy K. S., 1966, ApJ, 145, 174

Kuiper G. P., 1938, ApJ, 88, 472

Kunzli M., North P., 1998, A&AS, 127, 277

Kupka F., Piskunov N., Ryabchikova T. A., Stempels H. C., Weiss W. W., 1999, A&AS, 138, 119

Kurtz D. W., 1989, MNRAS, 238, 1077

Kurtz D. W., Bowman D. M., Ebo S. J., Moskalik P., Handberg R., Lund M. N., 2016, MNRAS, 455, 1237

Kurtz D. W., Saio H., Takata M., Shibahashi H., Murphy S. J., Sekii T., 2014, MNRAS, 444, 102

Kurucz R. L., 1979, ApJS, 40, 1

Lafrenière D., Jayawardhana R., Janson M., Helling C., Witte S., Hauschildt P., 2011, ApJ, 730, 42

Lagrange A. M. et al., 2009, A&A, 493, L21

—, 2019, Nature Astronomy, 3, 1135

Landstreet J. D., Bagnulo S., Andretta V., Fossati L., Mason E., Silaj J., Wade G. A., 2007, A&A, 470, 685

Lanz T., Mathys G., 1993, A&A, 280, 486

Lasker B. M., et al., 1990, The HST Guide Star Catalog Version 1.1 (1990, 0

Lasker B. M., Sturch C. R., McLean B. J., Russell J. L., Jenkner H., Shara M. M., 1990, AJ, 99, 2019

Laughlin G., Bodenheimer P., Adams F. C., 1997, ApJ, 482, 420

Lawton A. T., Wright P., 1989, Journal of the British Interplanetary Society, 42, 335

Le Verrier U. J., 1846, Astronomische Nachrichten, 25, 65

Leavitt H. S., 1908, Annals of Harvard College Observatory, 60, 87

Leavitt H. S., Pickering E. C., 1912, Harvard College Observatory Circular, 173, 1

Lebreton Y., Perrin M. N., Fernandes J., Cayrel R., Cayrel de Strobel G., Baglin A., 1997, in ESA Special Publication, Vol. 402, Hipparcos - Venice '97, Bonnet R. M., Høg E., Bernacca P. L., Emiliani L., Blaauw A., Turon C., Kovalevsky J., Lindegren L., Hassan H., Bouffard M., Strim B., Heger D., Perryman M. A. C., Woltjer L., eds., pp. 379–382

Lebzelter T. et al., 2023, A&A, 674, A15

Lenz P., Breger M., 2004, in The A-Star Puzzle, Zverko J., Ziznovsky J., Adelman S. J., Weiss W. W., eds., Vol. 224, pp. 786–790

—, 2005, Communications in Asteroseismology, 146, 53

Li M., Xiao L., 2016, ApJ, 820, 36

Li Y., 1992, A&A, 257, 145

Lindegren L., Dravins D., 2003, A&A, 401, 1185

Lissauer J. J., 1993, ARA&A, 31, 129

Luger R. et al., 2017, Nature Astronomy, 1, 0129

Ma S. et al., 2022, ApJ, 937, 80

Majaess D., Turner D., Lane D., 2009, Acta Astron., 59, 403

Mamajek E. E., Bell C. P. M., 2014, MNRAS, 445, 2169

Mancini L. et al., 2014, A&A, 568, A127

Mandel K., Agol E., 2002, ApJL, 580, L171

Mann A. W., Feiden G. A., Gaidos E., Boyajian T., von Braun K., 2015, ApJ, 804, 64

Mantegazza L., Poretti E., 1991, Information Bulletin on Variable Stars, 3690, 1

Marois C., Macintosh B., Barman T., Zuckerman B., Song I., Patience J., Lafrenière D., Doyon R., 2008, Science, 322, 1348

Marois C., Zuckerman B., Konopacky Q. M., Macintosh B., Barman T., 2010, Nature, 468, 1080

Mason B. D., Wycoff G. L., Hartkopf W. I., Douglass G. G., Worley C. E., 2001, AJ, 122, 3466

Mathys G., 1988, in Elemental Abundance Analyses, Adelman S. J., Lanz T., eds., p. 101

Mattsson L., Höfner S., 2011, A&A, 533, A42

Maury A. C., Pickering E. C., 1897, Annals of Harvard College Observatory, 28, 1

Mayor M., Queloz D., 1995, Nature, 378, 355

McDonald I., Zijlstra A. A., Boyer M. L., 2012, MNRAS, 427, 343

Meng H. Y. A. et al., 2017, ApJ, 847, 131

Ment K. et al., 2023, arXiv e-prints, arXiv:2304.01920

Miralda-Escudé J., 2002, ApJ, 564, 1019

Mohr P. J., Taylor B. N., Newell D. B., 2008, Reviews of Modern Physics, 80, 633

Montgomery M. H., O'Donoghue D., 1999, Delta Scuti Star Newsletter, 13, 28

Morrison J. E., Röser S., McLean B., Bucciarelli B., Lasker B., 2001, AJ, 121, 1752

Morton T. D., Bryson S. T., Coughlin J. L., Rowe J. F., Ravichandran G., Petigura E. A., Haas M. R., Batalha N. M., 2016, ApJ, 822, 86

Mróz P. et al., 2020, ApJL, 903, L11

Murphy S. J., Hey D., Van Reeth T., Bedding T. R., 2019, MNRAS, 485, 2380

Nave C., 2006, HyperPhysics. Georgia State University. Retrieved March, 1, 2008

Nelder J. A., Mead R., 1965, The Computer Journal, 7, 308

Nesterov V. V., Kuzmin A. V., Ashimbaeva N. T., Volchkov A. A., Röser S., Bastian U., 1995, A&AS, 110, 367

Newman J. A., Zepf S. E., Davis M., Freedman W. L., Madore B. F., Stetson P. B., Silbermann N., Phelps R., 1999, ApJ, 523, 506

Ngeow C., Kanbur S. M., 2006, ApJL, 642, L29

Nordström B. et al., 2004, A&A, 418, 989

North P., Debernardi Y., 2004, in Astronomical Society of the Pacific Conference Series, Vol. 318, Spectroscopically and Spatially Resolving the Components of the Close Binary Stars, Hilditch R. W., Hensberge H., Pavlovski K., eds., pp. 297–305

O'Donoghue D. E. et al., 2008, in Society of Photo-Optical Instrumentation Engineers (SPIE) Conference Series, Vol. 7018, Advanced Optical and Mechanical Technologies in Telescopes and Instrumentation, Atad-Ettedgui E., Lemke D., eds., p. 701813

Ouazzani R. M., Marques J. P., Goupil M. J., Christophe S., Antoci V., Salmon S. J. A. J., Ballot J., 2019, A&A, 626, A121

Packer D., 1890, Sid. Mess, 9, 381

Panahi A. et al., 2022, A&A, 663, A101

Papaloizou J., Pringle J. E., 1978, MNRAS, 182, 423

Parviainen H. et al., 2019, A&A, 630, A89

Paunzen E., 2015, A&A, 580, A23

—, 2022, A&A, 661, A89

Paxton B., 2004, PASP, 116, 699

Paxton B., Bildsten L., Dotter A., Herwig F., Lesaffre P., Timmes F., 2011, ApJS, 192, 3

Paxton B. et al., 2013, ApJS, 208, 4

—, 2015, ApJS, 220, 15

—, 2018, ApJS, 234, 34

—, 2019, ApJS, 243, 10

Pecaut M. J., Mamajek E. E., 2013, ApJS, 208, 9

Perrine C. D., 1932, Resultados del Observatorio Nacional Argentino, 21, 1

Perry C. L., 1991, PASP, 103, 494

Perry C. L., Christodoulou D. M., 1996, PASP, 108, 772

Perryman M., 2018, The Exoplanet Handbook

Pesnell W. D., 1987, ApJ, 314, 598

Peterson I., 1988, Science News, 134, 103

Pickering E. C., 1890, Annals of Harvard College Observatory, 27, 1

Pickering E. C., Bailey S. I., 1895, ApJ, 2, 321

Pigott E., 1785, Philosophical Transactions of the Royal Society of London Series I, 75, 127

Pinte C. et al., 2019, Nature Astronomy, 3, 1109

Platzman G. W., 1968, Quarterly Journal of the Royal Meteorological Society, 94, 225

Podolak M., 2018, in Oxford Research Encyclopedia of Planetary Science, p. 108

Pollacco D. L. et al., 2006, PASP, 118, 1407

Potekhin A. Y., Chabrier G., 2010, Contributions to Plasma Physics, 50, 82

Preston G. W., 1974, ARA&A, 12, 257

Privitera G., Meynet G., Eggenberger P., Vidotto A. A., Villaver E., Bianda M., 2016, A&A, 591, A45

Prša A. et al., 2016, AJ, 152, 41

Qian S. B., Liao W. P., Zhu L. Y., Dai Z. B., 2010, ApJL, 708, L66

Rameau J. et al., 2013, ApJL, 772, L15

Refsdal S., 1964, MNRAS, 128, 295

Reid I. N., Hawley S. L., 2005, New light on dark stars : red dwarfs, low-mass stars, brown dwarfs

Reiners A., 2006, A&A, 446, 267

Rempel M., 2004, ApJ, 607, 1046

Renka R. J., 1999, ACM Trans. Math. Softw., 25, 70–73

Renson P., Gerbaldi M., Catalano F. A., 1991, A&AS, 89, 429

Renson P., Manfroid J., 2009, A&A, 498, 961

Rey H. A., 1966, A new way to see the stars

Ricker G. R. et al., 2015, Journal of Astronomical Telescopes, Instruments, and Systems, 1, 014003

—, 2014, in Society of Photo-Optical Instrumentation Engineers (SPIE) Conference Series, Vol. 9143, Space Telescopes and Instrumentation 2014: Optical, Infrared, and Millimeter Wave, Oschmann Jacobus M. J., Clampin M., Fazio G. G., MacEwen H. A., eds., p. 914320

Rodgers A. W., 1957, MNRAS, 117, 85

Röeser S., Bastian U., 1988, A&AS, 74, 449

Roeser S., Bastian U., Wiese K., 1991, A&AS, 88, 277

Rogers F. J., Nayfonov A., 2002, ApJ, 576, 1064

Rogers F. J., Swenson F. J., Iglesias C. A., 1996, ApJ, 456, 902

Roman N. G., Morgan W. W., Eggen O. J., 1948, ApJ, 107, 107

Röser S., Bastian U., Kuzmin A., 1994, A&AS, 105, 301

Rossby C.-G., 1939, Journal of Marine Research, 2, 38

Rowe J. F. et al., 2014, ApJ, 784, 45

Russell J. L., Lasker B. M., McLean B. J., Sturch C. R., Jenkner H., 1990, AJ, 99, 2059

Rybicki G. B., Lightman A. P., 1986, Radiative Processes in Astrophysics

Saffe C. et al., 2020, A&A, 641, A145

Sage L. J., 2012, JRASC, 106, 88

Sahlmann J., Lazorenko P. F., Ségransan D., Martín E. L., Queloz D., Mayor M., Udry S., 2013, A&A, 556, A133

Sahu K. C. et al., 2006, Nature, 443, 534

—, 2008, in Astronomical Society of the Pacific Conference Series, Vol. 398, Extreme Solar Systems, Fischer D., Rasio F. A., Thorsett S. E., Wolszczan A., eds., p. 93

Saio H., Kurtz D. W., Murphy S. J., Antoci V. L., Lee U., 2018, MNRAS, 474, 2774

Salaris M., Cassisi S., 2005, Evolution of Stars and Stellar Populations

Sandin C., Höfner S., 2004, A&A, 413, 789

Sato S., Cuntz M., Guerra Olvera C. M., Jack D., Schröder K. P., 2014, International Journal of Astrobiology, 13, 244

Saumon D., Chabrier G., van Horn H. M., 1995, ApJS, 99, 713

Schuh S., 2010, Astronomische Nachrichten, 331, 489

Schuler S. C., King J. R., The L.-S., 2009, ApJ, 701, 837

Schwamb M. E. et al., 2012, ApJ, 754, 129

—, 2013, ApJ, 768, 127

Scuflaire R., 1974, A&A, 36, 107

Seach J. M., Marsden S. C., Carter B. D., Evensberget D., Folsom C. P., Neiner C., Mengel M. W., 2022, MNRAS, 509, 5117

Sefako R., 2015, Highlights of Astronomy, 16, 751

Shallue C. J., Vanderburg A., 2018, AJ, 155, 94

Silvotti R. et al., 2007, Nature, 449, 189

Smalley B., 2005, Memorie della Societa Astronomica Italiana Supplementi, 8, 130

Smalley B. et al., 2017, MNRAS, 465, 2662

—, 2014, Eclipsing Am binary systems in the SuperWASP survey

Smeyers P., 1966, Annales d'Astrophysique, 29, 539

—, 1967, Bulletin de la Societe Royale des Sciences de Liege, 36, 357

Smith M. A., 1972, A&A, 19, 312

Sperl M., 1998, Communications in Asteroseismology, 111, 1

Spruit H. C., 1997, Mem. Soc. Astron. Italiana, 68, 397

Squicciarini V. et al., 2022, A&A, 664, A9

Stassun K. G. et al., 2019, AJ, 158, 138

—, 2018, AJ, 156, 102

Sterne T. E., 1938, ApJ, 87, 133

Stobie R., Meiring J., Buckley D. A., 2000, in Society of Photo-Optical Instrumentation Engineers (SPIE) Conference Series, Vol. 4003, Optical Design, Materials, Fabrication, and Maintenance, Dierickx P., ed., pp. 355–362

Stoy R. H., 1966, Annals of the Cape Observatory, 21, 0

—, 1968, Annals of the Cape Observatory, 22

Struve O., 1952, The Observatory, 72, 199

Sun X.-Y., Zuo Z.-Y., Yang T.-Z., Chen X.-H., Li H.-R., 2021, ApJ, 922, 199

Székely P., Kiss L. L., Jackson R., Derekas A., Csák B., Szatmáry K., 2007, A&A, 463, 589

Tao L., Spiegel E., Umurhan O. M., 1998, in APS Division of Fluid Dynamics Meeting Abstracts, APS Meeting Abstracts, p. LC.10

Tassoul M., 1980, ApJS, 43, 469

Temple L. Y. et al., 2017, MNRAS, 471, 2743

Ter Braak C. J. F., 2006, Statistics and Computing, 16, 239

Tetzlaff N., Neuhäuser R., Hohle M. M., 2011, MNRAS, 410, 190

Thome J. M., 1892, Resultados del Observatorio Nacional Argentino, 16, 1

—, 1894, Resultados del Observatorio Nacional Argentino, 17, 1

—, 1900, Cordoba Durchmusterung. Brightness and position of every fixed star down to the 10. magnitude comprised in the belt of the heavens between 22 and 90 degrees of southern declination - Vol.18: -42 deg. to -52 deg.

—, 1914, Resultados del Observatorio Nacional Argentino, 21, 1

Thompson S. E. et al., 2012, ApJ, 753, 86

Thoul A. A., Bahcall J. N., Loeb A., 1994, ApJ, 421, 828

Timmes F. X., Swesty F. D., 2000, ApJS, 126, 501

Titus J., Morgan W. W., 1940, ApJ, 92, 256

Tominaga N., Umeda H., Nomoto K., 2007, ApJ, 660, 516

Torres G., 2010, AJ, 140, 1158

Torres G., Andersen J., Giménez A., 2010, A&A Rev., 18, 67

Toutain T., Froehlich C., 1992, A&A, 257, 287

Townsend R. H. D., Teitler S. A., 2013, MNRAS, 435, 3406

Turcotte S., 2000, in Astronomical Society of the Pacific Conference Series, Vol. 210, Delta Scuti and Related Stars, Breger M., Montgomery M., eds., p. 468

Turner D. G., 1996, JRASC, 90, 82

—, 2010, Ap&SS, 326, 219

Turon C. et al., 1993, Bulletin d'Information du Centre de Donnees Stellaires, 43, 5

—, 1992, Bulletin d'Information du Centre de Donnees Stellaires, 41, 9

Tyas L. M. G., 2012, PhD thesis, Durham University

Udalski A., 2003, Acta Astron., 53, 291

Udalski A., Zebrun K., Szymanski M., Kubiak M., Soszynski I., Szewczyk O., Wyrzykowski L., Pietrzynski G., 2002, Acta Astron., 52, 115

Uytterhoeven K. et al., 2008, A&A, 489, 1213

—, 2011, A&A, 534, A125

van Leeuwen F., 2007, A&A, 474, 653

Van Reeth T. et al., 2015, A&A, 574, A17

VandenBerg D. A., Clem J. L., 2003, AJ, 126, 778

Vidal-Madjar A., 1989, L'Astronomie, 103, 557

von Zeipel H., 1924, MNRAS, 84, 665

Šubjak J. et al., 2020, AJ, 159, 151

Wang J., Fischer D. A., 2015, AJ, 149, 14

Wang J., Fischer D. A., Horch E. P., Huang X., 2015, ApJ, 799, 229

Wang J., Zhong Z., 2018, A&A, 619, L1

Wang J. J. et al., 2018, AJ, 156, 192

Weidner C., Vink J. S., 2010, A&A, 524, A98

West R. G. et al., 2009, A&A, 502, 395

Williams J. P., Cieza L. A., 2011, ARA&A, 49, 67

Winters J. G. et al., 2019, AJ, 157, 216

Wolff S. C., 1983, The A-stars : problems and perspectives

Wolszczan A., 1994, Science, 264, 538

Wolszczan A., Frail D. A., 1992, Nature, 355, 145

Worley C. E., Douglass G. G., 1997, A&AS, 125, 523

Wright J. T., Eastman J. D., 2014, PASP, 126, 838

Yi S., Demarque P., Kim Y.-C., Lee Y.-W., Ree C. H., Lejeune T., Barnes S., 2001, ApJS, 136, 417

Zhang Z., Liu M. C., Claytor Z. R., Best W. M. J., Dupuy T. J., Siverd R. J., 2021, ApJL, 916, L11

Zhang Z. et al., 2020, ApJ, 891, 171

Zhou G. et al., 2019, AJ, 158, 141

—, 2016, AJ, 152, 136

Zhu W., Wang J., Huang C., 2016, ApJ, 832, 196

Zorec J., Royer F., 2012, A&A, 537, A120

Appendices

Appendix A

The MIDAS Pipeline

The following was sourced from Alexei Kniazev's 2016 SALT Document "MIDAS automatic pipeline for HRS data"[1].

The Munich Image Data Analysis System (MIDAS) pipeline works through three main stages. First is the "FLAT reduction", where an HRS flat image is reduced. The resultant file from this reduction contains a FITS table, smooth extracted flats from both the blue and red fibres, and the flats ratio. Second is the "ARC reduction", where an HRS arc image is reduced (an arc image being an image created from light generated from an electric arc). This process produces a file containing table used for wavelength calibrations of both the blue and red fibres, and a second table for the extracted, calibrated and merged ThAr+Ar spectra for both fibres as well. Third is the "Object reduction", the final reduction of the calibrated spectra. This process outputs two sets of reduced spectra, one merged (both blue and red fibres), and unmerged spectra.

Except for the configuration files, all outputs from the MIDAS pipeline are in FITS file form. The full list of output files, with descriptions, are hence as follows:

[1]Document Number: HRS0000006, Date: November 10^{th} 2016, extracted from *https://www.saao.ac.za/∼akniazev/pub/HRS_MIDAS*

mbgphH201506220014_1w.fits – extracted first fibre. Wavelength calibrated. Not merged. 2D spectrum, where each order is one line in 2D spectrum. This is the most compact format, but only MIDAS can understand it easily. See Section 5 for more information.

mbgphH201506220014_2w.fits – the same for the second fibre. 2D spectrum. MIDAS format for échelle data.

mbgphH201506220014_1we.fits – as above, but each order is written as separate FITS SALT HRS0000006 Version 1.0 Page 4 from 8 November 10, 2016 MIDAS automatic pipeline for HRS data 5 extension. FITS file has as many extensions as extracted orders. Can be easily understand by IRAF, where all programs can work with FITS extensions in the format i.e. 'mbgphH201506220014_1we.fits[1]' – for the first one. MIDAS understand it as well.

mbgphH201506220014_2we.fits – the same for the second fibre. 2D FITS spectrum with many extensions. Both MIDAS and IRAF understand it.

mbgphH201506220014_1wm.fits – extracted first fibre, wavelength calibrated and merged. 1D FITS spectrum. Both MIDAS and IRAF understand it.

mbgphH201506220014_2wm.fits – the same for the second fibre. 1D spectrum. Both MIDAS and IRAF understand it.

mbgphH201506220014_u1w.fits – extracted first fibre and divided to the flat. Wavelength calibrated. Not merged. 2D spectrum, where each order is one line

in 2D spectrum. MIDAS format for échelle data. See Section 5 for more information.

mbgphH201506220014_u2w.fits – the same for the second fibre. 2D spectrum. MIDAS format for échelle data.

mbgphH201506220014_u1we.fits – as above, but each order is written as separate FITS extension. Can be easily understand by IRAF. 2D FITS spectrum with many extensions.

mbgphH201506220014_u2we.fits – the same for the second fibre. 2D FITS spectrum with many extensions. Can be easily understand by IRAF.

mbgphH201506220014_u1wm.fits – extracted first fibre, divided to the flat, wavelength calibrated and merged. 1D FITS spectrum. Both MIDAS and IRAF understand it.

mbgphH201506220014_u2wm.fits – the same for the second fibre. 1D FITS spectrum. Both MIDAS and IRAF understand it.

mbgphH201506220014_uwm.fits – the final result after sky fibre was subtracted from the object fibre. 1D spectrum. Both MIDAS and IRAF understand it.

In the above filenames, the date "**20150622**" and frame number "**0014**" are just examples from the MIDAS pipeline document that the above section was extracted from, both numbers change for all new observations. The suffix "**uwm**" *without* numbers are the final reduced spectra files that were analysed in this work. The

capital letter “H” denotes that these files were outputted from the blue fibre. An equivalent set of files are additionally outputted from the red fibre, those filenames contain a capital “R” instead.

Appendix B

An Example MESA Model Inlist

```
&star_job

      !  begin with a pre-main sequence model
      !  create_pre_main_sequence_model = .true.

      Load_saved_model = .true.
      saved_model_name = ‘2.10.mod’

      !  save a model at the end of the run
      !  pause_before_terminate = .true.
      save_model_when_terminate = .true.
      save_model_filename = ‘model_mass_2.10_MSun_rotation_55_kms_overshoot_0.028.mod’
      Required_termination_code_string = ‘Log_l_upper_limit’

      !  display on-screen plots
      !  pgstar_flag = .true.

      new_rotation_flag .True.
      change_rotation_flag = .True.  !  rotation off until near zams

      new_surface_rotation_v = 60 !  kmsec
      set_surface_rotation_v = .True.
```

```
      set_initial_surface_rotation_v = .True.

      eos_file_prefix = 'mesa'

      write_profile_when_terminate = .TRUE.
      filename_for_profile_when_terminate =
'model_mass_2.10_MSun_rotation_60_kms_overshoot_0.028.profile'

      save_pulse_data_when_terminate = .TRUE.
      save_pulse_data_filename =
'model_mass_2.10_MSun_rotation_60_kms_overshoot_0.028.mesa'

/ !end of star_job namelist

&controls

      !  starting specifications
      initial_mass = 2.10 !  in MSun units

      !  options for energy conservation (see MESA V Section 3)
      use_gold_tolerances = .true.

      use_dedt_form_of_energy_eqn = .true.
      min_cell_energy_fraction_for_dedt_form = 0
      use_correction_for_KE_plus_PE_with_eps_grav_in_energy_eqn = .true.
      !use_eosDT_ideal_gas = .true.

      !  stop when the star nears ZAMS (Lnuc/L » 0.99)
      Lnuc_div_L_zams_limit = 0.99d0
      stop_near_zams = .false.

      !  stop when the center mass fraction of h1 drops below this limit
      xa_central_lower_limit_species(1) = 'h1'
```

```
      xa_central_lower_limit(1) = 1d-3

      initial_z = 0.02d0 !  metallicity

      use_Type2_opacities = .true.
      Zbase = 0.0244d0

      log_L_upper_limit = 4.3

      mixing_length_alpha = 1.73

      overshoot_scheme = 'exponential'
      overshoot_zone_type = 'burn_H'
      overshoot_zone_loc = 'core'
      overshoot_bdy_loc = 'top'

      overshoot_f = 0.028
      overshoot_f0 = 0.003

      profile_interval = 0
      photo_interval = 0
      history_interval = 1
      terminal_interval = 1
      write_header_frequency = 0

      pulse_data_format = 'GYRE'
      add_center_point_to_pulse_data = .TRUE.
      add_double_points_to_pulse_data = .TRUE.
      threshold_grad_mu_for_double_point = 10.

/ !  end of controls namelist
```

Appendix C

An Example MESA Master Inlist

```
&star_job

     read_extra_star_job_inlist1 = .true.
     extra_star_job_inlist1_name =
'model_mass_2.10_MSun_rotation_60_kms_overshoot_0.028'

/ !  end of star_job namelist

&controls

     read_extra_controls_inlist1 = .true.
     extra_controls_inlist1_name =
'model_mass_1.99_MSun_rotation_60_kms_overshoot_0.028'

/ !  end of controls namelist

&pgstar

     read_extra_pgstar_inlist1 = .true.
     extra_pgstar_inlist1_name = 'pgstar'

/ !  end of pgstar namelist
```

Appendix D

An Example GYRE Model Inlist

```
&constants

/

&model

      model_type = 'EVOL'
      file = 'model_mass_2.10_MSun_rotation_60_kms_overshoot_0.028.mesa'
      file_format = 'MESA'
/

&mode

      l = 3
      m = 0
/

&osc

      outer_bound = 'VACUUM'
      nonadiabatic = .FALSE.
/
```

```
&num

      diff_scheme = 'COLLOC_GL4'
/

&scan

      grid_type = 'INVERSE'
      freq_min_units = 'CYC_PER_DAY'
      freq_max_units = 'CYC_PER_DAY'
      freq_min = 0.5
      freq_max = 50.0
      n_freq = 250
/

&grid

      alpha_osc = 10
      alpha_exp = 2
      n_inner = 5
/

&ad_output

      summary_file = 'm=0,l=3.txt'
      summary_file_format = 'TXT'
      summary_item_list = 'M_star,R_star,l,m,n_pg,n_p,n_g,omega,
freq,freq_units,Delta_p,E_norm'
      mode_template = 'mode.%J.txt'
      mode_file_format = 'TXT'
      mode_item_list = 'l,n_pg,omega,x,xi_r,xi_h'
      freq_units = 'CYC_PER_DAY'
```

Appendix E

An Example EXOFASTv2 File

The following is an example of the main EXOFASTv2 executable file, in the required syntax, used for modelling the companion around TIC 409934330.

```
exofastv2, nplanets=1,$
    tranpath='n20*.dat',$
    /rvpath=' ',$
    /fluxfile=' ',$
    priorfile='tic_409934330.priors',$
    fittran=[1],circular=[0], $
    prefix='fitresults'+path_sep()+'TIC_409934330',$
    nthin=5, maxsteps=50000
```

Appendix F

The SPOC Pipeline

The TESS Science Processing Operations Center (SPOC) reduces the raw observations and extracts photometry from each pixel in each observation frame, writing new data files which become publicly available for download. These files include Full Frame Image (FFI) files, which are the full camera field-of-view images taken by TESS (four taken at once, one per camera); the Target Light Curve files, the time series data consisting of time stamps and photometry (plus errors) that are used to build light curves; and Target Pixel files, which contain both raw and processed pixel data. Additionally, SPOC lifts astrometry data from each star, providing updated celestial coordinates; corrects for systematic errors that arise from TESS itself, for example, and are not of astrophysical origin (spacecraft drift, time variations throughout an orbit, etc); and — most importantly for this work — flags any signatures of transiting exoplanets (Jenkins et al., 2016, 2021).

Appendix G

The Extracted Pulsation Frequencies of TIC 409934330

Table G.1: The 87 extracted pulsation frequencies of TIC 409934330 identified from the Fourier transform shown in Figure 5.3

Frequency Number	Frequency ν (c/d)	Amplitude (mmag)
ν_1	0.8739 ± 0.0014	0.0927 ± 0.0081
ν_2	1.3662 ± 0.0013	0.1109 ± 0.0081
ν_3	1.4489 ± 0.0018	0.0844 ± 0.0081
ν_4	1.5385 ± 0.0033	0.1127 ± 0.0081
ν_5	1.9130 ± 0.0026	0.0506 ± 0.0081
ν_6	2.0924 ± 0.0013	0.0396 ± 0.0081
ν_7	2.2067 ± 0.0036	0.0538 ± 0.0081
ν_8	2.5830 ± 0.0034	0.0342 ± 0.0081
ν_9	2.6990 ± 0.0008	0.0349 ± 0.0081
ν_{10}	2.8907 ± 0.0038	0.0290 ± 0.0081
ν_{11}	3.0489 ± 0.0037	0.0418 ± 0.0081
ν_{12}	3.2529 ± 0.0006	0.0319 ± 0.0081
ν_{13}	3.3549 ± 0.0009	0.0295 ± 0.0081
ν_{14}	3.7646 ± 0.0038	0.0327 ± 0.0081
ν_{15}	3.8701 ± 0.0025	0.0466 ± 0.0081
ν_{16}	4.3026 ± 0.0040	0.0296 ± 0.0081
ν_{17}	4.6244 ± 0.0029	0.0235 ± 0.0081
ν_{18}	4.8899 ± 0.0020	0.0278 ± 0.0081
ν_{19}	5.8833 ± 0.0067	0.0221 ± 0.0081
ν_{20}	6.1928 ± 0.0041	0.0271 ± 0.0081
ν_{21}	12.7056 ± 0.0059	0.0231 ± 0.0081
ν_{22}	13.2894 ± 0.0028	0.0395 ± 0.0081

ν_{23}	14.6081 ± 0.0065	0.0239 ± 0.0081
ν_{24}	15.3167 ± 0.0037	0.0397 ± 0.0081
ν_{25}	16.5106 ± 0.0060	0.0356 ± 0.0081
ν_{26}	16.5898 ± 0.0064	0.0344 ± 0.0081
ν_{27}	17.0645 ± 0.0010	0.1500 ± 0.0081
ν_{28}	17.1788 ± 0.0085	0.0348 ± 0.0081
ν_{29}	17.2474 ± 0.0024	0.0497 ± 0.0081
ν_{30}	17.4408 ± 0.0004	0.3935 ± 0.0081
ν_{31}	17.5762 ± 0.0006	0.2971 ± 0.0081
ν_{32}	17.6061 ± 0.0146	0.0483 ± 0.0081
ν_{33}	17.6500 ± 0.0050	0.0189 ± 0.0081
ν_{34}	17.7133 ± 0.0024	0.0715 ± 0.0081
ν_{35}	17.7801 ± 0.0021	0.0685 ± 0.0081
ν_{36}	17.8294 ± 0.0129	0.0406 ± 0.0081
ν_{37}	18.0456 ± 0.0024	0.0560 ± 0.0081
ν_{38}	18.1599 ± 0.0018	0.0805 ± 0.0081
ν_{39}	18.5503 ± 0.0023	0.0677 ± 0.0081
ν_{40}	18.7068 ± 0.0018	0.0890 ± 0.0081
ν_{41}	19.0426 ± 0.0033	0.0428 ± 0.0081
ν_{42}	19.4330 ± 0.0006	0.2554 ± 0.0081
ν_{43}	19.9464 ± 0.0009	0.1669 ± 0.0081
ν_{44}	20.1785 ± 0.0025	0.0671 ± 0.0081
ν_{45}	20.3104 ± 0.0020	0.0854 ± 0.0081
ν_{46}	20.9662 ± 0.0037	0.0479 ± 0.0081
ν_{47}	21.0946 ± 0.0021	0.0770 ± 0.0081
ν_{48}	21.4779 ± 0.0038	0.0412 ± 0.0081
ν_{49}	21.9158 ± 0.0038	0.0420 ± 0.0081
ν_{50}	22.8757 ± 0.0037	0.0407 ± 0.0081
ν_{51}	23.1606 ± 0.0036	0.0390 ± 0.0081
ν_{52}	23.6424 ± 0.0061	0.0279 ± 0.0081
ν_{53}	24.0046 ± 0.0047	0.0301 ± 0.0081
ν_{54}	24.7853 ± 0.0032	0.0509 ± 0.0081
ν_{55}	26.0038 ± 0.0030	0.0559 ± 0.0081
ν_{56}	26.3203 ± 0.0028	0.0498 ± 0.0081
ν_{57}	26.7704 ± 0.0012	0.1379 ± 0.0081
ν_{58}	27.3823 ± 0.0031	0.0478 ± 0.0081
ν_{59}	28.6782 ± 0.0008	0.1960 ± 0.0081
ν_{60}	29.0492 ± 0.0046	0.0297 ± 0.0081
ν_{61}	29.8282 ± 0.0036	0.0426 ± 0.0081
ν_{62}	30.0883 ± 0.0065	0.0363 ± 0.0081
ν_{63}	30.4154 ± 0.0010	0.1606 ± 0.0081
ν_{64}	30.7214 ± 0.0012	0.1239 ± 0.0081
ν_{65}	30.7917 ± 0.0033	0.0518 ± 0.0081
ν_{66}	32.4251 ± 0.0044	0.0385 ± 0.0081

ν_{67}	33.6190 ± 0.0021	0.0802 ± 0.0081
ν_{68}	33.8459 ± 0.0008	0.2009 ± 0.0081
ν_{69}	34.5193 ± 0.0017	0.0964 ± 0.0081
ν_{70}	35.4196 ± 0.0054	0.0319 ± 0.0081
ν_{71}	36.1915 ± 0.0057	0.0273 ± 0.0081
ν_{72}	36.4043 ± 0.0045	0.0360 ± 0.0081
ν_{73}	38.2891 ± 0.0055	0.0289 ± 0.0081
ν_{74}	39.3160 ± 0.0020	0.0723 ± 0.0081
ν_{75}	39.7064 ± 0.0040	0.0361 ± 0.0081
ν_{76}	41.2467 ± 0.0059	0.0267 ± 0.0081
ν_{77}	41.8691 ± 0.0042	0.0378 ± 0.0081
ν_{78}	42.3157 ± 0.0042	0.0357 ± 0.0081
ν_{79}	44.0582 ± 0.0057	0.0284 ± 0.0081
ν_{80}	45.4913 ± 0.0063	0.0266 ± 0.0081
ν_{81}	46.2034 ± 0.0030	0.0518 ± 0.0081
ν_{82}	47.0667 ± 0.0070	0.0237 ± 0.0081
ν_{83}	47.5432 ± 0.0066	0.0238 ± 0.0081
ν_{84}	47.9881 ± 0.0027	0.0603 ± 0.0081
ν_{85}	48.0444 ± 0.0050	0.0379 ± 0.0081
ν_{86}	49.6461 ± 0.0039	0.0410 ± 0.0081
ν_{87}	53.7941 ± 0.0044	0.0362 ± 0.0081

Table G.2: The final list of of the 70 astrophysical extracted pulsation frequencies of TIC 409934330, with the non-astrophysical combination frequencies listed in Table 5.7 removed.

Frequency Number	Frequency ν (c/d)	Amplitude (mmag)
ν_1	0.8739 ± 0.0014	0.0927 ± 0.0081
ν_2	1.3662 ± 0.0013	0.1109 ± 0.0081
ν_3	1.4489 ± 0.0018	0.0844 ± 0.0081
ν_5	1.9130 ± 0.0026	0.0506 ± 0.0081
ν_6	2.0924 ± 0.0013	0.0396 ± 0.0081
ν_7	2.2067 ± 0.0036	0.0538 ± 0.0081
ν_8	2.5830 ± 0.0034	0.0342 ± 0.0081
ν_9	2.6990 ± 0.0008	0.0349 ± 0.0081
ν_{10}	2.8907 ± 0.0038	0.0290 ± 0.0081
ν_{12}	3.2529 ± 0.0006	0.0319 ± 0.0081
ν_{14}	3.7646 ± 0.0038	0.0327 ± 0.0081
ν_{16}	4.3026 ± 0.0040	0.0296 ± 0.0081
ν_{17}	4.6244 ± 0.0029	0.0235 ± 0.0081
ν_{18}	4.8899 ± 0.0020	0.0278 ± 0.0081
ν_{19}	5.8833 ± 0.0067	0.0221 ± 0.0081
ν_{20}	6.1928 ± 0.0041	0.0271 ± 0.0081
ν_{21}	12.7056 ± 0.0059	0.0231 ± 0.0081
ν_{22}	13.2894 ± 0.0028	0.0395 ± 0.0081
ν_{23}	14.6081 ± 0.0065	0.0239 ± 0.0081
ν_{24}	15.3167 ± 0.0037	0.0397 ± 0.0081
ν_{26}	16.5898 ± 0.0064	0.0344 ± 0.0081
ν_{27}	17.0645 ± 0.0010	0.1500 ± 0.0081
ν_{29}	17.2474 ± 0.0024	0.0497 ± 0.0081
ν_{30}	17.4408 ± 0.0004	0.3935 ± 0.0081
ν_{32}	17.6061 ± 0.0146	0.0483 ± 0.0081
ν_{33}	17.6500 ± 0.0050	0.0189 ± 0.0081
ν_{34}	17.7133 ± 0.0024	0.0715 ± 0.0081
ν_{35}	17.7801 ± 0.0021	0.0685 ± 0.0081
ν_{36}	17.8294 ± 0.0129	0.0406 ± 0.0081
ν_{38}	18.1599 ± 0.0018	0.0805 ± 0.0081
ν_{39}	18.5503 ± 0.0023	0.0677 ± 0.0081
ν_{40}	18.7068 ± 0.0018	0.0890 ± 0.0081
ν_{41}	19.0426 ± 0.0033	0.0428 ± 0.0081
ν_{42}	19.4330 ± 0.0006	0.2554 ± 0.0081
ν_{43}	19.9464 ± 0.0009	0.1669 ± 0.0081
ν_{44}	20.1785 ± 0.0025	0.0671 ± 0.0081
ν_{45}	20.3104 ± 0.0020	0.0854 ± 0.0081
ν_{46}	20.9662 ± 0.0037	0.0479 ± 0.0081
ν_{48}	21.4779 ± 0.0038	0.0412 ± 0.0081

ν_{50}	22.8757 ± 0.0037	0.0407 ± 0.0081
ν_{52}	23.6424 ± 0.0061	0.0279 ± 0.0081
ν_{53}	24.0046 ± 0.0047	0.0301 ± 0.0081
ν_{55}	26.0038 ± 0.0030	0.0559 ± 0.0081
ν_{56}	26.3203 ± 0.0028	0.0498 ± 0.0081
ν_{57}	26.7704 ± 0.0012	0.1379 ± 0.0081
ν_{58}	27.3823 ± 0.0031	0.0478 ± 0.0081
ν_{59}	28.6782 ± 0.0008	0.1960 ± 0.0081
ν_{60}	29.0492 ± 0.0046	0.0297 ± 0.0081
ν_{61}	29.8282 ± 0.0036	0.0426 ± 0.0081
ν_{62}	30.0883 ± 0.0065	0.0363 ± 0.0081
ν_{63}	30.4154 ± 0.0010	0.1606 ± 0.0081
ν_{64}	30.7214 ± 0.0012	0.1239 ± 0.0081
ν_{65}	30.7917 ± 0.0033	0.0518 ± 0.0081
ν_{66}	32.4251 ± 0.0044	0.0385 ± 0.0081
ν_{67}	33.6190 ± 0.0021	0.0802 ± 0.0081
ν_{68}	33.8459 ± 0.0008	0.2009 ± 0.0081
ν_{69}	34.5193 ± 0.0017	0.0964 ± 0.0081
ν_{70}	35.4196 ± 0.0054	0.0319 ± 0.0081
ν_{71}	36.1915 ± 0.0057	0.0273 ± 0.0081
ν_{72}	36.4043 ± 0.0045	0.0360 ± 0.0081
ν_{74}	39.3160 ± 0.0020	0.0723 ± 0.0081
ν_{75}	39.7064 ± 0.0040	0.0361 ± 0.0081
ν_{76}	41.2467 ± 0.0059	0.0267 ± 0.0081
ν_{77}	41.8691 ± 0.0042	0.0378 ± 0.0081
ν_{78}	42.3157 ± 0.0042	0.0357 ± 0.0081
ν_{79}	44.0582 ± 0.0057	0.0284 ± 0.0081
ν_{80}	45.4913 ± 0.0063	0.0266 ± 0.0081
ν_{81}	46.2034 ± 0.0030	0.0518 ± 0.0081
ν_{82}	47.0667 ± 0.0070	0.0237 ± 0.0081
ν_{83}	47.5432 ± 0.0066	0.0238 ± 0.0081
ν_{84}	47.9881 ± 0.0027	0.0603 ± 0.0081
ν_{85}	48.0444 ± 0.0050	0.0379 ± 0.0081
ν_{87}	53.7941 ± 0.0044	0.0362 ± 0.0081

Appendix H

The Chi-squared Results for TIC 409934330

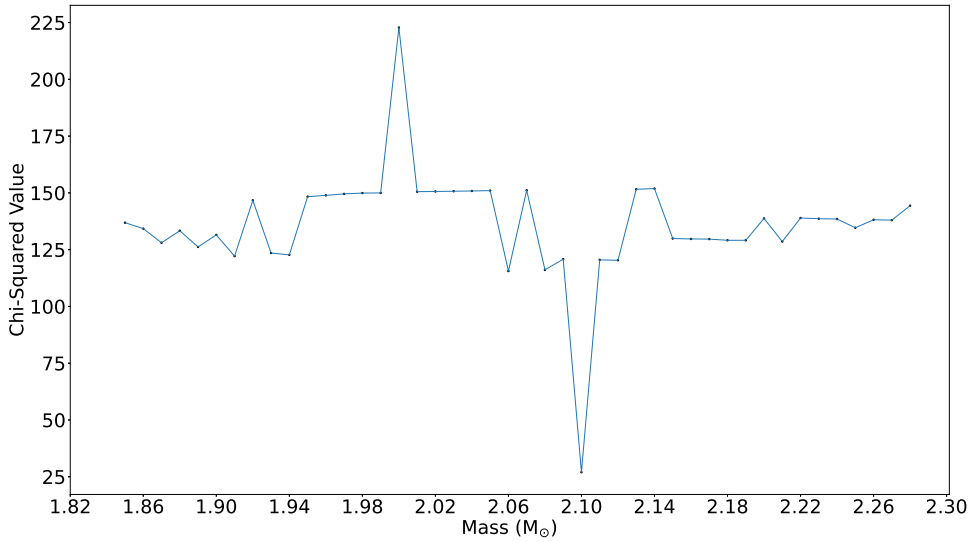

Figure H.1: A plot of the chi-squared values per pulsation frequency-match iteration showing the global minimum for mass lies at $2.10\,M_\odot$. Hence, with no adjacent minimum being of similar value, the error was taken to be ±half of the mass interval as the lowest chi-squared value is within this resolution.

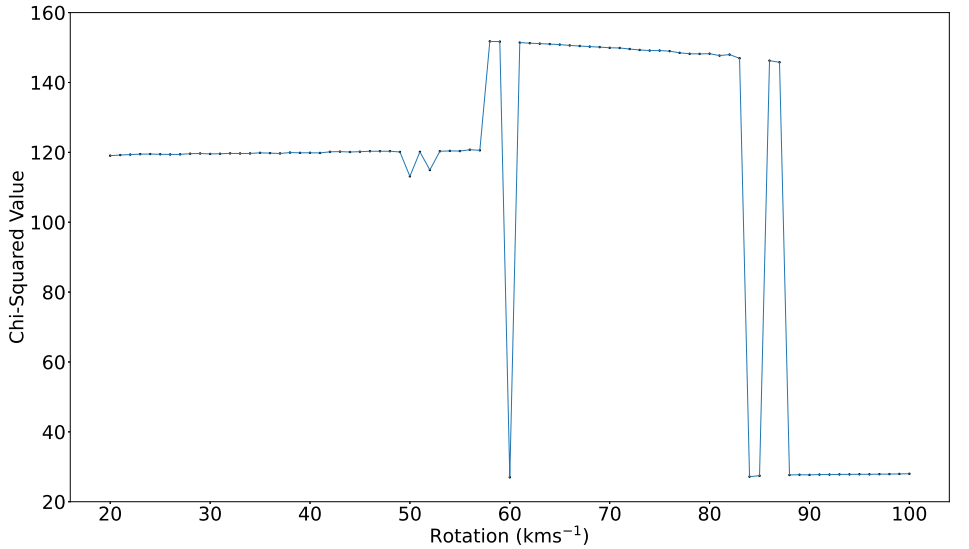

Figure H.2: A plot of the chi-squared values per pulsation frequency-match iteration showing the global minimum for rotation lies at $60\,kms^{-1}$. Hence, with no adjacent minimum being of similar value, the error was taken to be ±half of the rotation interval as the lowest chi-squared value is within this resolution.

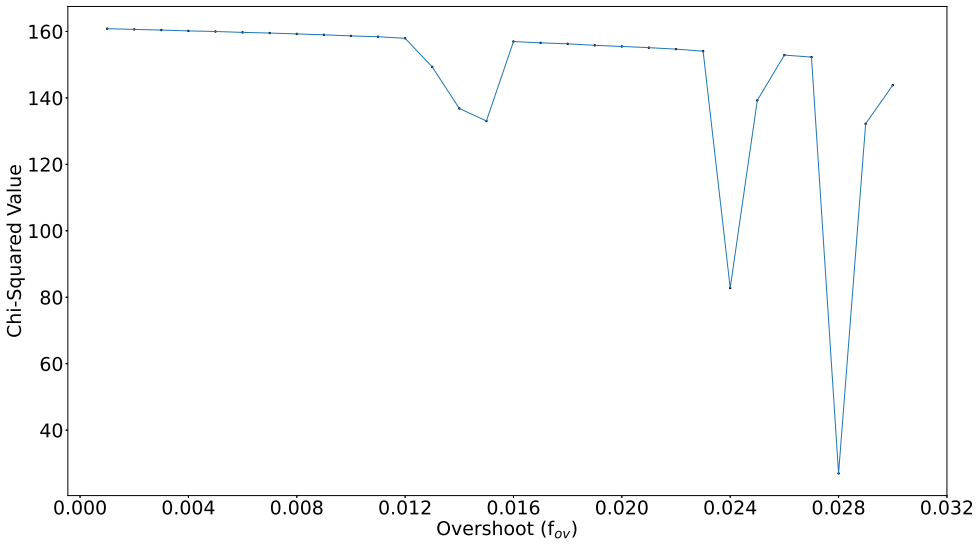

Figure H.3: A plot of the chi-squared values per pulsation frequency-match iteration showing the global minimum for overshoot lies at 0.028 $f_{\rm ov}$. Hence, with no adjacent minimum being of similar value, the error was taken to be ±half of the overshoot interval as the lowest chi-squared value is within this resolution.

Appendix I

SALT RV Measurements of TIC 409934330

Table I.1: The 82 RVs obtained from the SALT observations of TIC 409934330. The entry under "2021 10 07" has been highlighted red as, by a nice coincidence, this spectra was taken during close to the mid-point of a transit of the companion to TIC 409934330, and so acts as a zero-point for the relative RVs of all other data points.

Observation Midpoint Timestamp (UTC)	Observation Midpoint Timestamp (BJD)	Raw RVs ($km\,s^{-1}$)	Barycentric Correction ($km\,s^{-1}$)	Final RVs ($km\,s^{-1}$)	Δ RVs From Zero-Point ($km\,s^{-1}$)	RV Error ($km\,s^{-1}$)
2021 05 02 02:20:23.796	2459336.59994838	-26.77	17.26	-9.51	-0.10	$\pm$0.30
2021 05 02 02:53:22.312	2459336.62284919	-26.85	17.24	-9.61	-0.20	$\pm$0.30
$km\,s^{-1}$ 2021 05 03 02:04:51.109	2459337.58920999	-26.56	17.12	-9.44	-0.03	$\pm$0.22
2021 05 03 03:26:31.015	2459337.64592502	-26.49	17.07	-9.42	-0.01	$\pm$0.31
2021 05 03 03:43:22.475	2459337.65763239	-26.39	17.06	-9.33	+0.08	$\pm$0.31
2021 05 11 02:21:21.609	2459345.60111259	-25.35	15.75	-9.60	-0.19	$\pm$0.31
2021 05 13 01:32:57.437	2459347.56760129	-24.76	15.39	-9.40	+0.01	$\pm$0.31
2021 05 25 00:44:51.328	2459359.53475821	-22.23	12.75	-9.48	-0.06	$\pm$0.31
2021 05 26 01:39:28.038	2459360.57272661	-22.12	12.47	-9.65	-0.24	$\pm$0.32
2021 05 28 00:55:40.171	2459362.54239164	-21.46	12.00	-9.46	-0.05	$\pm$0.30
2021 07 27 21:47:43.670	2459423.41248519	-3.10	-6.44	-9.54	-0.13	$\pm$0.31
2021 07 30 20:16:00.375	2459426.34872204	-2.31	-7.28	-9.59	-0.18	$\pm$0.31
2021 08 02 00:05:24.296	2459428.50797145	-1.54	-8.04	-9.58	-0.17	$\pm$0.31
2021 08 02 22:00:44.601	2459429.42137623	-1.28	-8.24	-9.52	-0.11	$\pm$0.31
2021 08 03 20:03:52.191	2459430.34018833	-1.29	-8.45	-9.74	-0.33	$\pm$0.32
2021 09 23 20:12:20.046	2459481.34360617	8.96	-18.67	-9.71	-0.30	$\pm$0.31
2021 10 07 19:20:55.812	2459495.30702295	9.88	-19.23	-9.41	0.00	$\pm$0.31
2021 10 08 19:32:24.953	2459496.31493446	0.22	-9.30	-9.08	+0.33	$\pm$0.32
2021 10 09 19:18:53.296	2459497.30547669	10.12	-19.28	-9.16	+0.25	$\pm$0.31

2021 10 26 18:27:51.406	2459514.26896954	9.39	-18.33	-8.94	+0.47	±0.32
2022 05 02 02:57:41.507	2459701.62584373	-26.64	17.29	-9.35	+0.06	±0.32
2022 05 05 03:20:37.031	2459704.64193533	-25.66	16.81	-8.85	+0.56	±0.32
2022 05 09 02:18:54.312	2459708.59929690	-25.61	16.16	-9.45	-0.04	±0.32
2022 05 16 02:23:54.312	2459715.60313020	-23.85	14.79	-9.06	+0.35	±0.35
2022 05 17 00:57:32.718	2459716.54320398	-24.34	14.64	-9.70	-0.29	±0.35
2022 05 18 01:07:29.375	2459717.55015835	-23.39	14.42	-8.97	+0.44	±0.32
2022 05 23 01:35:52.000	2459722.57009579	-22.95	13.28	-9.67	-0.26	±0.31
2022 05 24 00:37:29.492	2459723.52959949	-22.69	13.08	-9.61	-0.20	±0.33
2022 05 24 01:54:17.554	2459723.58293581	-22.66	13.03	-9.63	-0.22	±0.33
2022 06 07 01:07:50.718	2459737.55120388	-18.79	9.37	-9.42	-0.01	±0.32
2022 06 09 00:43:39.093	2459739.53446267	-18.61	8.82	-9.79	-0.38	±0.33
2022 06 10 00:09:36.562	2459740.51085042	-18.27	8.56	-9.71	-0.30	±0.33
2022 06 10 02:44:56.203	2459740.61871968	-18.24	8.44	-9.80	-0.39	±0.30
2022 07 12 23:52:16.578	2459773.49919562	-7.83	-1.75	-9.58	-0.17	±0.32
2022 07 13 21:31:56.578	2459774.40173625	-7.36	-1.96	-9.32	+0.09	±0.32
2022 07 13 23:50:06.429	2459774.49768300	-7.42	-2.07	-9.49	-0.08	±0.32
2022 07 14 00:01:58.836	2459774.50592834	-7.28	-2.08	-9.36	+0.05	±0.32
2022 07 14 00:13:25.164	2459774.51387189	-7.19	-2.08	-9.27	+0.14	±0.32
2022 07 14 00:24:47.461	2459774.52176883	-7.35	-2.09	-9.44	-0.03	±0.33
2022 07 15 00:48:37.640	2459775.53831429	-6.88	-2.43	-9.31	+0.10	±0.33
2022 07 15 21:06:44.453	2459776.38421938	-6.87	-2.58	-9.45	-0.04	±0.32
2022 07 15 22:07:49.078	2459776.42663361	-6.73	-2.62	-9.35	+0.06	±0.32
2022 07 16 00:12:48.671	2459776.51343374	-6.62	-2.72	-9.34	+0.07	±0.32
2022 07 16 00:41:22.328	2459776.53326746	-6.83	-2.74	-9.57	-0.16	±0.32
2022 07 16 00:52:35.711	2459776.54106119	-6.78	-2.75	-9.53	-0.12	±0.32
2022 07 16 01:05:53.570	2459776.55029560	-6.84	-2.76	-9.60	-0.19	±0.31
2022 07 16 01:17:06.367	2459776.55808253	-6.82	-2.77	-9.59	-0.18	±0.31
2022 07 16 01:28:17.570	2459776.56585106	-6.70	-2.77	-9.47	-0.06	±0.30

2022 07 16 21:32:14.843	2459777.40192264	-6.66	-2.92	-9.58	-0.17	±0.31
2022 07 16 21:43:46.265	2459777.40992516	-6.71	-2.92	-9.63	-0.21	±0.31
2022 07 17 01:22:51.882	2459777.56207194	-6.39	-3.09	-9.48	-0.07	±0.32
2022 07 17 21:31:32.609	2459778.40142341	-6.11	-3.23	-9.34	+0.07	±0.32
2022 07 17 23:58:09.625	2459778.50323959	-6.17	-3.34	-9.51	-0.10	±0.32
2022 07 18 00:09:50.359	2459778.51134990	-5.99	-3.35	-9.34	-0.07	±0.31
2022 07 18 00:20:34.218	2459778.51880182	-6.11	-3.36	-9.47	-0.06	±0.33
2022 07 18 00:32:02.671	2459778.52676993	-6.40	-3.37	-9.77	-0.26	±0.33
2022 07 18 00:43:10.187	2459778.53449574	-6.37	-3.37	-9.74	-0.23	±0.33
2022 07 18 00:54:18.625	2459778.54223225	-6.05	-3.38	-9.43	-0.02	±0.34
2022 07 18 01:06:50.812	2459778.55093795	-5.96	-3.39	-9.35	+0.06	±0.32
2022 07 18 01:18:03.671	2459778.55872567	-6.18	-3.40	-9.58	-0.17	±0.30
2022 07 18 21:10:39.984	2459779.38691410	-5.76	-3.53	-9.29	+0.12	±0.33
2022 07 18 21:47:48.062	2459779.41270179	-5.89	-3.56	-9.45	-0.04	±0.33
2022 07 18 21:58:26.046	2459779.42008570	-5.78	-3.57	-9.35	+0.06	±0.33
2022 07 18 22:09:43.796	2459779.42793001	-5.72	-3.58	-9.30	+0.11	±0.33
2022 07 31 21:17:42.921	2459792.39156573	-1.84	-7.56	-9.40	+0.01	±0.33
2022 08 04 19:55:08.093	2459796.33411082	0.22	-9.11	-8.89	+0.52	±0.36
2022 08 05 00:07:40.437	2459796.50947999	-0.45	-8.85	-9.30	+0.11	±0.33
2022 08 05 20:07:28.858	2459797.34265454	0.22	-8.97	-8.75	+0.66	±0.37
2022 08 06 19:35:18.484	2459798.32028246	-0.09	-9.23	-9.32	+0.09	±0.33
2022 08 08 20:23:05.772	2459800.35340369	0.40	-9.82	-9.42	-0.01	±0.49
2022 08 11 20:03:16.234	2459803.33953361	1.89	-10.62	-8.73	+0.68	±0.36
2022 08 11 23:23:19.640	2459803.47845696	1.32	-10.76	-9.44	-0.03	±0.33
2022 08 11 23:36:19.640	2459803.48748433	1.43	-10.77	-9.34	+0.07	±0.34
2022 08 15 19:36:21.765	2459807.32069900	1.96	-11.65	-9.69	-0.28	±0.33
2022 08 15 23:05:11.250	2459807.46571052	2.03	-11.80	-9.77	-0.36	±0.35
2022 08 16 19:27:37.311	2459808.31458967	2.67	-11.90	-9.23	+0.18	±0.35
2022 08 20 20:22:39.531	2459812.35264192	3.77	-12.93	-9.16	+0.25	±0.33

2022 08 21 19:13:09.703	2459813.30433853	3.47	-13.13	-9.66	-0.25	±0.32
2022 08 22 19:29:47.390	2459814.31584105	3.70	-13.38	-9.68	-0.27	±0.33
2022 08 26 19:06:48.201	2459818.29969376	4.63	-14.27	-9.64	-0.23	±0.41
2022 08 27 22:43:55.734	2459819.45041991	5.30	-14.63	-9.33	+0.08	±0.33
2022 08 28 21:59:29.906	2459820.41951810	5.47	-14.82	-9.35	+0.06	±0.36

Appendix J

Chemical Abundances in Spectra of TIC 409934330

The following are plots of the absorption lines for each chemical species listed in Table 5.13, which were studied for species abundance anomalies. The plots consist of the co-added SALT spectrum of TIC 409934330 (blue) and a model synthetic spectrum for comparison (red).

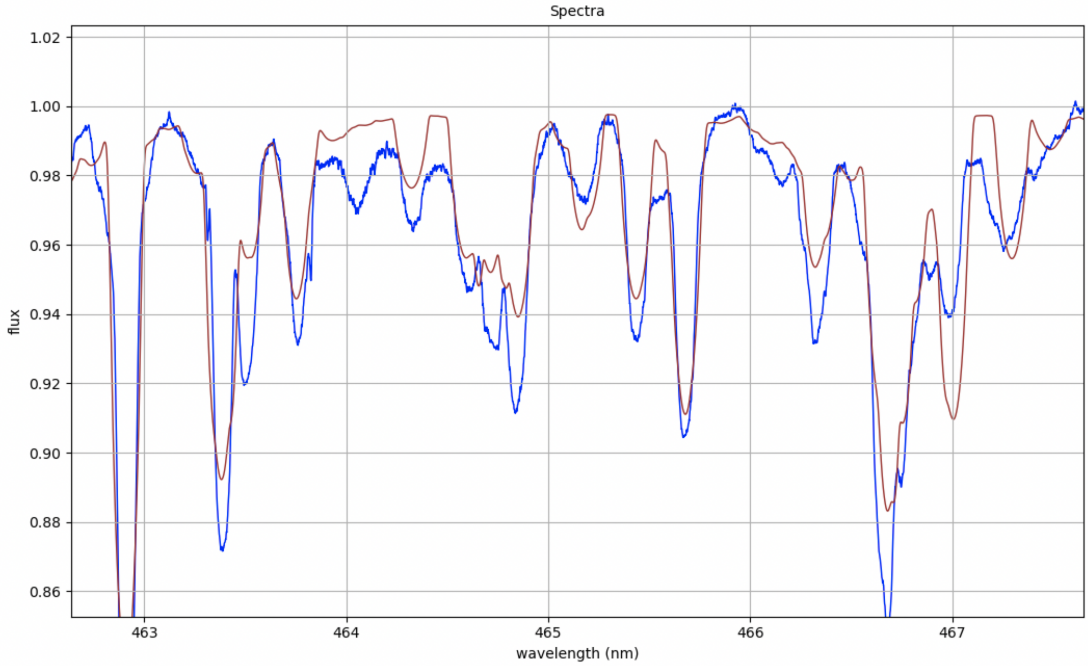

Figure J.1: The C III line at 465.1 nm showing the co-added spectra of TIC 409934330 (blue) to be possibly-underabundant, in comparison with the synthetic model (red), as predicted.

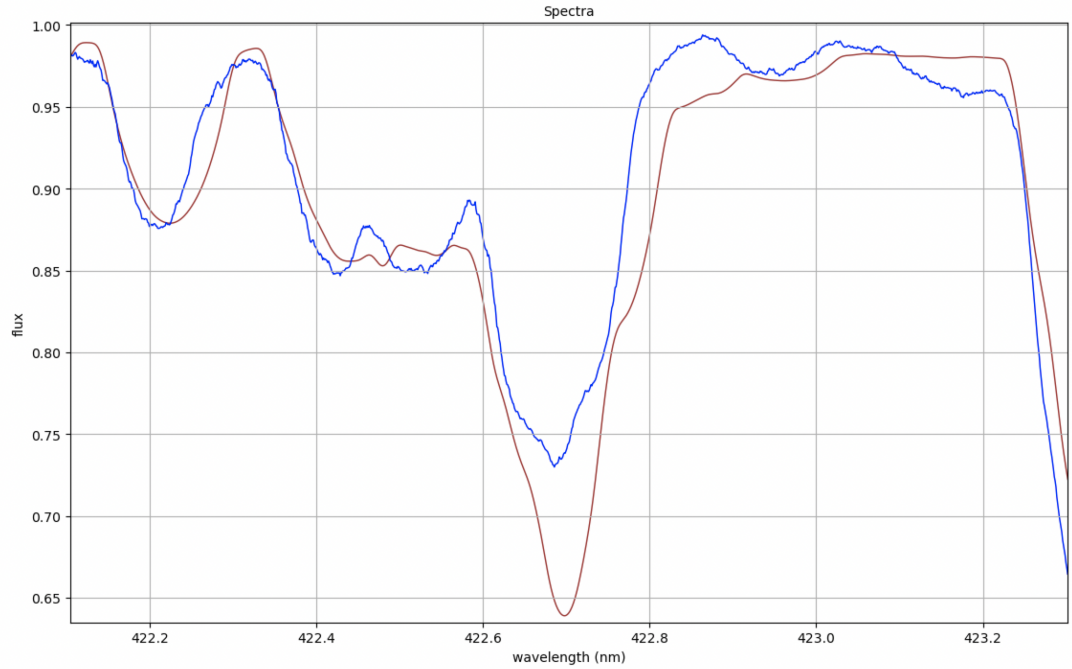

Figure J.2: The Ca I line at 422.673 nm showing the co-added spectra of TIC 409934330 (blue) to be underabundant, in comparison with the synthetic model (red), as predicted.

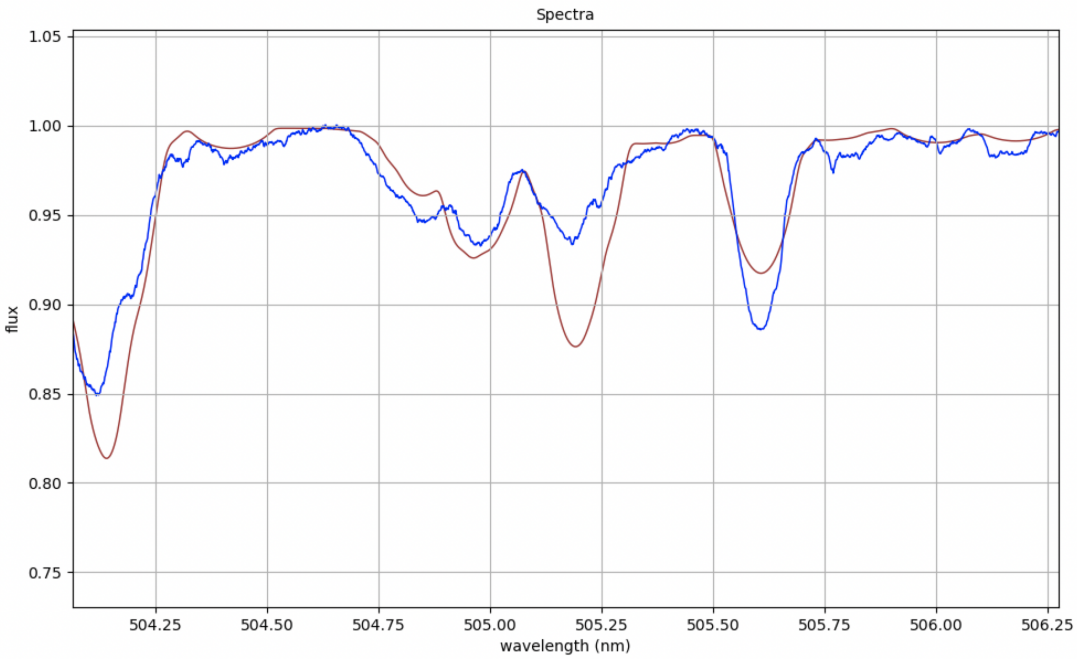

Figure J.3: The Cu II line at 505.1793 nm showing the co-added spectra of TIC 409934330 (blue) to be overabundant, in comparison with the synthetic model (red), as predicted.

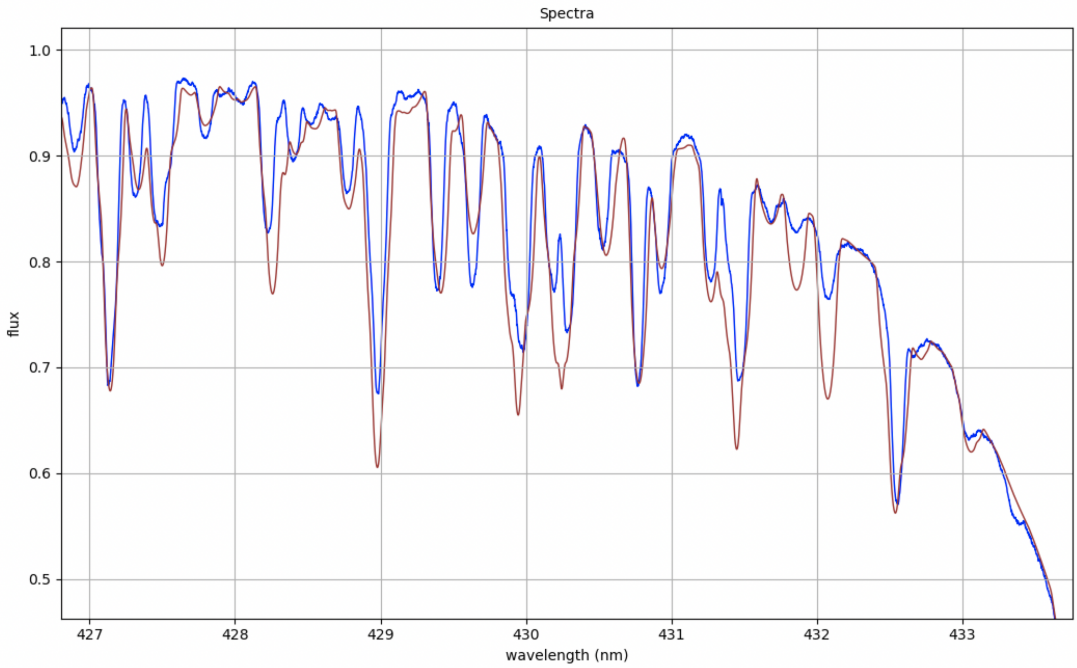

Figure J.4: The O II line at 430.281 nm showing the co-added spectra of TIC 409934330 (blue) to be underabundant, in comparison with the synthetic model (red), as predicted.

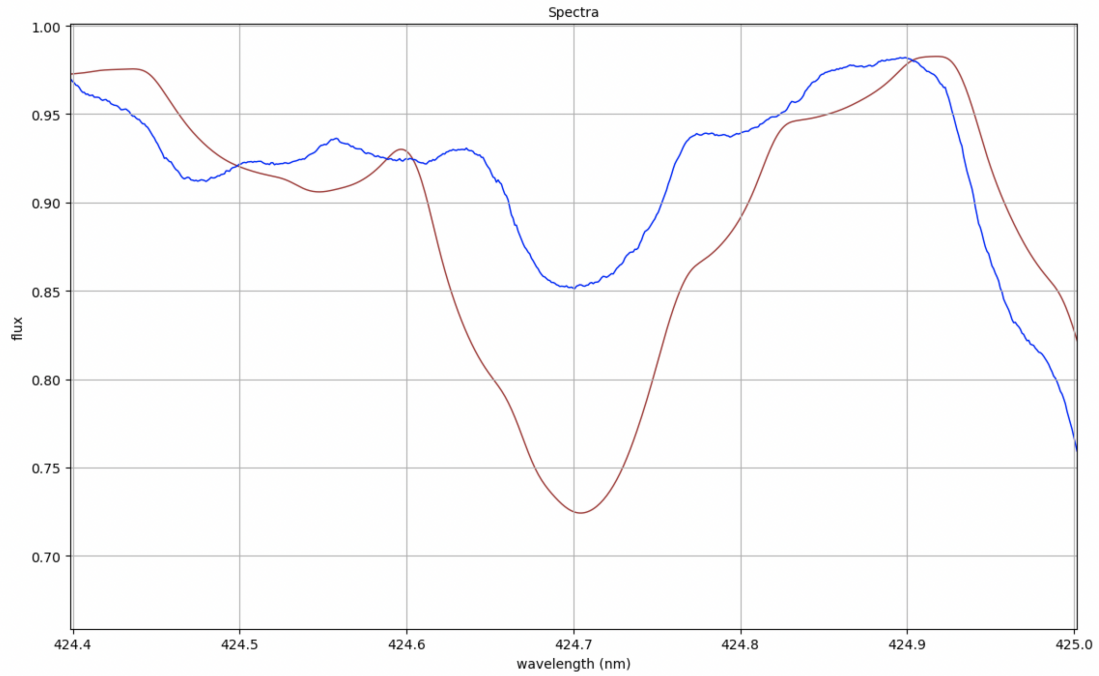

Figure J.5: The Sc II line at 424.7 nm showing the co-added spectra of TIC 409934330 (blue) to be underabundant, in comparison with the synthetic model (red), as predicted.

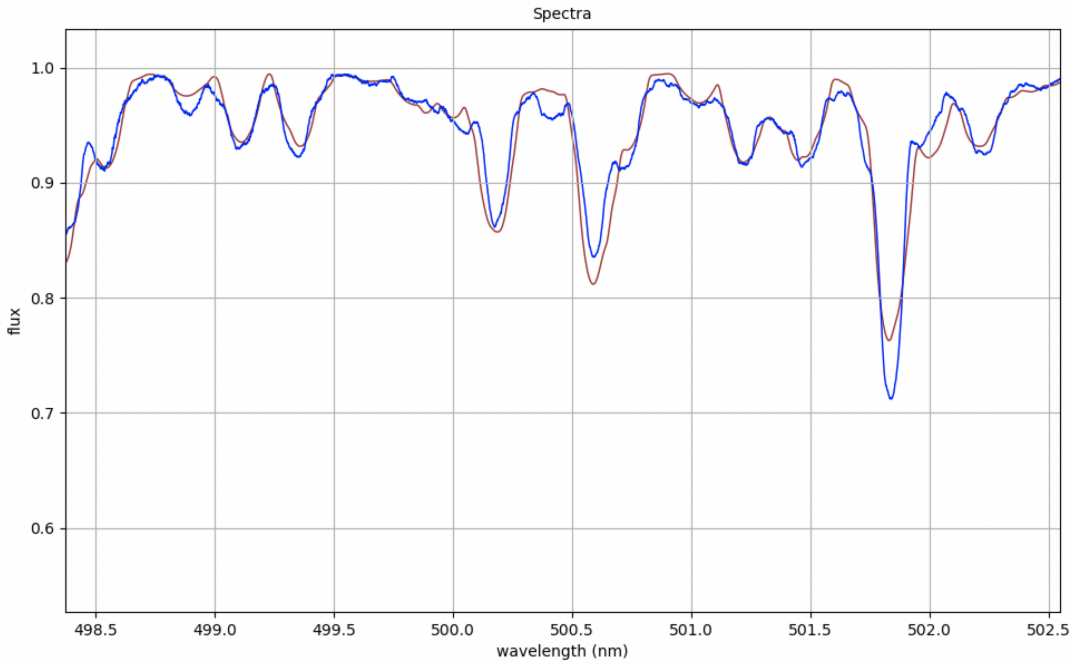

Figure J.6: The K II line at 500.5600 nm showing the co-added spectra of TIC 409934330 (blue) to be possibly-underabundant, in comparison with the synthetic model (red), as predicted.

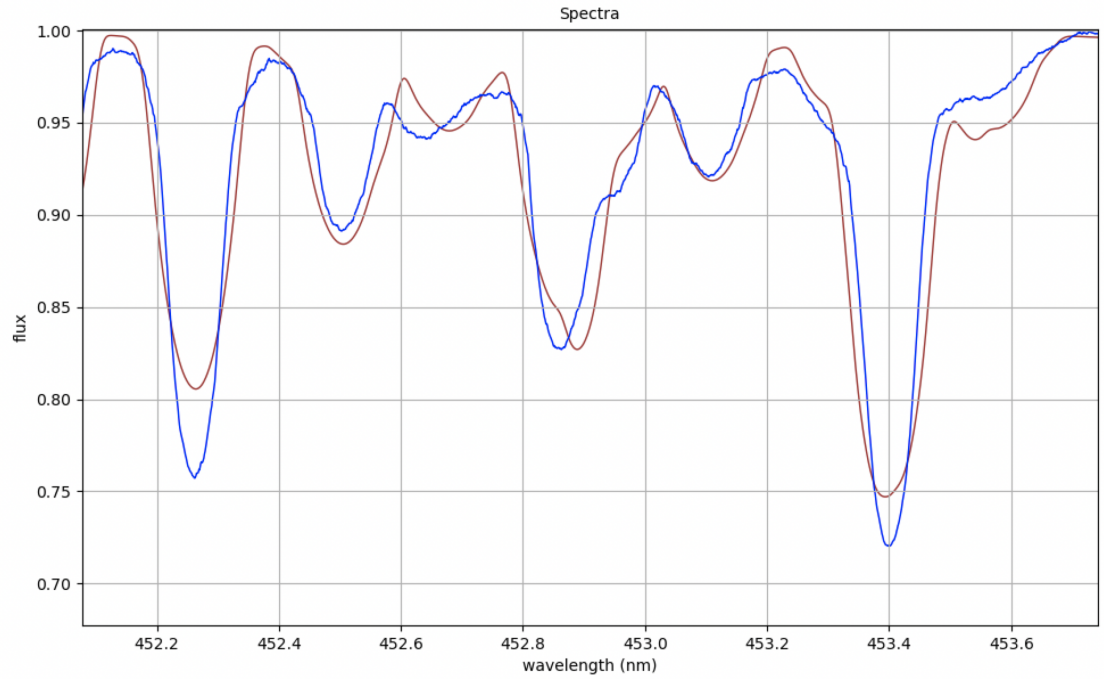

Figure J.7: The Al III line at 452.9 nm showing the co-added spectra of TIC 409934330 (blue) to have the same abundance level as the synthetic model (red). This was not expected.

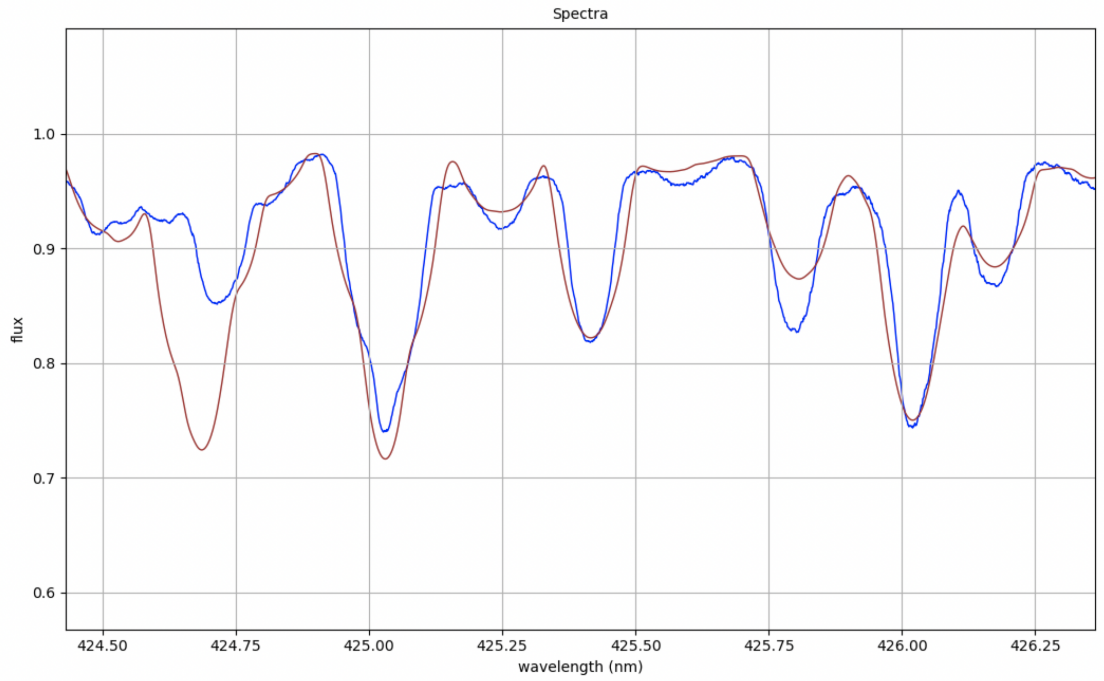

Figure J.8: The S II line at 425.4 nm showing the co-added spectra of TIC 409934330 (blue) to be normal, in comparison with the synthetic model (red), as predicted.

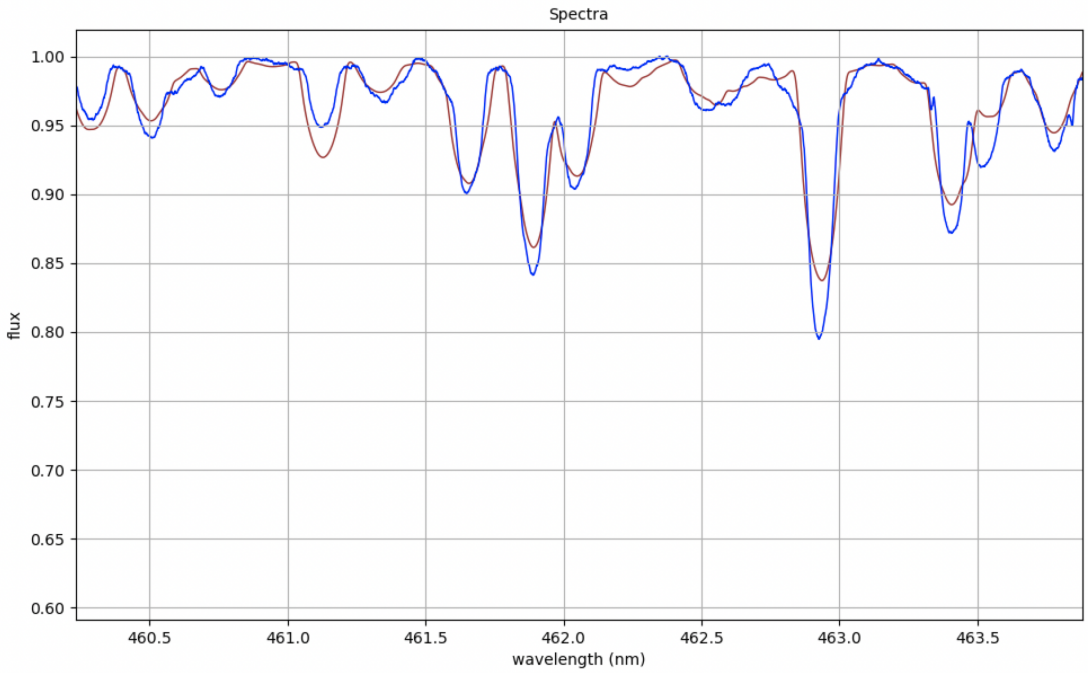

Figure J.9: The N III line at 462.1390 nm showing the co-added spectra of TIC 409934330 (blue) to have the same abundance level as the synthetic model (red). This was not expected.

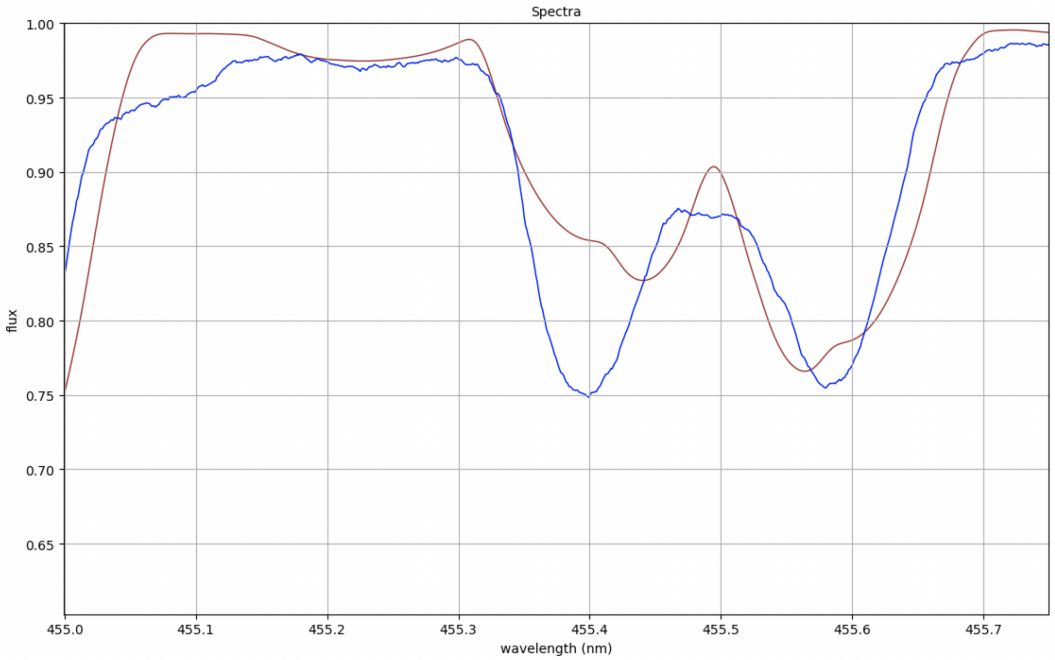

Figure J.10: The Ba II line at 455.4 nm showing the co-added spectra of TIC 409934330 (blue) to be overabundant, in comparison with the synthetic model (red), as predicted.

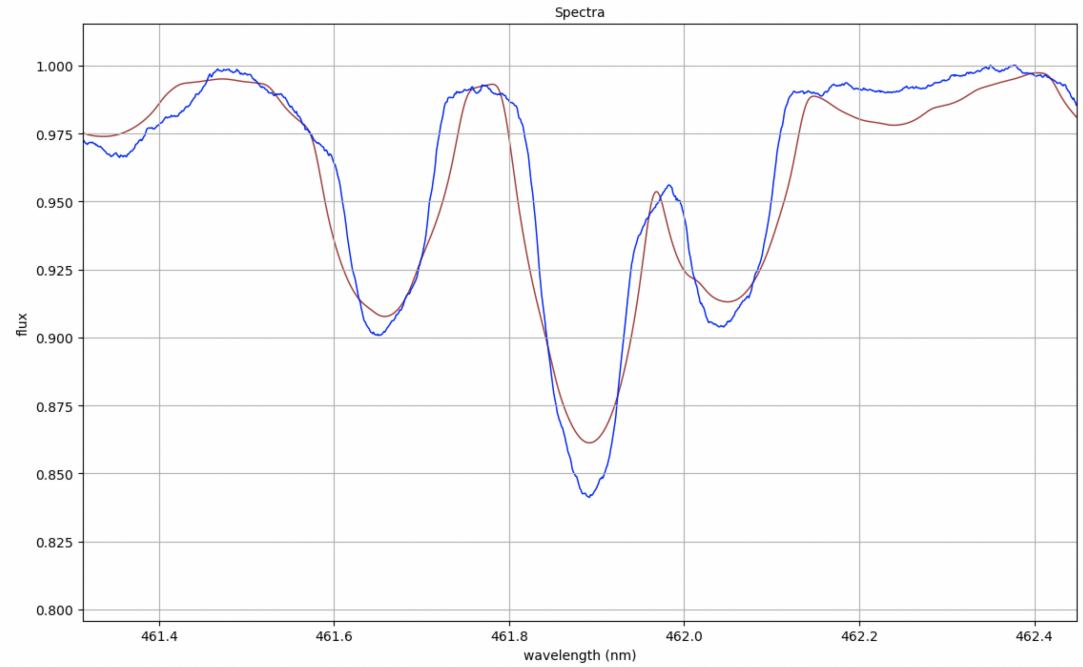

Figure J.11: The Cr II line at 461.9 nm showing the co-added spectra of TIC 409934330 (blue) to be overabundant, in comparison with the synthetic model (red), as predicted.

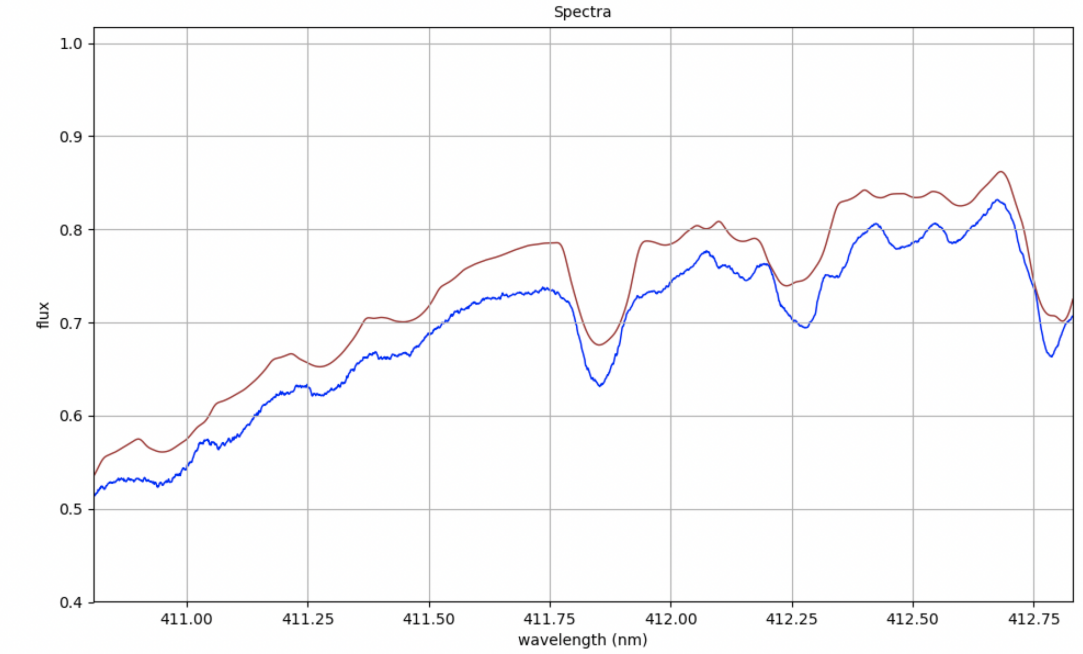

Figure J.12: The Co I line at 411.9 nm showing the co-added spectra of TIC 409934330 (blue) to be overabundant, in comparison with the synthetic model (red), as predicted.

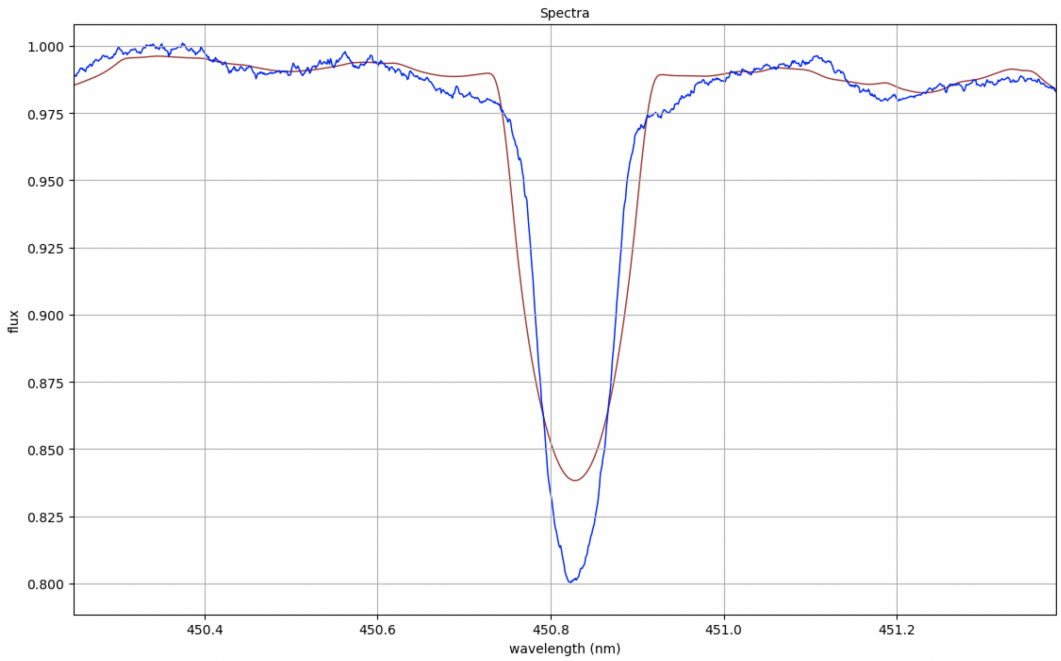

Figure J.13: The Fe II line at 450.8 nm showing the co-added spectra of TIC 409934330 (blue) to be overabundant, in comparison with the synthetic model (red), as predicted.

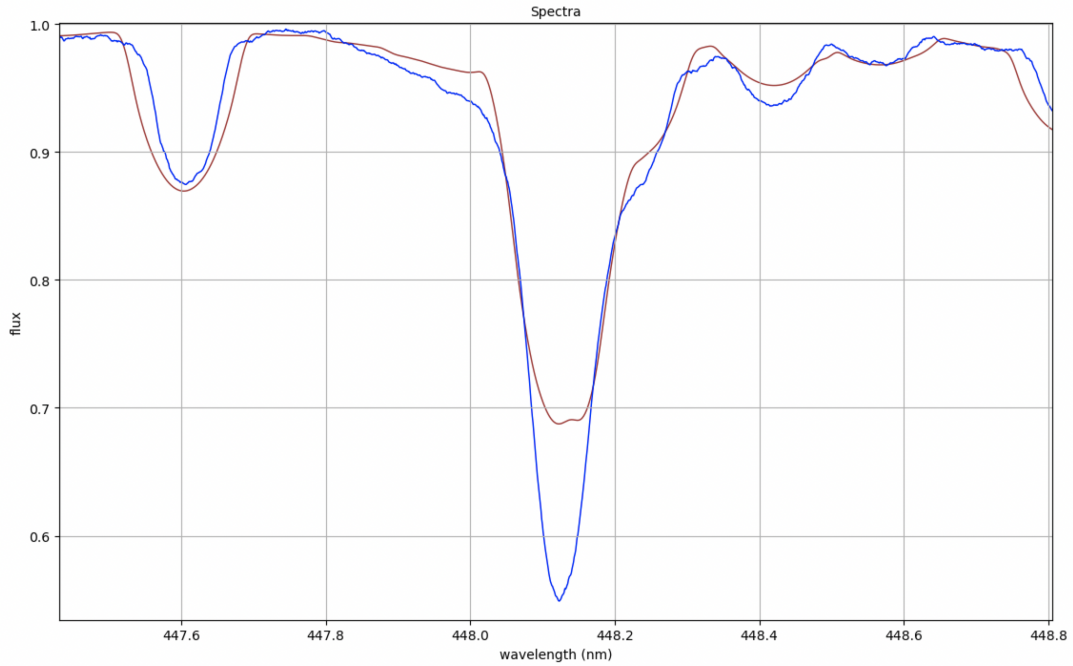

Figure J.14: The Mg II line at 448.113 nm showing the co-added spectra of TIC 409934330 (blue) to be overabundant, in comparison with the synthetic model (red). This species is not amongst the typical species population from which Am-star nature is discovered, therefore Mg II can be added to that list.

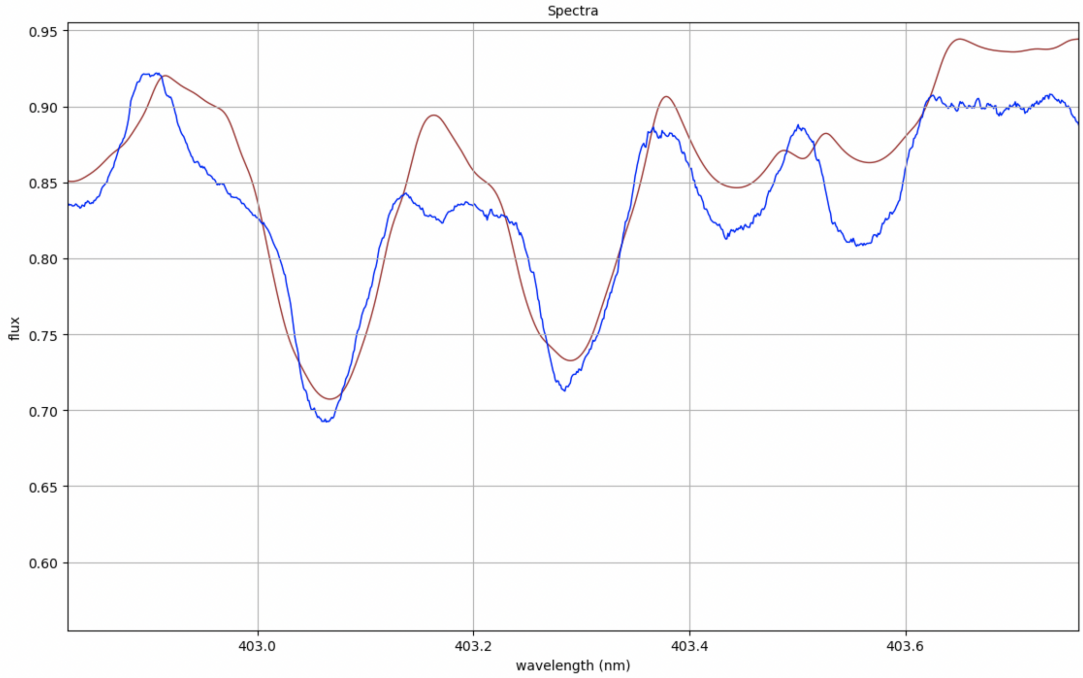

Figure J.15: The Mn I lines at 403.1 − 403.6 nm showing the co-added spectra of TIC 409934330 (blue) to be overabundant, in comparison with the synthetic model (red), as predicted.

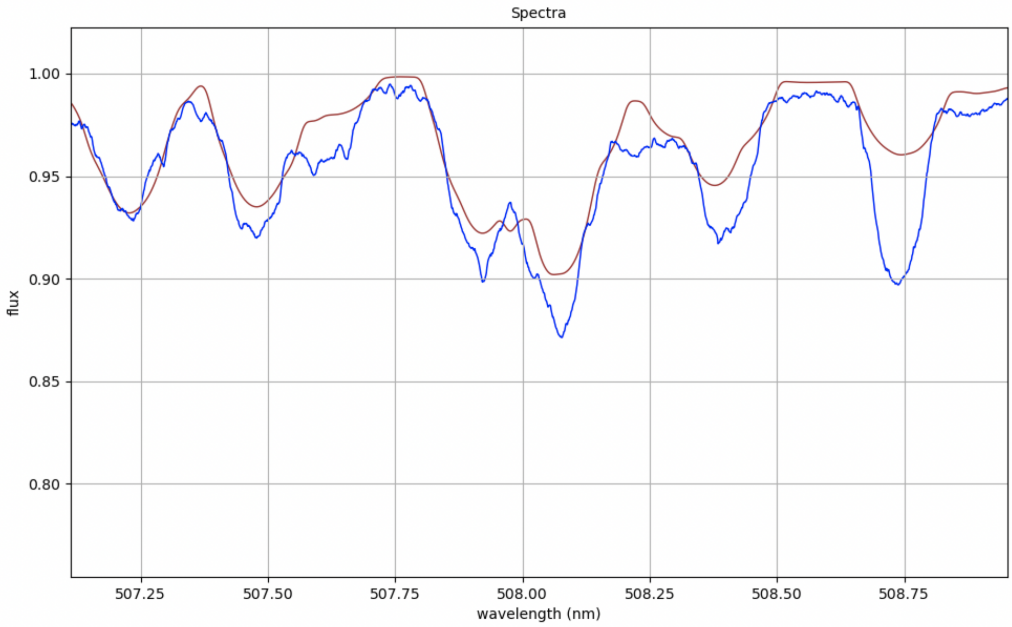

Figure J.16: The Ni I lines at 507.9/508.1 nm showing the co-added spectra of TIC 409934330 (blue) to be overabundant, in comparison with the synthetic model (red), as predicted.

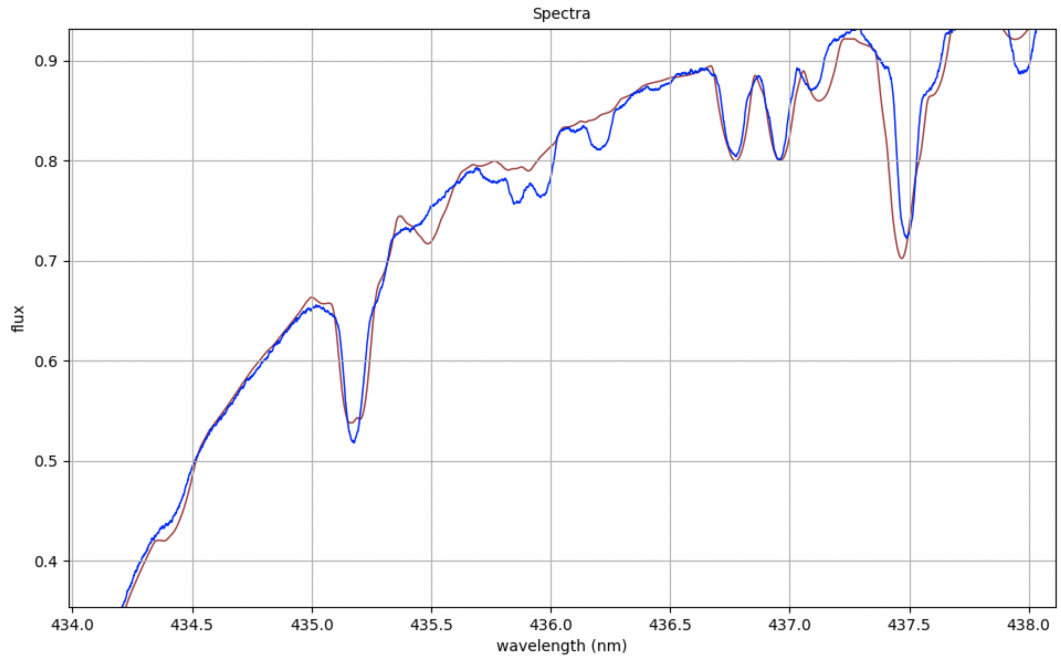

Figure J.17: The Re I lines at 435.869 nm showing the co-added spectra of TIC 409934330 (blue) to be overabundant, in comparison with the synthetic model (red), as predicted.

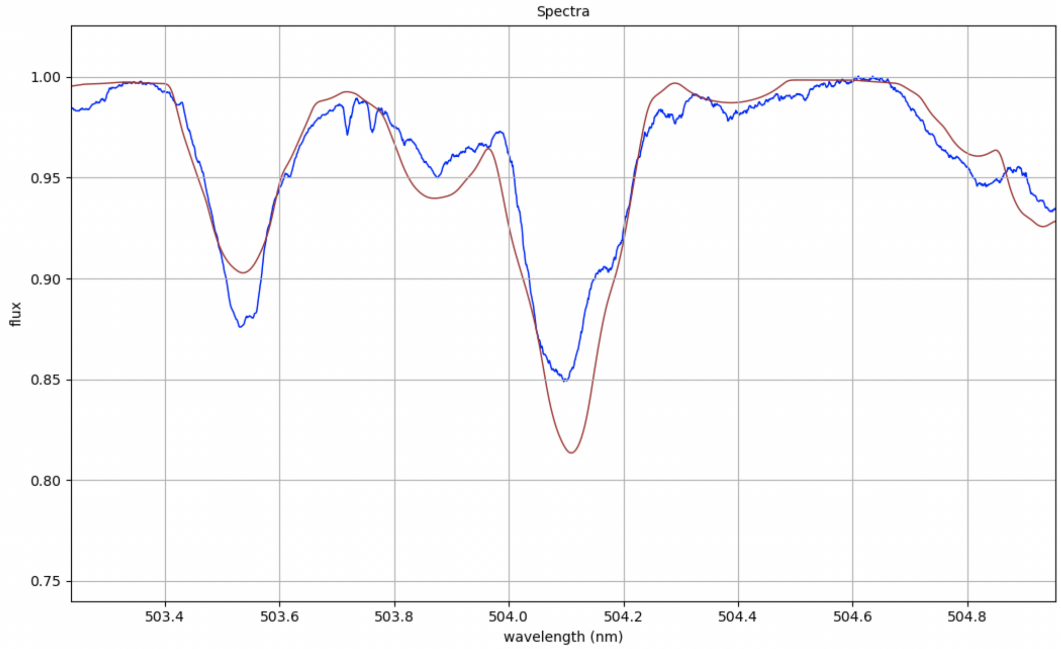

Figure J.18: The Si II lines at 504.1026 nm showing the co-added spectra of TIC 409934330 (blue) to be overabundant, in comparison with the synthetic model (red), as predicted.

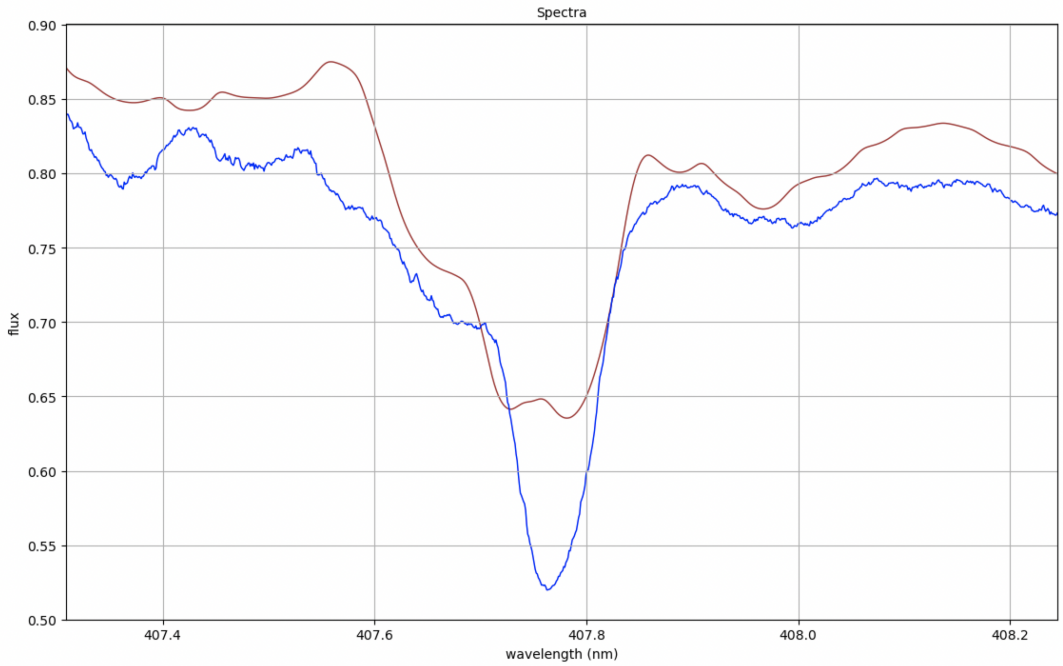

Figure J.19: The Sr II line at 407.771 nm showing the co-added spectra of TIC 409934330 (blue) to be overabundant, in comparison with the synthetic model (red), as predicted.

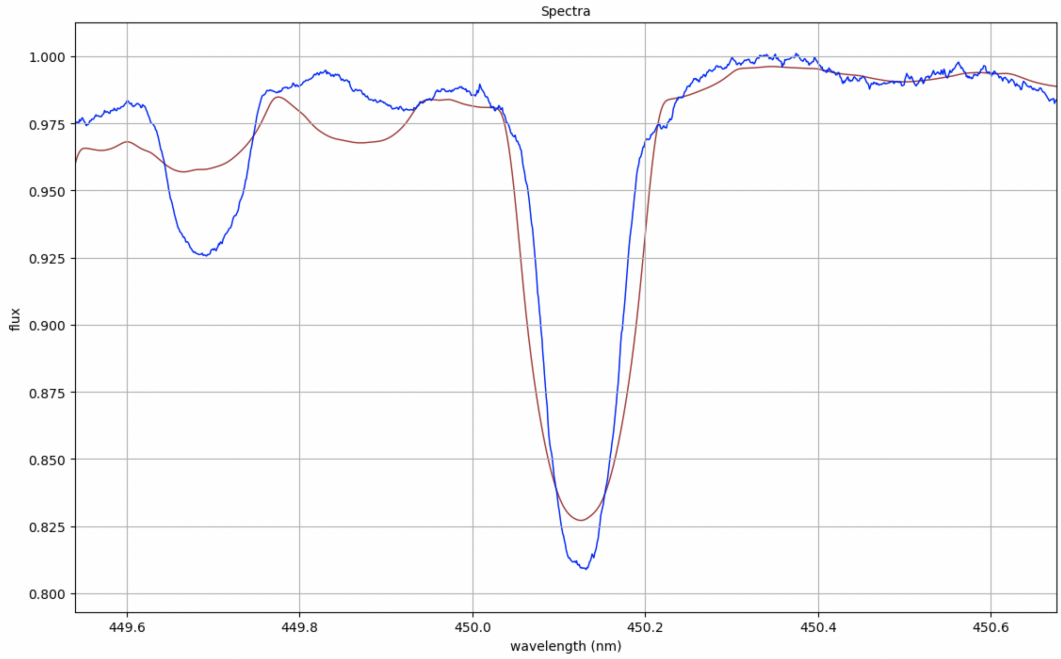

Figure J.20: The `Ti II` line at 450.127 nm showing the co-added spectra of TIC 409934330 (blue) to be overabundant, in comparison with the synthetic model (red). This species is not amongst the typical species population from which Am-star nature is discovered, therefore Ti II can be added to that list.

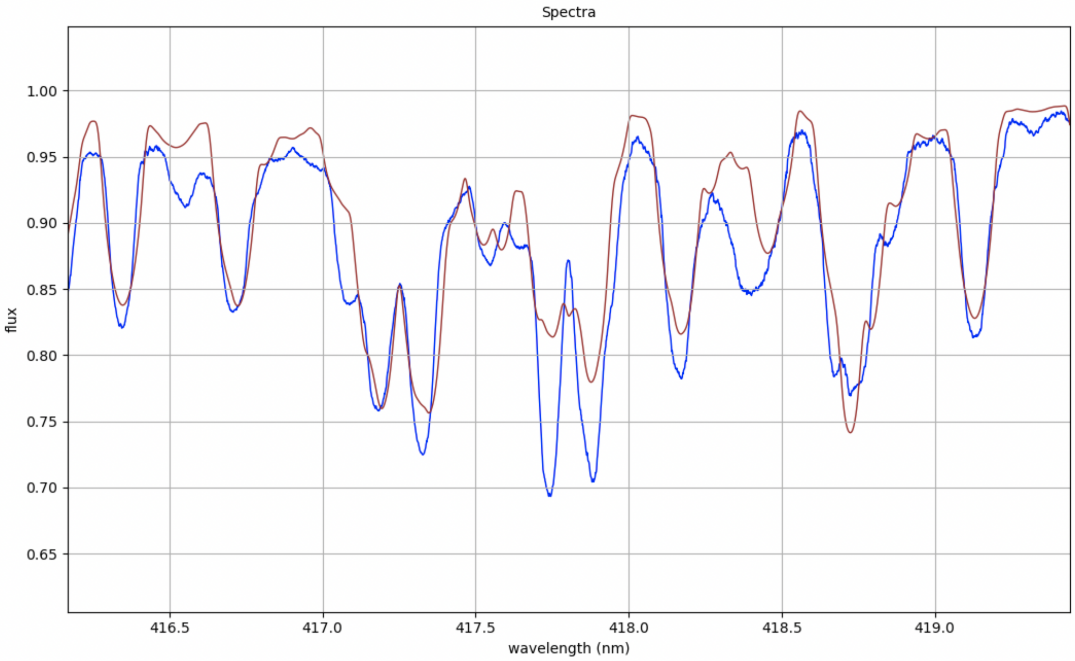

Figure J.21: The `Y II` line at 417.7528, nm showing the co-added spectra of TIC 409934330 (blue) to be overabundant, in comparison with the synthetic model (red), as predicted.

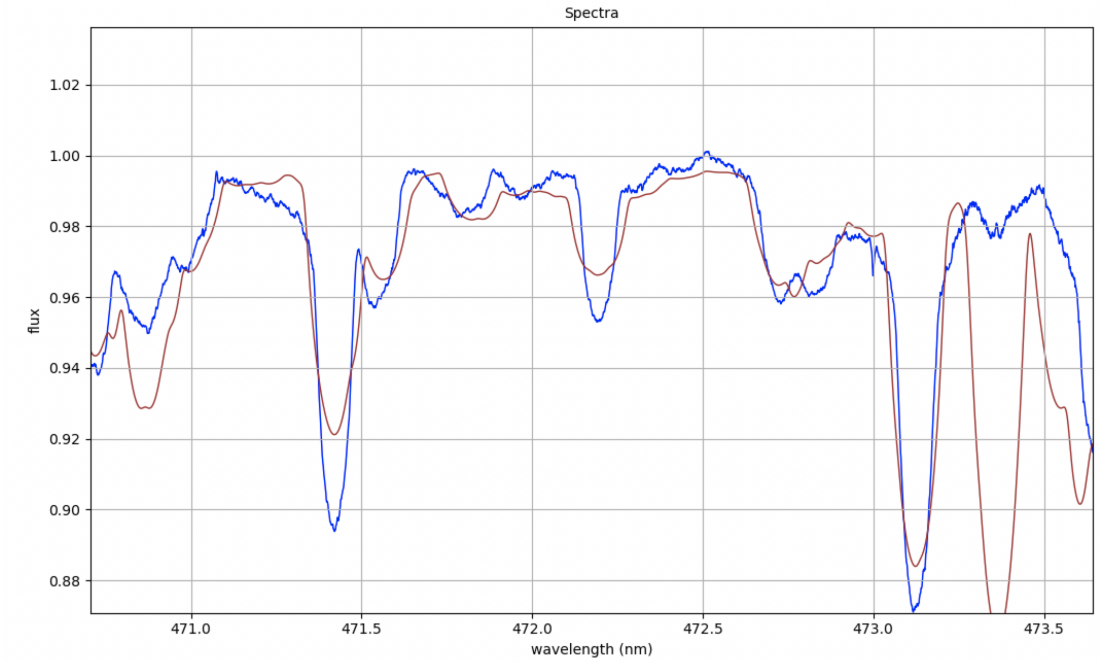

Figure J.22: The Zn I line at 472.21569 nm showing the co-added spectra of TIC 409934330 (blue) to be overabundant, in comparison with the synthetic model (red), as predicted.

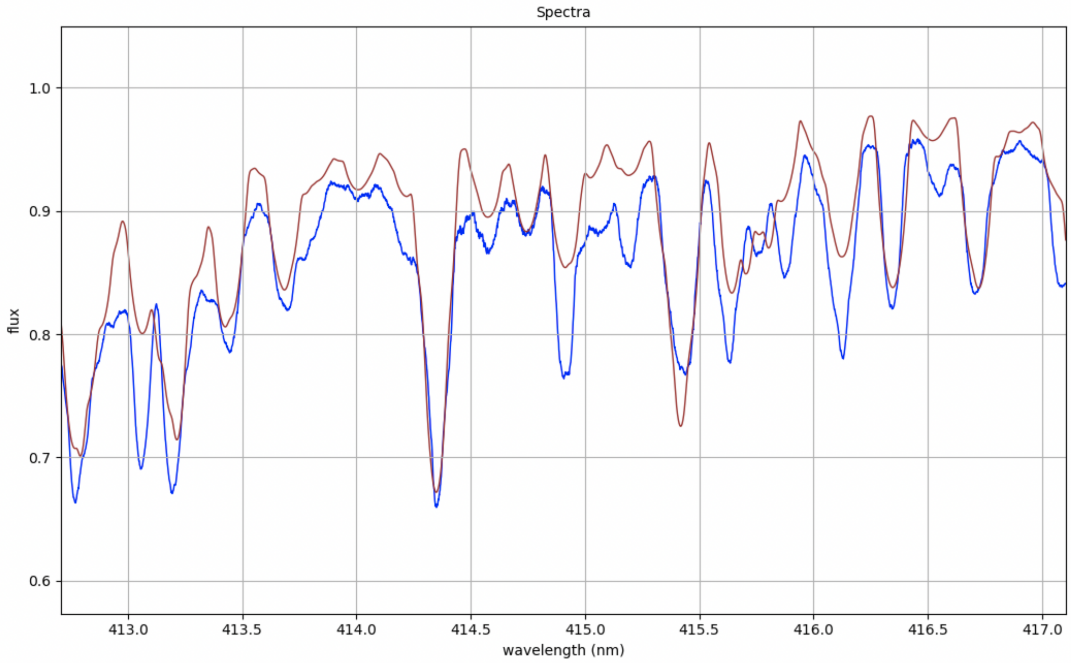

Figure J.23: The Zr II line at 414.9 nm showing the co-added spectra of TIC 409934330 (blue) to be overabundant, in comparison with the synthetic model (red), as predicted.

Appendix K

The Priors File Used by EXOFASTv2 in the Modelling of TIC 409934330's Companion

The following is the "priors" file that was fed into EXOFASTv2 as part of the modelling of the companion to TIC 409934330. Its three-column format consists of a parameter, its value and its error, in the syntax EXOFASTv2 requests.

```
mstar 2.10 0.09
rstar 4.72 0.21
teff 8062 29
feh 0.00 0.2
tc 2459038.62 0.000683626
period 2.488885 0.000142
parallax 4.02 1.41
vsini 55 3
logg 3.86 0.21
av 0.00000 0.07409
```

- Where:
    - `mstar` is stellar mass in units of $M_\odot$
    - `rstar` is stellar radius in units of $R_\odot$
    - `teff` is $T_{\rm eff}$ in units of K
    - `feh` is metalicity in units of dex
    - `tc` is time of conjunction in BJD
    - `period` is orbital period in BJD
    - `parallax` is the parallax measurement from *GAIA* in arcseconds ($''$)
    - `vsini` is the stellar rotation rate in unit of $\mathrm{km\,s^{-1}}$
    - `logg` is the stellar surface gravity log $\mathrm{cm\,s^{-2}}$
    - `av` is the extinction factor

Appendix L

The Extracted Pulsation Frequencies of TIC 156987351

Table L.1: The 71 extracted pulsation frequencies of TIC 156987351 identified from the Fourier transform shown in Figure 6.3

Frequency Number	Frequency ν (c/d)	Amplitude (mmag)
ν_1	0.3617 ± 0.0010	0.2016 ± 0.0112
ν_2	0.8871 ± 0.0021	0.1255 ± 0.0112
ν_3	1.0391 ± 0.0011	0.2521 ± 0.0112
ν_4	1.2678 ± 0.0002	0.3537 ± 0.0112
ν_5	1.3433 ± 0.0002	0.4666 ± 0.0112
ν_6	1.4717 ± 0.0006	0.4308 ± 0.0112
ν_7	2.0352 ± 0.0024	0.1370 ± 0.0112
ν_8	2.4666 ± 0.0015	0.1773 ± 0.0112
ν_9	2.5795 ± 0.0021	0.1297 ± 0.0112
ν_{10}	2.8871 ± 0.0017	0.1381 ± 0.0112
ν_{11}	3.5657 ± 0.0005	0.1020 ± 0.0112
ν_{12}	3.6207 ± 0.0003	0.2028 ± 0.0112
ν_{13}	4.0587 ± 0.0015	0.1982 ± 0.0112
ν_{14}	4.2072 ± 0.0009	0.2749 ± 0.0112
ν_{15}	4.3556 ± 0.0023	0.1175 ± 0.0112
ν_{16}	4.7840 ± 0.0029	0.0992 ± 0.0112
ν_{17}	5.0139 ± 0.0012	0.2358 ± 0.0112
ν_{18}	5.1550 ± 0.0011	0.2542 ± 0.0112
ν_{19}	5.4958 ± 0.0013	0.2153 ± 0.0112
ν_{20}	5.6082 ± 0.0008	0.2874 ± 0.0112
ν_{21}	5.7844 ± 0.0003	0.8539 ± 0.0112
ν_{22}	5.9609 ± 0.0011	0.2406 ± 0.0112

ν_{23}	6.1586 ± 0.0016	0.1713 ± 0.0112
ν_{24}	6.2682 ± 0.0014	0.1839 ± 0.0112
ν_{25}	6.4342 ± 0.0014	0.2192 ± 0.0112
ν_{26}	6.5676 ± 0.0010	0.0962 ± 0.0112
ν_{27}	6.6688 ± 0.0003	0.8716 ± 0.0112
ν_{28}	6.7427 ± 0.0005	0.5423 ± 0.0112
ν_{29}	6.8156 ± 0.0003	0.6304 ± 0.0112
ν_{30}	6.8796 ± 0.0001	0.2102 ± 0.0112
ν_{31}	7.0144 ± 0.0004	0.6554 ± 0.0112
ν_{32}	7.0641 ± 0.0003	0.0699 ± 0.0112
ν_{33}	7.1595 ± 0.0002	0.3721 ± 0.0112
ν_{34}	7.2532 ± 0.0007	0.1928 ± 0.0112
ν_{35}	7.4385 ± 0.0012	0.3171 ± 0.0112
ν_{36}	7.7860 ± 0.0008	0.6609 ± 0.0112
ν_{37}	7.9574 ± 0.0004	0.1505 ± 0.0112
ν_{38}	8.0372 ± 0.0014	0.2039 ± 0.0112
ν_{39}	8.1229 ± 0.0005	0.1793 ± 0.0112
ν_{40}	8.2789 ± 0.0016	0.2617 ± 0.0112
ν_{41}	8.6810 ± 0.0011	0.2153 ± 0.0112
ν_{42}	8.9216 ± 0.0013	0.1212 ± 0.0112
ν_{43}	9.4245 ± 0.0025	0.3933 ± 0.0112
ν_{44}	9.9713 ± 0.0007	0.1186 ± 0.0112
ν_{45}	10.1946 ± 0.0025	0.1019 ± 0.0112
ν_{46}	11.8533 ± 0.0026	0.2769 ± 0.0112
ν_{47}	12.0550 ± 0.0005	0.9220 ± 0.0112
ν_{48}	12.1159 ± 0.0002	0.0754 ± 0.0112
ν_{49}	12.9706 ± 0.0039	0.0833 ± 0.0112
ν_{50}	13.2082 ± 0.0034	0.4573 ± 0.0112
ν_{51}	13.4462 ± 0.0006	0.1182 ± 0.0112
ν_{52}	13.6227 ± 0.0023	0.6796 ± 0.0112
ν_{53}	14.2104 ± 0.0004	0.1597 ± 0.0112
ν_{54}	15.3121 ± 0.0008	0.5861 ± 0.0112
ν_{55}	15.6180 ± 0.0005	0.2195 ± 0.0112
ν_{56}	16.4746 ± 0.0013	0.1266 ± 0.0112
ν_{57}	16.7324 ± 0.0022	0.2520 ± 0.0112
ν_{58}	17.6663 ± 0.0010	0.2624 ± 0.0112
ν_{59}	18.0428 ± 0.0010	0.4101 ± 0.0112
ν_{60}	18.1698 ± 0.0007	0.3038 ± 0.0112
ν_{61}	19.4280 ± 0.0009	0.0983 ± 0.0112
ν_{62}	20.0899 ± 0.0029	0.2855 ± 0.0112
ν_{63}	21.1710 ± 0.0010	0.1213 ± 0.0112
ν_{64}	21.9602 ± 0.0021	0.1381 ± 0.0112
ν_{65}	22.0538 ± 0.0020	0.7148 ± 0.0112
ν_{66}	22.8060 ± 0.0004	0.1589 ± 0.0112

ν_{67}	23.3850 ± 0.0018	0.1307 ± 0.0112
ν_{68}	25.3228 ± 0.0022	0.7021 ± 0.0112
ν_{69}	27.7047 ± 0.0004	0.0520 ± 0.0112
ν_{70}	30.0953 ± 0.0008	0.0860 ± 0.0112
ν_{71}	36.0939 ± 0.0033	0.8117 ± 0.0112

Table L.2: The final list of of the 69 astrophysical extracted pulsation frequencies of TIC 156987351, with the non-astrophysical combination frequencies listed in Table 6.6 removed.

Frequency Number	Frequency ν (c/d)	Amplitude (mmag)
ν_1	0.3617 ± 0.0010	0.2016 ± 0.0112
ν_2	0.8871 ± 0.0021	0.1255 ± 0.0112
ν_3	1.0391 ± 0.0011	0.2521 ± 0.0112
ν_4	1.2678 ± 0.0002	0.3537 ± 0.0112
ν_6	1.4717 ± 0.0006	0.4308 ± 0.0112
ν_7	2.0352 ± 0.0024	0.1370 ± 0.0112
ν_8	2.4666 ± 0.0015	0.1773 ± 0.0112
ν_9	2.5795 ± 0.0021	0.1297 ± 0.0112
ν_{10}	2.8871 ± 0.0017	0.1381 ± 0.0112
ν_{11}	3.5657 ± 0.0005	0.1020 ± 0.0112
ν_{12}	3.6207 ± 0.0003	0.2028 ± 0.0112
ν_{13}	4.0587 ± 0.0015	0.1982 ± 0.0112
ν_{14}	4.2072 ± 0.0009	0.2749 ± 0.0112
ν_{15}	4.3556 ± 0.0023	0.1175 ± 0.0112
ν_{16}	4.7840 ± 0.0029	0.0992 ± 0.0112
ν_{17}	5.0139 ± 0.0012	0.2358 ± 0.0112
ν_{18}	5.1550 ± 0.0011	0.2542 ± 0.0112
ν_{19}	5.4958 ± 0.0013	0.2153 ± 0.0112
ν_{20}	5.6082 ± 0.0008	0.2874 ± 0.0112
ν_{21}	5.7844 ± 0.0003	0.8539 ± 0.0112
ν_{22}	5.9609 ± 0.0011	0.2406 ± 0.0112
ν_{23}	6.1586 ± 0.0016	0.1713 ± 0.0112
ν_{24}	6.2682 ± 0.0014	0.1839 ± 0.0112
ν_{25}	6.4342 ± 0.0014	0.2192 ± 0.0112
ν_{26}	6.5676 ± 0.0010	0.0962 ± 0.0112
ν_{27}	6.6688 ± 0.0003	0.8716 ± 0.0112
ν_{28}	6.7427 ± 0.0005	0.5423 ± 0.0112
ν_{29}	6.8156 ± 0.0003	0.6304 ± 0.0112
ν_{30}	6.8796 ± 0.0001	0.2102 ± 0.0112
ν_{31}	7.0144 ± 0.0004	0.6554 ± 0.0112
ν_{32}	7.0641 ± 0.0003	0.0699 ± 0.0112
ν_{33}	7.1595 ± 0.0002	0.3721 ± 0.0112
ν_{34}	7.2532 ± 0.0007	0.1928 ± 0.0112
ν_{35}	7.4385 ± 0.0012	0.3171 ± 0.0112
ν_{36}	7.7860 ± 0.0008	0.6609 ± 0.0112
ν_{37}	7.9574 ± 0.0004	0.1505 ± 0.0112
ν_{38}	8.0372 ± 0.0014	0.2039 ± 0.0112
ν_{39}	8.1229 ± 0.0005	0.1793 ± 0.0112
ν_{40}	8.2789 ± 0.0016	0.2617 ± 0.0112

ν_{41}	8.6810 ± 0.0011	0.2153 ± 0.0112
ν_{42}	8.9216 ± 0.0013	0.1212 ± 0.0112
ν_{43}	9.4245 ± 0.0025	0.3933 ± 0.0112
ν_{44}	9.9713 ± 0.0007	0.1186 ± 0.0112
ν_{45}	10.1946 ± 0.0025	0.1019 ± 0.0112
ν_{46}	11.8533 ± 0.0026	0.2769 ± 0.0112
ν_{47}	12.0550 ± 0.0005	0.9220 ± 0.0112
ν_{48}	12.1159 ± 0.0002	0.0754 ± 0.0112
ν_{49}	12.9706 ± 0.0039	0.0833 ± 0.0112
ν_{50}	13.2082 ± 0.0034	0.4573 ± 0.0112
ν_{51}	13.4462 ± 0.0006	0.1182 ± 0.0112
ν_{52}	13.6227 ± 0.0023	0.6796 ± 0.0112
ν_{53}	14.2104 ± 0.0004	0.1597 ± 0.0112
ν_{54}	15.3121 ± 0.0008	0.5861 ± 0.0112
ν_{55}	15.6180 ± 0.0005	0.2195 ± 0.0112
ν_{56}	16.4746 ± 0.0013	0.1266 ± 0.0112
ν_{57}	16.7324 ± 0.0022	0.2520 ± 0.0112
ν_{58}	17.6663 ± 0.0010	0.2624 ± 0.0112
ν_{59}	18.0428 ± 0.0010	0.4101 ± 0.0112
ν_{60}	18.1698 ± 0.0007	0.3038 ± 0.0112
ν_{61}	19.4280 ± 0.0009	0.0983 ± 0.0112
ν_{62}	20.0899 ± 0.0029	0.2855 ± 0.0112
ν_{64}	21.9602 ± 0.0021	0.1381 ± 0.0112
ν_{65}	22.0538 ± 0.0020	0.7148 ± 0.0112
ν_{66}	22.8060 ± 0.0004	0.1589 ± 0.0112
ν_{67}	23.3850 ± 0.0018	0.1307 ± 0.0112
ν_{68}	25.3228 ± 0.0022	0.7021 ± 0.0112
ν_{69}	27.7047 ± 0.0004	0.0520 ± 0.0112
ν_{70}	30.0953 ± 0.0008	0.0860 ± 0.0112
ν_{71}	36.0939 ± 0.0033	0.8117 ± 0.0112

Appendix M

Chi-squared Results for TIC 156987351

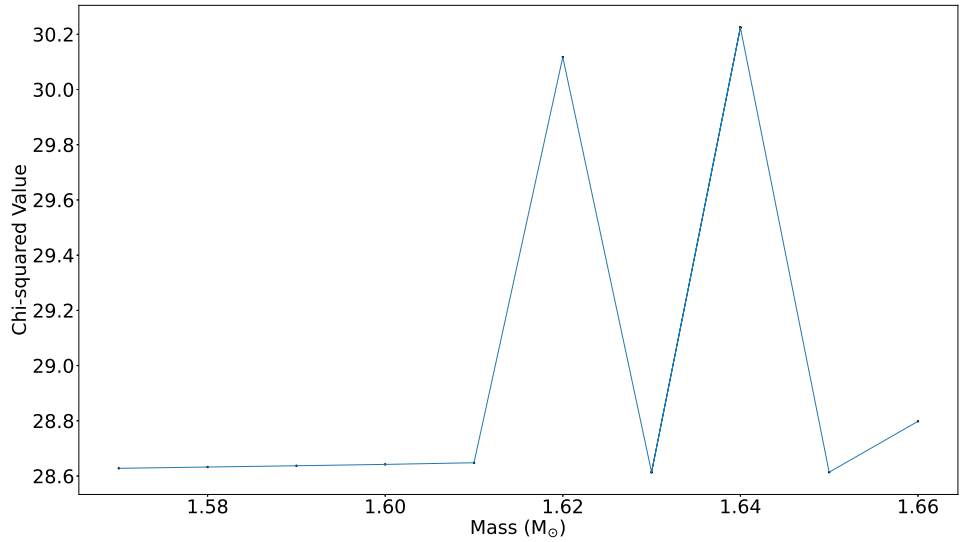

Figure M.1: A plot of the chi-squared values per pulsation frequency-match iteration showing the global minimum for mass lies at $1.63\,\mathrm{M}_\odot$. Hence, with no adjacent minimum being of similar value, the error was taken to be ±half of the mass interval as the lowest chi-squared value is within this resolution.

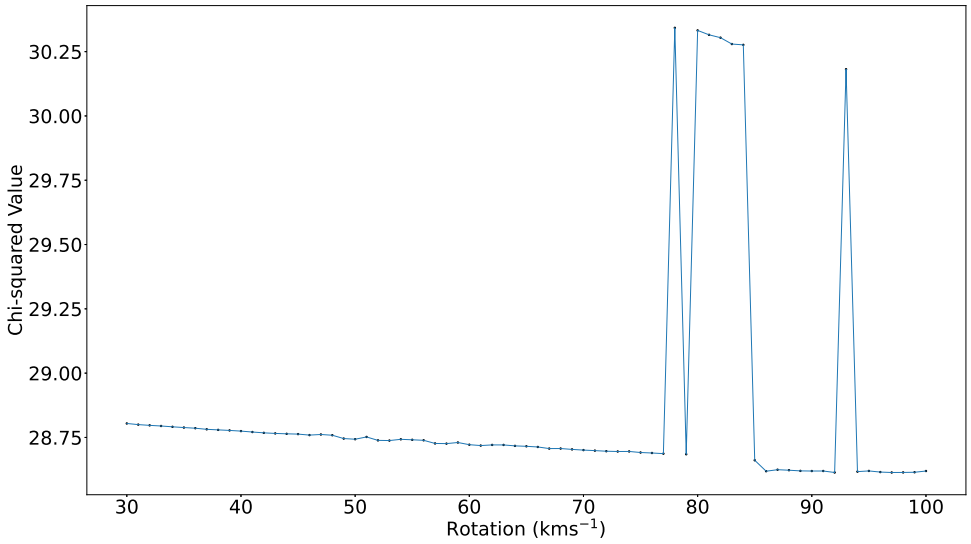

Figure M.2: A plot of the chi-squared values per pulsation frequency-match iteration showing the global minimum for rotation lies at $97\,\mathrm{kms}^{-1}$. Hence, with no adjacent minimum being of similar value, the error was taken to be ±half of the rotation interval as the lowest chi-squared value is within this resolution.

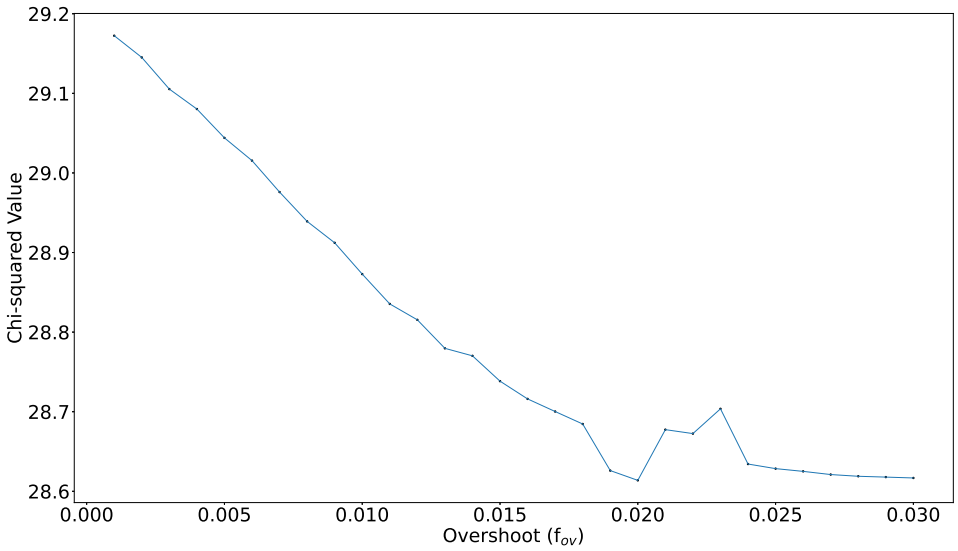

Figure M.3: A plot of the chi-squared values per pulsation frequency-match iteration showing the global minimum for overshoot lies at 0.020 $f_{\rm ov}$. Hence, with no adjacent minimum being of similar value, the error was taken to be ±half of the overshoot interval as the lowest chi-squared value is within this resolution.

Appendix N

SALT RV Measurements of TIC 156987351

Table N.1: The 17 RVs obtained from the SALT observations of TIC 156987351. The entry under "2021 11 18" has been highlighted red as, by a nice coincidence, this spectra was taken approximately one hour after the egress of an occultation of the companion to TIC 156987351, and so acts as a zero-point for the relative RVs of all other data points.

Observation Midpoint Timestamp (UTC)	Observation Midpoint Timestamp (BJD)	Raw RVs ($km\,s^{-1}$)	Barycentric Correction ($km\,s^{-1}$)	Final RVs ($km\,s^{-1}$)	Δ RVs From Zero-Point ($km\,s^{-1}$)	RV Error ($km\,s^{-1}$)
2021 11 02 23 15 08.735	2459521.47034962	-15.45	9.55	-5.90	4.62	$\pm$1.03
2021 11 06 23 02 33.906	2459525.46173596	-17.76	9.28	-8.48	2.04	$\pm$1.01
2021 11 09 22 41 27.125	2459528.44716332	-17.13	9.05	-8.08	2.44	$\pm$1.05
2021 11 12 22 46 11.906	2459531.45054673	-18.16	8.78	-9.38	1.14	$\pm$1.08
2021 11 15 22 11 36.718	2459534.42661215	-20.85	8.51	-12.34	-1.82	$\pm$0.98
2021 11 18 22 17 17.828	2459537.43064194	-18.71	8.19	-10.52	0.00	$\pm$1.03
2022 02 18 21 57 40.515	2459629.41732196	-6.98	-6.62	-13.60	-3.08	$\pm$1.08
2022 02 25 21 34 34.639	2459636.40112075	-8.65	-7.51	-16.16	-5.64	$\pm$1.01
2022 03 09 20 58 46.484	2459648.37593837	-1.56	-8.77	-10.33	0.19	$\pm$1.19
2022 03 16 20 32 56.984	2459655.35779767	-2.16	-9.32	-11.48	-0.96	$\pm$1.20
2022 03 26 19 41 56.312	2459665.32205945	-2.75	-9.86	-12.61	-2.09	$\pm$0.97
2022 10 08 01 10 58.495	2459860.54992308	-13.19	10.15	-3.04	7.48	$\pm$1.01
2022 11 09 22 57 00.882	2459893.45795781	-15.79	9.06	-6.73	3.79	$\pm$1.12
2022 11 18 22 24 36.218	2459902.43570353	-21.08	8.22	-12.86	-2.34	$\pm$1.21
2022 12 04 21 15 03.593	2459918.38778629	-13.80	6.24	-7.56	2.96	$\pm$1.20
2023 01 03 19 34 30.015	2459948.31832293	-11.64	1.36	-10.28	0.24	$\pm$0.97
2023 02 04 23 08 49.585	2459980.46698447	-14.80	-4.54	-19.34	-8.82	$\pm$1.26

Appendix O

The Priors File Used by EXOFASTv2 in the Modelling of TIC 156987351's Companion

The following is the "priors" file that was fed into EXOFASTv2 as part of the modelling of the companion to TIC 156987351. Its three-column format consists of a parameter, its value and its error, in the syntax EXOFASTv2 requests.

```
mstar 1.63 0.15
rstar 3.05 0.28
teff 7321 63
feh 0.00 0.2
tc 2459982.990599 0.001004
period 3.062987 0.000004
parallax 4.1665 0.0129
vsini 71 9
logg 4.02 0.14
av 0.00000 0.07409
```

- Where:
    - `mstar` is stellar mass in units of $M_\odot$
    - `rstar` is stellar radius in units of $R_\odot$
    - `teff` is $T_{\rm eff}$ in units of K
    - `feh` is metalicity in units of dex
    - `tc` is time of conjunction in BJD
    - `period` is orbital period in BJD
    - `parallax` is the parallax measurement from *Gaia* in arcseconds ($''$)
    - `vsini` is the stellar rotation rate in unit of $\mathrm{km\,s^{-1}}$
    - `logg` is the stellar surface gravity log $\mathrm{cm\,s^{-2}}$
    - `av` is the extinction factor

Appendix P

Light Curves of the 15 Potential δ Scuti Host Star TOIs

The following pages contain the light curves, phased curves and Fourier transforms (Figures P.1 to P.45) of the 15 potential δ Scuti host star TOIs — one set of plots per star per page — created from TESS data. The orbital period data for each TOI was taken from the TIC (Guerrero et al., 2021).

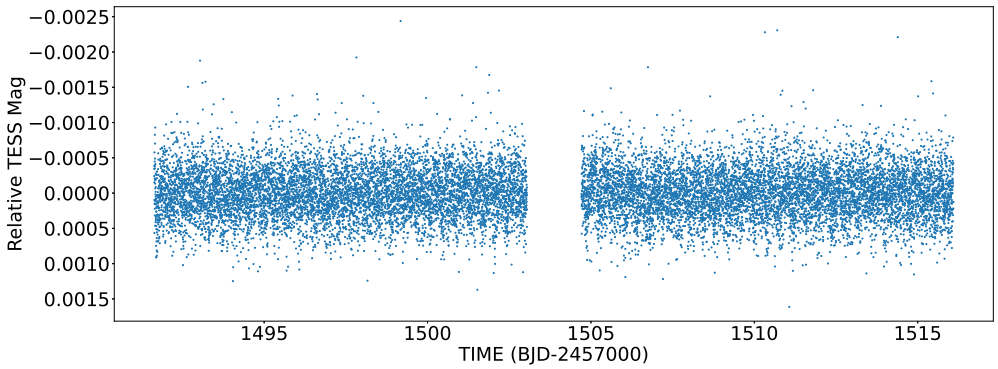

Figure P.1: The light curve of TOI 522 (TIC 19451711), created from TESS Sector 7 observations.

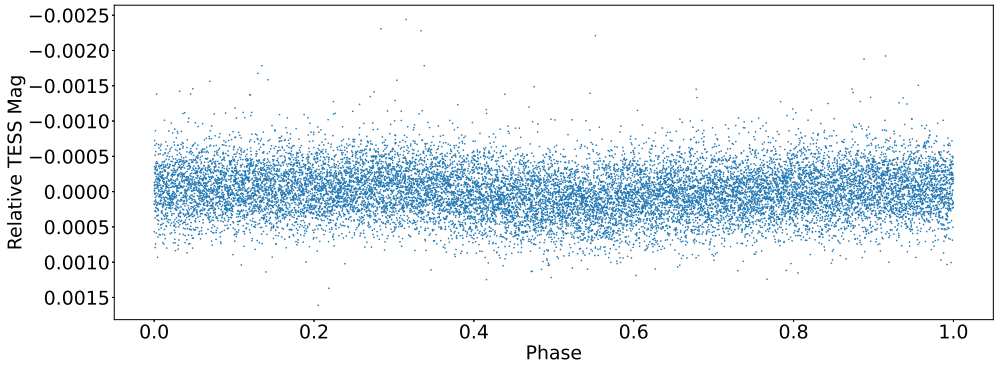

Figure P.2: The phase curve of TOI 522 (TIC 19451711), phased on its companion's orbital period of 0.397853 ± 0.000022 d.

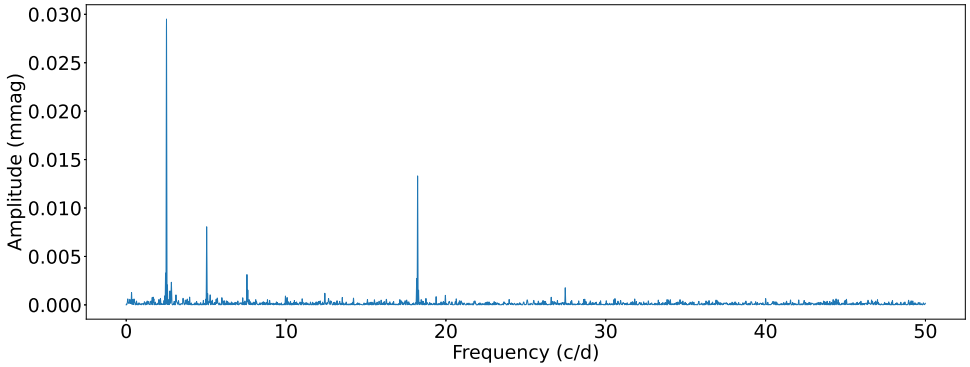

Figure P.3: The Fourier transform of TOI 522 (TIC 19451711), created using the light curve in Figure P.1.

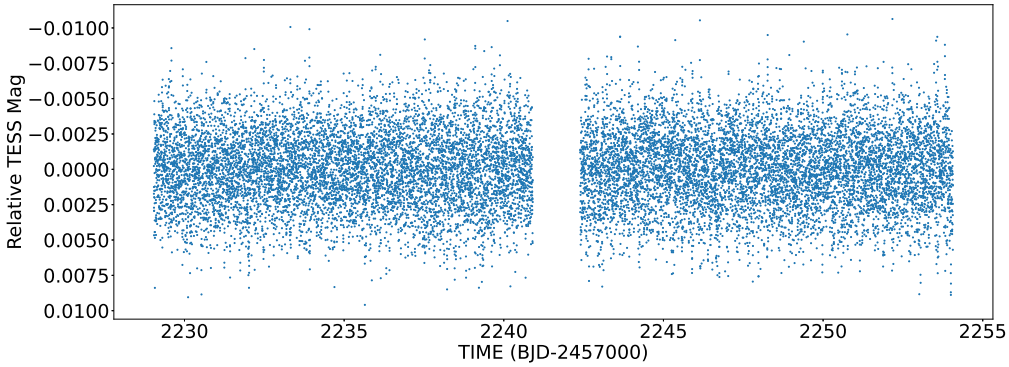

Figure P.4: The light curve of TOI 610 (TIC 80275202), created from TESS Sector 34 observations.

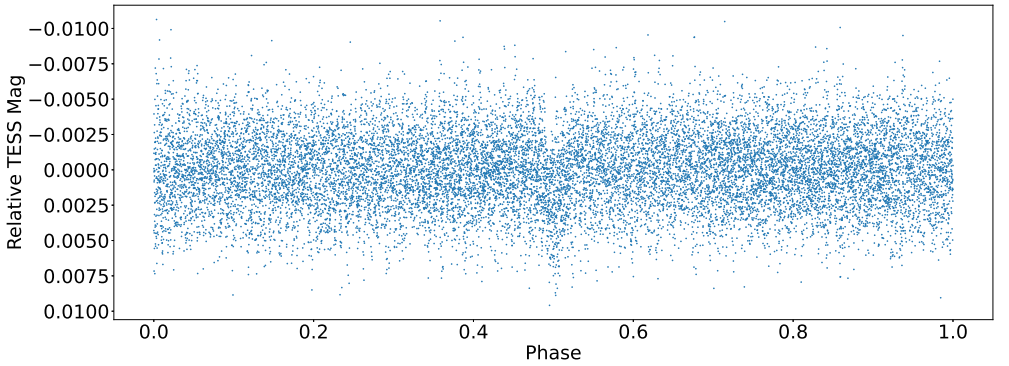

Figure P.5: The phase curve of TOI 610 (TIC 80275202), phased on its companion's orbital period of 3.664953 ± 0.000009 d.

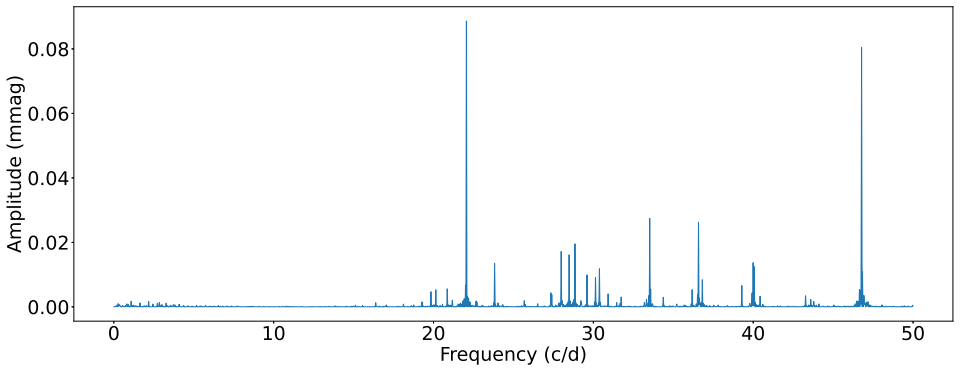

Figure P.6: The Fourier transform of TOI 610 (TIC 80275202), created using the light curve in Figure P.4.

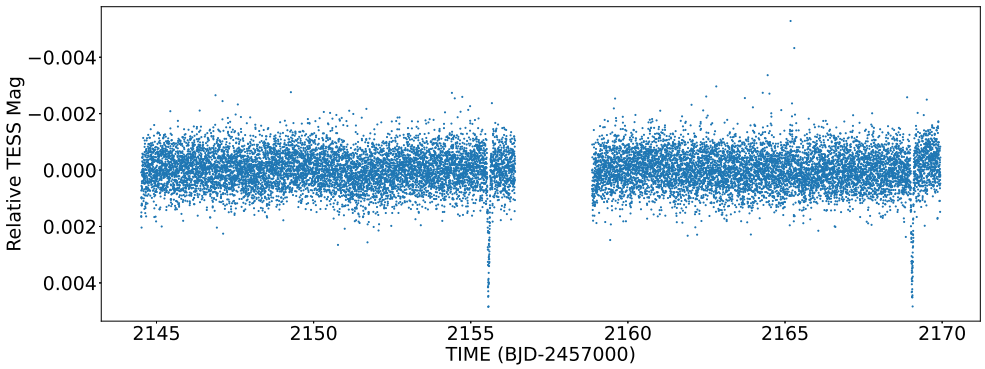

Figure P.7: The light curve of TOI 861 (TIC 372913430), created from TESS Sector 31 observations.

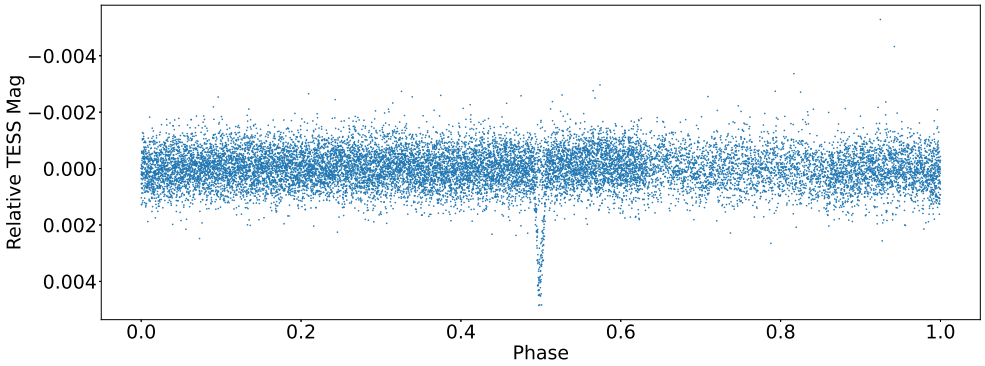

Figure P.8: The phase curve of TOI 861 (TIC 372913430), phased on its companion's orbital period of 6.739160 ± 0.000024 d.

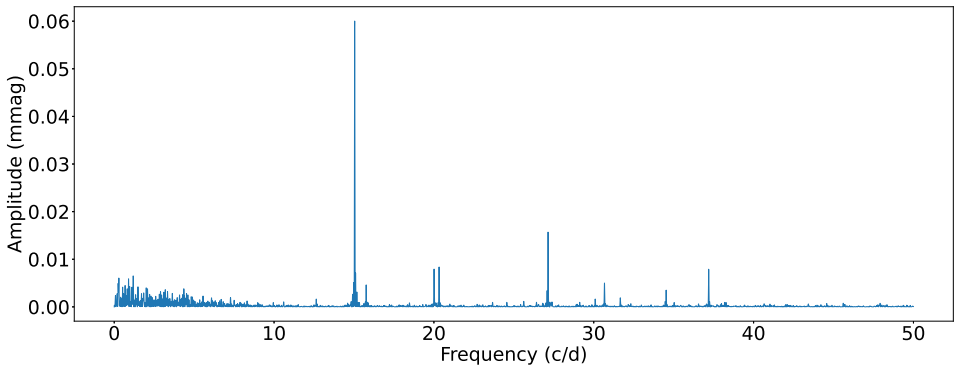

Figure P.9: The Fourier transform of TOI 861 (TIC 372913430), created using the light curve in Figure P.7.

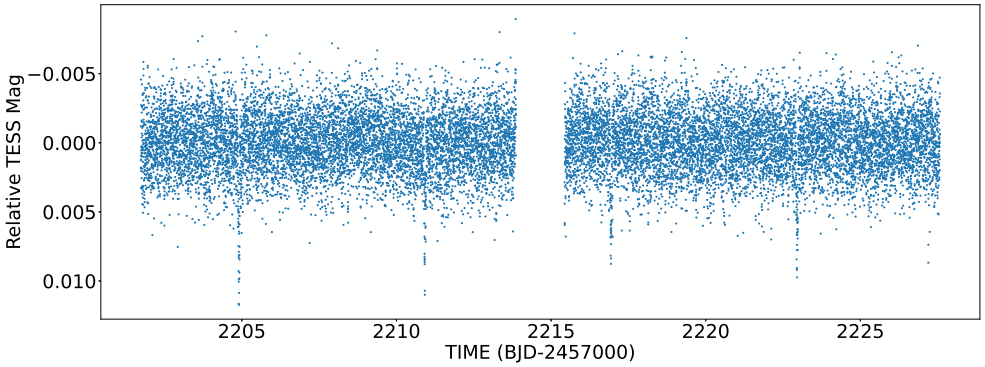

Figure P.10: The light curve of TOI 877 (TIC 255704097), created from TESS Sector 33 observations.

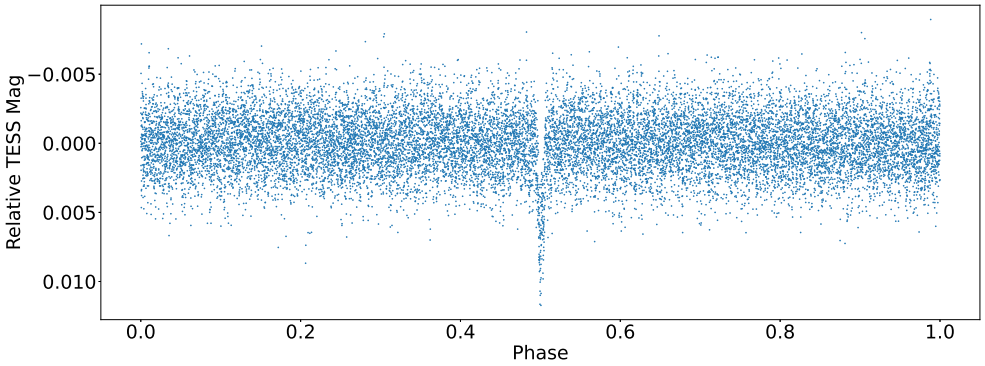

Figure P.11: The phase curve of TOI 877 (TIC 255704097), phased on its companion's orbital period of 6.014943 ± 0.000659 d.

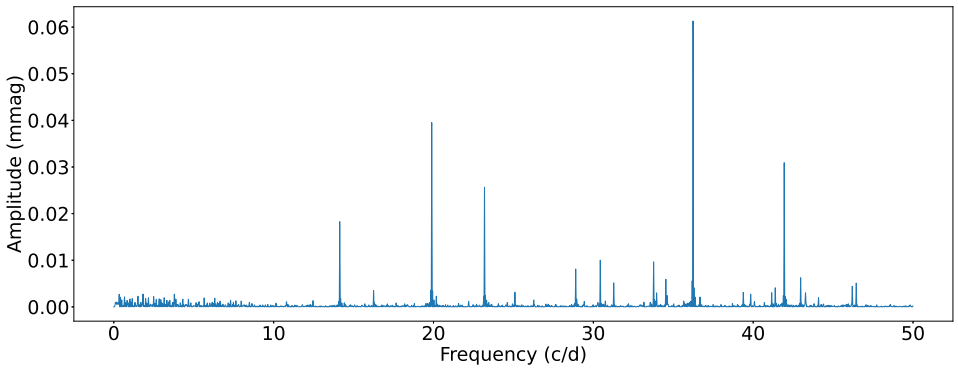

Figure P.12: The Fourier transform of TOI 877 (TIC 255704097), created using the light curve in Figure P.10.

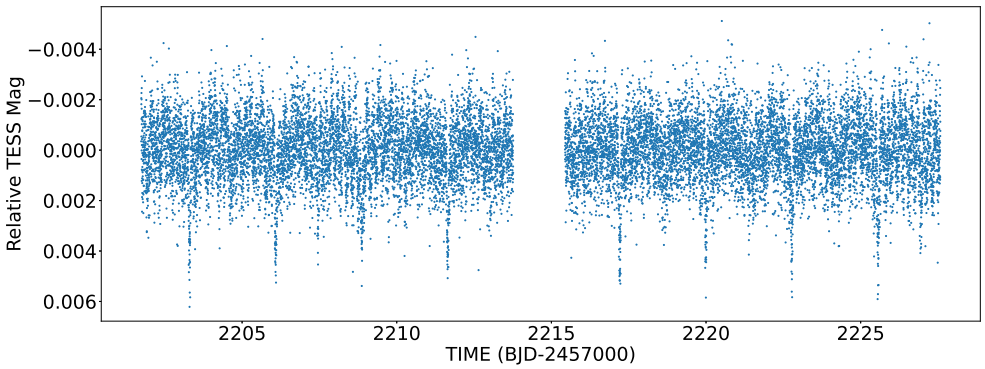

Figure P.13: The light curve of TOI 884 (TIC 167031605), created from TESS Sector 33 observations.

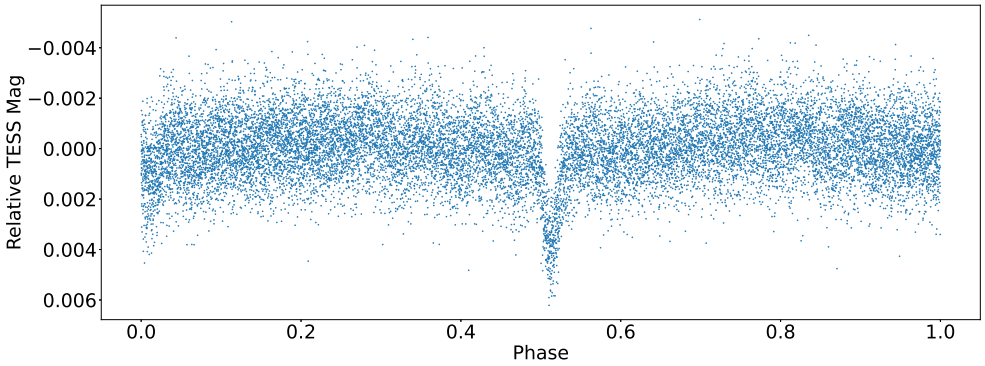

Figure P.14: The phase curve of TOI 884 (TIC 167031605), phased on its companion's orbital period of 2.780900 ± 0.000610 d.

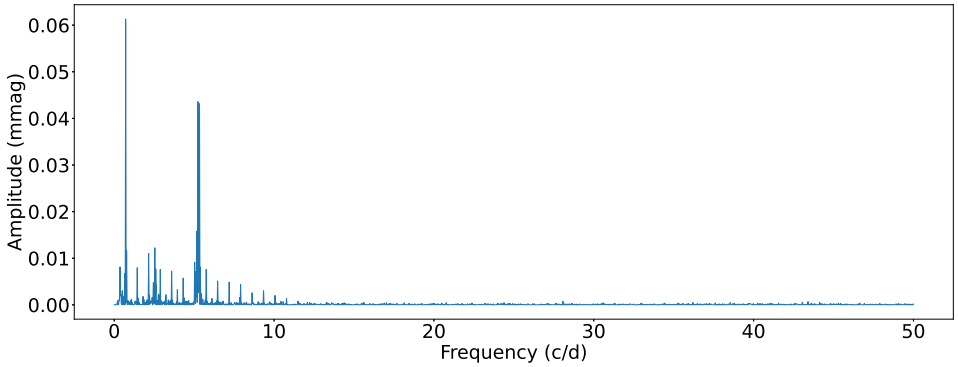

Figure P.15: The Fourier transform of TOI 884 (TIC 167031605), created using the light curve in Figure P.16.

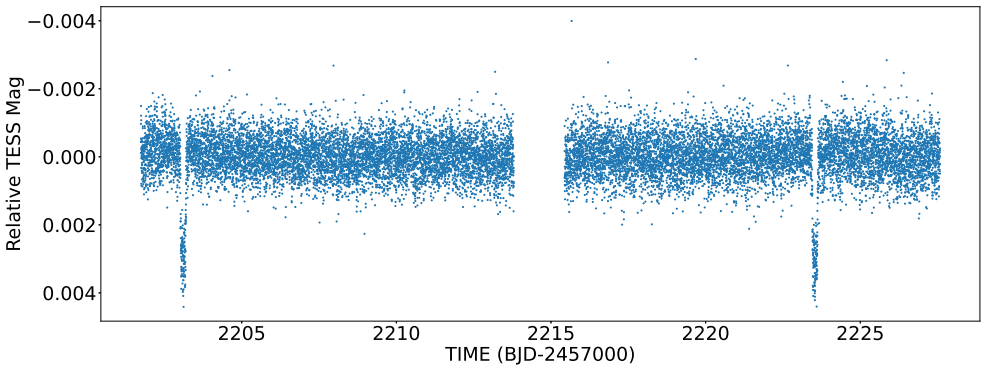

Figure P.16: The light curve of TOI 886 (TIC 120269103), created from TESS Sector 33 observations.

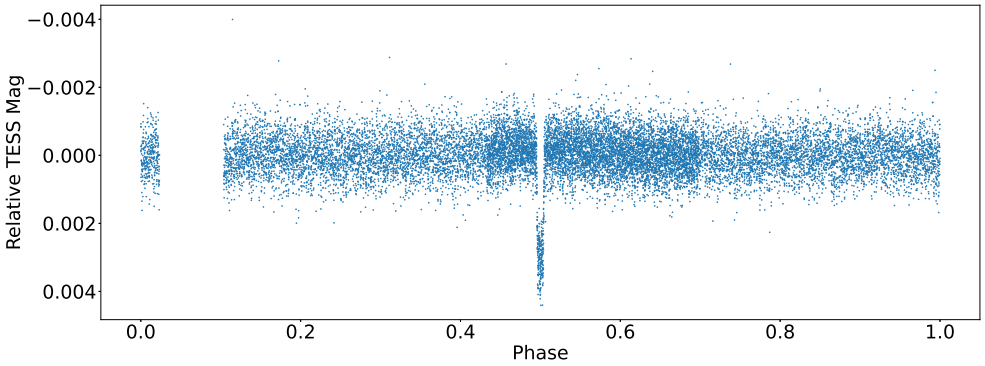

Figure P.17: The phase curve of TOI 886 (TIC 120269103), phased on its companion's orbital period of 20.427673 ± 0.002103 d.

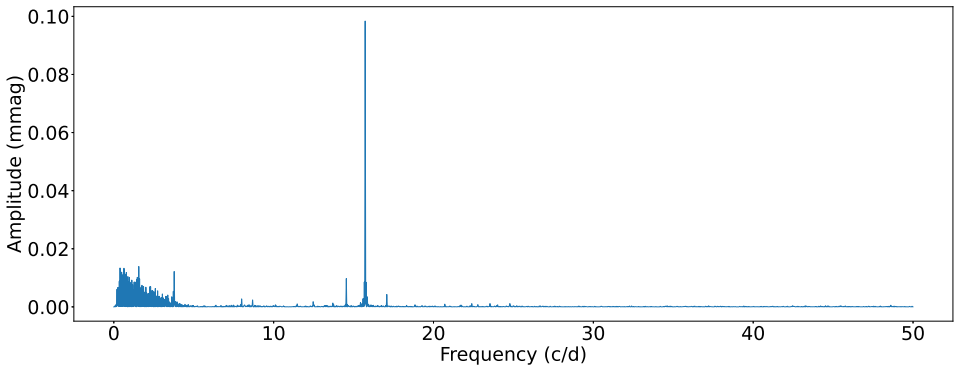

Figure P.18: The Fourier transform of TOI 886 (TIC 120269103), created using the light curve in Figure P.16.

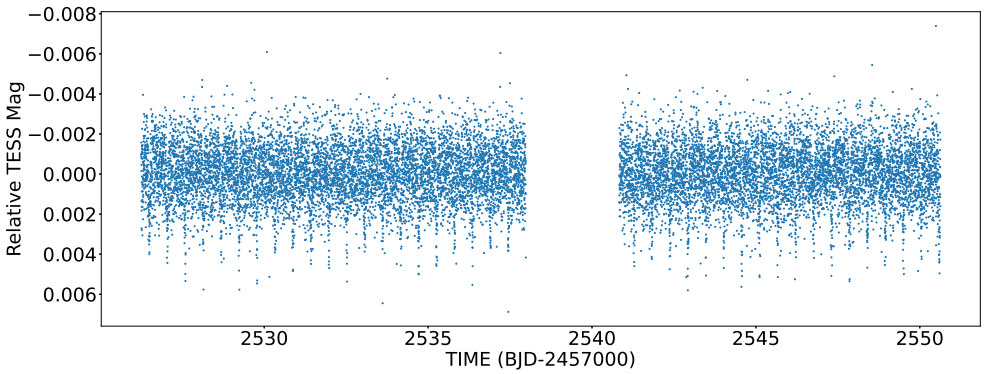

Figure P.19: The light curve of TOI 522 (TIC 320536216), created from TESS Sector 45 observations.

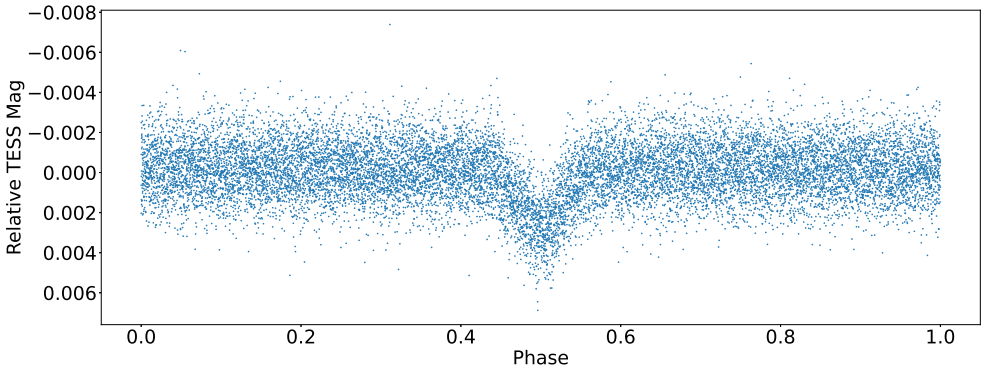

Figure P.20: The phase curve of TOI 522 (TIC 320536216), phased on its companion's orbital period of 0.547669 ± 0.000000 d.

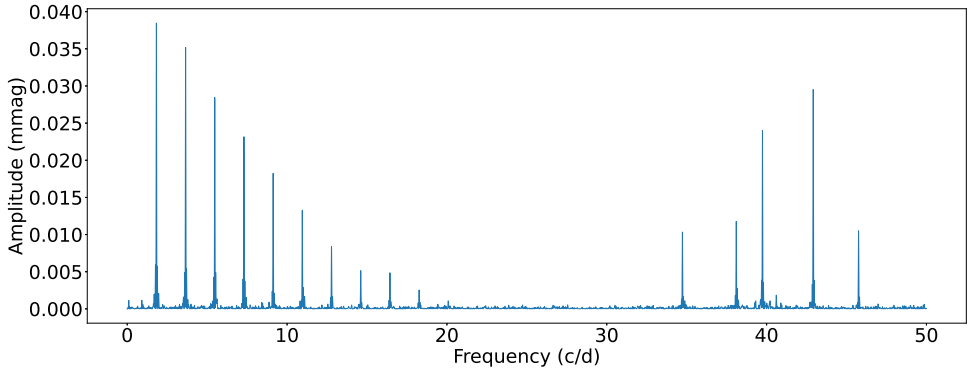

Figure P.21: The Fourier transform of TOI 986 (TIC 320536216), created using the light curve in Figure P.19.

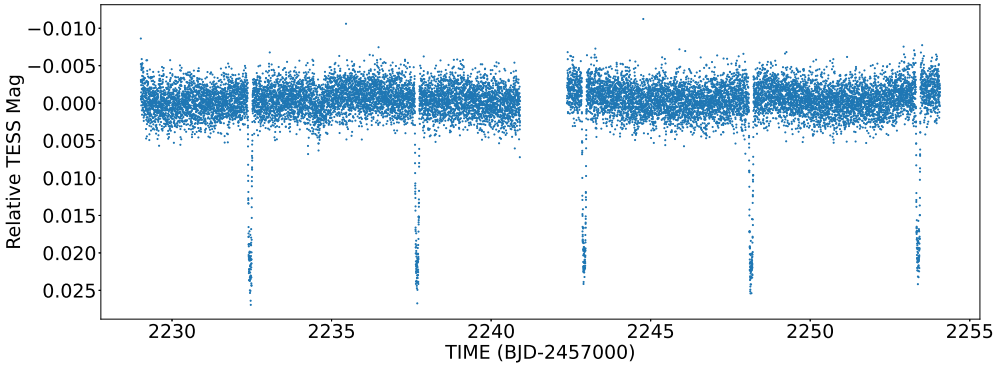

Figure P.22: The light curve of TOI 1019 (TIC 341420329), created from TESS Sector 34 observations.

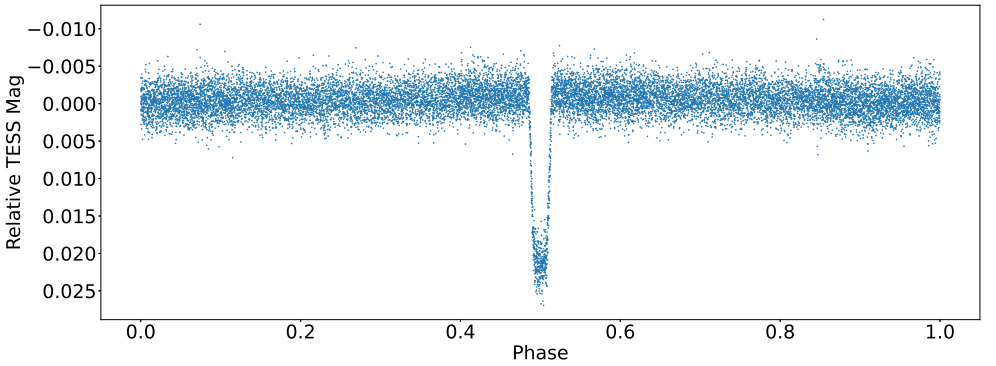

Figure P.23: The phase curve of TOI 1019 (TIC 341420329), phased on its companion's orbital period of 5.234096 ± 0.000027 d.

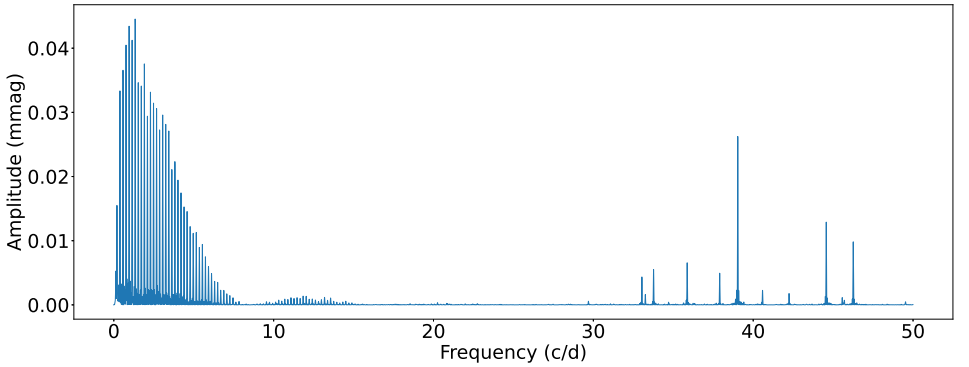

Figure P.24: The Fourier transform of TOI 1019 (TIC 341420329), created using the light curve in Figure P.22.

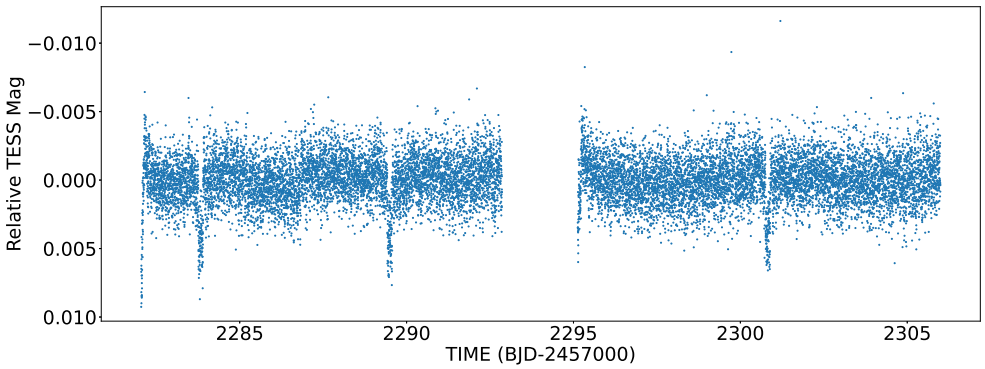

Figure P.25: The light curve of TOI 1032 (TIC 146589986), created from TESS Sector 36 observations.

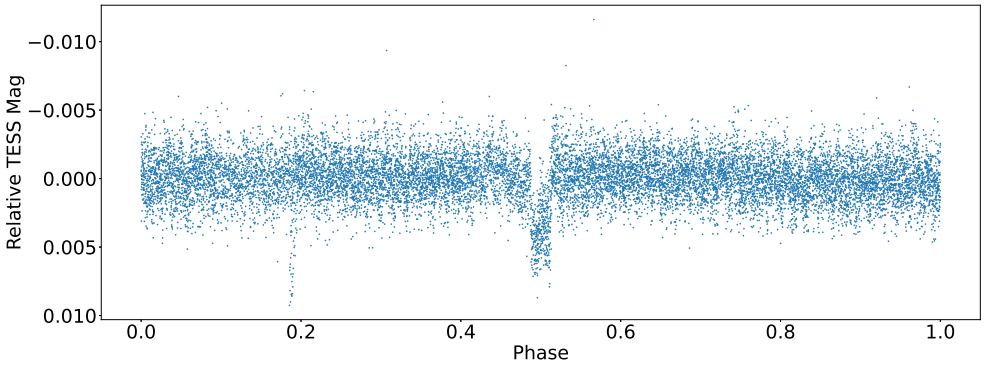

Figure P.26: The phase curve of TOI 1032 (TIC 146589986), phased on its companion's orbital period of 5.664473 ± 0.000769 d.

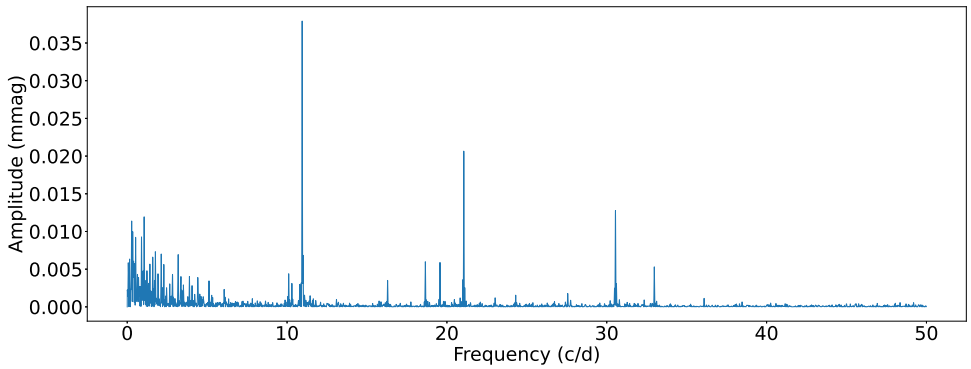

Figure P.27: The Fourier transform of TOI 1032 (TIC 146589986), created using the light curve in Figure P.25.

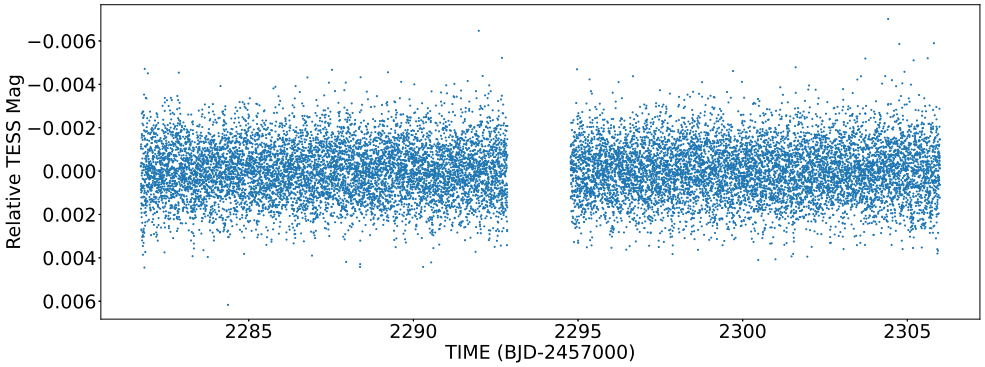

Figure P.28: The light curve of TOI 522 (TIC 400595342), created from TESS Sector 36 observations.

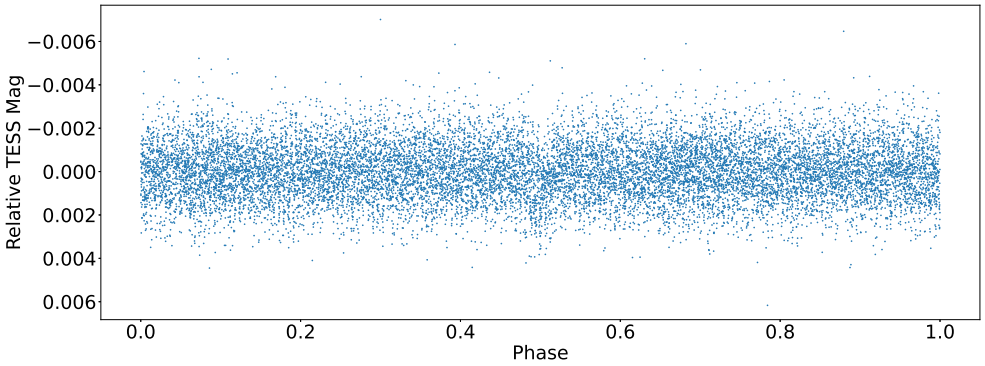

Figure P.29: The phase curve of TOI 522 (TIC 400595342), phased on its companion's orbital period of 3.634469 ± 0.000977 d.

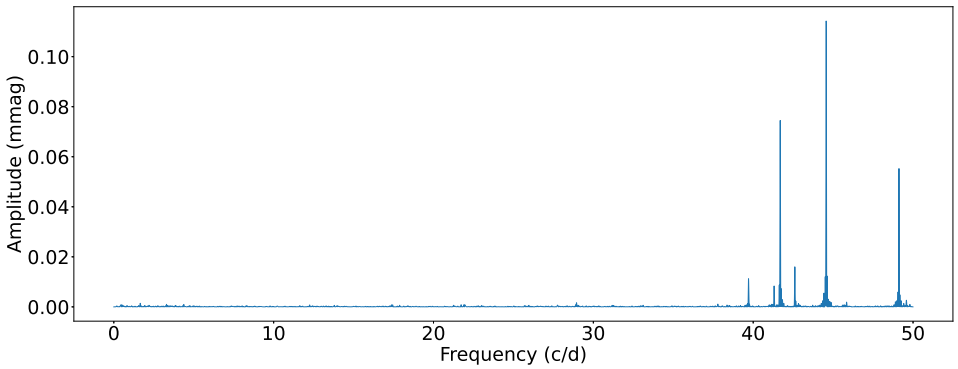

Figure P.30: The Fourier transform of TOI 522 (TIC 400595342), created using the light curve in Figure P.28.

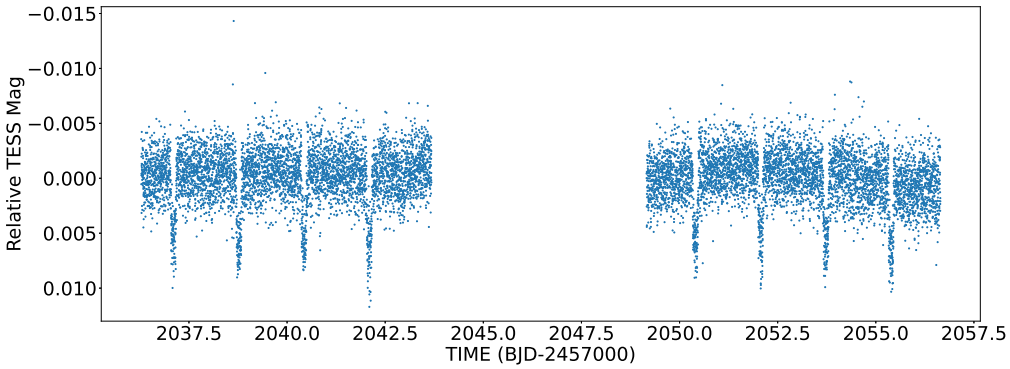

Figure P.31: The light curve of TOI 1120 (TIC 143257766), created from TESS Sector 27 observations.

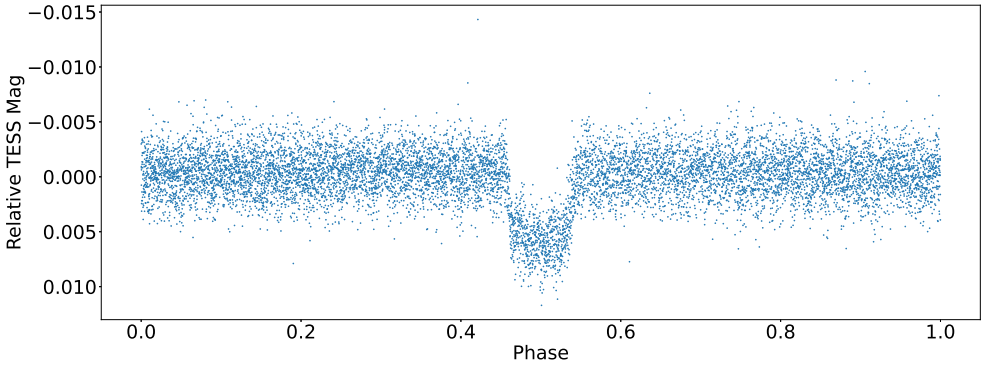

Figure P.32: The phase curve of TOI 1120 (TIC 143257766), phased on its companion's orbital period of 1.66226 d.

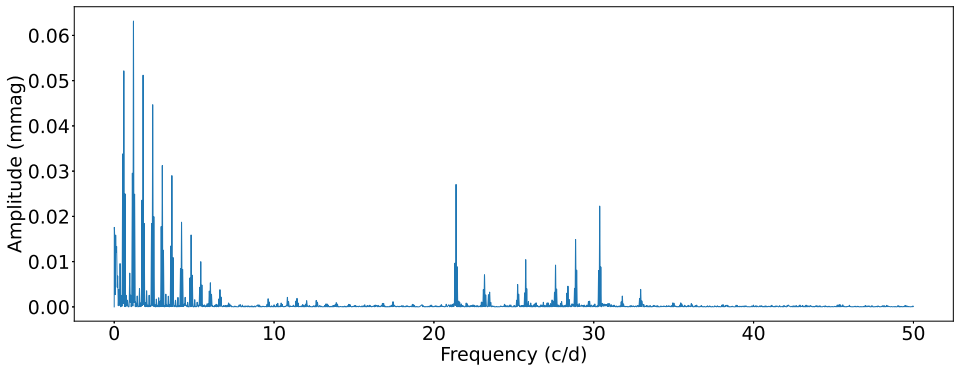

Figure P.33: The Fourier transform of TOI 522 (TIC 143257766), created using the light curve in Figure P.31.

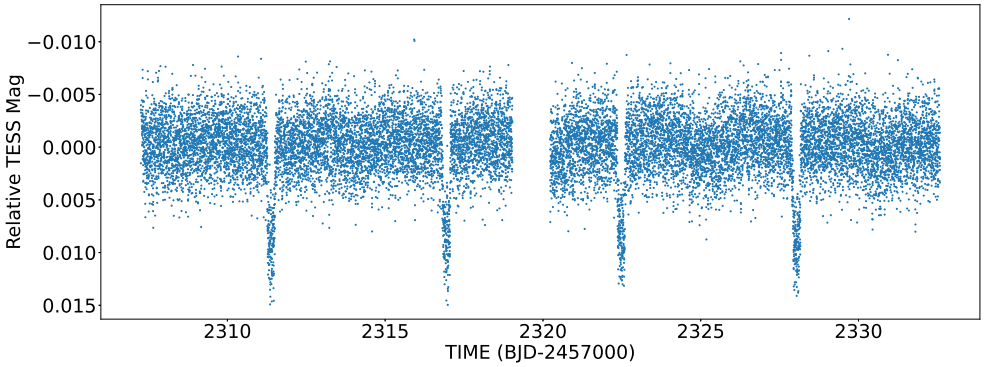

Figure P.34: The light curve of TOI 1888 (TIC 459997997), created from TESS Sector 37 observations.

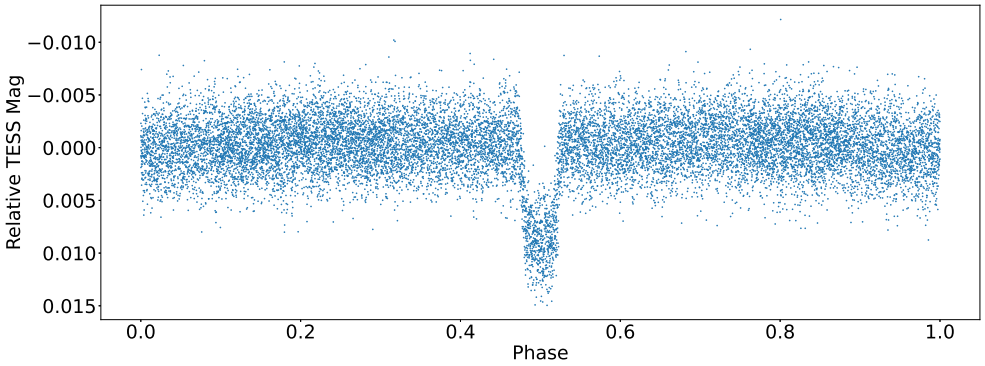

Figure P.35: The phase curve of TOI 1888 (TIC 459997997), phased on its companion's orbital period of 5.547485 ± 0.000025 d.

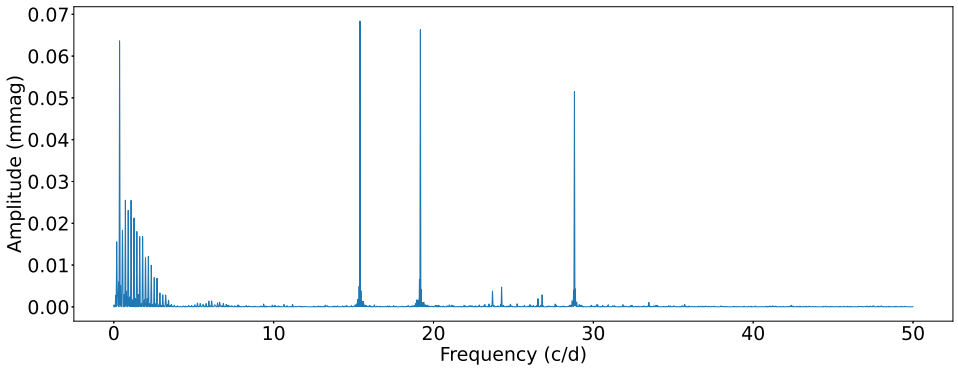

Figure P.36: The Fourier transform of TOI 1888 (TIC 459997997), created using the light curve in Figure P.34.

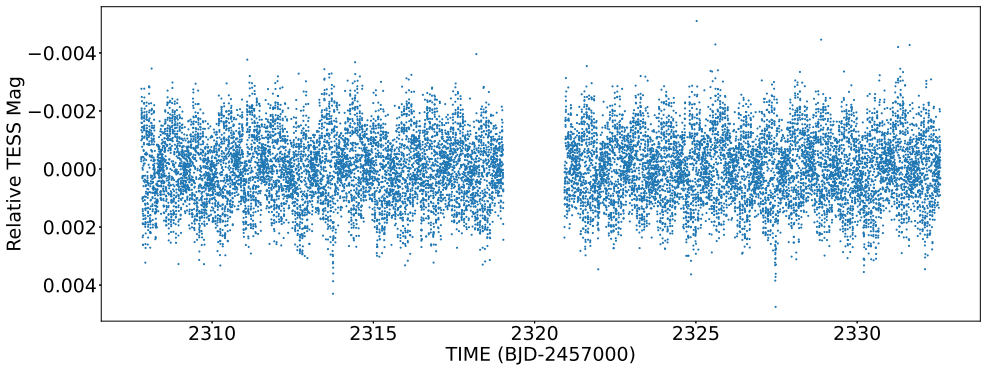

Figure P.37: The light curve of TOI 2001 (TIC 118084044), created from TESS Sector 37 observations.

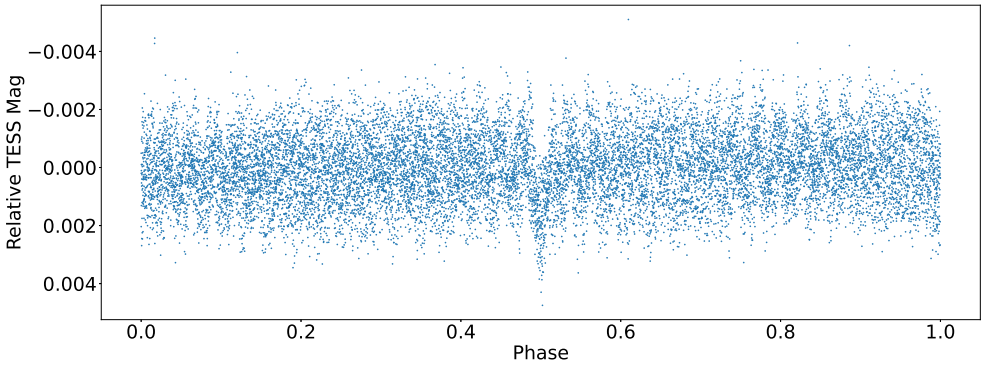

Figure P.38: The phase curve of TOI 2001 (TIC 118084044), phased on its companion's orbital period of 2.743456 ± 0.000124 d.

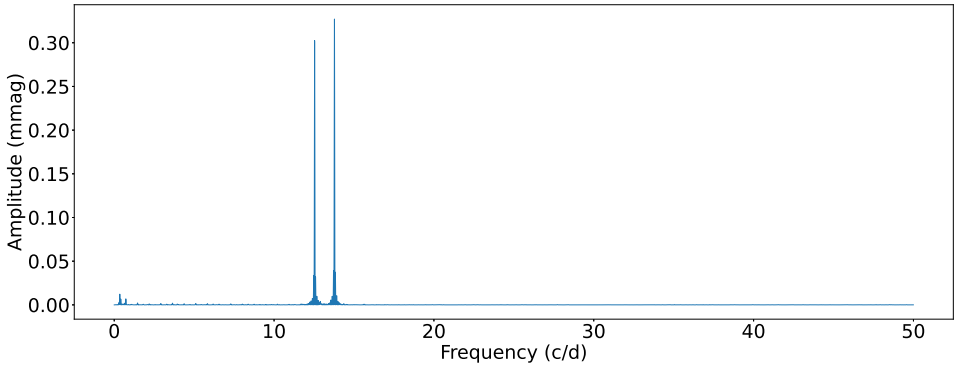

Figure P.39: The Fourier transform of TOI 2001 (TIC 118084044), created using the light curve in Figure P.37.

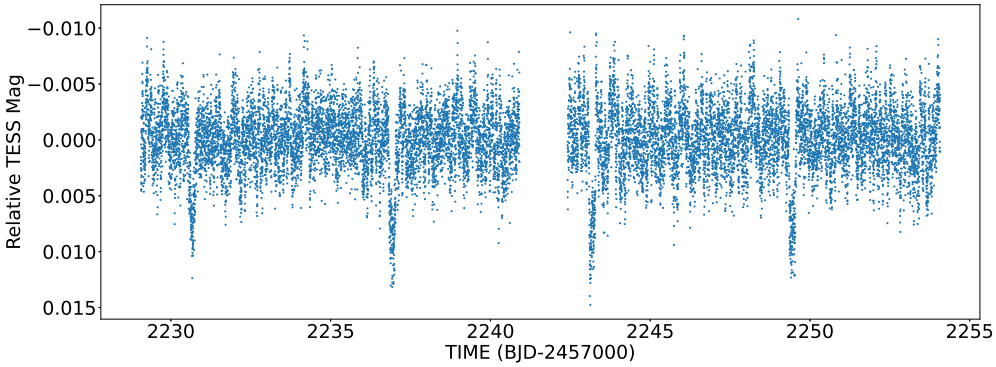

Figure P.40: The light curve of TOI 2554 (TIC 144043410), created from TESS Sector 34 observations.

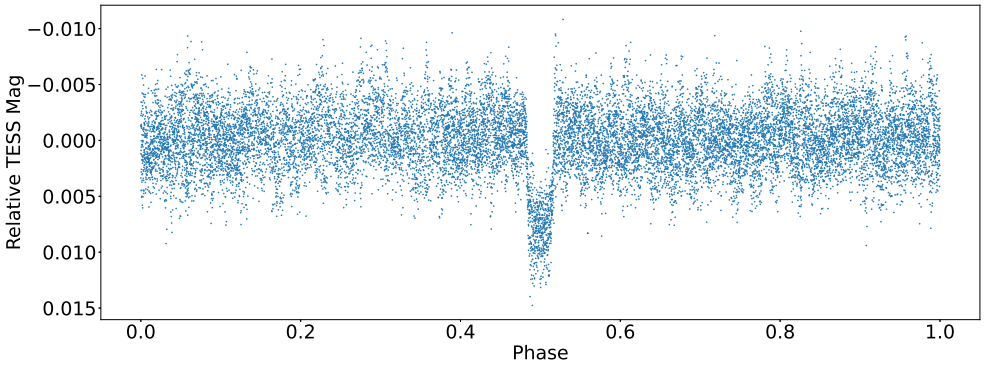

Figure P.41: The phase curve of TOI 2554 (TIC 144043410), phased on its companion's orbital period of 6.263650 ± 0.001046 d.

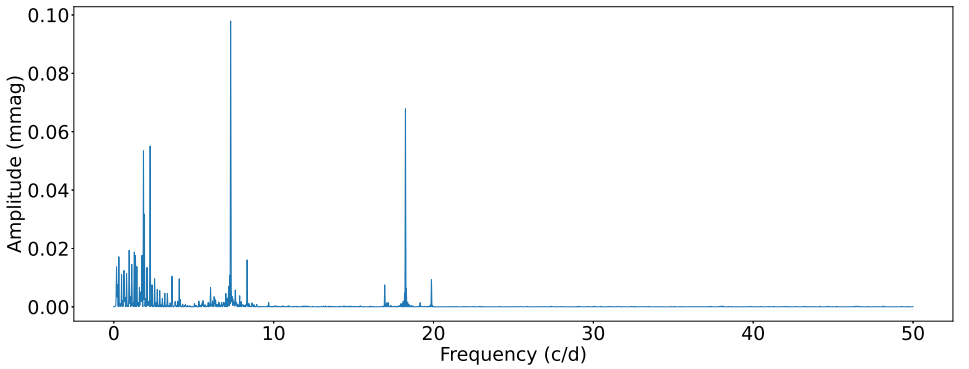

Figure P.42: The Fourier transform of TOI 2554 (TIC 144043410), created using the light curve in Figure P.40.

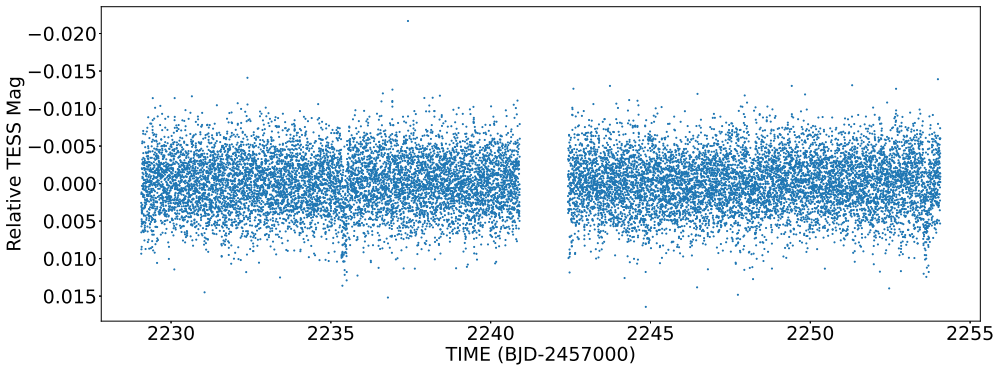

Figure P.43: The light curve of TOI 2633 (TIC 386131764), created from TESS Sector 34 observations.

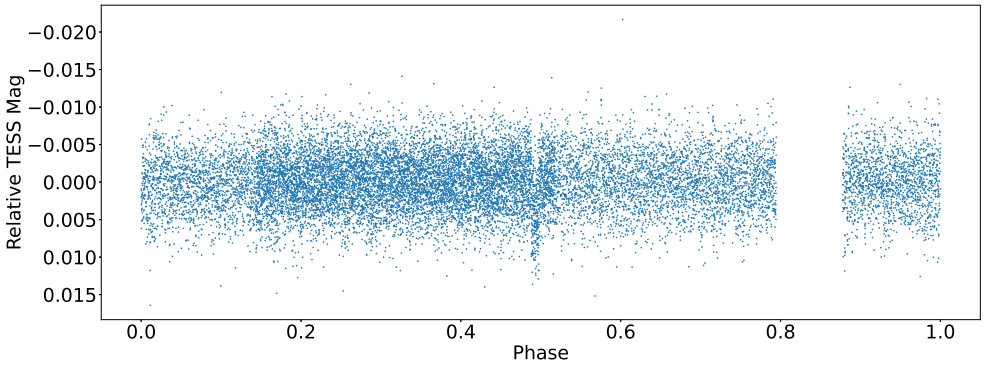

Figure P.44: The phase curve of TOI 2633 (TIC 386131764), phased on its companion's orbital period of 18.196049 ± 0.003232 d.

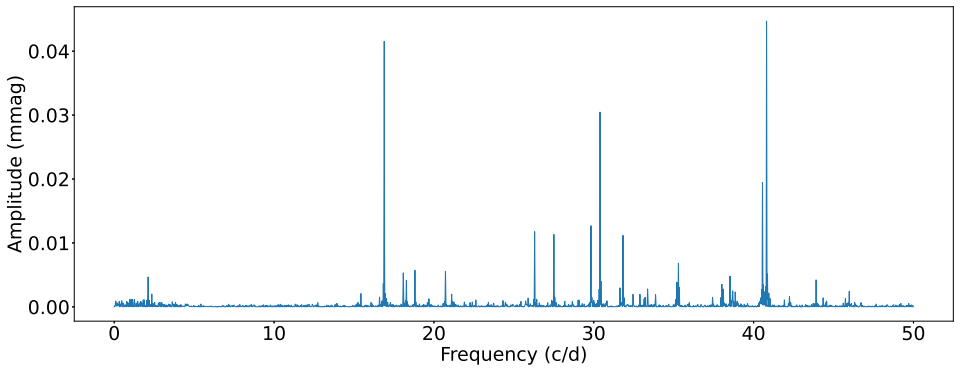

Figure P.45: The Fourier transform of TOI 2633 (TIC 386131764), created using the light curve in Figure P.43.